

LEVEL II

1

AGARD-AG-254

AGARD-AG-254

AGARD

ADVISORY GROUP FOR AEROSPACE RESEARCH & DEVELOPMENT

BULEVAR DE LA LIBERTE 1022100 MONTREUIL-SUR-SEINE FRANCE

AD A101446

AGARDograph No. 254

**Advances in Inertial Navigation
Systems and Components**

This document has been approved
for public release and sale; its
distribution is unlimited.

DTIC
ELECTE
S JUL 16 1981 **D**

F

NORTH ATLANTIC TREATY ORGANIZATION



DISTRIBUTION AND AVAILABILITY
ON BACK COVER

NORTH ATLANTIC TREATY ORGANIZATION
 ADVISORY GROUP FOR AEROSPACE RESEARCH AND DEVELOPMENT
 (ORGANISATION DU TRAITE DE L'ATLANTIQUE NORD)

AGARDograph No.254

ADVANCES IN INERTIAL NAVIGATION SYSTEMS
 AND COMPONENTS

Edited by

Dr. Helmut Sorg
 Universität Stuttgart
 Institut A fuer Mechanik
 Pfaffenwaldring 9
 D-7000 Stuttgart 80

11 Apr 81
 12 14 E

Accession For	
NTIS GRA&I	<input checked="" type="checkbox"/>
PTIC TAB	<input type="checkbox"/>
Unannounced	<input type="checkbox"/>
Justification for file	for file
By	
Distribution/	
Availability Codes	
Avail and/or	
Dist	Special
A	

DISTRIBUTION STATEMENT A

Approved for public release;
 Distribution Unlimited

THE MISSION OF AGARD

The mission of AGARD is to bring together the leading personalities of the NATO nations in the fields of science and technology relating to aerospace for the following purposes:

- Exchanging of scientific and technical information;
- Continuously stimulating advances in the aerospace sciences relevant to strengthening the common defence posture;
- Improving the co-operation among member nations in aerospace research and development;
- Providing scientific and technical advice and assistance to the North Atlantic Military Committee in the field of aerospace research and development;
- Rendering scientific and technical assistance, as requested, to other NATO bodies and to member nations in connection with research and development problems in the aerospace field;
- Providing assistance to member nations for the purpose of increasing their scientific and technical potential;
- Recommending effective ways for the member nations to use their research and development capabilities for the common benefit of the NATO community.

The highest authority within AGARD is the National Delegates Board consisting of officially appointed senior representatives from each member nation. The mission of AGARD is carried out through the Panels which are composed of experts appointed by the National Delegates, the Consultant and Exchange Programme and the Aerospace Applications Studies Programme. The results of AGARD work are reported to the member nations and the NATO Authorities through the AGARD series of publications of which this is one.

Participation in AGARD activities is by invitation only and is normally limited to citizens of the NATO nations.

The content of this publication has been reproduced directly from material supplied by AGARD or the author.

Published April 1981

Copyright © AGARD 1981
All Rights Reserved

ISBN 92-835-1383-5



Printed by Technical Editing and Reproduction Ltd
Harford House, 7-9 Charlotte St, London, W1P 1HD

PREFACE

The topic of this Agardograph has already been the subject of three symposia of the Guidance and Control Panel, two meetings in 1968 and the third meeting in 1972. To update their activities, the Guidance and Control Panel decided to cover the state of the art in an AGARDograph.

The period between 1972 and today can be characterized by three major developments: the dry tuned gyro, the laser gyro and the strapdown technology. And for all developments two important goals had to be considered, to reduce the costs and at the same time to increase the reliability. The papers of this AGARDograph are reports on recent developments and thus contribute to show the state of the art.

I have to express my sincere thanks to all the authors as well as to the people of AGARD-Headquarters in Paris.

HELMUT W.SORG
Editor

CONTENTS

	Page
PREFACE by H.W.Sorg	iii
	Reference
→ TUNED GYRO COST REDUCTION THROUGH A NOVEL HINGE DESIGN by R.Haberland and H.Karnick	1
→ OPTICAL ROTATION RATE SENSORS by G.E.Knausenberger	2
→ A NUCLEAR MAGNETIC RESONANCE GYRO USING NOBLE GAS ISOTOPES by E.Kanegsberg	3
→ HAMILTON STANDARD SUPERJET™ SOLID STATE FLUIDIC RATE SENSOR by R.E.Swartz, R.J.Slabinski and M.F.Lopiccolo	4
→ THE CACTUS ACCELEROMETER by A.Bernard, M.Gay and R.Juillerat	5
→ INERTIAL SYSTEM ALIGNMENT AND CALIBRATION ON A MOVING BASE by M.B.Ignagni	6
→ IDENTIFICATION AND DETERMINATION OF STRAPDOWN ERROR-PARAMETERS BY LABORATORY TESTING by D.K.Joos and U.K.Krogmann	7

Tuned Gyro Cost Reduction Through
a Novel Hinge Design

by
Dr. Rüdiger Haberland
and
Hartmut Karnick

ANSCHUTZ & CO GMBH
Postfach 6040 2300 Kiel 14
Germany

Summary

A fundamental study on cost reduction of dynamically tuned gyros funded by the German Ministry for Research and Technology yielded a novel type of gyro suspension which is, besides advantages in gyro design and operation, suited to generate remarkable direct and indirect cost reductions. The paper surveys the relations between the characteristics of a dtg suspension and the gyro production effort. The novel hinge is described, the direct cost advantages due to its design principle and technology are discussed. Indirect cost-saving consequences of using the novel hinge or such one of comparable goodness and the limits of their utilization are considered with respect to a homologous series of strapdown gyroscopes.

The research work dealt with in this paper has been sponsored by the German Minister for Research and Technology under contract no. 13 N 1015. The contents, however, underly the sole responsibility of the authors.

Symbols

a	acceleration, esp. by shock	m	rotor mass
a_r	radial -	m_K	gimbal mass
A_j	rotor moments of inertia about	N	spin speed
B	axes at right angles to spin	P_F	torquing power
C	rotor moment of inertia about	R	rotor radius
	spin axis	Δ	axial separation of suspension
A_K, B_K, C_K	applying to gimbal		axes from each other
d	angular spring rate of suspension	s_r	radial oscillating amplitude
e_{Kz}	axial separation of gimbal	T	temperature
	mass centre from suspension	s_e	detuning sensitivity
	centre	s_{d2N}	2-N angular sensitivity
E'	modulus of elasticity	s_{r2N}	2-N radial sensitivity
F	suspension load	u_e	drift due to detuning
f_Q	torquer Q-factor	u_d	--- 2-N angular oscillation
f_G	suspension Q-factor	u_{ar}	--- 2-N radial -
f_R	rotor Q-factor	ω_P	torquing rate
f_{GR}	rotor-suspension Q-factor	ω_N	nutation frequency
F_M	Craig's figure of merit	σ	admissible stress in spring
H	angular momentum of spinning rotor	e	rotor offset with respect to case
J	$1/2 (A_K + B_K - C_K)$	θ	shaft or case angle with respect
k_C	rotor inertia factor		to the inertial frame about an
k_M	rotor mass factor		axis perpendicular to spin
L_L	axial bearing distance		

Subscript "0": Nominal design values

Subscript "h": values of bias state

1. Introduction

The elastic suspension plays a key role in a dynamically tuned gyro, not only for its operation and performance but not less for its total production effort. Keeping this in mind, a well-aimed suspension development became one central objective of a fundamental study on cost reduction of dtg's for commercial use funded by the German Ministry for Research and Development in 1974 to 1979. It resulted in a unique novel hinge design described in the second section.

To better understand the aspects of the development, some discussion might be useful on the major relations between the characteristics of a dtg suspension and the effort to produce a gyro using that suspension. They are schematically shown in the diagram fig. 1. The interrelations of the geometric design and the applied technology and their direct effect on the effort needed for machining and assembling the suspension are evident. The tasks of tuning and gimbal balancing are conventionally ascribed to the common gyro test and calibration procedure; in a more detailed sense, however, they can be considered to be a matter of the suspension - as particularly will appear in the later discussion. These items including the necessary tests can occupy a considerable share of the suspension production effort; the best means to reduce their effort is to omit or to significantly simplify them. This is favoured by good inherent machining quality of the chosen technology and good performance characteristics of the suspension type.

The effect of the suspension's performance capability on the gyro production effort needed to meet given specifications, may equal or exceed that one of the direct manufacturing and integration effort of the suspension. Fig. 2 shows the primary mechanisms. Keeping all sensitivities low - detuning, 2-N angular, anisoelectricity, 2-N radial - facilitates the quality requirements noted on the bottom of the diagram and thereby cheapens a gyro. Low sensitivities result from high values of the characteristic magnitudes in the second line of the diagram: load capability, rotatory compliance, translatory stiffness, and the typical hinge features mentioned (although these are no performance characteristics in a severe sense).

An exception has to be made regarding the relation of load capability and anisoelectricity sensitivity. While utilizing high load capability by using large rotor mass decreases all other sensitivities due to the increase of the angular momentum, this measure generally tends to slightly increase the sensitivity with respect to a isoelasticity which is proportional to the square of the rotor mass. Linear growth of a rotor increases the angular momentum according to the fifth, the square of the rotor mass according to the sixth power. Other important limiting factors for choosing the rotor mass are the required torquing power - which is proportional to the square of the angular momentum - and resonance frequency considerations.

The manifold relations between the characteristics of a gyro suspension and the total manufacturing cost of the gyro shortly discussed above formed a guideline for the development of the novel hinge which will be described now.

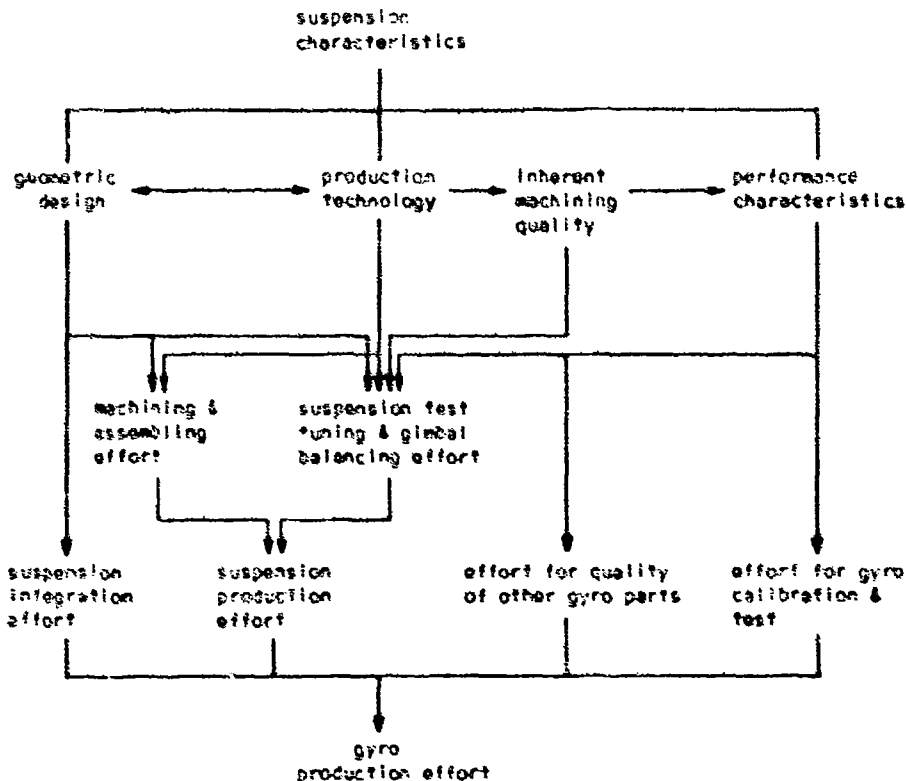


Fig. 1 Relation network between suspension characteristics and dtg production effort

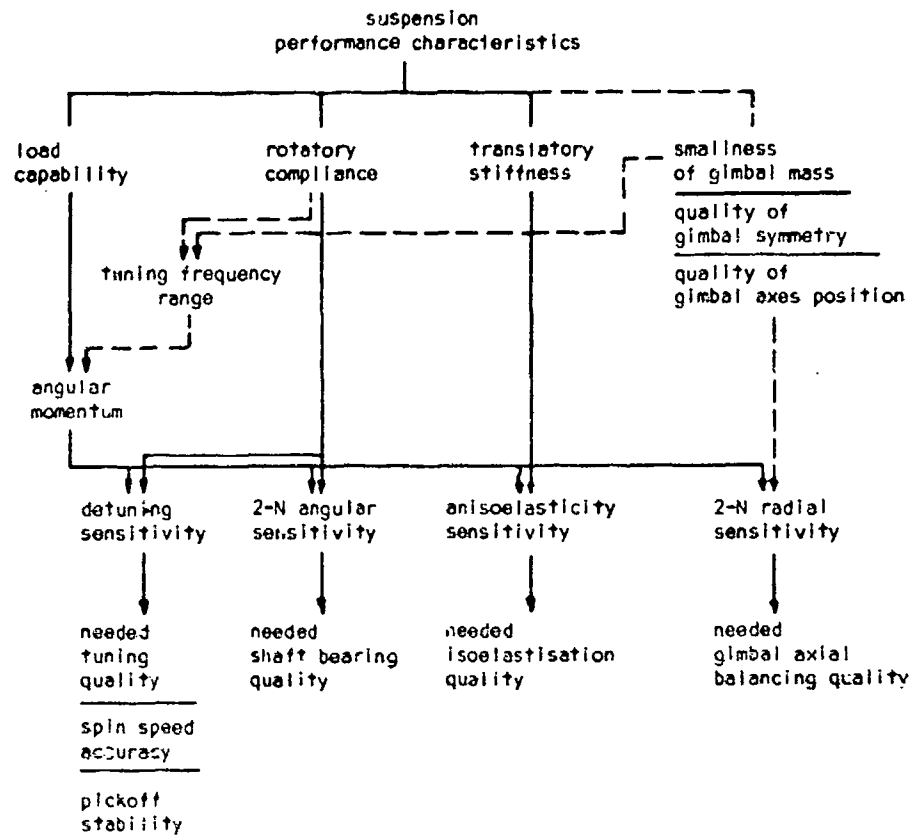


Fig. 2 Relation network between suspension performance and needed quality of gyro parts/calibrations/operation parameters. (The dotted lines affiliate indirectly performance-effective parameters)

2. The Novel Hinge and its Technology

Principle

The conventional cross-flexure-hinge is using separated flexure leaves.

The novel hinge design is leaving this principle by connecting the flexure leaves to each other at the deflection axis, thus creating new and unexpected properties most of which contribute to gyro quality. Clearer than explanations the figures 3 and 4 show the new hinge - named UKF* - in principle and as deflected.

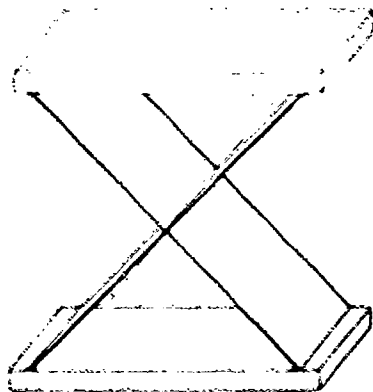


Fig. 3 UKF - unseparated cross flexure hinge

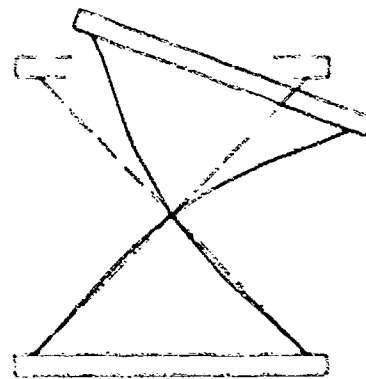


Fig. 4 Deflected UKF, the axis remains stationary despite deflection

In a single-gimbal, dry tuned gyro (dtg) two of these hinges form one suspension axis. The complete 2-axis dtg suspension thus consists of four hinges.

It is obvious that this UKF-hinge has a somewhat higher deflection stiffness than a conventional cross flexure hinge of the same flexure dimensions, but can also accommodate more than double the buckling force. Hence its optimization laws differ significantly from those of a conventional cross flexure hinge.

Important differences

Important differences between the UKF and the conventional cross flexure hinge in a dtg suspension are:

- The UKF leaves - due to their mutually traversing arrangement - occupy less than half the radial space of the flexures of a conventional hinge, resulting in an unequaled small suspension diameter.
- The tolerable (no load) deflection angle of the UKF is approximately half the value of the conventional hinge.
- The linear compliances equal those of a conventional hinge as the translational deformation of the flexures is not significantly affected by their central connection.
- The buckling strength is doubled in comparison to a conventional cross flexure hinge due to the central connection and further increased due to a considerable decrease of sensitivity to flexure shape tolerances.
- The definition of the angular deflection axis is significantly more precise than in a conventional cross flexure hinge. The axis location is unaffected by deflection.
- Load-dependent (twist) torques of a UKF are extremely low on account of its well-defined axis position.
- Load-dependent torques due to elastic deformation of the solid suspension portions are significantly lower with a UKF due to its compactness and symmetry.
- The compact UKF design renders smaller gimbal inertias than the conventional design, thus allowing higher tuning speed at equal angular spring rates and reducing gimbal balancing requirements.
- The principal geometry and compactness of the UKF design allow the manufacturing of monolithic suspensions by wire erosion with a minimum of steps and time and a maximum of accuracy.
- In-line machining of all flexure surfaces of one axis in one workpiece setting minimizes unwanted increase in deflection stiffness from misalignment of the two hinges of one axis and from misalignment of the two flexure leaves of one hinge.

Commons with other cross flexure hinges

Besides the mentioned differences there are some features which are not - or only slightly - different with the UKF and the conventional cross flexure hinge:

- Linear compliances can be calculated by the same equations.
- Isoelasticity can be achieved by using flexure crossing angles greater than 90 degrees.

An optimal UKF design makes use of some features which are found also in other hinges of highest quality:

- Flexures are profiled preferably with a slender circular curved contour, giving a marked increase in the ratio of load to angular spring rate.
- The complete dtg suspension is monolithic in order to avoid internal stress, to avoid load stress accumulations in the flexure end sections, and to obtain the best possible quality of geometry.

Technology

A specially adapted wire erosion technique proved to be best suited for manufacturing the UKF hinges and suspensions under the aspects of accuracy, economy and flexibility. Normal EDM will do also, but owns characteristic problems in making the electrodes and aligning the hinges to each other.

The UKF layout suited for single-gimbal DTGs to be cut on a wire EDM machine is shown in Fig. 5. All cuts for one axis are made in one position without any need of re-positioning, adjusting, and handling, the two hinges of one axis being cut simultaneously. After completion of the axis the workpiece is turned by 90 degrees and all cuts of the other axis are made. The benefits are evident: simultaneous cutting renders the best possible flexure orientation and minimum machining time. The compact design with a minimum of surfaces to be machined and the economical utilization of all eroded surfaces for suspension functions exhibit an optimum solution with respect to needed volume and production cost.

These positive aspects are not limited to single-gimbal DTGs, since by assembling pre-fabricated parts in a stage before cutting the flexures a pseudo-monolithic structure

can be achieved and the principal advantages in axis definition can be maintained. In a thorough experimental research the limits of this technique have been investigated and machining has been developed to a safe reproducible standard beyond the capability of any machine on the market. A pilot production of more than 40 suspensions yielded completely satisfying results considering machining time and quality. The achieved tolerances, better than necessary, qualify these suspensions for use in inertial grade gyros.

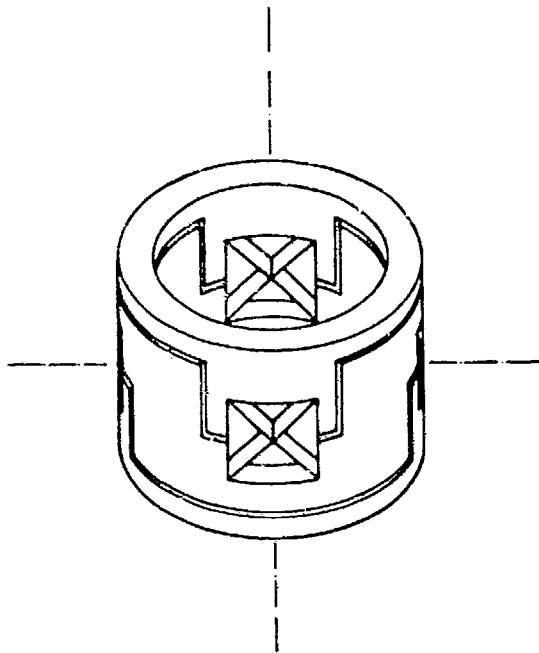


Fig. 5
UKF-Suspension for single gimbal DTG

3. Direct Cost Benefits of the Novel Hinge

Most of the earlier stated differences between the UKF hinge and conventional designs have a more or less significant influence on the production cost of a gyro.

The direct cost savings through the use of the UKF hinge, i. e. that ones related to production and integration of the suspension according to fig. 1, can be summarized as follows:

- minimization of needed material volume - less than half of a conventional suspension - results in less material and processing cost
- minimization of machined surfaces and re-setting steps, simultaneous cutting of the hinges of one complete axis, and abandoning leaf-separating operations render significantly less machining cost

- inherent axis position accuracy of the technology and smallness of the gimbal mass abolish the effort of gimbal balancing in nearly all cases
- decreased sensitivity of buckling strength to flexure shape and dimension allows greater flexure tolerances, resulting in higher cutting speed and less measuring effort.

4. Indirect Cost Savings by Using the Novel Hinge in a Gyro Design

Some possibilities of indirect cost reduction by using the optimized traversing-leaf (UKF) suspension may now be discussed, referring to the three predominant suspension-dependent sensitivity types of fig. 2. They can for this objective and for a single-gimbal gyro be described by these simplified equations:

Detuning sensitivity

$$s_{\tau} = \frac{v_{\tau}}{2N/N_0} = 2 \theta \frac{d_0}{N} \quad (1)$$

2-N angular sensitivity

$$s_{d2N} = \frac{v_{d(2N)}}{\theta_{2N}} = \frac{1}{2} \frac{d_0}{N} \quad (2)$$

1-K radial sensitivity

$$s_{r2N} = \frac{v_{r(2N)}}{a_{r2N}} = \frac{1}{4N} (2s_2 \cdot m_K e_{F_2}) \quad (3)$$

Herein the suspension characteristics appear as d_0/N - the ratio of rotatory stiffness and angular momentum, which latter is related to the suspension's load capability -, as the axial separation s_2 of both gimbal axes, and the gimbal pendulosity $m_K e_{F_2}$.

Determining their effect in quantity requires to quantify their magnitudes for real gyros of varying size and related performance, i. e. the use of suited dimensioning and growth laws of tuned gyros. The needed relations and magnitudes will be summarized in the following section.

Design magnitudes of dynamically tuned gyros

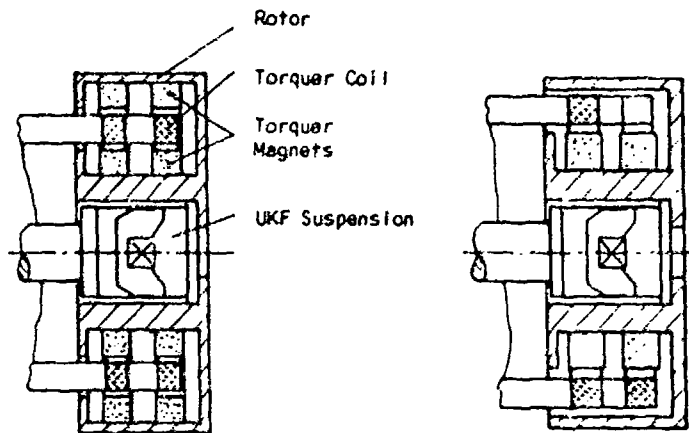


Fig. 6
Rotor-Suspension-Sets for Strapdown Use
a: 4-Magnet Torquer, b: 2-Magnet Torquer

The main performance characteristics of a homologous series can be expressed by almost fully size-independent coefficients and quality factors which are determined by ratios of dimensions and by material parameters. The coefficients vary by less than 2% over the considered range of rotor radii of 12 to 23 mm; just the suspension Q-factor, however, may significantly decrease from its thus calculated value at radii falling under 16 mm due to technological thickness limits of the suspension leaves. Such decrease is recognized in the later calculations and diagrams.

The design coefficients of the chosen exemplary gyro configuration are listed in table 1.

The rotor-suspension Q-factor f_{GR} might deserve some interest in comparison with Craig's figure of merit

$$f_m = \frac{N^2}{2} \frac{C}{d} \quad (4)$$

as another widely used performance parameter. Both coefficients in a particular manner represent the ratio C/d which determines the detuning and 2-N angular sensitivity according to equations (1) and (2).

f_{GR} is independent on size and spin speed, but recognizes the admissible shock acceleration, and therefore is a universal and very suitable measure for the performance capability of a mechanical rotor-torquer-suspension design. To describe the detuning and 2-N angular sensitivities of a specific gyro requires additional data on spin speed, rotor size, and admissible shock acceleration.

f_m is a measure for the detuning and 2-N angular sensitivities of a specific gyro if accompanied by information on the spin speed. To compare the efficiency of different gyro designs requires additional data on rotor size and admissible shock acceleration.

Table 1

Design coefficients of optimized gyros with 4-magnet $\Sigma\Omega\Omega$ torquer, nutation frequency $\omega_n = 1.77$ Hz, and traversing-leaf suspension for rotor radii between 12 and 23 mm resp. 16 and 23 mm (1).

Coefficient	Definition	Typical Value	
rotor mass factor	$f_B = \frac{m}{m_0}$	7600	$\frac{m}{m_0}$
rotor inertia factor	$f_C = \frac{C}{C_0}$	4100	$\frac{C}{C_0}$
suspension Q-factor	$f_G = \frac{C}{d} \frac{1}{Q}$	$1.0 \cdot 10^3$	$\frac{C}{d} \frac{1}{Q}$ (1)
rotor Q-factor	$f_R = \frac{C}{d} \frac{1}{Q}$	$6.25 \cdot 10^{-3}$	$\frac{C}{d} \frac{1}{Q}$ (1)
rotor-suspension Q-factor	$f_{GR} = \frac{C}{d} \frac{1}{Q}$	635	$\frac{C}{d} \frac{1}{Q}$ (1)
torquer Q-factor	$f_T = \frac{C}{d} \frac{1}{Q}$	190	$\frac{C}{d} \frac{1}{Q}$

Using the design coefficients of table 1 for the following discussion requires to determine some further exemplary data which are chosen as:

$$\begin{aligned} \text{spin speed} & N = 2\pi \cdot 100 \text{ s}^{-1} \\ \text{shock acceleration (> 3 ms)} & a = 1000 \text{ m/s}^2 \end{aligned}$$

It should be noted that table 1 is valid for a relative nutation frequency of 1.77 this magnitude, however, being of moderate influence.

For ω_r ros thus specified characteristic data can be plotted versus the rotor radius as shown in fig. 7:

- the angular momentum H ,
- the specific torquing power P_F/ω_r^2 which in the gyro design has determining influence on the choice of the rotor radius,
- the characteristic ratio of angular momentum to spring rate H/d which determines the detuning and 2-N angular sensitivity.

For reference purposes a plot of Craig's f_m is added although incorporated in the H/d value. Two examples may be noted as typical data sets:

1. A 22 mm radius gyro needs a specific torquing power of $3 \text{ W}/(100^\circ/\text{s})^2$ and yields $H/d \approx 2 \text{ s}$ and $f_m \approx 600$.
2. A 15 mm radius gyro needs a specific torquing power of $.44 \text{ W}/(100^\circ/\text{s})^2$ and yields $H/d \approx 1.5 \text{ s}$ and $f_m \approx 450$.

The data plotted in fig. 7 represent the model gyro series for the following discussions on the effort aspects of the equations (1) to (3).

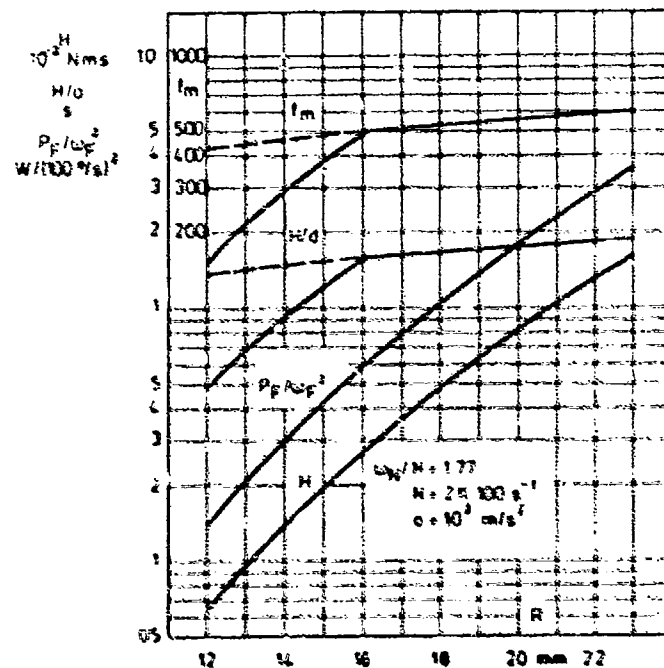


Fig. 7
Performance Data of Rotor-Suspension-Sets for Strapdown Use According to Fig. 6a. --- indicates theoretical data neglecting technological thickness limitations of monolithic springs.

Detuning Drift

For the following it is useful to express the detuning drift appearing in equation (1) as a function of the differences of the input magnitudes from their nominal design values which satisfy the tuning condition.

Generally the spring rate resulting from detuning

$$k_s = N^2 J - J$$

produces the drift rate

$$\omega_t = d_t \frac{\theta}{H} \quad (6)$$

Introducing $J = J_0 + \Delta J$, $N = N_0 + \Delta N$ and $d = d_0 + \Delta d$ with J_0 , N_0 , d_0 as the nominal design values and using the tuning condition

$$d_0 = J_0 N_0^2 \quad (7)$$

renders the resulting spring rate as

$$d_t = d_0 \left(2 \frac{\Delta N}{N_0} + \frac{\Delta J}{J_0} + \frac{\Delta d}{d_0} \right) \quad (8)$$

The effect of detuning requires attention in double respect:

The bias

$$\omega_{tb} = d_{tb} \frac{\theta}{H_b} \quad (9)$$

where the subscript b marks the magnitudes effective in the bias state, and its instability

$$\Delta \omega_t = d_{tb} \Delta \left(\frac{\theta}{H_b} \right) + \frac{\theta}{H_b} \Delta d_{tb} \quad (10)$$

Introducing the differences of actual from nominal values in the bias state, $\Delta_b N = N_b - N_0$, $\Delta_b J = J_b - J_0$, $\Delta_b d = d_b - d_0$, and the time-dependent variations with respect to the bias state, $\Delta \theta$, ΔN etc., yields the detuning bias

$$\omega_{tb} = \frac{\theta}{H/d_0} \left(2 \frac{\Delta_b N}{N_0} + \frac{\Delta_b J}{J_0} + \frac{\Delta_b d}{d_0} \right) \quad (11)$$

and the instability

$$\Delta \omega_t \approx \omega_{tb} \left(\frac{\Delta \theta}{\theta} - \frac{\Delta N}{N_0} - \frac{\Delta J}{J_0} \right) + \frac{\theta}{H/d_0} \left(2 \frac{\Delta N}{N_0} + \frac{\Delta J}{J_0} + \frac{\Delta d}{d_0} \right) \quad (12)$$

Now, regarding the aim of simplification and cost reduction, the question followed so far shall be inverted:

We will no longer primarily ask for the drift which comes as a result of detuning, but for the need and acuity of tuning to meet given drift specifications. Hereto we first look at the gyro which has not undergone any tuning procedures whatsoever in order to find out the limits within of which tuning - other than by design - will be needed at all.

Then we examine the gyro with tuning treatment in order to get knowledge on the required acuity of tuning and to reflect upon a cost-saving procedure.

The Tuning Error of an Untuned Gyro

"Untuned" stands for lacking any tuning treatment after machining the gyro piece-parts.

In the machining procedure the gimbal inertia J can be produced to match the nominal value within less than 1% without any particular effort, maintaining the nominal spin speed in the gyro operation to even much less is no problem either. The spring rate of the suspension, however, determined by the third power of the leaf thickness, due to the small absolute thickness dimensions constitutes the highly predominant share of the original tuning error. Thus equation (11) can be reduced for the untuned initial state with fully sufficient approximation to

$$\omega_{t0} = \frac{\theta}{H/d_0} \frac{\Delta_b d}{d_0} \quad (13)$$

wherein $\Delta_b d$ now stands for the difference of the spring rate from its nominal value. Is this in essential traced back to the mean thickness error of the spring leaves of one suspension, the maximum spring rate error $\Delta_b d/d_0$ and the resulting bias drift rate at a rotor offset of $\theta = 1^\circ$ come out as plotted in fig. 8.

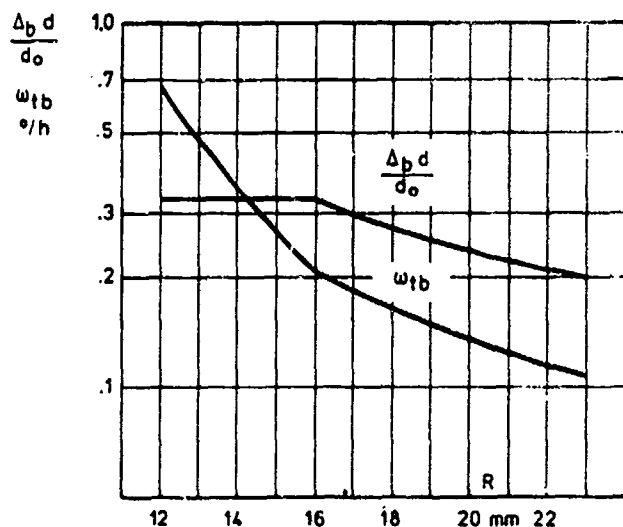


Fig. 8
Untuned Gyro, Spring Rate Error due to
Machining Tolerances and Resulting Gyro Bias

Thus stands in sufficient approximation

$$\Delta\omega_t \sim \frac{\Delta b d}{d_o} \cdot \frac{\Delta\theta}{H/d_o} + \frac{\theta}{H/d_o} \cdot \frac{\Delta_T d}{d_o} \quad (14)$$

where $\Delta b d$ marks the stiffness variation due to temperature. Any tuning operations can be abandoned completely inasmuch as the instability of the detuning drift, $\Delta\omega_t$, does not exceed the value specified for this drift component in the gyro's error budget. In what regions of performance this is the case, may be estimated from the diagram of fig. 9. It shows the instability of the detuning drift versus the rotor radius as only due to the rotor offset - for instance in case of compensation of the temperature effect on elasticity - as with additional regard to the temperature effect. The rotor offset instability is therein considered to amount to half the absolute offset.

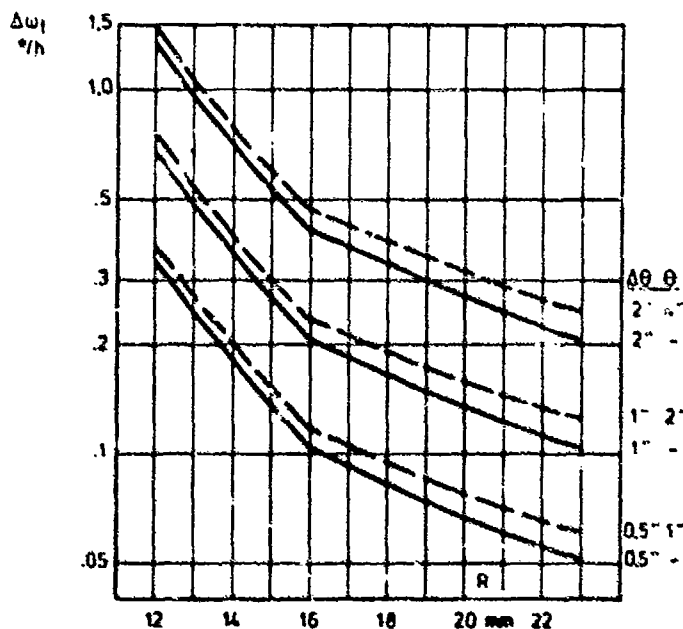


Fig. 9
Untuned Gyro, Instability of Detuning Drift due to
Machining Tolerances
——— Non-Regarding Temperature Effect
----- Including Temperature Effect,
Temperature Coefficient of Elastic Modulus
300 ppm/K, $\Delta T = 70$ K

The diagram shows that the detuning due to spring tolerances can amount up to 33 % with small rotors, decreasing to 20 % in the upper region of rotor sizes. This always refers to stiffness, an equivalent detuning of spin speed would amount to about half these values.

Despite the large relative spring rate error the resulting bias values of less than .7%/h are so small, due to the low absolute stiffness of the hinges, that with regard to bias for itself any tuning procedure could completely be renounced even if the rotor offset attained a multiple of the assumed value.

Now looking at the drift instability described by equation (12), the introduction of reasonable exemplary values shows that the only essential variations come with the rotor offset θ and the temperature dependency of the suspension springs, the latter being effective as long as it is not reduced by compensation or choice of material.

Result:

The diagram shows that, due to the suspension's little elastic spring rate, gyros for applications outside the inertial domain can in most cases be used without any particular tuning procedure in case the rotor offset stability ranges around 0.5 to 1 seconds of arc. The temperature effect on elasticity plays just a minor role. Thus in this range of applications the denomination "tuned gyro" has to suffer a wide-hearted interpretation.

The Required Acuity Using Tuning Treatment

The result obtained for the non-tuning case encourages to examine even higher-graded gyro classes for their potential of significant reduction of effort by using tuning treatment of limited, but sufficient accuracy. There is, indeed, again a distinct threshold. It marks that range within of which the suspension can be satisfactorily tuned already in its manufacturing process, before being mounted in the gyro, and in particular as long as it is clamped in its machining fixture.

An example of doing this is: Immediately after the electro-erosive cutting of the suspension its natural frequencies when oscillating about

the two gimbal axes are measured. As the contributing inertias of the gimbal and the rotor-sided mounting ring match their nominal values to better than 0.5 % due to the manufacturing process used, the natural frequencies establish a well-suited measure for the actual angular stiffness of the gimbal axes. Electro-erosive machining the gimbal based on calculated data obtained from the natural frequencies, possibly in the suspension's original setting, allows to tune the suspension to considerably better than $\Delta d/d_0 = 0.01$. Thus it is delivered to the gyro assembly line readily tuned. Measuring and adjusting the tuning frequency in the assembly and calibration process cease as well as design precautions like threads and tuning screws with their securing problems. The simplicity of the suspension takes its full effect.

In scanning the limits of utility the bias aspect can be neglected. The instability equation (12) can be reduced to

$$\Delta\omega_t \approx \frac{\theta}{H/d_0} \left[\left(\frac{\Delta_b J}{J_0} + \frac{\Delta_b d}{d_0} + \frac{\Delta_T d}{d_0} \right) \frac{\Delta\theta}{\theta} + \frac{\Delta_T d}{d_0} \right] \quad (15)$$

provided the spin speed being maintained within 0.1 % from its nominal value. The effect of the last term of the right side can be compensated inasmuch as the rotor offset θ is stable. In most cases θ is adjusted to zero to the best possible anyway. Provided this compensation or zeroing being effective, the contribution of the last term decreases to

$$\frac{\Delta\theta}{H/d_0} \cdot \frac{\Delta_T d}{d_0}$$

and it comes, furthermore using maximum terms, i. e. plain adding of all the error components,

$$\Delta\omega_t \approx \frac{\Delta\theta}{H/d_0} \left(\frac{\Delta_b J}{J_0} + \frac{\Delta_b d}{d_0} + 2 \frac{\Delta_T d}{d_0} \right) \quad (16)$$

The first two terms in the brackets are due to remaining off-tuning of the pre-tuned suspension, the third term expresses the residual effect of the springs' temperature coefficient when using temperature compensation.

Putting exemplary values of good realizability, $\Delta_b J/J_0 = 0.005$, $\Delta_b d/d_0 = 0.01$, $\Delta_T d/d_0 = 0.015$ (corresponding to a temperature coefficient of $TK(E) = 300$ ppm/K and a temperature range of + 50 K), renders the values of detuning drift instability due to both, initial off-tuning and temperature effect, as plotted in fig. 10.

Now the temperature effect which is uncompensable due to the rotor offset uncertainty appears twice as large as the effect of the pre-tuning error. Its further reduction for example by choice of the suspension material or by temperature stabilization has to be considered particularly for still more stringent requirements.

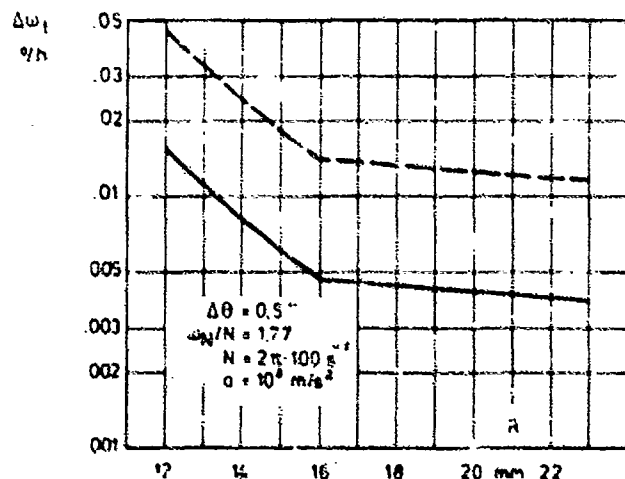


Fig. 10
Gyro With Pre-Tuned Suspension, Instability of Detuning Drift.

— Non-Regarding Temperature Effect
 ---- Including Residual Temperature Effect on Elastic Modulus due to Pico's Instability; Temperature Coefficient of Elastic Modulus 300 ppm/K, $\Delta T = 50K$

Nevertheless, under the provision of a rotor offset stability of 0.5 seconds of arc being rather moderate for inertial grade gyros, the drift instability due to the pre-tuning error ranges essentially under .01%/h for rotor radii of more than 14 mm, the total instability including the temperature effect amounts to the triple of these values. Thus it can be stated as a

Result:

Within a range of applications extending far into the inertial grade domain the defined production of pre-tuned suspensions can be used to replace any tuning treatment of the gyro as a whole.

2-N Angular Sensitivity

The predominant internal sources of 2-N angular oscillation in a dynamically tuned gyro are the shaft bearings and the spin motor. Since the spin motor influence, however, can be sufficiently reduced by design and operation measures as for in-

stance are reported in /1/, here just the bearings shall be regarded. Their imperfections produce a spectrum of radial wobble which, disregarding other components, contains the integer harmonics of the spin frequency. The radial motions of the shaft in the bearing planes are transformed into angular motion of the shaft axis in the general case of the radial motions occurring out-of-phase (see fig. 11).

With gyro ball bearings of good quality, 2-N radial wobble has been observed of typical 10 nm amplitude. Together with a typical bearing distance of 20 mm it produces a 2-N angular oscillation of the shaft of $\phi_{2N} = 1 \mu\text{rad}$ under worst case conditions, i. e. the 2-N radial wobble of the two bearing being in counterphase. The bearing distance determines the radial-to-angular transformation and should be made as large as possible regarding this mechanism.

The 2-N angular wobble excites the drift rate $\omega_d(2N)$ according to equation (2). Much more interest than by its absolute value is, as before, attracted by its stability. The day-to-day repeatability of the 2-N angular wobble can according to experienced data be quantified to less than 15 % of the absolute value including phase variations.

The resulting maximum instability of the drift rate is plotted in fig. 12 versus the rotor radius.

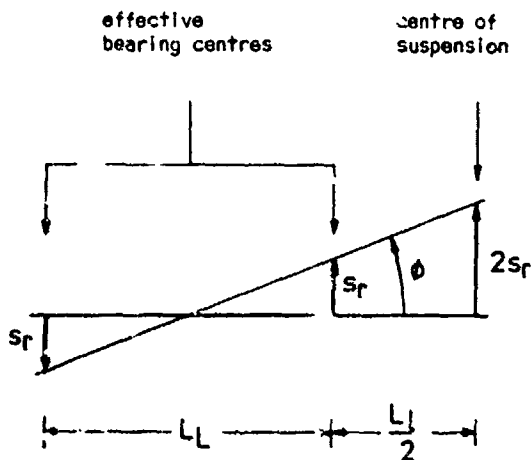


Fig. 11 Model for the Generation of Radial Wobble

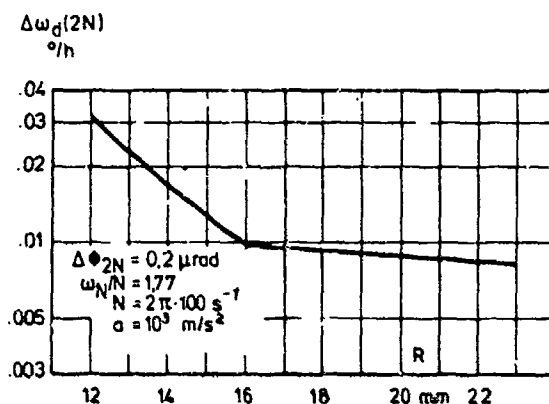


Fig. 12 Maximum Instability of Bearing-Excited Drift Due to 2-N Angular Sensitivity

Result:

Using a ball bearing supported shaft with a good, but not extreme bearing quality, characterized by an instability of 2-N angular wobble of 0.15 μrad , inertial grade gyros with a day-to-day repeatability down to 0.01°/h can be implemented with a one-gimbal suspension.

Accordingly low is the 2-N angular sensitivity of these gyros in response to external excitation, for example due to variations of the elasticity of the ambient structure.

Reverse Conclusion:

For less stringent requirements which admit drift instabilities due to bearing wobble in order of 0.05°/h or more, bearings do not need any critical quality specification with respect to 2-N wobble.

2-N Radial Sensitivity

The internal excitation of 2-N radial wobble in a gyro has the same origin as that of the 2-N angular wobble and as was dealt with in the preceding section. For the mechanism see fig. 11. In this case 2-N radial oscillations of the suspension centre with the amplitude $2s_r$ are effective. According to equation (3) they produce the drift rate

$$\omega_{ar}(2N) = \frac{a_r}{4H} (ms_z + m_K c_{Kz}) \tag{3}$$

It depends from the axial separation s_z of the suspension axes and from the gimbal pendulosity $m_K c_{Kz}$. Its instability is

$$\Delta \omega_{ar}(2N) = \frac{1}{4H} (ms_z + m_K c_{Kz}) \Delta a_r + (m \Delta s_z + m_K \Delta c_{Kz}) a_r \tag{17}$$

The gimbal mass needed for the estimation of this drift component is for gyros with UKF suspension, with performance data according to fig. 7 and rotor radii ≥ 16 mm, given by

$$\frac{m_K}{\text{kg}} = 0.053 \left(\frac{m}{\text{kg}}\right)^{\frac{7}{6}} \quad (18)$$

It remains nearly constant for smaller rotors.

The 2-N radial amplitude of the centre of suspension due to the bearing wobble reported in the preceding section can amount to twice the radial wobble of a single bearing in a usual gyro geometry according to fig. 11. Thus the radial amplitude comes to 20 nm. The axial distances in equation (17) can due to experience in the prototype production of suspensions be rated with good safety to

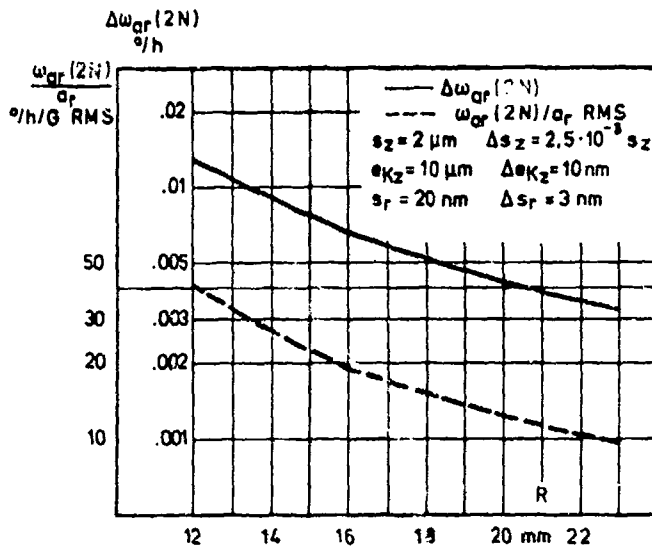


Fig. 13
2-N Radial Sensitivity and Instability of Drift due to 2-N Radial Shaft Wobble of the Amplitude s_r without Gimbal Balancing

features, which arise from characteristics of the specially developed machining process and the mass-saving design concept.

Balancing of the gimbal could prove necessary only in case the radial sensitivity with respect to external 2-N accelerations shall further be reduced. Its values range between 40 and 10°/h/G RMS. Its dominant share originates from the axial separation of the suspension axes, which in this suspension due to the manufacturing process is already very small and which according to equation (3) can be compensated for by deliberately producing a gimbal axial unbalance.

5. Final Conclusions

The novel gyro hinge design described combines outstanding producibility thanks to a design of unique simplicity with high performance capability due to optimal flexure contour and utilization of design space. Its indirect effect on the design and the effort for manufacturing and calibrating dtg's has been shown with respect to strap-down gyros in the size ranging from 12 to 23 mm rotor radius. The following cost-reducing consequences on gyro design and calibration can be noted:

1. No need for multi-gimbal design even in the inertial quality domain with day-to-day repeatability down to 0.01°/h.
2. No need for gimbal balancing in the same domain.
3. No tuning treatment whatsoever for gyros of day-to-day repeatability of more than 0.1°/h to 1°/h, dependent on size and pickoff stability.
4. Reduction of tuning treatment to suspension pre-tuning for most inertial grade gyros.
5. Reduced influence of elastic modulus variations.

Consequent utilization of this potential renders gyro concepts of specific simplicity and cost effectiveness in each application range from low performance to inertial quality.

$$s_z = 2 \mu\text{m} \quad \Delta s_z = 5 \text{ nm}$$

$$e_{Kz} < 10 \mu\text{m} \quad \Delta e_{Kz} = 10 \text{ nm}$$

Using these data equation (17) renders the 2-N radial sensitivity and the instability of the resulting drift due to the 2-N radial bearing wobble as plotted in fig. 13.

Result:

The drift instability induced by the 2-N radial wobble or the gyro's own shaft bearings falls even with wide-hearted presumptions regarding bearing quality and gimbal pendulosity, definitely below 0.01°/h for rotor radii over 14 mm. No further reduction by gimbal balancing is necessary even for applications in the 1/100°/h-domain with usual rotor radii of 15 mm and up.

The primary reason is the minute axial separation of the suspension axes, secondary ones are the small gimbal mass and small initial unbalance,

6. Reference

- /1/H. Karnick, Experience Based Upon Experimental Dry Tuned Gyros,
Deutsche Gesellschaft fuer Ortung und Navigation, Symposium Gyro Technology 1979,
pp. 2.11, 2.12.

OPTICAL ROTATION RATE SENSORS

G. E. Knausenberger, Consultant
 Air Force Office of Scientific Research
 Bolling Air Force Base
 Washington DC 20332

INTRODUCTION

The measurement of inertial rotation using optical methods has been under active development for more than 15 years. The approaches so far have been based on two principles: one based on the Sagnac effect, leading to the ringlasers (RLG) and its new derivatives; the other based on the spin of the nuclei leading to the nuclear magnetic resonance gyro (NMRG or MRG). In the case of the RLG, the inertial reference quantity is the velocity of light, since it is independent of the platform motion. In the case of the MRG, one attempts to derive the inertial reference from the spin vector of a conglomerate of oriented atomic nuclei. Successful approaches are so far limited to inertial, angular velocity measurement via comparison with a magnetic field induced Larmor precession of the nuclei. Both methods rely on optical operating and readout means, the RLG by necessity and the MRG by convention.

The research and development for both systems is dictated by the promise of cost reduction or performance increase, or both, in strapdown inertial systems, and they benefit from the application of modern optics and micro-electronics technology. (Fig 1)

As to status and progress, it is fair to say that the RLG has reached production stage in its original conventional version, while the MRG is more or less still in the exploratory development or research stage.

Justification for pursuing both approaches derives from the fact that the RLG requires a certain (large) size and mechanical precision in construction while the MRG has the potential for greater miniaturization, especially for relaxed structure tolerances. On the other hand, recent RLG work indicates new possibilities for significant sensitivity increase and optimum adaptability to specific environments and missions. (Fig 27)

The paper will be primarily concerned with an analytical review of various approaches to the measurement of inertial rotation by optical means with emphasis on the more recent concepts.

LIST OF SYMBOLS

- γ gyromagnetic ratio of particle
- A number of pulse counts
- C phase velocity of light wave in vacuum
- C^R phase velocity of light in rotating optical medium
- f optical carrier frequency
- ϕ optical phase
- $\Delta f, f$ beat frequency, RLG output signal frequency
- L length of closed optical path
- n refractive index of path medium
- N number of turns in optical path
- P number of recirculations of waves in closed optical path
- P fractional polarization of nuclear particles in specific gas volume
- $\psi(t)$ phase difference between the electrical vectors of the clockwise (CW) and the counterclockwise (CCW) traveling optical waves
- s/n signal to noise ratio of electrical signal at motion detection
- τ integration time at detector output
- T photon transit time over path
- T_r relaxation time for particle
- Ω rotation rate as mechanical input, to be determined
- ω angular frequency, wave rotation rate

ΔZ relative shift of interference fringe location

RINGLASER

1. Concept

Sagnac, in a 1913 publication, demonstrated an optical system capable of sensing inertial rotation. Using mirrors, a single light beam was split into two beams which were then made to travel in opposite directions around a single closed path. After traversing the path, the beams were superimposed to produce optical interference fringes. When the system was rotated, a small shift in position of the fringes on the rotating platform was observed. This shift is proportional to the velocity of inertial rotation of the system platform.

The ringlaser rotation sensor (RLG) is a device which uses the basic Sagnac effect in a particular way. A laser is incorporated into the closed loop optical path. Its frequency is determined by the resonant frequency of the loop. When the system rotates, the resonant frequency splits into two frequencies; the difference frequency of these two simultaneous laser oscillation frequencies is proportional to the rotational velocity and is measured.

The phase of the beat signal, which is measured in the Sagnac case, is here simply measured by transforming the sinusoidal beat signals into pulses and by counting these pulses. The number of pulse is proportional to the described angle while the pulse rate is proportional to the rotation rate. (Figs 2 to 17)

Different from conventional gyros, the RLG is a static device. It has excellent and wide linearity up to 10^8 °/hr from a few hundredths with deviations from linearity $\sim 10^{-3}$. It has direct digital readout, and a 20 cm side triangle renders easily a fraction of arc sec resolution. Signal processing is easy and avoids the problem of weak analog signals. The RLG is insensitive to vibration and acceleration in a sufficiently rigid structure.

The RLG is intrinsically, weakly sensitive to temperature and magnetic field. Difficulties arise from the coupling of the optical waves, the non-reciprocity of the properties of the optical trajectories in the amplification and resonator medium, and from the need of conservation of optical path alignment in spite of environment influences.

Since 1963, Maceck and Davis at Sperry first demonstrated a ringlaser; the R&D community has successfully dealt with the RLG's detailed materials, shielding and stabilization problems; has developed a theoretical framework for understanding the phenomena for mathematical models to aid design and testing; and has succeeded to produce a reliable inertial grade gyro with excellent operating and shelf life. (Fig 14)

2. New Approaches

New technologies and new solutions for overcoming costly intrinsic difficulties have stimulated new approaches. These new approaches to inertial rotation sensing are also aimed at providing high sensitivity in the measurement down to very low rates, as required in present and anticipated navigation and control applications in particular, with the expectation of increased applicability and lower overall cost. They, too, render the direct quantitative absolute inertial rotation rate measurement, requiring no comparison with other standards for calibration and are basically unaffected by acceleration.

The new systems are based on the Sagnac effect but are designed to be inherently free of one serious problem encountered when the laser is in the ring: the mode locking effect. As a result of this effect, zero rotation rate will be indicated below a certain rate. So, the goal is to lower this lock-in threshold by improved design such that its value is below the minimum rotation rate to be measured or to find means to overcome or circumvent the locking effect altogether. This leads to the application of a "bias" rotation rate where, for instance, by imposed known steady rotation simply an operating range outside the lock-in region is used or, more frequently, where the bias rotation is oscillating symmetrically far across the lock-in range, which then allows the measurement from zero rate over a wide range of rotation rates. Unfortunately, these latter "dither" bias (mechanically, magnetically, or optically induced) methods create noise which defeats the attempt toward minimum rate measurement thresholds, and introduce error sources of their own. (Figs 2, 3, 9 to 14) A novel "self-dither" proposal suggests simplification of the biasing system by laser internal periodic bias generation. (Appendix A, II)

Another approach to avoid the lock-in problem is to apply stationary bias on two separate optical oscillators in the same ring such that, with opposite bias polarity, the one beat frequency increases while the other decreases from the stationary operating point. The degree of symmetry and reciprocity in the optical paths of the two lasing systems will determine whether the maximum sensitivity (shot noise limit) and stability can be achieved. The results so far are encouraging. (Figs 15 to 17, Appendix A, Fig 11)

More recent approaches attempt to avoid the complications of the active resonator, including the lock-in problem, by putting the laser outside the ring. The measurement becomes, again, a phase shift measurement. The light beams in the ring, which now acts as passive Fabry-Perot resonator, are essentially decoupled and guaranteed a maximum of reciprocity in their propagation. While in such a system, one can apply a desirable high signal level; the indication of the rotation, and the accuracy of the phase shift readout is a major problem for opto-electronics. (Figs 4 to 7)

The solutions for an accurate and practical detection are sought essentially in four directions:

- a. Improvement of the classical fringeshift reading through differential two-detector schemes and application of very low loss components.
- b. The modulation or switching of the optical carrier and application of synchronous detection and a feedback signal servo at the output.
- c. Feedback from the output to the input to tune the laser line to the rotation shifted resonance frequency of the passive ring resonator. Direct frequency difference reading is possible.
- d. A pulse system featuring, like an RLG, a rotation sensing loop comprising a single reentrant closed optical path, but with the laser oscillator outside and a laser amplifier within the loop. The signals from the external source are short, optical pulses and are sensed each time they traverse the turns of the loop and the rotation data is extracted from these sampled pulses. This reentrant system has inherently the sensitivity and digital output as a ringlaser would have with the same loop dimensions if mode locking were absent. (Figs 18 to 24)

As seen, these new systems have the source outside the ring, the beams are decoupled in the ring; so, no mode locking obscures the rotation effect; the frequency of the oscillator is not influenced by the counter traveling wave and multiple turns of low loss optical waveguides can be profitably applied to increase sensitivity as can most components of integrated optics. In return, this technology benefits from the very stringent requirements of this new instrumentation. With these concepts, application adaptive optimum devices can be conceived, cheap small sensors on a chip and large fiber loops around a vehicle.

Progress in the short time of activity in the above mentioned direction is very encouraging although still far from the goals. Shot noise limited thresholds and earth rate measurements have been achieved in the laboratory.

The figures following this text attempt to illustrate the main implementation and trends. The new devices and their potential should broadly cover the foreseeable application needs and at reasonable cost.

3. Russian Activity (IV)

Also, casual observation showed that during the last decade a relatively large number of Russian scientists have published on ringlaser related subjects. Aside from review papers, detailed technology aspects and some stimulating, as well as puzzling topics, were discussed; topics like lock-in range reduction by backscatter radiation reduction in servoed mirror shift arrangements (App A, Fig 12), application of a saturable absorber medium to prevent mode locking, and theory to explain observations made with an all solid-state ringlaser. The latter subject, although of some general interests, remains controversial.

4. Ringlaser Summary

All the known approaches are based on the principle that two identical light beams propagating in opposite directions around the same closed path suffer unequal phase shifts in the presence of inertial rotation. The phenomena was first described by Sagnac in 1913, and its validity demonstrated by research workers (Harriss, Michelson, a.o.) since then. The magnitude of the rotation induced non-reciprocal phase shift is proportional to the inertial rotation rate about an axis perpendicular to the plane of the light path, to the area enclosed by the path, the frequency of the light and to the inverse of the square of the vacuum velocity of the light. Notice that it is, in first order, independent of the properties of the light path. Because the phase shift is very small for the rotation rates of interest in inertial navigation (e.g., for $\omega = 10^{-3}$ x earth rate and a 100 cm^2 area of the ring, the phase shift is 10^{-10} radians), sophisticated approaches must be used for the measurement of the phase shifts.

The most popular and successful technique developed so far is based on the ringlaser (RLG) approach in which the ring resonator or cavity is "active," i.e., it contains a laser as oscillator and the phase shift manifests itself as a frequency difference between the two oppositely propagating beams.

As light sources, HeNe lasers have found predominant use, and excellent operating and reliability conditions have been reported. RLGs have been demonstrated in strapdown systems over sensitivity ranges of 10^{-3} to 10^1 °/hr, however, are not currently cost competitive with conventional gyros from about 1 to 10^1 °/hr while the newer optical

rotation sensors are expected to be. Multioscillator system experiments indicate satisfying the high sensitivity end of the range. It also appears that a single optical rotation sensor can cover five orders of magnitude of measurement and accuracy requirements. Related research and development efforts promote new advances for sensitivity, accuracy, operating range, reliability and cost improvements by new biasing arrangements, new optical components, and laser sources.

While the conventional gaseous dithered systems experience continued improvement, they are being complemented by solid-state systems which draw on fiber and integrated optics advances. Recently, several "passive" approaches for the measurement of the phase or fringeshift have been under investigation. These include the use of passive ring resonators with light sources external to the ring and external means of phase shift measurement as well as multi-turn fiber optic interferometers employing semiconductor lasers and various sensitive schemes for the readout of the non-reciprocal, rotation-induced phase shifts.

OPTICAL PUMPED NUCLEAR MAGNETIC RESONANCE GYRO

1. Concept

The nuclear magnetic resonance gyroscope is a rate integrating single axis instrument. The inertial rotation sensing element is a collection of oriented atomic nuclei. Aside from the motion of the atoms, there are no moving parts; the operation should not be influenced by high acceleration and should create no reaction torque. It can also accommodate large input rates and angle ranges.

Here lies the practical interest in its development; physical sciences motivation derives from a simplified picture of certain atomic nuclei which possess inherent angular momentum and act like spinning perfect gyroscopes at the center of atoms with no power input and nearly perfect gimbaling. The spinning nucleus (or atom) has also a magnetic moment which, fortunately, allows readout of the orientation of the spin but, on the other hand, requires careful magnetic field equalizations and shielding to hold the disturbing moments at a low level ($< 10^{-8}$ gauss, e.g.). The ideal situation would be the removal of all ambient magnetic field and the precession-free operation of the gyroscope deriving "space reference" from the collection of ordered spins fixed in inertial space. Since a single atom would have too low a magnetic and spin moment, collection must be such as to have an accumulated magnetic and angular momentum strength above the tolerable interfering influences. The surplus of angular momentum as in a mechanical gyro cannot (yet) be obtained.

At present a compromise is used. A sizeable, constant magnetic field is introduced and a Larmor precession of nuclear magnetization initiated. Rotation information sensed arises from changes in the phase and frequency of the measured signal when the observers' platform rotates about the direction of the applied constant magnetic field. This is, then, a rate gyro instead of a directional gyro with the input axis along the spin axis of the Larmor precession.

To compensate for magnetic field changes, two kinds of nuclei are used, hence, two output frequencies. Further, in order to minimize effects of nuclear magnetic vector fluctuations (by light), two equal precessions in opposite magnetic fields are employed.

While one talks of a "gyro," it must be cautioned that the principle applied in the NMR is one very different from that of a gyro. An axis tilt would not render a signal because, in principle, the plane of precession follows the direction of the applied magnetic field. So, the inertial reference pertains only to the rotation about that direction. In my present judgement, whether the signal arising, in case the magnetic field is switched off, can be used and, more practically, how cross-axis coupling can be eliminated, remains open. (Figs 10 to 14)

In the following, further details are given, focussing on some essentials in an otherwise broad, far from theoretically and experimentally finalized, research and development effort.

2. Why Optical Pumping

Known magnetic resonance gyro developments use optically pumped atomic vapors. The effective size of nuclear moments in a gas sample is extremely small in the natural equilibrium situation where a near random orientation of moments exists. Optical pumping is then a technique to orient a large portion of these moments in a single spatial direction so that a macroscopic moment results, the position and velocity of which can be determined precisely, as needed for the gyroscope application. One should notice that such measurement would not be possible for a single particle, but that a certain conglomerate of particles is necessary. The number of participating particles (temperature, pressure) necessary is a subject of further research in conjunction with the signal generation and detection improvement problem.

Although many other magnetic resonance measurement schemes exist, the advantages of an optically pumped gas system are dominating; they are threefold:

- a. While in standard work, the spin polarization of a sample at fields below a hundred gauss is too small to be of use, one can obtain large spin polarization by optical pumping also in a weak or zero magnetic field.

- b. One obtains very long spin relaxation times in an optically pumped vapor so that magnetic resonance line widths are narrow and the precision of measurement is high.
- c. By monitoring the magnetization with light, one can attain high signal-to-noise ratios.

Nevertheless, it seems prudent to watch development work in classical nuclear magnetic resonance such as magnetometers based on dynamic polarization of nuclei by VHF pumping of a liquid ensemble. Extrapolations of such a system could, in principle, lead to a gyroscope.

In optical pumping, a light beam interacts selectively with a vapor to populate angular momentum states of the atom, thus providing a large degree of spatial orientation while the light penetrates the sample. Once pumped, because of various relaxation mechanisms, this orientation decays toward equilibrium with a characteristic time constant T_1 . This time must be long enough for an efficient pumping to be completed and to have time to permit precise measurement of the precession frequency.

The optical pumping process is used either in a one-step or two-step process. In one step, a system of vapor atoms is optically pumped by absorption of spectral light from a vapor discharge lamp or a laser. This results in a magnetic moment of a significant number of atoms being orientated in the direction that is parallel to the incident light. If the optical pumping rate is $1/T_p$ and the decay rate is $1/T_d$, then the fractional polarization at equilibrium will be:

$$p = \frac{1/T_p}{1/T_p + 1/T_d} = \frac{T_d}{T_p + T_d} \quad (\text{Eq. 1})$$

In systems where a second step follows, that is, where spin exchange collisions take place from one gas to another, the fractional polarization p must not only be large but the spin exchange times must be much smaller than the decay times of the polarized species.

While the spatial orientation of the spin system is caused to vary in time in a prescribed way by the application of a suitable combination of AC and DC magnetic fields, the absorption of light (from the same light that is used for optical pumping) depends on this spatial orientation. The intensity of the transmitted light beam varies, therefore, in accordance with the applied fields and with the magnetic fields created by the precessing nuclear moments which vary in time at their respective Larmor frequencies, and which cause corresponding sinusoidal amplitude modulations of the transmitted light. The advantages aimed at with such a system are:

- a. The same light source for pumping and readout.
- b. Good operation at low magnetic fields for which field uniformity is easier to achieve thus obtaining desirable, long coherence times for the nuclear precession.
- c. The modulation information on the light contains information not only about the nuclear moment fields but about other magnetic fields. By suitably processing this information, it is possible to precisely control these fields along the three orthogonal axes.
- d. The effective moment fields determining the readout signals can be much smaller than in a case of an induction coil pick-up.

3. Elimination of the Effects of Ambient Magnetic Fields

The NMR system is sensitive both to the inertial rotation rate of the apparatus and the ambient magnetic fields. Rather than attempting to eliminate this field, it has been customary to measure the fields simultaneously with the rotation rate by using two different nuclear species since two unknowns, the field and the rotation rate, require two measurements. The problems of eliminating the effects of external fields by using two species is central to the "room temperature" NMR systems of Singer-Kearfott, Litton, and Texas Instruments.

In contrast, Stanford University is working on a helium 3 nuclear gyro system where at cryogenic temperatures the ambient magnetic fields and then the spin disturbing moments are minimized through the employment of superconductive shields.

a. NRG Mechanization (Fig 35)

In one example of an NRG, the cell (1 cm ϕ) of high purity synthetic fused silica contains ^{199}Hg and ^{201}Hg in the form of mon-atomic vapor (10^{-6} millimeter Hg, 10^{12} atoms/cc).

The Larmor signals occur at 1 KHz and 269 Hz, respectively, in a 1.2 gauss applied field. An optical pumping beam imparts angular momentum from the circularly polarized light to the mercury atoms so the net nuclear magnetization becomes oriented and enhanced

by a factor of about 10^9 .

The precessional motion of the magnetization causes the monitor light beam to be modulated at the two frequencies. The modulation on the light beam is converted to electrical signals, amplified and fed back to drive the magnetization in a steady precession. The gyro output signal is derived from two such NMR controlled oscillators as "spin generators." The two oscillators are arranged with their constant magnetic fields pointing in opposite directions so that rotations, which add to the phase of the signals in one oscillator subtract from the phases in the other loop. This improves the phase detection accuracy and minimizes disturbing environment influences.

Gyro performance depends on phase and frequency stability of, and noise in, the spin generator loop and on the directional stability and uniformity of the magnetic fields.

The noise, arising from the photon beams in the spin generator and from the fundamental magnetization phenomena, can be minimized by achieving large S/N ratios in the magnetic resonance cell (>40 db).

The degree to which the output of the oscillator follows the precession motion depends on the phase stability of the oscillators where a large amount of feedback is warranted.

A change in applied magnetic field direction changes the direction of the gyro-sensitive axis. Small shifts can be accommodated by shielding or orientation change of the AC driving coils.

At what precession rate the magnitude of the resonance is a maximum (and the phaseshift at median value) and is---aside from magnetic field and the gyromagnetic ratio---also weakly dependent on the spectral distribution, polarization and intensity of the applied light. The influence of light intensity changes is reduced by careful equivalent adjustment of the light in the two cells.

Further discussion will focus on some principal aspects of interest in the attempt to utilize the full information stored in the phase of the precessing nuclear magnetization.

5. Choice of Nuclei (Figs 36, 39)

From the expressions for the phase error, it can be seen that the effective relaxation times and the difference of the gyromagnetic ratios should be maximized. Favorable choice of atoms and nuclei means, of course, simplification by avoiding intrinsic difficulties. For instance, choice of atoms with a closed electronic shell, like noble gases have, may render minimum interaction and high relaxation times. The choice of the particle is, however, mostly constrained by the available knowledge and experience with a particular system and its behavior in NMR operation (Bloch equation parameters). Further research will certainly be helpful.

The known NMR gyro effects employ:

a. Two isotopes Hg^{199} and Hg^{201} , the basic physics of which has been extensively researched in the past; they can be directly pumped with UV resonance light (253.7, 185.0 nm) requiring quartz optics and suffering absorption by atmospheric oxygen.

b. Odd isotopes of noble gases which have the advantage of longer relaxation times, but may have the disadvantage in that they cannot be pumped with their own resonance light which may lie too far in the ultraviolet. One may use, then, a technique of spin exchange pumping in which alkali metal vapor is mixed with the noble gases and the polarization of the optically pumped vapor is transferred to the noble gas, the pumping light requiring only glass optics.

c. Being explored is the combination of nuclear spin systems, He^3 (11S), with electronic spin system He^4 (2^3S_1) with the He^3 's very long relaxation time in the gyromode and the He^4 with short relaxation time in the magnetometer mode. Since a long relaxation time, coupled with a high signal to noise ratio, renders a minimum gyro error, the goal is to reduce the influence of He^4 with its short relaxation time (its metastable atoms are destroyed in collisions) on the He^3 system, noting that the gyromagnetic ratio compensates for the fast relaxation of He^4 . The measurement threshold for the MSG is determined by the statistical error of the scale factor and by practical limitations due to shot noise, frequency, and phase drifts.

That the practical error is larger than the theoretically determined statistical error and shows drift---where the exponent indicates the uncertainty of the time function for the drift from one system to another---is subject of further research and development. One concern is the shot noise influence. To decrease it, one increases the intensity of the light; this however broadens the magnetic resonance line which counteracts the improvement from reduced shot noise. Optimum light level is reached when the relaxation rate of the atoms, due to the light, is equal to the intrinsic relaxation rate. Further, the detection scheme should be such that the coupling between shot noise and linewidth is a minimum by arranging that a maximum of atoms are available to interact with the light, and the interaction rate per atom can be relatively small.

6. MRG Summary

The NMR Gyro or MRG employs nuclear magnetic resonance phenomena to measure inertial rotation rate.

The rotating mass of a flywheel of the classical gyroscope as sensing element is replaced by the dynamics of nuclear and/or atomic spins and resulting magnetisms of certain atomic species.

Unlike its mechanical counterpart, there is no bearing to wear, and there is intrinsic motion isolation. Reduced maintenance requirements, compact design, and reliable electronic-optical components should lead to significant savings in acquisition and life cycle cost if similar ratio of angular momentum to disturbing momentum can be achieved, as is the case with a classical mechanical gyro.

Basic to the MRG is the fact that a magnetic moment generated from a multitude of spinning particles precesses about a magnetic field H with the Larmor precession frequency $\omega = \gamma H - \Omega$. That is, the inertial rate Ω can be inferred from the precise measurement of the Larmor precession frequency, given γ and H . (Figs 30 to 32)

Here lies the practical measurement difficulty since the nuclear magnetic moments may be $<10^{-8}$ gauss. First, to maintain the magnetic field to the desired degrees of stability and uniformity over the sample may require special shielding arrangements and close loop servo controls. However, by observing two magnetic resonances simultaneously instead of one in the same magnetic field, the effect of field fluctuations can be minimized.

Second, the magnetic moment characteristic γ originates from a conglomerate of "polarized" single particles; it has a stochastic part and is sensitive to field gradient and other environmental influences. The choice of the particles is of prime importance for the composition and lifetime of the magnetic moment vector and thereby, for the output signal to noise ratio, the sensitivity and scale factor of the device.

Several designs of MMRO are currently being investigated. They all employ optical pumping to create orientation of the particle spins. This has proven to be a convenient approach; however, it should not exclude other approaches like electromagnetic pumping of liquids.

CONCLUDING REMARK

To the final question, why considering these optical gyros at all, when very good mechanical ones had been perfected at expense, one may say that the use of any unconventional gyro in a guidance system should not be thought of as simple replacement of a conventional one. In order to fully realize all the unique advantages of a new device, the system application should be studied and worked through in terms of all aspects of input and output characteristics of the new device. How much from R&D equipment finally finds entry into production cannot be predicted exactly, however, is proportional to the perceived and demonstrated innovative and cost saving value, the demonstration of which is not without risks and may take a long time. The optical gyros have a good head-start.

NS: Morris A OSTGAARD and Staff took competitive care of the exigent changes with the figures and the final reproduction of the article.

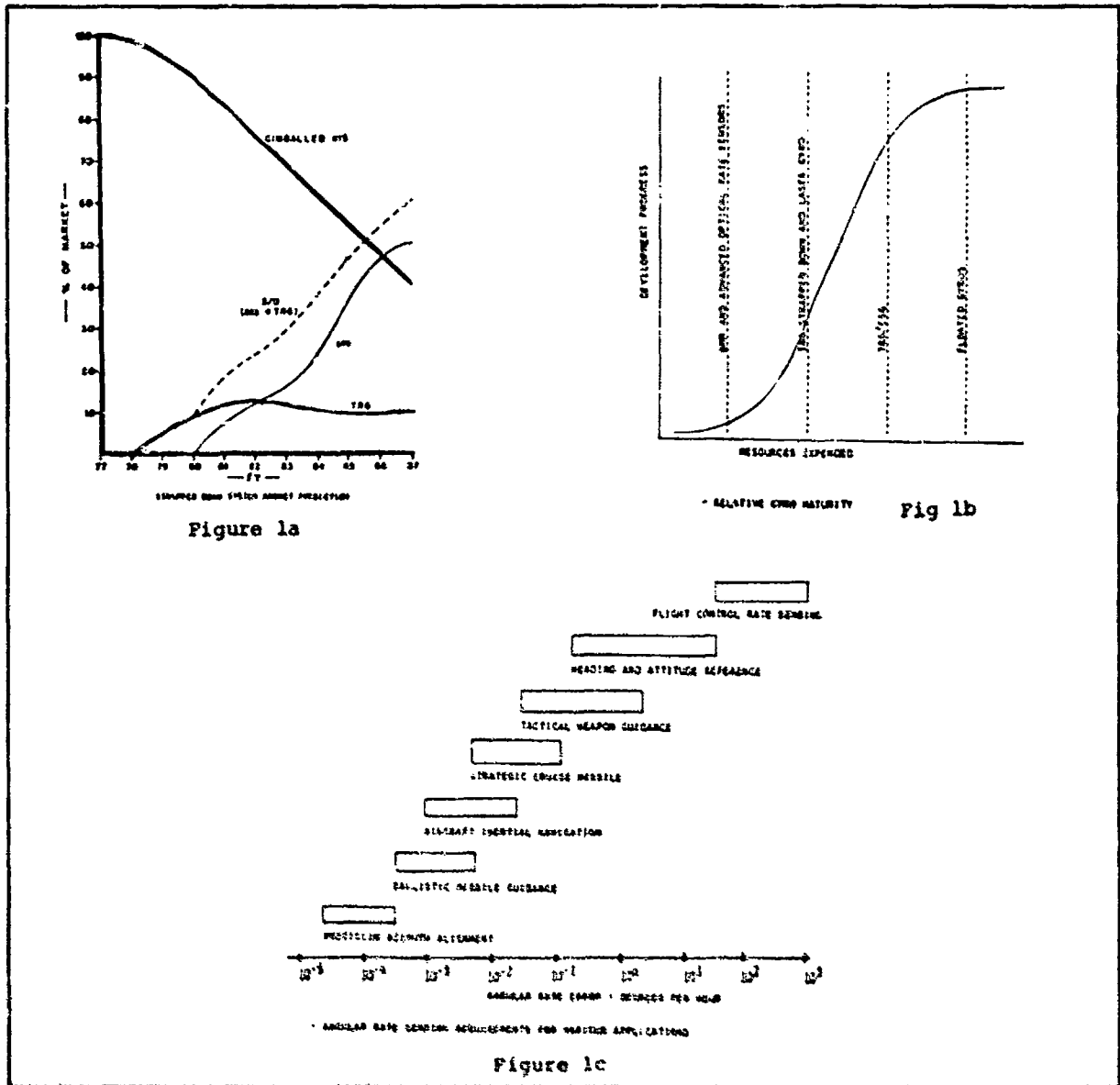


FIGURE 1. A strapdown market prediction shows increased opportunity for optical rotation sensors (ORS) in comparison to tuned rotor gyros (TRG) and gimbaled inertial systems. Considering the requirement for various applications, the ORS is likely to be cost effective for a wide range of accuracies, with the RIQ-systems for the higher accuracies and the MRG's for the lower ones. Development is, however, only in the early stages. (III, #76)

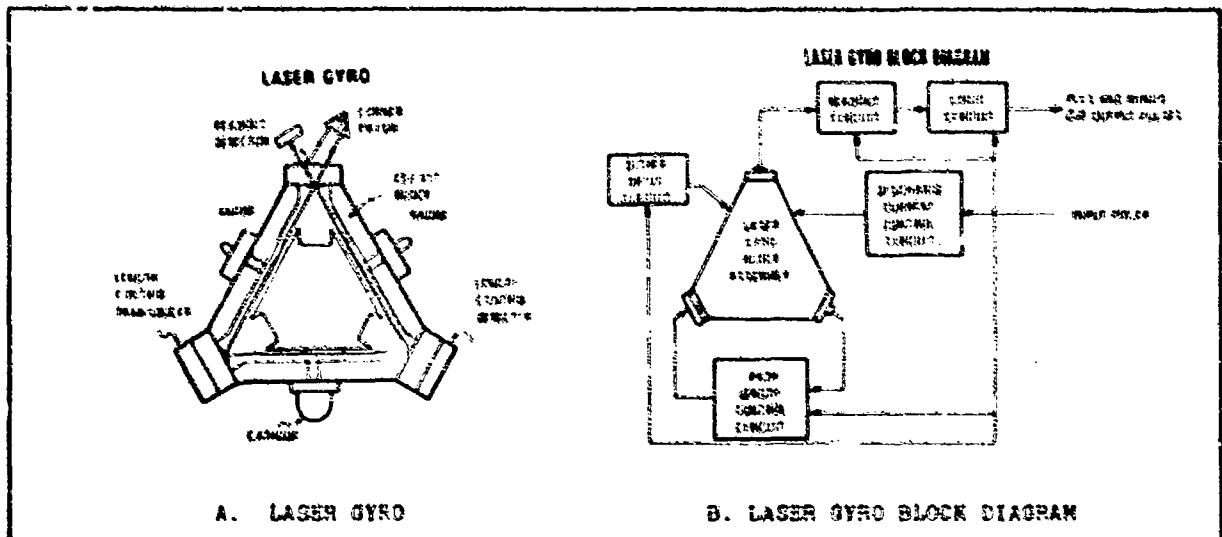


FIGURE 2. A standard ringlaser configuration and the required electronic control, drive, and readout circuit blocks are shown. (I, #43)

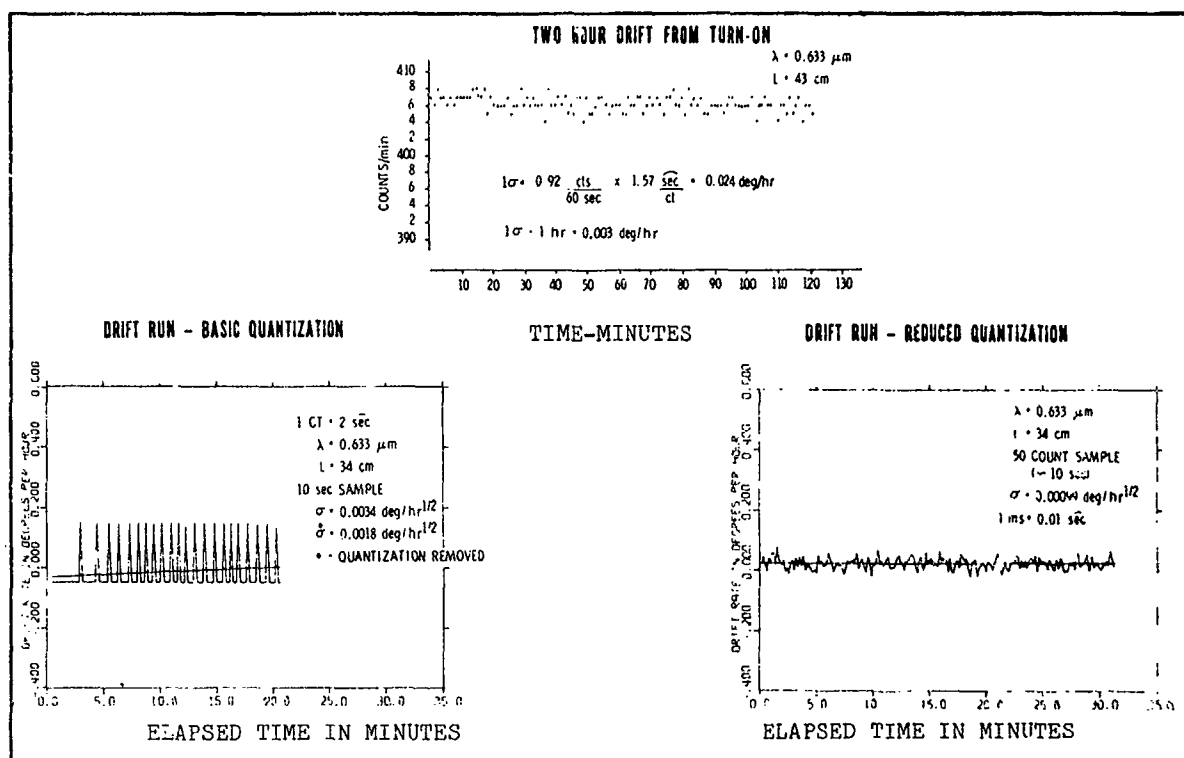


FIGURE 3. Examples of typically achieved practical accuracies, with the influence of the choice of quantization are given. (Ref I, #43)

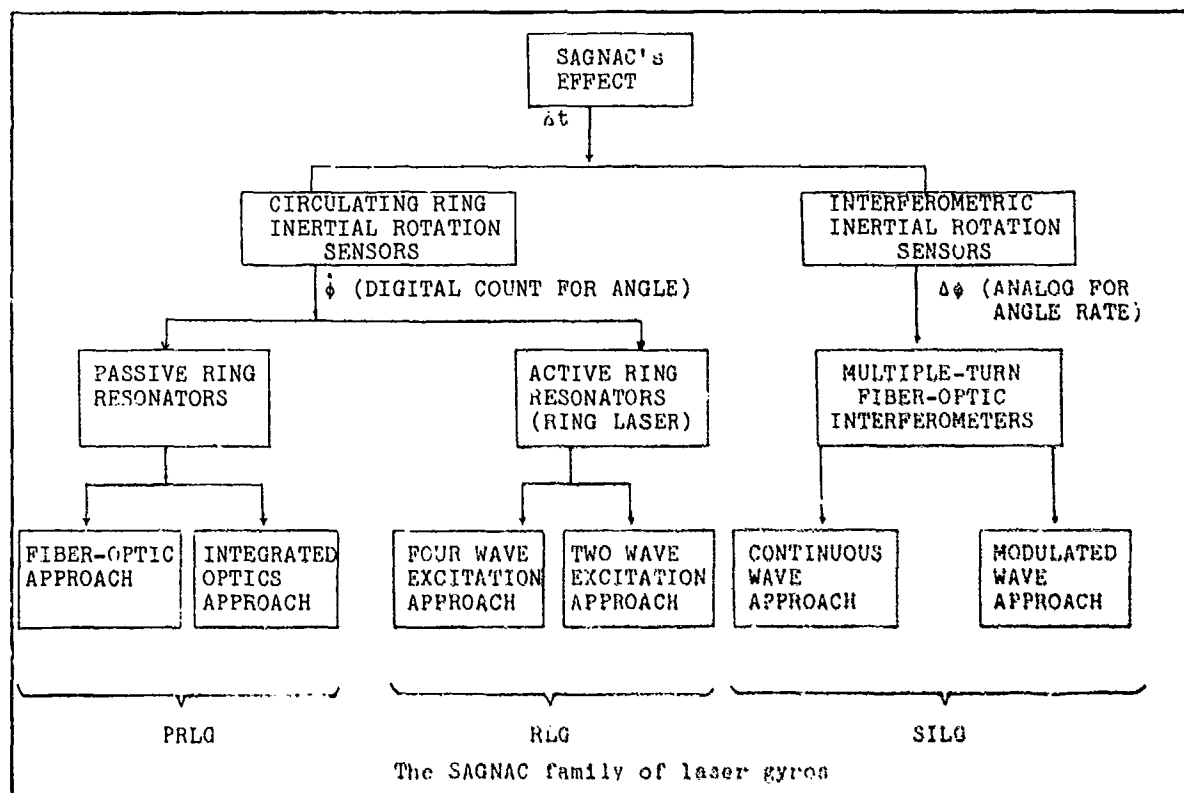
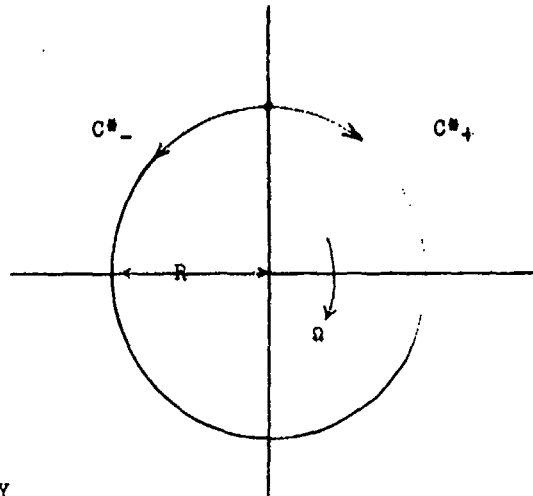


FIGURE 4. The standard ringlaser is only one branch of presently considered laser gyros based on the "Sagnac effect," with the "passive ringlaser gyro" and the "Sagnac interferometer gyro" competing. With no claim to nomenclature, the difference derives from the Sagnac phase measurement versus frequency measurement (ref: I, #41)



C VACUUM LIGHT VELOCITY

C* VELOCITY OF LIGHT PROPAGATION IN MOVING LIGHTPATH WITH INDEX OF REFRACTION n AND MOTION v RELATIVE TO INERTIAL SPACE $C^* = \frac{C}{n} \pm (1 - n^{-2})v$

L LENGTH OF LIGHTPATH IN RING FROM SEPARATION OF BEAMS TO RECOMBINATION $L = NP$

P PERIPHERY OF RING, N NUMBER OF LOOPS

$$\Delta t = \frac{L_+}{\frac{C}{n} + (1 - \frac{1}{n^2})v - v} - \frac{L_-}{\frac{C}{n} - (1 - \frac{1}{n^2})v + v}$$

Δt DIFFERENCE BETWEEN TIMES OF THE COUNTER PROPAGATING BEAMS

FOR $L_{\pm} = L_{\pm} + L$

$$n_+ = n_- = n$$

$$\Delta t = \frac{2L}{C^2} v \quad \text{INDEPENDENT OF } n \text{ (in 1. order)}$$

FIGURE 5. The basic relation of the Sagnac effect for the interference of two light beams traversing equal closed path in opposite directions, while the path is rotated. (Ref II)

USE OF INTERFERENCE PHENOMENA IN TWO WAYS:

STATIONARY OR MOVING FRINGES
LASER OUTSIDE OR INSIDE RING

FIGURE 6. Result of optical interference is either a stationary or moving fringe pattern dependent on whether the laser is outside the ring of the resonator, is "passive," or inside the ring ("active" or regenerative resonator). (Ref I and Appendix A, 5)

FIGURE 7. The measurements which the Sagnac effect then allows are rotation rate expressed either by a phase or fringe shift, or by a difference between two resonance frequencies. The relative shifts are equal under stationary conditions. For high resolution and digital readout frequency output is desirable. (Ref Appendix A, Figs 1 and 2)

PRINCIPAL MEASUREMENTS

$$\text{SAGNAC } \frac{\Delta T}{T} = 2 \frac{v}{C}$$

		RESOLUTION
FRINGE SHIFT	Δ_z	$10^{-4} +$
PHASE SHIFT	$\frac{\Delta\phi}{2\pi}$	$10^{-5} +$
FREQUENCY	$\frac{\Delta f}{f} = \frac{\Delta T}{T}$	10^{-17}

GENERAL RELATION FOR "SAGNAC SYSTEMS"

$$\left(\frac{\Delta T}{T}\right) = \frac{\Delta L}{L} = \frac{\Delta z}{z} = \frac{\Delta\phi}{\phi} = \left(\frac{\Delta f}{f}\right)$$

L Optical Path Length
 T Photontransition Time
 Over L with $z = \frac{C}{\lambda_0} T$; $\phi = 2\pi \frac{C}{\lambda_0} T$

$\Delta_z, \Delta\phi$ FROM STATIONARY FRINGE PATTERN

Δf FROM MOVING FRINGE PATTERN

FIGURE 8. Example showing that frequency measurement allows easily detection of a fraction of earth rate, while fringe shift measurement allows only a multiple of it (without advanced techniques discussed later).

DESIRABILITY OF Δf MEASUREMENTS

EXAMPLE:

$$L = 400 \text{ cm} \quad \lambda = 1.153 \text{ } \mu\text{m}$$

$$\Delta f (t/z) = 6.275 \cdot 10^5 \cdot \Omega \text{ (rad/sec)}$$

$$\Delta z = 2.88 \cdot 10^{-3} \Omega \text{ (rad/sec)}$$

$$\Omega = 10^{-2} \Omega_E = 7.3 \cdot 10^{-7} \text{ (rad/sec) gives}$$

$$\Delta f = 0.5 \text{ Hz while}$$

$$\Omega = 10^{+2} \Omega_E \text{ renders only}$$

$$\Delta z = 2 \cdot 10^{-5} \text{ at limit of readability}$$

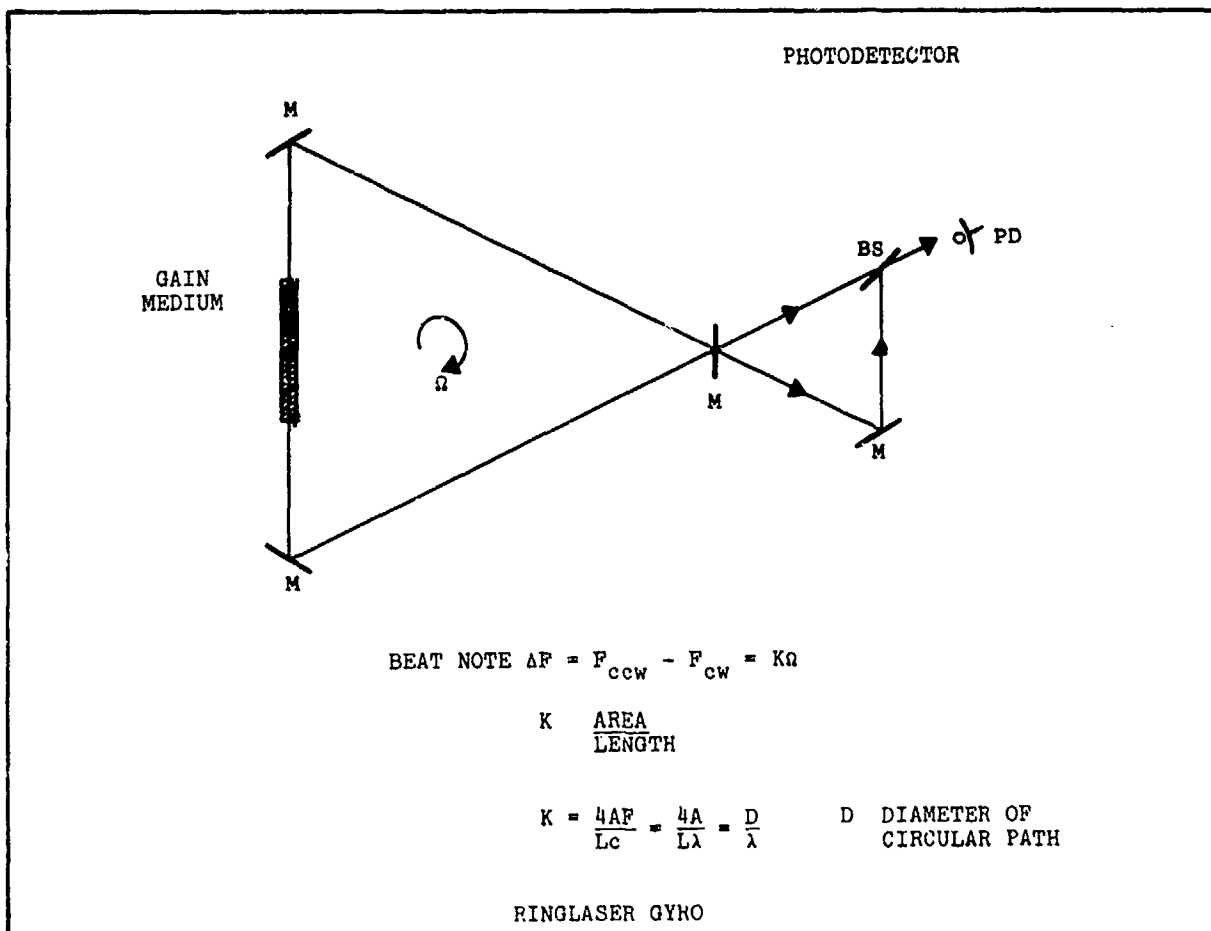


FIGURE 9. The conventional RLG renders a difference frequency or a pulse rate proportional to the rotation rate, as long as the gain medium inside the ring supports two regenerative oppositely directed modes of different frequencies along paths of identical properties. At low rotation rates, the modes do not separate, they "lock in."

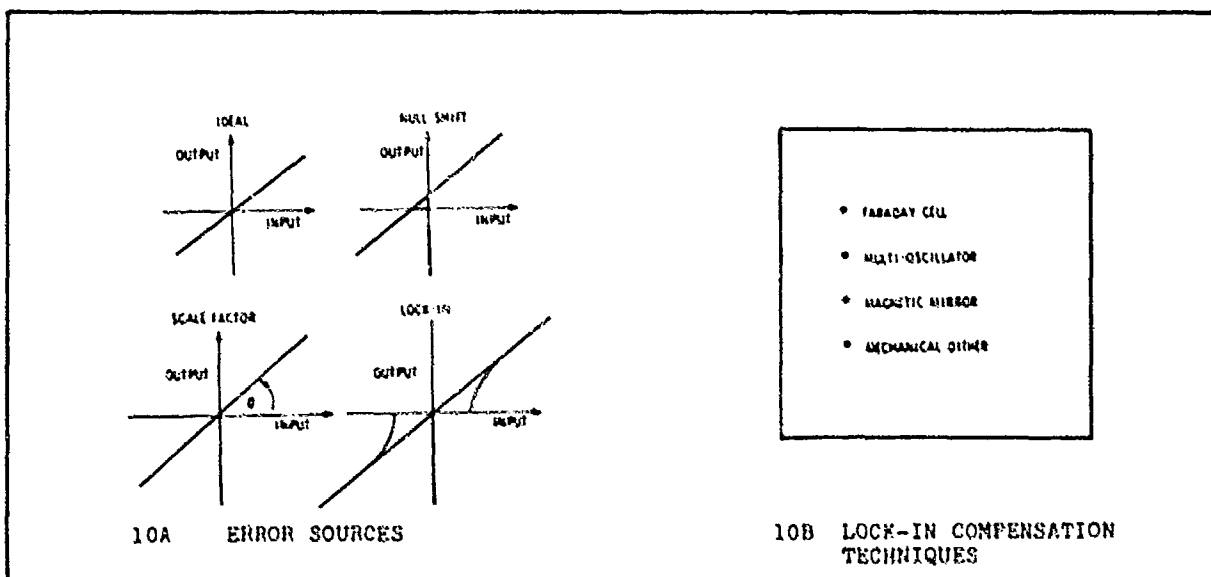


Figure 10. Error sources of practical devices and compensation of the lock-in phenomena by mechanical or magnetic oscillatory bias rotation, "dither," so the resulting operating characteristic renders detection also around zero rate input. The equation for the phase difference between the oscillation modes shows a random phase, i.e., noise with non-zero lock-in range (Ref I, and Appendix A, Figs 7 and 8)

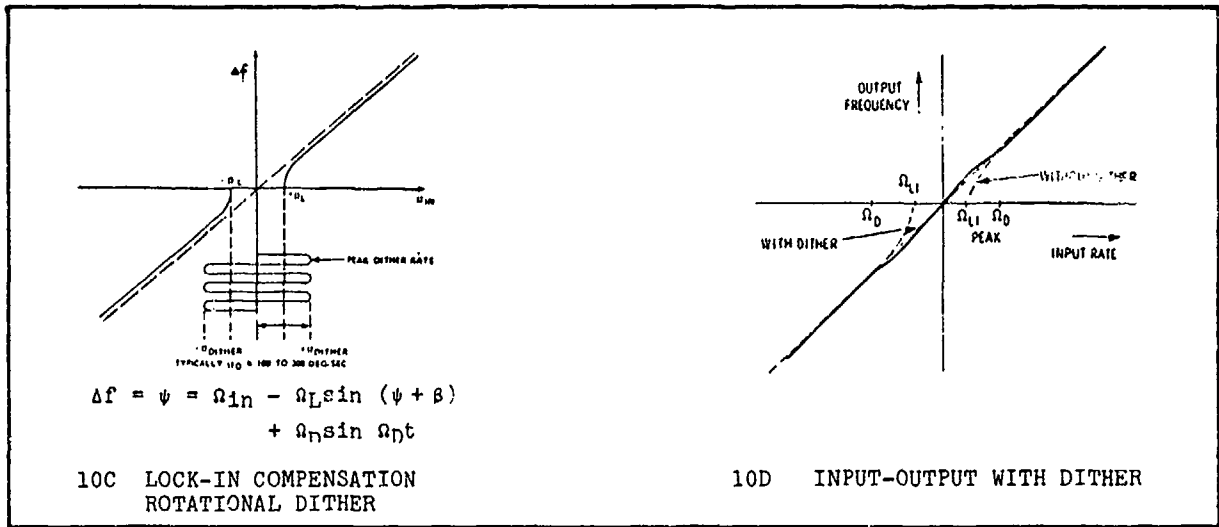


FIGURE 10. Error sources of practical devices and compensation of the lock-in phenomena by mechanical or magnetic oscillatory bias rotation, "dither," so the resulting operating characteristic renders detection also around zero rate input. The equation for the phase difference between the oscillation modes shows a random phase i.e. noise with non-zero lock-in range.

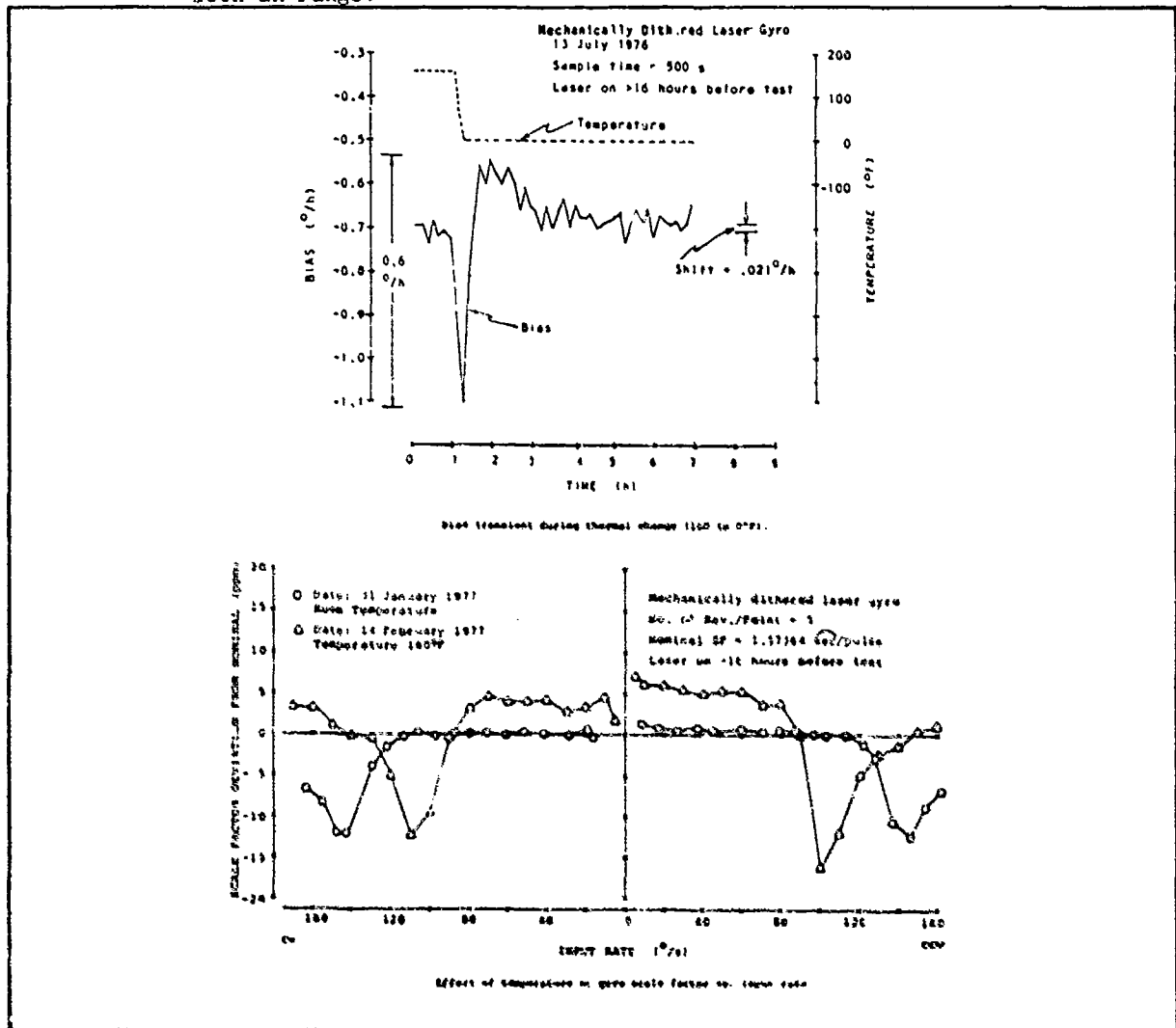


FIGURE 11. Examples of RLG operating bias and scale factor changes through thermal changes. The scale factor deviations occur near the peak dither rate. (Ref III, 479)

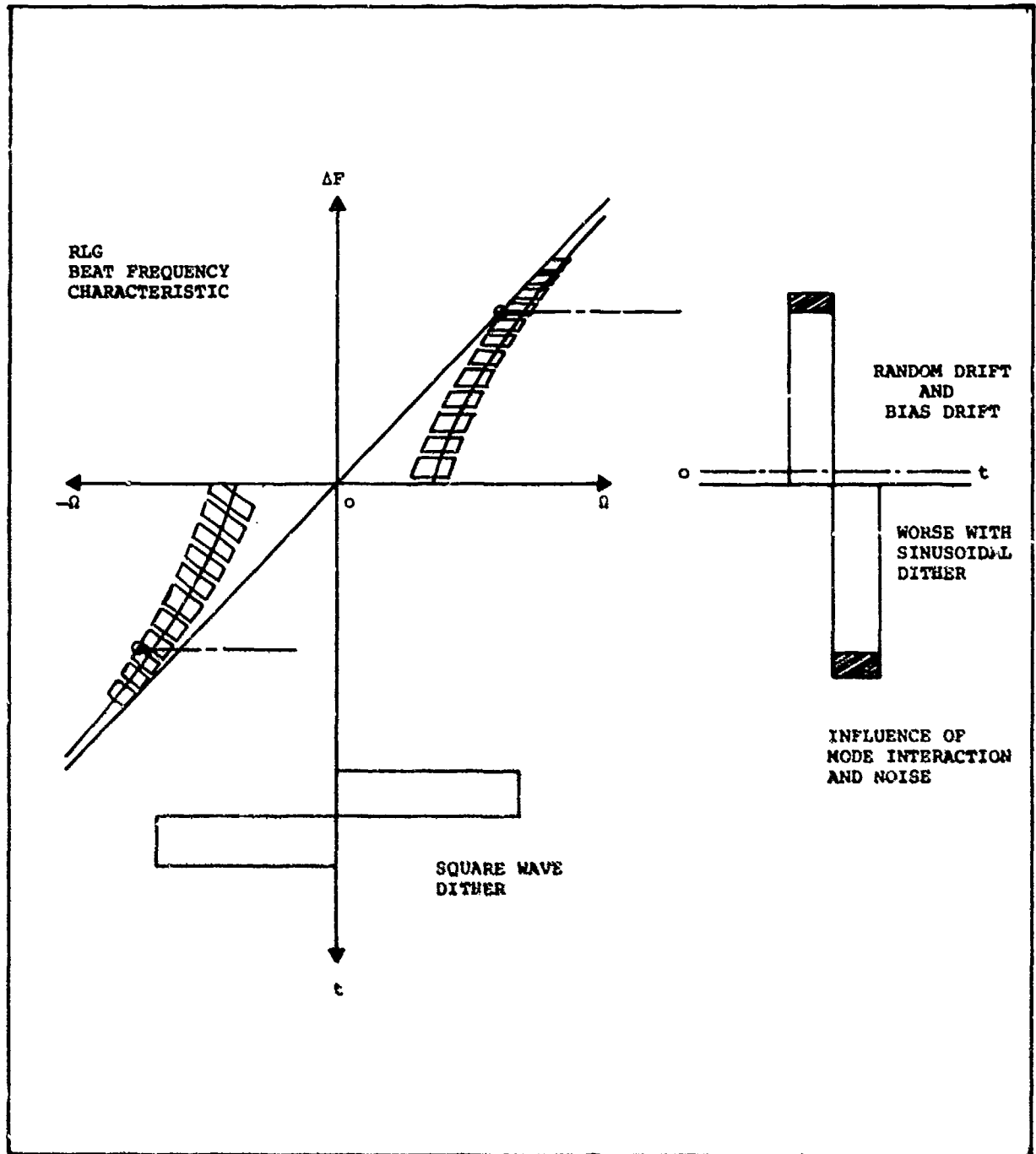


FIGURE 12. Demonstration of how even under square wave dithering random drift and bias drift is produced, because of random oscillator starting phase and stochastic behavior of the operating characteristic especially close to the lock-in range. (Ref 1, #36; Appendix A, Fig 8)

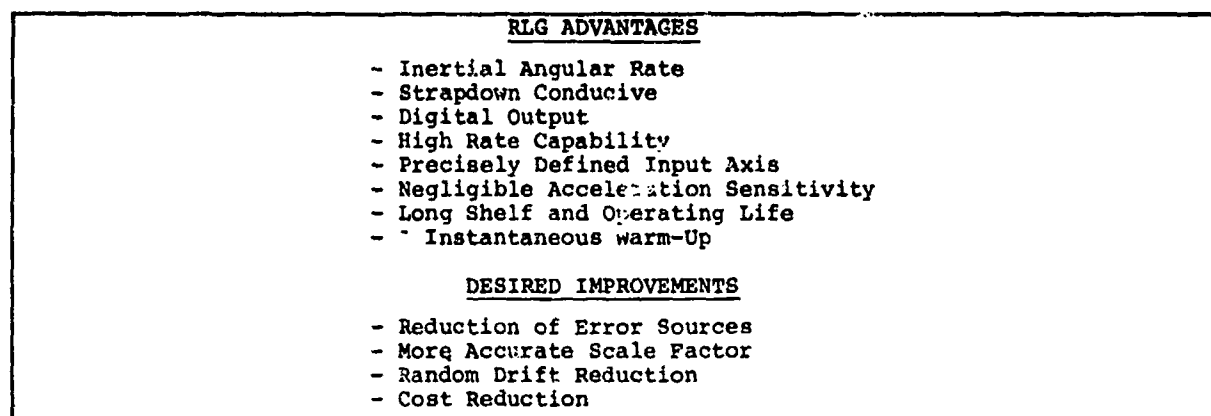


FIGURE 13. The conventional RLG renders considerable performance and cost advantage, especially if the improvements underway are realized. A major effort is directed toward lock-in range reduction by reducing the backscatter radiation especially from mirrors. (Ref I, 41, 46 and Appendix A, Figure 12)

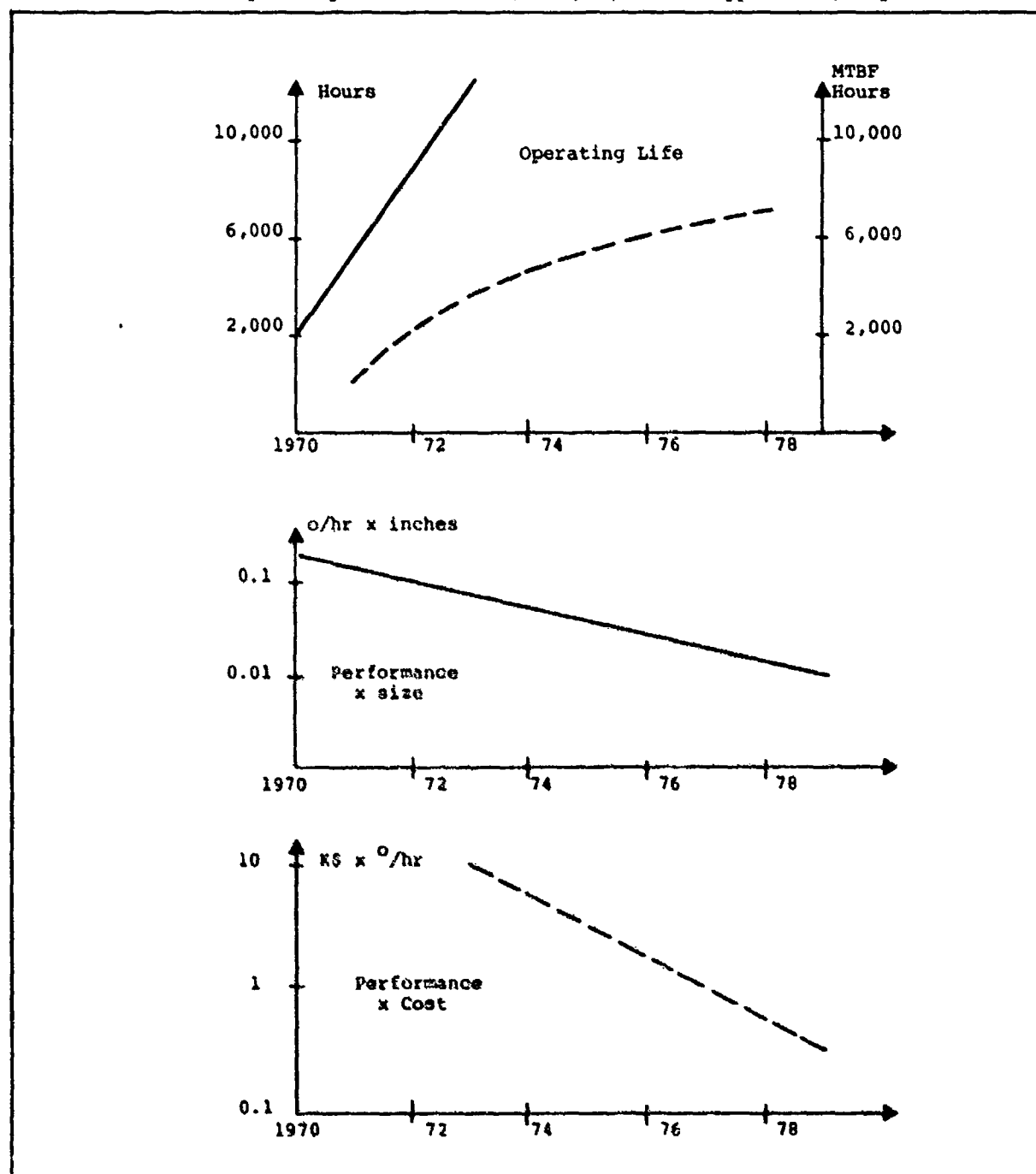
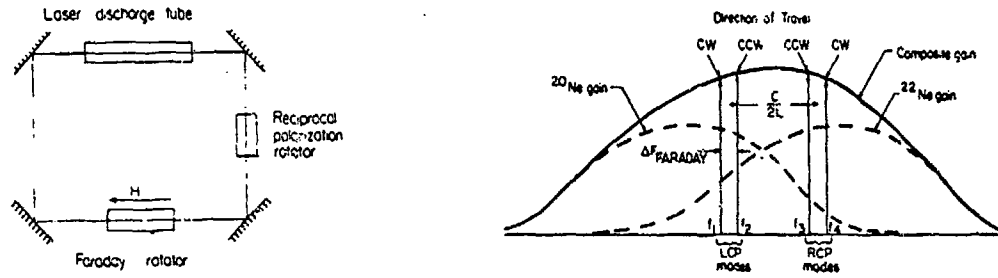


FIGURE 14. Median values characterizing the availability and improvements of practical RLGs based on company and test station reports.

Four-frequency ring laser gyroscope resonator. The "Faraday" rotator may comprise a Faraday cell or may be incorporated into another element, e.g., a magnetic mirror or a magnetic field on the discharge.



Lasing modes of a four-frequency ring laser gyroscope. The composite gain curve (solid line) is a sum of the (dashed) single-isotope gain curves. The Faraday splitting $f_2 - f_1 = f_3 - f_4$ is shown greatly exaggerated for clarity.

FIGURE 15. Principle of the four frequency multioscillator or differential laser gyro (DILAG) to avoid dithering.

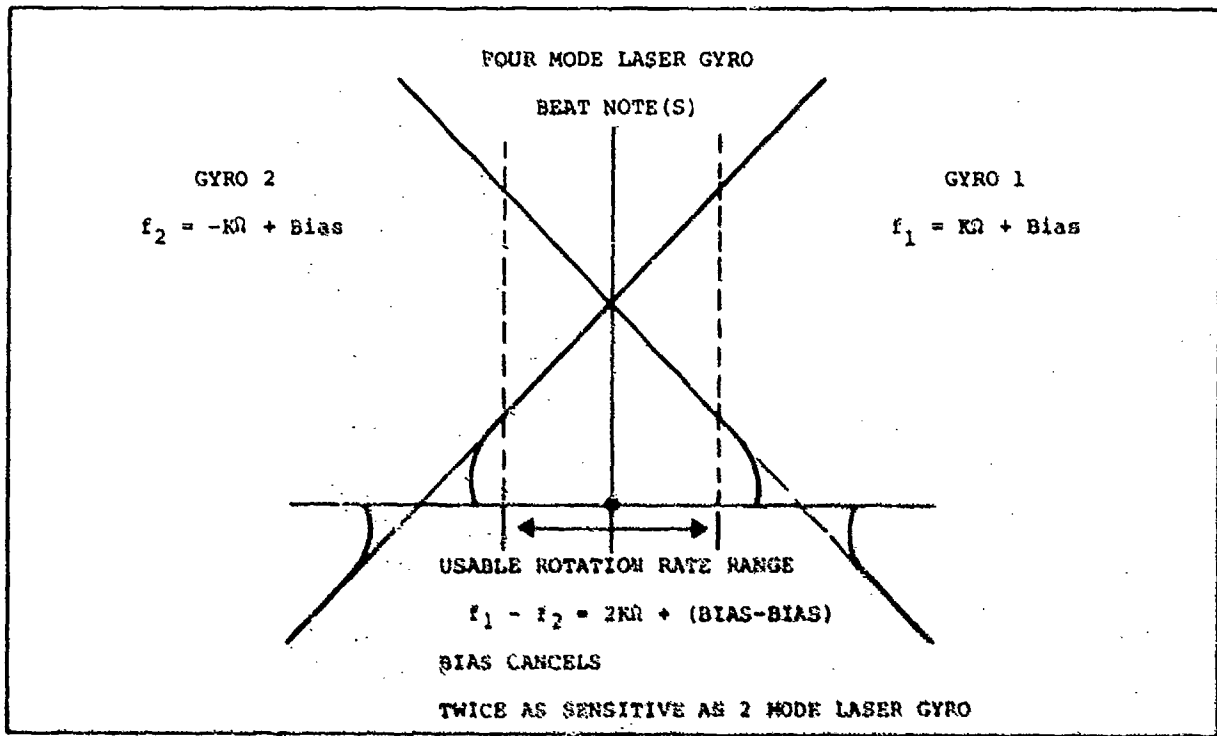
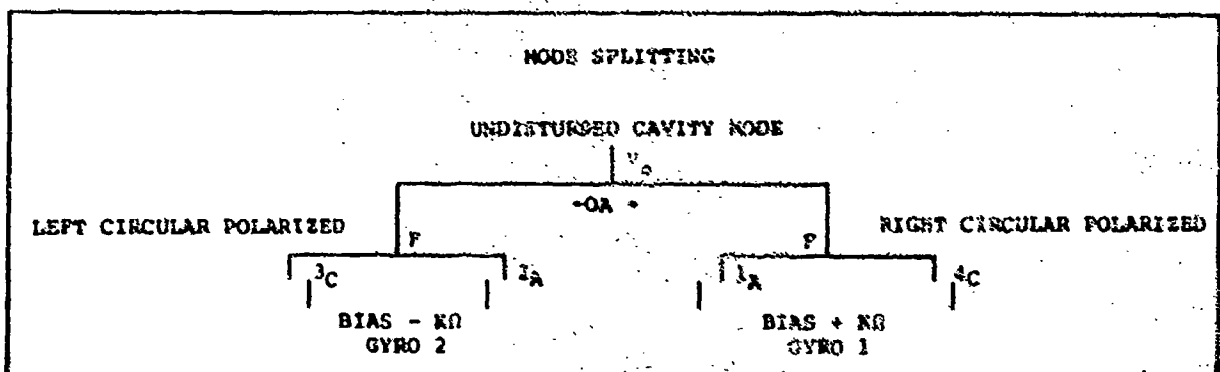
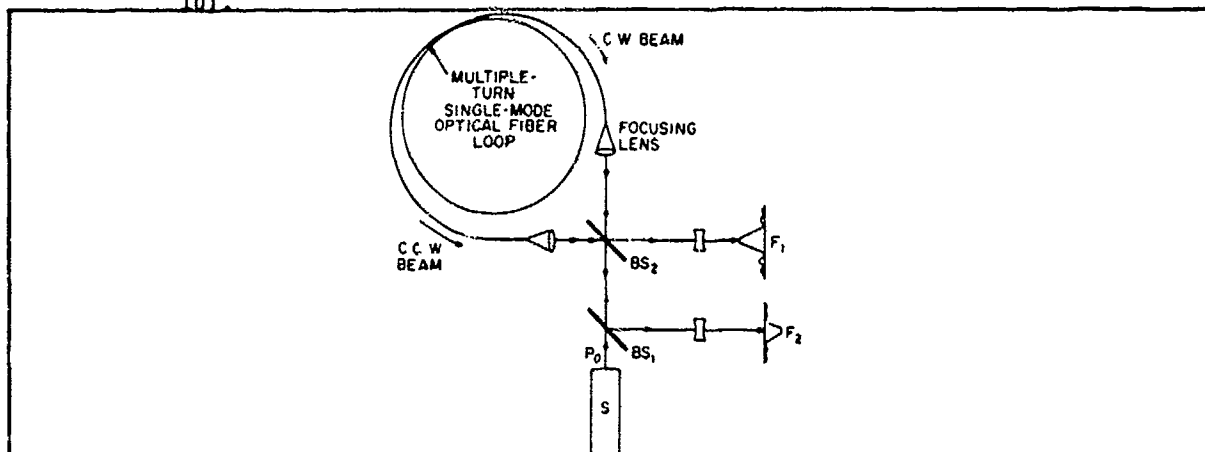


FIGURE 16. Four oscillation modes are biased stationary and differentially by a reciprocal polarization rotator (OA) (typically quartz cut normal to its c-axis) and a non-reciprocal polarization rotator (Faraday cell) (F). Operating zero is at the cross-over of the characteristics; sensitivity to rotation is doubled.

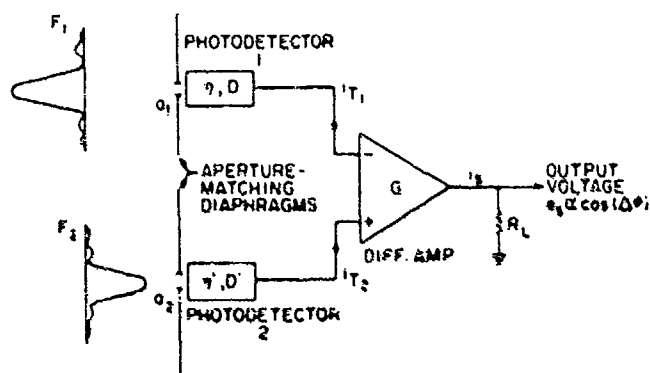


$$\begin{aligned} \nu_0 &\approx 10^{14} \text{ Hz} \\ \Omega &\approx 400 \text{ MHz} \\ F &\approx 1 \text{ MHz} \\ K\Omega &\approx \pm 100 \text{ KHz} \end{aligned}$$

FIGURE 17. The mode splitting produced by the elements in the ring results in two gyros of left and right circularly polarized waves which, in turn, have clockwise and counterclockwise traveling parts split by the Faraday cell. At ccw rotational input, the frequencies of the ccw waves shift down, the others up. The condition for obtaining the necessary non-reciprocal bias is stringent stationary path symmetry. Ref I, 39, 40, 44 and Appendix A, Figure 10).

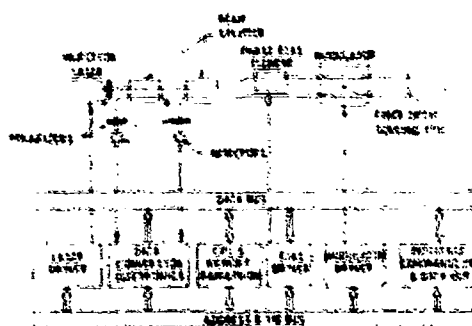


Optical setup of the ring interferometer for the analysis.



Differential detection scheme with balanced inputs to eliminate common-mode noises adaptable to the optical setup.

FIGURE 18. Optical fiber Sagnac interferometer system with analog readout via complementary fringe patterns and intensity comparison. (Ref II, #61, #69)



Fiber Optic Rotation Sensor Block Diagram

FIGURE 19a

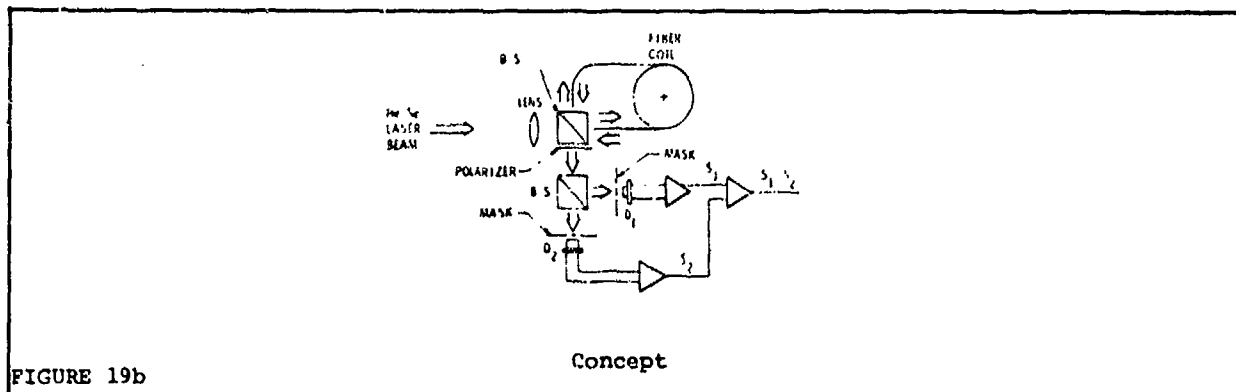


FIGURE 19b

FIGURE 19. Optical fiber Sagnac interferometer system with differential interference pattern readout, built-in 180° phase bias element, modulated, input reversed optical carrier. (Ref II, #65)

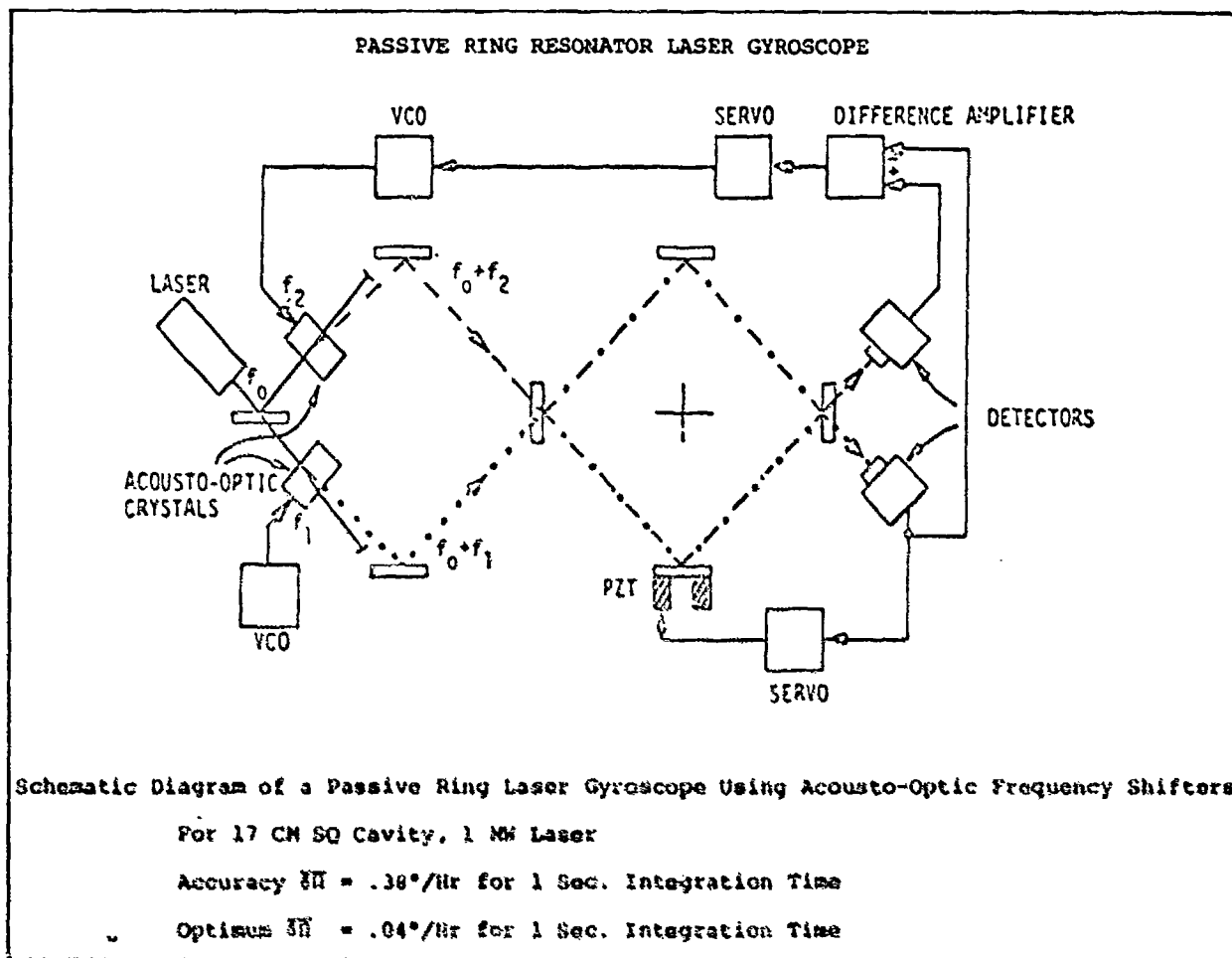


FIGURE 20. Passive ring resonator system, tracking change of resonator resonance via servo-feedback varying one optical input frequency and one optical path-length; allowing frequency readout. (Ref

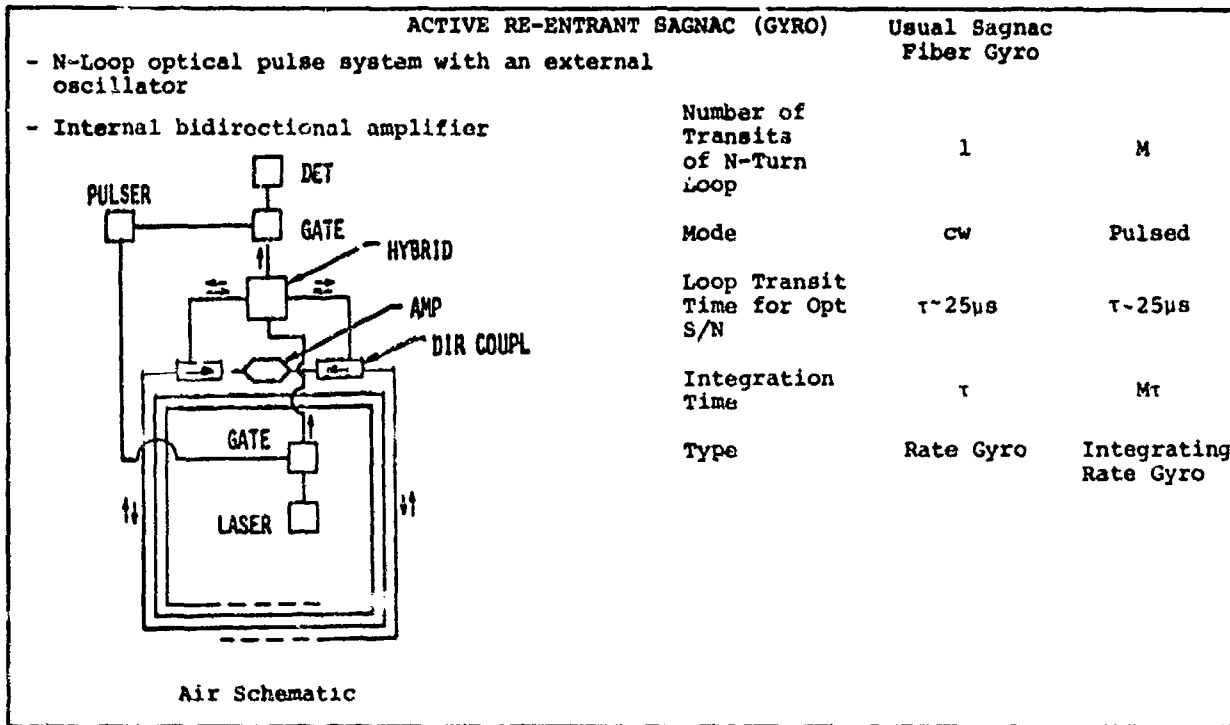


FIGURE 21. ACTIVE RE-ENTRANT SAGNAC SYSTEM USING OPTICAL PULSES WITH MULTIPLE TRANSITIONS THROUGH MULTITURN LOOP, RENDERING FREQUENCY READOUT LIKE RLG. (Ref II, #68)

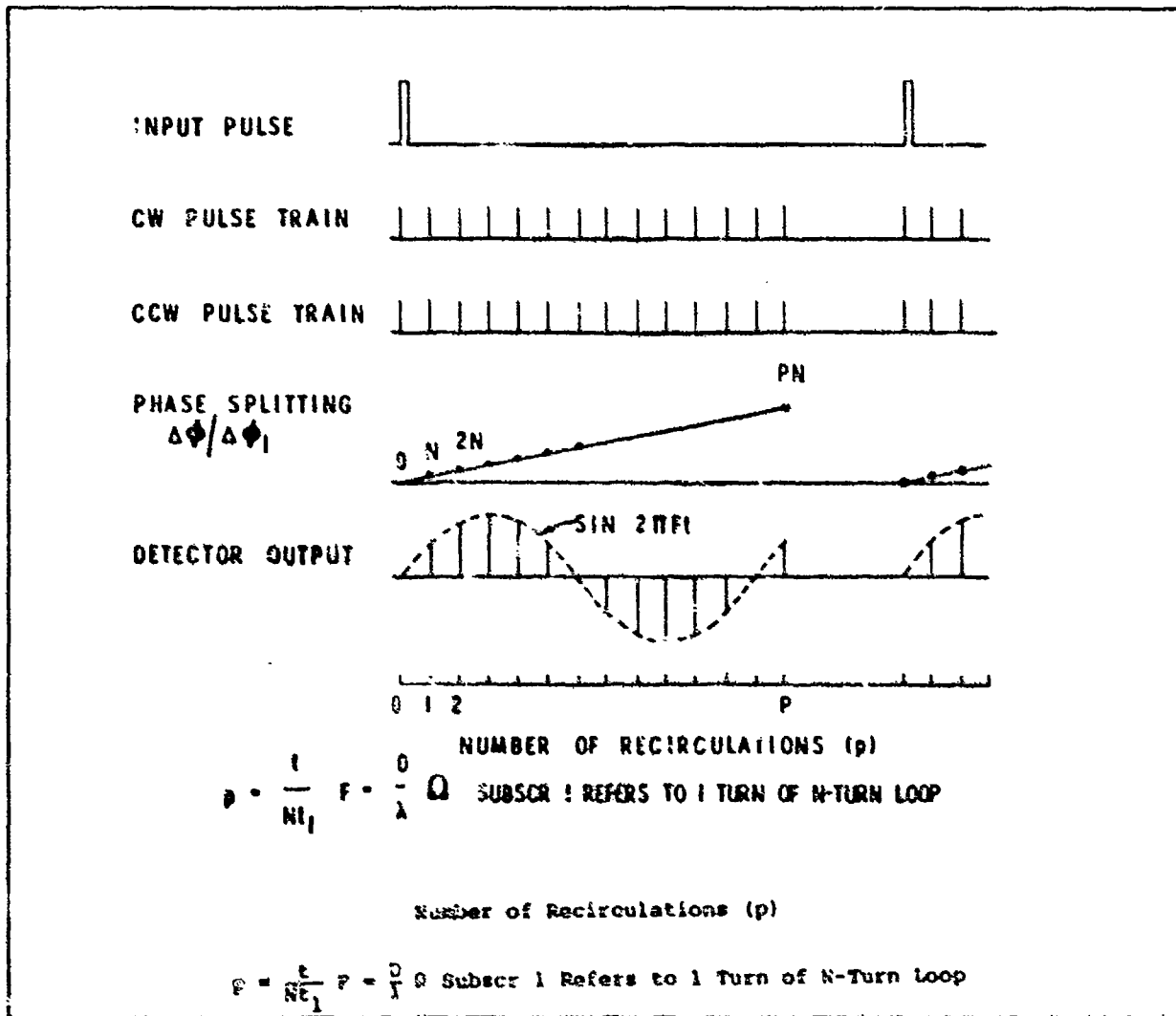


FIGURE 22. Explanation of result of vectorial addition of monitored optical pulses in the active re-entrant Sagnac Gyro (ARS) during rotation of the fiber coil. (Ref II, #64)

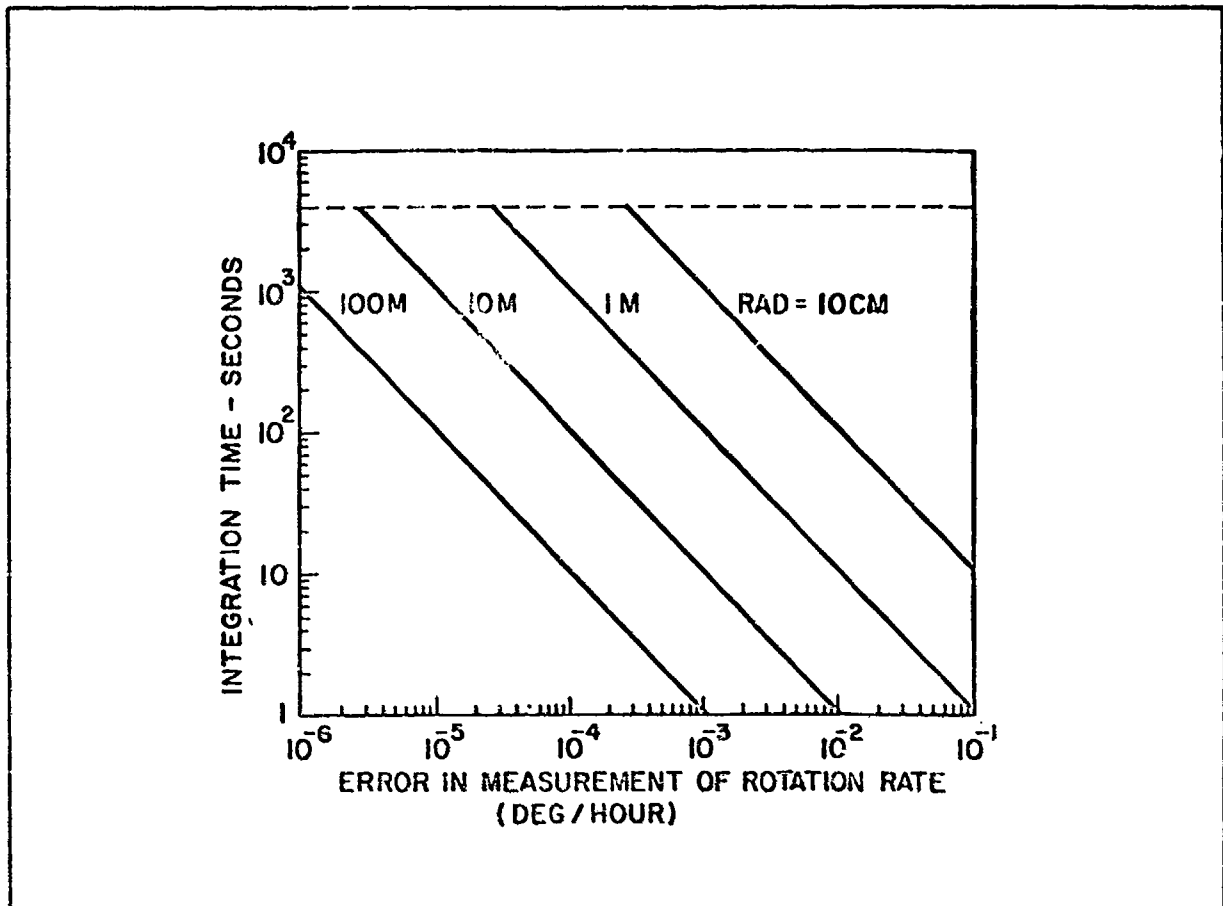


FIGURE 23. Example of possible performance of the ARS gyro for different radii of the fiber coil. Intrinsic benefit of the Sagnac effect through large loops can be realized optimally. (Ref II, #68)

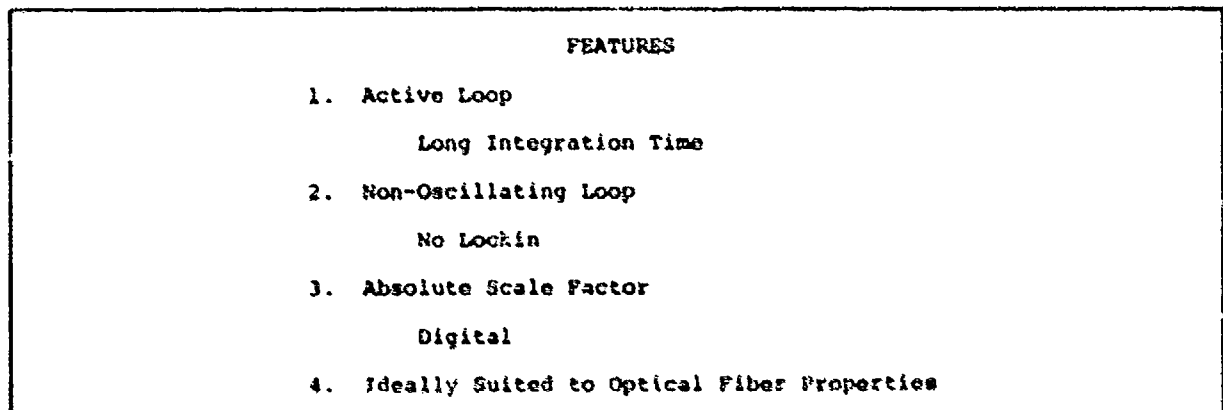


FIGURE 24. Basic features of the ARS development. Essentially a rate integrating system, succeeding in removal of path instabilities and environmental sensitivities, with a challenging integrated optics bidirectional amplifier project. (Ref II, #69)

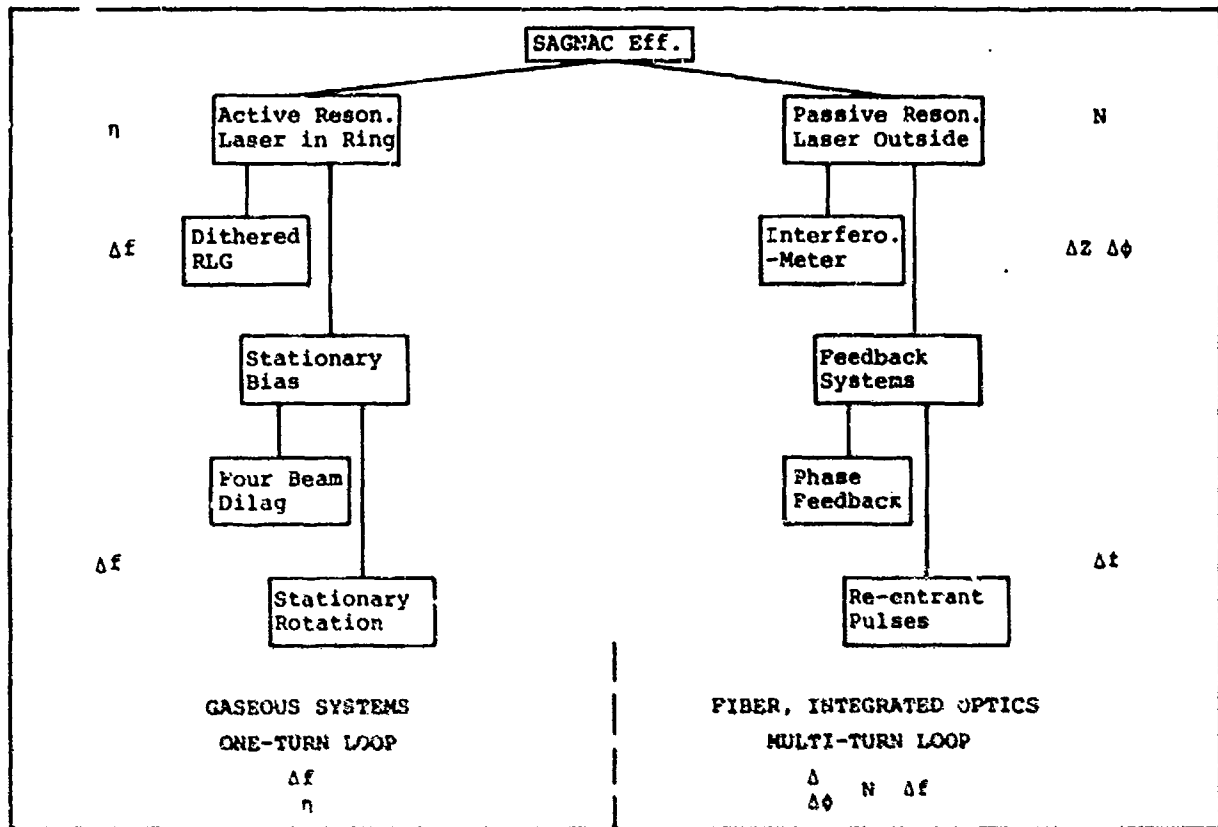


FIGURE 25. How the categories of Sagnac systems are realized and what their output and determining influence parameter is.

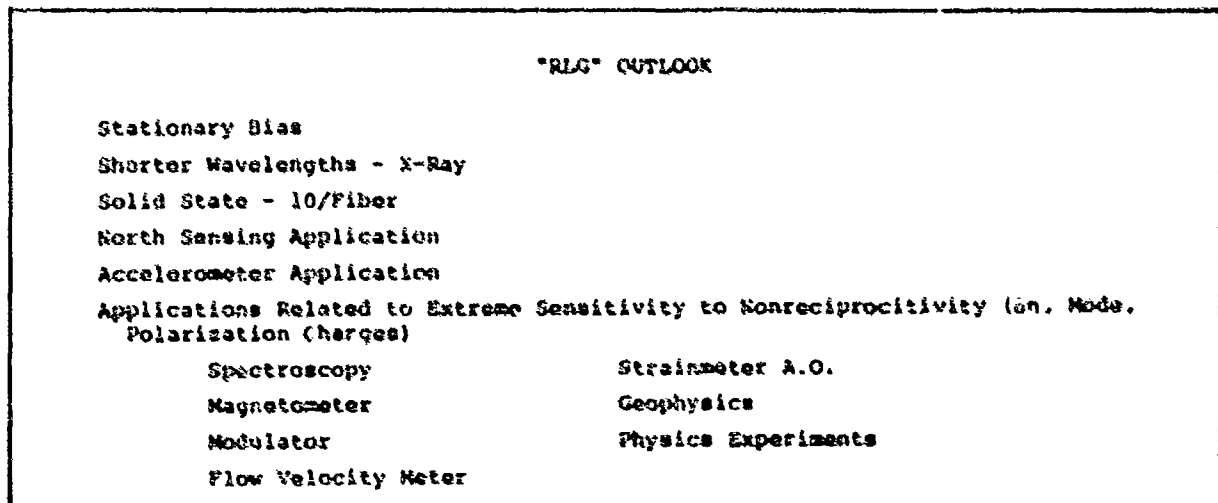


FIGURE 26. Trends and possibilities for application and extension of the Sagnac systems. (Ref 1, #1)

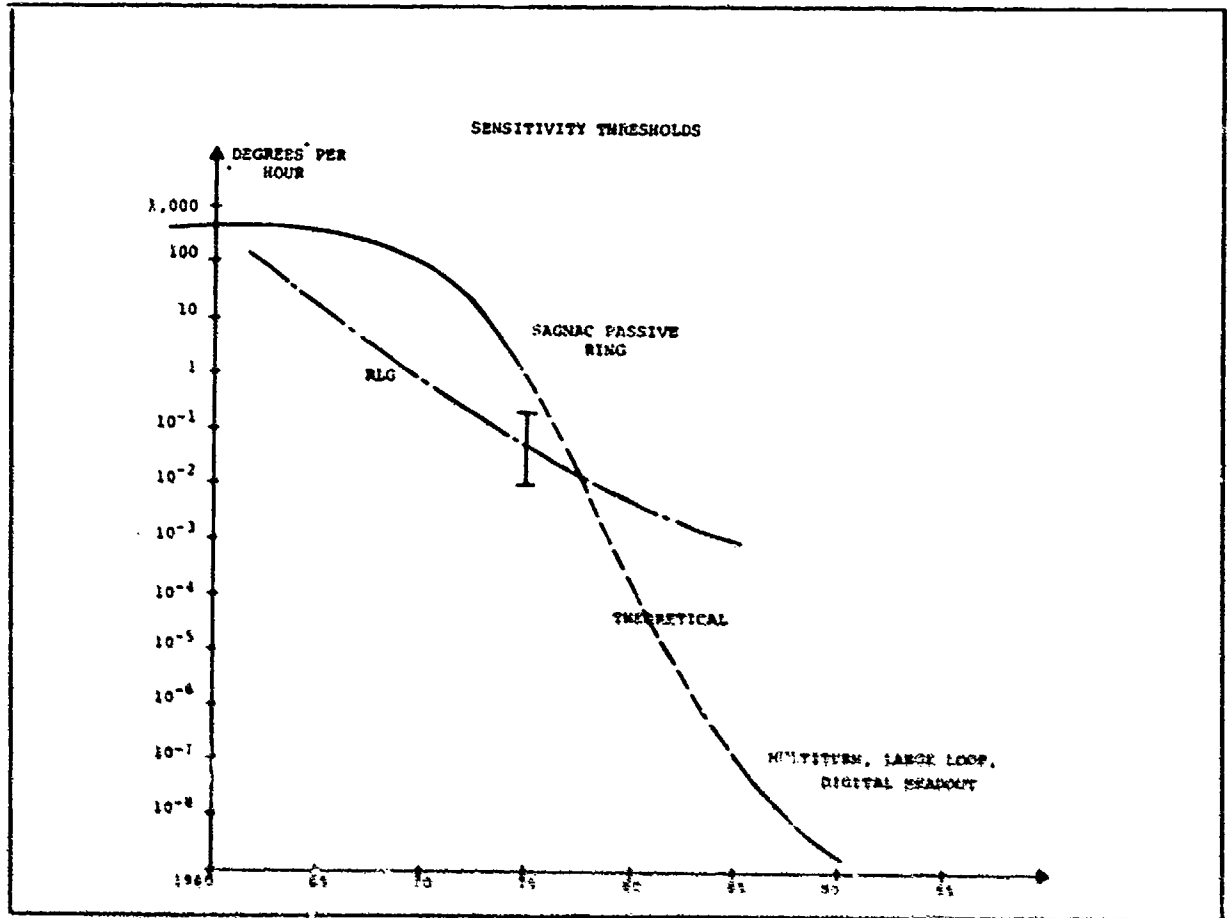


FIGURE 27. Performance (threshold sensitivity in degrees per hour) median values over time and trend estimation.

RESEARCH TOPICS

- o Rotational Accelerometer
- o RLG North Sensing and Seeking System
- o All Solid State Inertial Navigation System
- o Application of Shorter Wavelength Sources
- o Utilization of Effects Related to:
 - Refractive Index Changes
 - Medium Flow

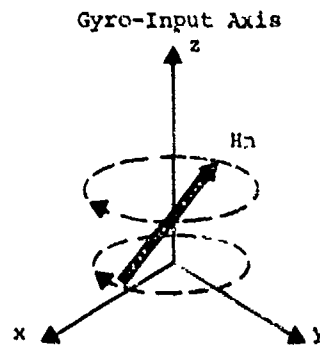
FIGURE 28. Recommended long range R&D topics, based on present research trends and available equipment experience.

ACTIVITIES

<u>RLG</u>	<u>SAGNAC</u>
Autonetics	Jet Propulsion Lab
Honeywell	Lear Siegler
Hamilton Standard	Martin Marietta
Kearfott	MIT
Lear Siegler	Northrop
Litton	Rockwell
Nortronics	Siemens
Raytheon	Stanford University
Sperry	Univ. of Utah
C.S. Draper Lab	Texas Instruments
SFENA	Thomson C.S.F.
SFIM	MBB
Ferranti	

FIGURE 29. Companies and institutions known through publications to be involved in RLG and passive Sagnac system research or development activities.

NMR GYRO



Magnetic Field H_n Rotates Around Gyro Input Axis

Frequency of Rotation-Nuclear Precession Frequency - Is Constant in Inertial Space

Inertial Rotation Rate Measurement Only about Input Axis

Measured Frequency is Precession Frequency Shifted Higher or Lower by Amount Equal to Gyro Rotation Rate

FIGURE 30. Principle of the Nuclear Magnetic Resonance (NMR) gyro or Magnetic Resonance Gyro (MRG).

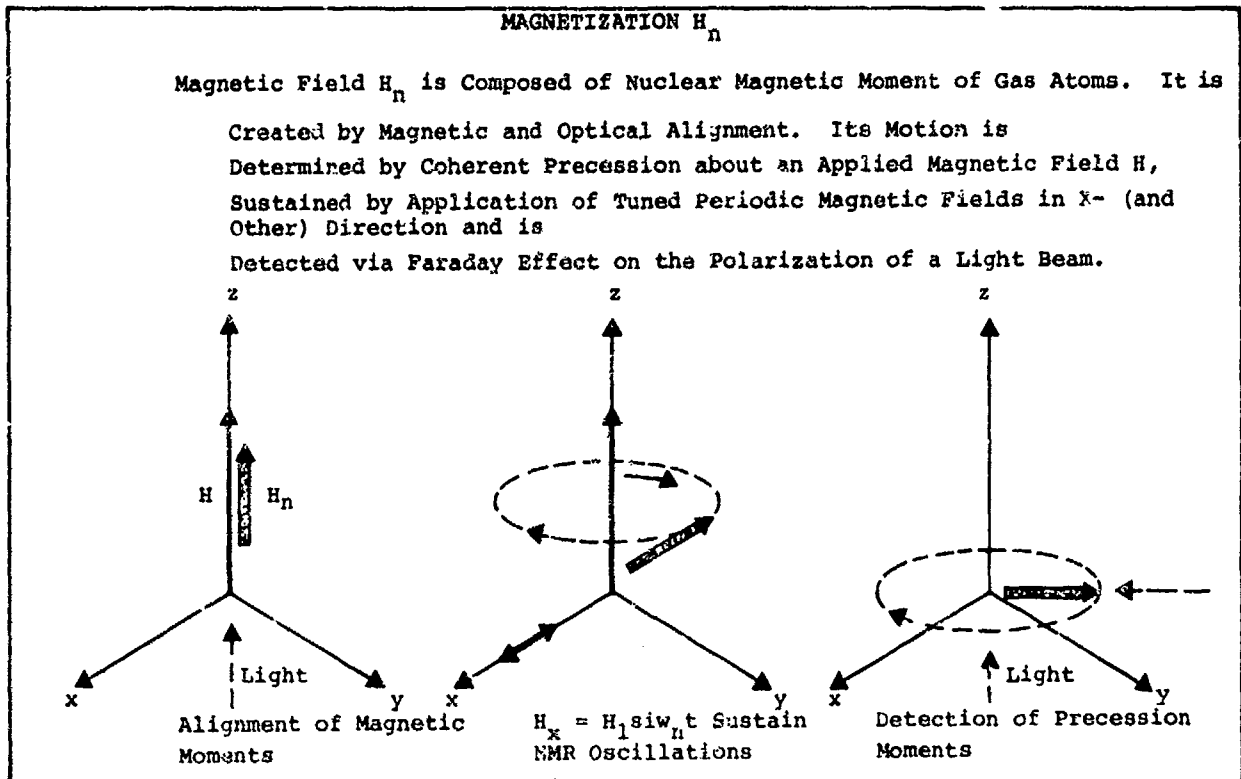


FIGURE 31. How the nuclear magnetic field precession vector is established by optical pumping and driving magnetic field.

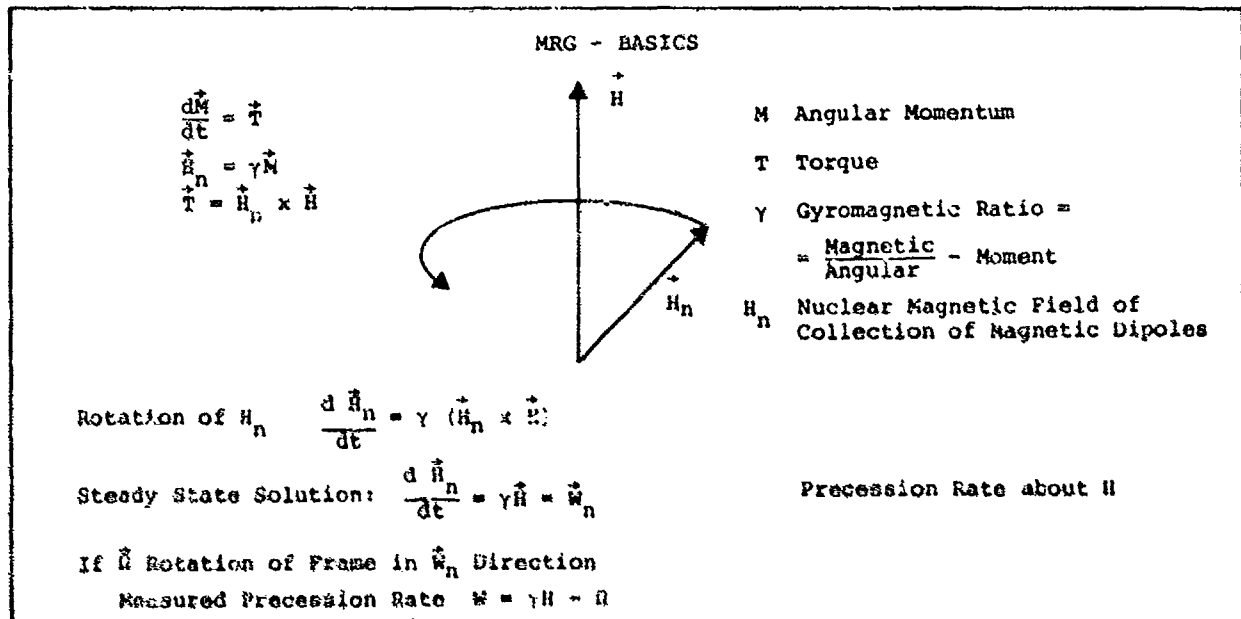


FIGURE 32. Basic relation defining the Larmor precession in relation to the input rotational rate.

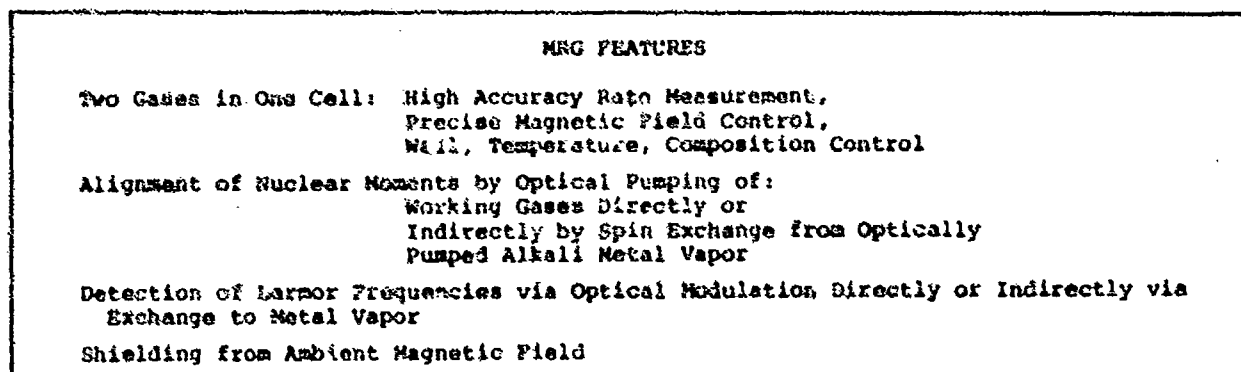


FIGURE 33. Features of MRG realizations.

MRG PRINCIPLE

Two Species Implementation (A, B)

$$\text{If } W_A = \gamma_A H - \Omega$$

$$W_B = \gamma_B H - \Omega$$

$$\text{Then } \Omega = \frac{\left(\frac{\gamma_B}{\gamma_A} W_A - W_B\right)}{\left(1 - \frac{\gamma_B}{\gamma_A}\right)} \quad H = \frac{1}{\gamma_A} \cdot \frac{(W_A - W_B)}{\left(1 - \frac{\gamma_B}{\gamma_A}\right)}$$

Requires High Accuracy for $\frac{\gamma_B}{\gamma_A}$

Duplicate Cell in Oppositely Directed Magnetic Field

$$\begin{aligned} W_A^1 &= -\gamma_A H^* - \Omega & \Omega &= \frac{\left(\frac{\gamma_B}{\gamma_A} W_A^1 - W_B^1\right)}{\left(1 - \frac{\gamma_B}{\gamma_A}\right)} & H^* &= \frac{1}{\gamma_A} \cdot \frac{(W_B^1 - W_A^1)}{\left(1 - \frac{\gamma_B}{\gamma_A}\right)} \\ W_B^1 &= \gamma_B H^* - \Omega \end{aligned}$$

Then Combined

$$\Omega = \frac{1}{2 \left(1 - \frac{\gamma_B}{\gamma_A}\right)} \cdot \left(W_B^1 + W_B + \frac{\gamma_B}{\gamma_A} (W_A + W_A^1)\right)$$

$$\text{For } \Omega = 0 \quad \frac{\gamma_B}{\gamma_A} = \frac{W_B^1 + W_B}{W_A^1 + W_A}$$

$$\text{If } W_B + W_B^1 = 0 \quad \text{By Control of } H \text{ One has } \Omega = \frac{(W_A + W_A^1)}{2 \left(\frac{\gamma_A}{\gamma_B} - 1\right)}$$

$$\text{And } H - H^* = \frac{(W_A + W_A^1)}{\gamma_A \left(1 - \frac{\gamma_B}{\gamma_A}\right)} = \frac{2\Omega}{\gamma_B}$$

FIGURE 34. Explanation of the dual particle usage.

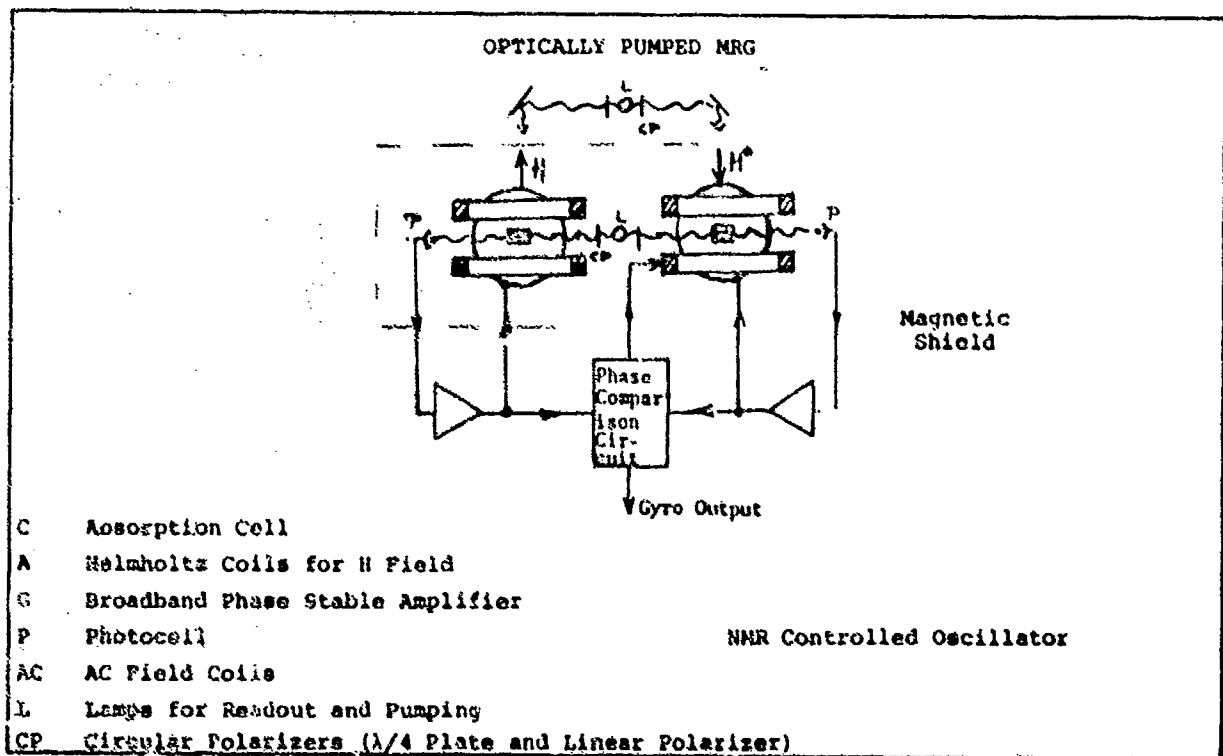


FIGURE 35. A typical MRG realization example.

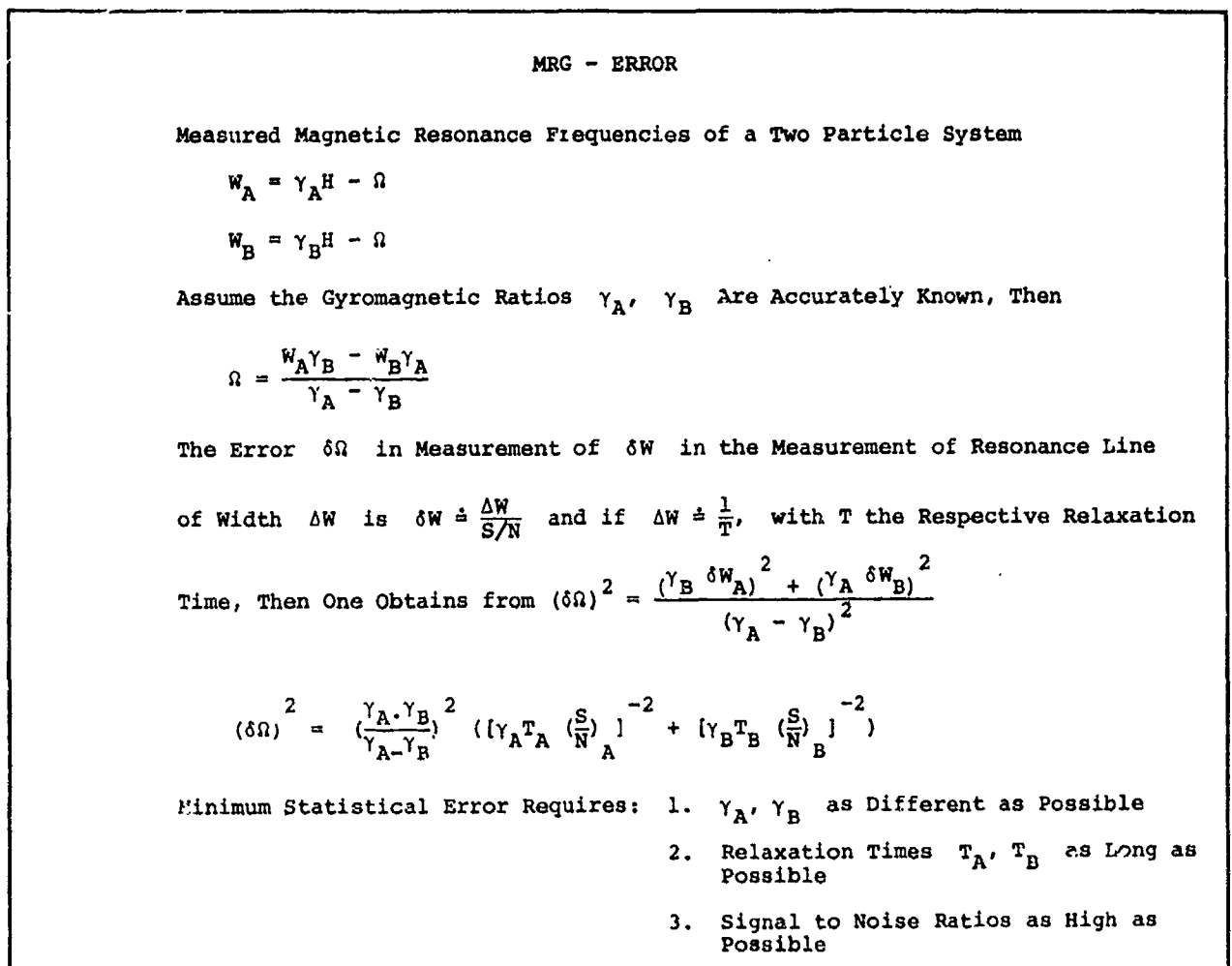


FIGURE 36. Theoretical measurement error of a two particle MRG and design recommendations.

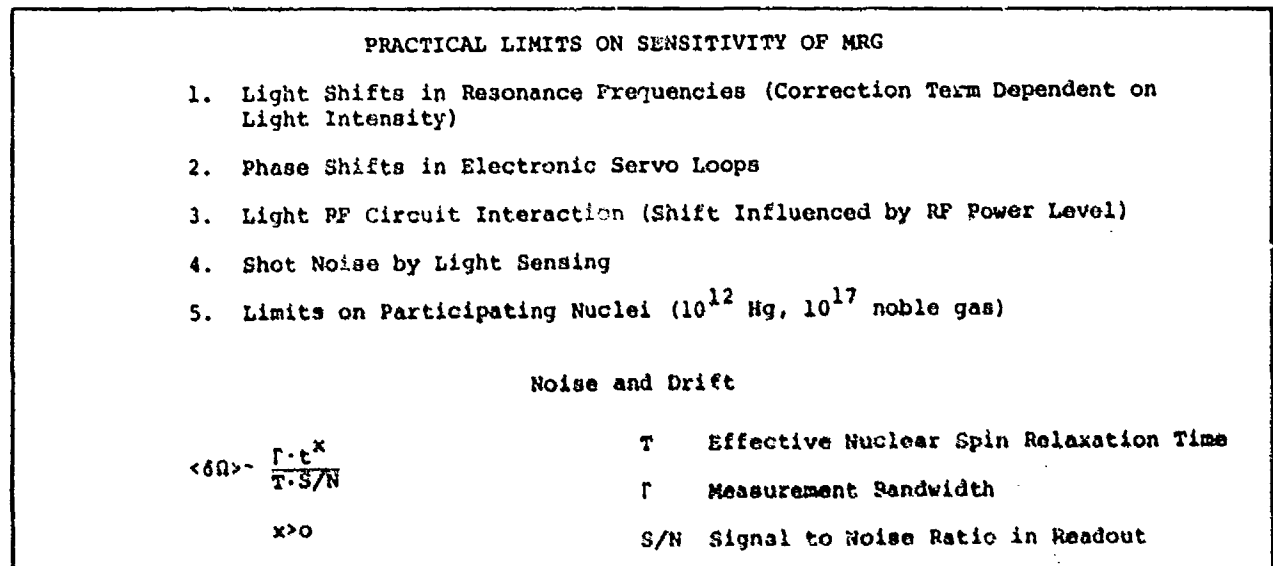


FIGURE 37. Errors observed in practical devices and related research indicate existing sensitivity limiting influences. The practical limit contains drift term and is larger than error shown in Fig. 36.

NMR-MRG-DEVELOPMENT TRENDS

<u>Mercury</u>	<u>Noble Gases</u>	<u>Helium-Systems</u>
Direct Pumping and Readout	Indirect Pumping and Readout Collisional Spin - - Exchange	Direct Pumping Indirect Readout
Two Particle System at Room Temperature (or Above)		
A.C. Field NMR Oscillators		
Combine Two Cells with Equal Materials in Opposite Magnetic Fields		
Four Cells for Three-Axis Inertial Measurement		
Exception:		
Low Temperature System Employing He ³ , Ambient Magnetic Field Dilution, Pulse Type Precession Initiation (Varian-Packard), Magnetic Superconductive Readout Method (Squid).		

FIGURE 38. Presently known MRG system characteristics. (Ref V)

ORDER OF MAGNITUDE COMPARISON OF ROOM TEMPERATURE MRGs

System	Spin		T (Sec)		γ (KHz/GAUSS)		δΩ (Hz)
	A	B	A	B	A	B	
I	199 Hg	201 Hg	10 ²	10 ²	1	1/2	9 · 10 ⁻³
II	Noble Gas	Isotopes	10 ³	10 ³	1	1	F · 10 ⁻³ F > 1
III	He ³ (1 ¹ S ₀)	He ⁴ (2 ³ S ₁)	10 ⁴	1	1	10 ³	1 · 10 ⁻³

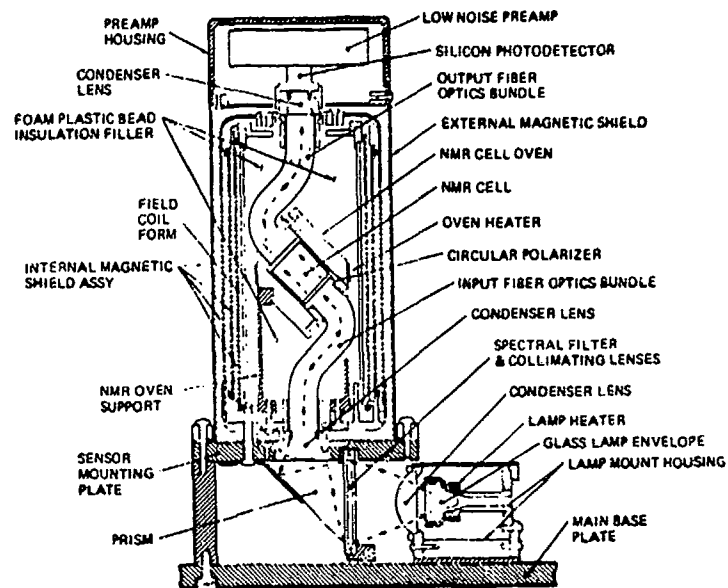
$$\text{With } \delta\Omega = \left[\left(\frac{\gamma_B}{\gamma_A - \gamma_B} \right)^2 (\Delta W_A)^2 + \left(\frac{\gamma_A}{\gamma_B - \gamma_A} \right)^2 (\Delta W_B)^2 \right]^{1/2}$$

$$\text{And } \Delta W \text{ (Hz)} \doteq \frac{1}{T} \left(\frac{1}{\text{Sec}} \right) \text{ One Has for System III}$$

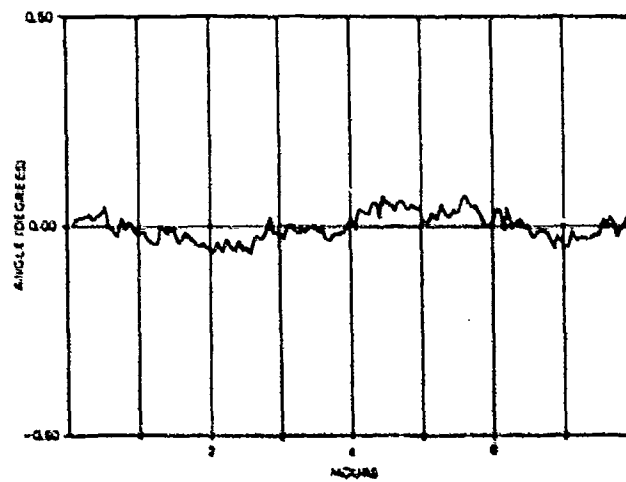
$$\delta\Omega \doteq [10^{-8} + 10^{-6}]^{1/2} = 10^{-3} \text{ Hz}$$

FIGURE 39. Theoretical comparison of known systems using order of magnitude values of physical parameters, showing the difficulty of particle choice and reaching the earth rate measurement sensitivity. Using high S/N and actual parameters improves the error value.

A NUCLEAR MAGNETIC RESONANCE (NMR) GYRO WITH OPTICAL MAGNETOMETER DETECTION



Assembly drawing of NMR breadboard gyro sensor.



Gyro angle data. Selected segment with average bias removed.

FIGURE 40. Typical MRG device realization. (Ref V, #100)

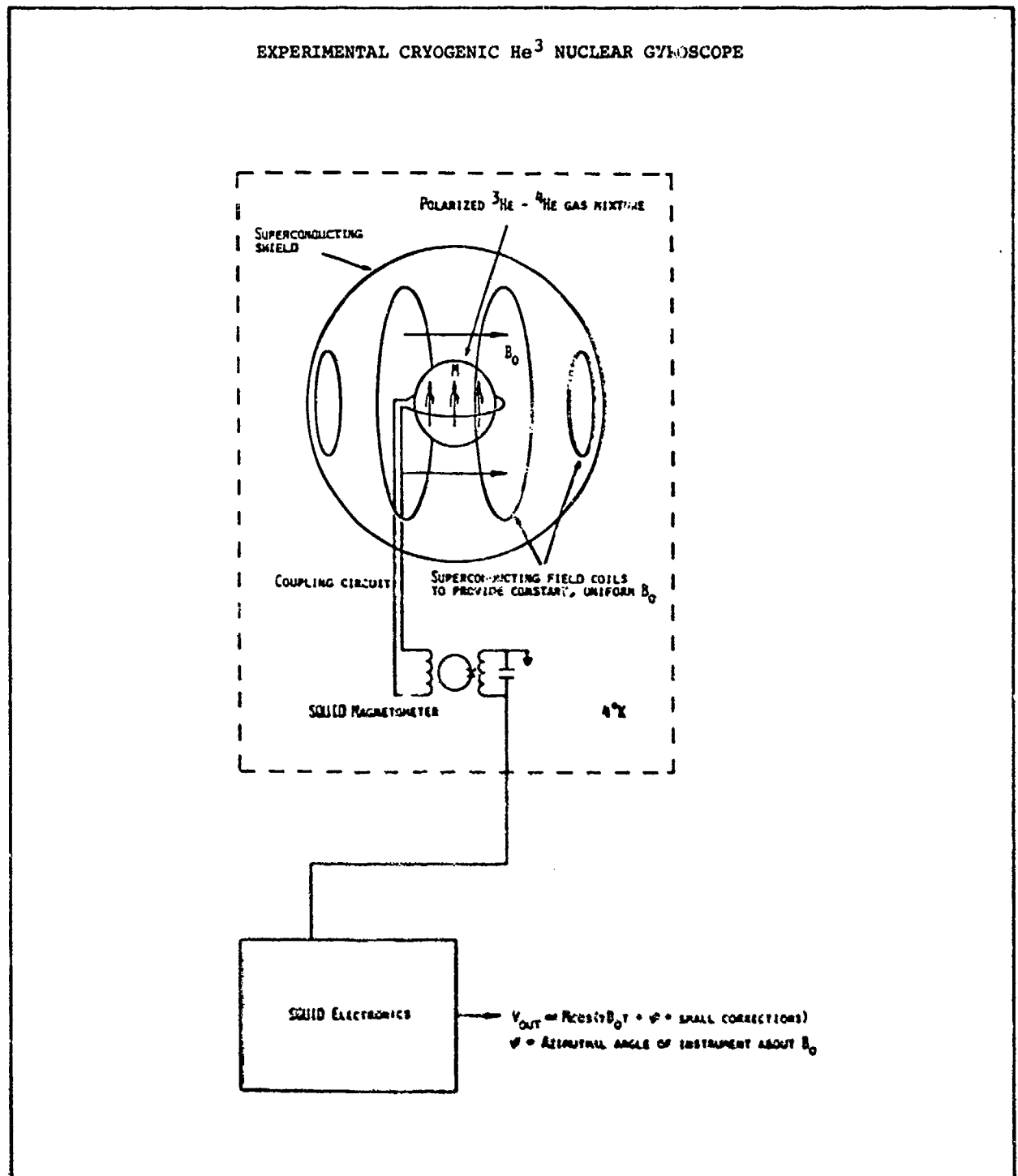


FIGURE 41. Schematic of cryogenic nuclear gyroscope, using He^3 Larmor precession about minimum stationary magnetic field in superconductive magnetic shield, with superconductive magnetometer readout of precession motion. Since magnetic field stability provided by shield, only one spin species necessary. Nuclear relaxation times (He^3 in He^4 mixture) in the order of days or longer. (Ref V, #89)

MRG POTENTIAL ADVANTAGES	
	No Critical Mechanical Dimensions
	No Moving Mechanical Parts
	Strapdown Conductive
	High G-Capability
	High Reliability
	Low Cost
PROBLEM AREAS	
Drift	(Increase of Relaxation Times Dependent on Cell Geometry and Particle Environment. Reduction of Light Induced Frequency Shift.)
Noise	
Shielding	
Theory Development	
Cross Axis Interactions	
System Use	

FIGURE 42. Suggested MRG potential advantages and work for improvement of present experimental models.

HISTORIC NOTE			
<u>RLG</u>			
1962/63	Rosenthal, Maceck, Davis Aronowitz	1958	Greenwood, Bailey, Simpson
1970	0.1°/Hr		10°/Hr
1978	0.01°/Hr		1°/Hr
1982	0.001°/Hr		0.1°/Hr
(Order of Magnitude Expected Thresholds for 100 sec Samples)			

FIGURE 43. Indicates different development history and status of RLGs and MRGs.

RLG/MRG - COMPARISON OF PROBLEMS, STATUS, POTENTIAL			
<u>RLG</u>	<u>MRG</u>	<u>Both</u>	
Optical and Mechanical Precision	Simpler	No Moving Mechanical Parts	
Mirror Cost	No Critical Dimension	Strapdown Conductive High G-Resistant	
Status: Research Development Production	Research Exploratory Development	High Reliability Lower Cost Integrated Rate Output	
Instantaneous Readiness	Warmup	Miniaturization Possibility	
Long Life (Shelf and Operating)	Realignment	Digital Output	
Adaptive to Geometry			
Miniature (Low Sensitivity)		Needs: Noise & Drift Reduction	
Large (Highest Sensitivity)		Higher S/N Short Sample Digital Readout Application Broadening	

FIGURE 44. Differences and similarities of RLGs (potentially general "Sagnac systems") and MRGs.

BIOGRAPHICAL REFERENCES

I RINGLASER REFERENCES

1. Rosenthal, A.H., "Regenerative Circulatory Multiple-Beam Interferometry for the Study of Light-Propagation Effects," *Jorn Optic Soc Am*, Vol 52, Nr 10, pp 1143-1148, Oct 1962
2. Macek, W.M., and Davis, D.T.M., Jr., "Rotation-Rate Sensing with Traveling-Wave Ringlasers," *Appl Phys Lett*, Vol 2, Nr 3, pp 67-68, Feb 1963
3. Macek, W.M., Davis, D.T.M., Jr., Olthuis, R.W., Schneider, J.R., and White, G.R., "Proceedings of the Symposium Optical Lasers," Microwave Research Institute Symposium Series, Vol XIII, Polytechnic Press of the Poly Inst of Brooklyn, Brooklyn, NY, 1963, pp 199
4. Harmon, W.L., "Rotating Sensing," Aeronautical Systems Div (AFSC), Wright-Patterson AFB, Ohio, 10th Ann AF Science & Engrg Symposium, Oct 1963
5. Macek, W.M., Davis, D.T.M., Jr., Olthuis, R.W., Schneider, J.R., and White, G.F., "Ringlaser Rotation Rate Sensor," In P. Grivet and N. Bloembergen (Editors), *Comptes-rendues de la 3^e Conference Internationale, Quantum Electronics, Proceedings of 3rd Int'l Congress (Paris 1963)*, Dunod Editeurs Paris and Columbia Univ Press, New York, 1963, pp 1313-1317
6. Macek, W.M., Schneider, J.R., Salomon, R.M., "Measurement of Fresnel Drag with the Laser," *Journal of Applied Phys*, Vol 35, Nr 8, pp 2556-2557, Aug 1964
7. Lamb, W.E., Jr., "Theory of Optical Maser," *Phys Rev*, Vol 134, Nr 6A, pp A1429-A1450, Jun 1964
8. Aronowitz, F., "Theory of Traveling Wave Optical Maser," *Phys Rev*, Vol 138A, p 6356, (1965)
9. Chodorow, M., "Dispositif de Mesure de Vitesse de Rotation," *Brevet d'invention Nr 1 482 775 (France 1967)*, USA 21.5.1965.
10. McCartney, E.J., "The Laser Inertial Sensor," *Navigation: Journal of the Instit of Navigation*, Vol 13, Nr 3, pp 260-269 (Autumn, 1966)
11. Macek, W.M., McCartney, E.J., "The Ring Laser," *Sperry Eng Rev*, Vol 19, Nr 1, pp 8-15 (1966)
12. Levin, St.M., "High-Acceleration Missiles," *Space/Aeronautics*, pp 93-101, Sep 1966
13. Aronowitz, F., Collins, R.J., "Mode Coupling Due to Backscattering in a He-Ne-Traveling-Wave Laser," *Appl Phys Ltrs*, Vol 9, Nr 1, pp 55-58, 1 Jul 1966
14. Fenster, P., and Kahn, W.K., "Sing-Beam Laser Rotation-Rate Sensor," *Electronic Ltrs*, Vol 2, Nr 10, p 380, Oct 1966
15. Lee, P.m., and Atwood, J.G., "Measurement of Saturation Induced Optical Nonreciprocity in a Ring Laser Plasma," *IEEE J. Quantum Electronics*, QE 2, p 235, Sep 1966
16. Hutchins, T.J., et al, "Amplitude and Frequency Characteristics of a Ring Laser," *Phys Rev*, Vol 152, p 467, (1966)
17. Dessus, B., Migne, J., and Catherin, J.M., "Effects non Reciproques et Couplage Dans un Laser en Anneau," *Compt Rend Acad Sc (Paris)*, Vol 262, p 1691 (1966)
18. Catherin, J.M., and Dessus, B., "Traveling Wave Laser Gyrocompass," *Conf on Laser Eng and Appl*, Washington DC, Jun 1967
19. Wang, C.C., U.S. Pat 3 382 758 (1968); Ringlaser Symposium on Proceedings of the Modern Optics (Polytechnic Press, Brooklyn, NY, 1967)
20. Kilpatrick, J.E., "The Laser Gyro," *IEEE-Spectrum*, Vol 4, Nr 10, pp 44-55 (1967)
21. Bass, M., Statz, H., and DeMars, G., "Suppression of Close-Lying Modes in Ring Lasers and Related Devices," *Journ of Appl Phys*, Vol 39, Nr 8, pp 4015-4018, Jul 1968
22. Macek, W.J., US Pat 3 382 759 (1968), Ringlaser...
23. Fedgorski, T.J., Aronowitz, F., "Langmuir Flow Effects in the Laser Gyro," *IEEE J. Quantum Electronics* Vol QE-4, Nr 1, Jan 1968
24. Boot, H.A.H., King, P.G.R., Chersby-Harvie, R.R.R., "Ring Laser Bias Using Reciprocal Optical Components," *Electronics Letters*, Vol 5, Nr 15, pp 347-348, 24 July 1969

25. Minor, J.W., "Strapdown Inertial Guidance," Space/Aeronautics, Oct 1969, pp 54-60
26. Whitney, C.K., and Coccoli, J.D., "A General Theory of Ring Laser Mode Coupling in the Presence of Phase Modulation," Report R-782, C.S. Draper Labs, Sep 1970
27. Whitney, C.K., "Contributions to the Theory of Ring Laser," Phys Rev 181, Nr 2, p 535 (1969)
28. Whitney, C.K., "Ringlaser Mode Coupling," Phys Rev 181, Nr 2, pp 542-548, May 1969
29. Aronowitz, F., "Loss Lock-In in Ringlaser," J. Appl Physics 41, 130 (1970)
30. Malota, F., "Ringlaser and Ringinterferometer," Laser and Angewandte Strahlentechnik, Nr 2, S 13-18 (1970)
31. Aronowitz, F., "The Laser Gyro," in Monte Ross (editor): "Laser Applications," Vol 1, pp 133-200, Academic Press, New York 1971
32. Hutchinson, K.N., and Inglis, P.K., "An Improved Ring Laser Rate Sensor for Use in Strapdown Inertial System," AIAA paper 70-1025, Guidance, Control and Flight Dynamics Conference, St Barbara, USA, Aug 1970
33. Wax, S.I., and Chodorow, M., "Phase Modulation of a Ring Laser Gyro, Part 1: Theory," "Experimental Results, Part 11," IEEE J. Quant Electronics, Vol QE-8, Nr 3, pp 343-361, Mar 1972
34. O'Bryan, S.C., Sargent, M., "Theory of Multimode Laser Operations," Phys Rev, A8, 3071 (1973)
35. Roland, J.J., and Lamfreen, J.M., "Periodic Faraday Bias and Lock-In Phenomena," Appl Optics, Vol 12, Nr 7, p 1460, Jul 1973
36. Menegozzi, L.N., Lamb, W.E., Jr., "Theory of a Ring Laser," Phys Review A., Vol 8, Nr 4, pp 2103-2125, Oct 1973
37. Sargent, J., Scully, M., and Lamb, W.E., "Laser Physics," Addison Wesley, 1974
38. Hanson, D.R., Sargent, M., "Theory of a Zeeman Ring Laser," Phys Rev A9, 466 (1974)
39. Yntema, G., Grant, D., Jr., and Warner, R., "Differential Laser Gyro System," US Pat #3862 803, 28 Jan 1975
40. Grant, D., Hambene, J., Hutchings, T., Sanders, V., and Schully, M., "A Multi-oscillator (Four Mode) Ringlaser Gyro Report," NAECON 77 Record, pp 1028-32
41. Coccoli, J.D., "An Overview of Laser Gyros," The C.S. Draper Labs., Rpt P-684, Aug 1978
42. Aronowitz, F., and Lim, W.L., "Dispersion and Gas Flow Effects in the Ring Laser Gyro," Proc of the Society of Photo-Optical Inst Engineers, (SPIE), Vol 157 (Laser Inertial Rot Sens), pp 7-20, (1978)
43. Aronowitz, F., "The Laser Gyro-Tutorial Review," Proc SPIE, Vol 157 (Laser Inertial Rotation Sensors) pp 2-6 (1978)
44. Smith, I.K., Borschner, T.A., "Biasing the Raytheon Four Frequency Ring Laser Gyroscope," Proc SPIE, Vol 157 (Laser Inertial Rotation Sensors), pp 21-29 (1978)
45. Sanders, V.E., Anderson, D., Scully, M.O., "A Four Mode Solution to the Locking Problem in Two Mode Ring Laser Gyros," Proc SPIE, Vol 157 (Laser Inertial Rotation Sensors), pp 30-33 (1978)
46. Engbreksten, J.H., "Ring Laser Gyro Program at Rockwell," Proc SPIE, Vol 157 (Laser Inertial Rotation Sensors) pp 34-40 (1978)

11. SAGNAC-SYSTEMS REFERENCES

47. Sagnac, G., "L'Ether lumineux Démontré Par L'Effet du Vent Relatif d'Ether Dans un Interferometre en Rotation Uniforme," Comp Rend (Paris), Tome 157, pp 708-711 (1913)
48. Sagnac, G., "Effet Tourbillonnaire Optique. La Circulation de L'Ether Lumineux Dans un Interferographe Tournant," Journ de Physique Theo et Appliq, 4me ser., tome iv, pp 177-195.
49. Post, E.J., "Sagnac Effect," Review of Mod Phys, 32, Nr 2, pp 475-493, Apr 1967
50. Langevin, M.P., "Sur la Theorie de Relativite et L'Experience de M. Sagnac," Compt Rend (Paris), Tome 113, pp 831-834 (1912)

51. Langevin, M.P., "Sur L'Experience de Sagnac," Compt Rend (Paris), Tomé 205, pp 304-306 (1937)
 52. Silverstein, L., "The Propagation of Light in Rotating Systems," J. Optic Soc Am (JOSA), Vol V, Nr 4, pp 291-307 (July 1921)
 53. VonLaue, M., "Zum Versuch von F. Harress," Annalen der Physik, 4. Folge, Bd 62, Nr 13, S.448-463
 54. Sommerfeld, A., and Runge, Iris, Ann.d.Phys, 4te Folge, Bd 35, S. 277-298 (1911)
 55. Knopt, O., "Die Versuche von F. Harress Ober Die Geschwindigkeit des Lichtes in Bewegten Korpern," App d. Phys, 4te Folge, Bd 62, S 389-447 (1920)
 56. Pogany, B., "Urber Eine Wiederholung des Harress Scher Versuches, (II.Mitteilung)," Ann D. Phys, 4te Folge, Bd 85, S.244-256 (1928)
 57. Dufour, A., and Prunier, F., "Sur L'Observation du Phenomene de Sagnac Avec Une Source Eclairante non Entrainee," Compt Rend, Paris, Seance du 3.Mai 1937, Tomé 204, S.1322-1324 (1937)
 58. Dufour, A., and Prunier, F., "Sur un Deplacement de France en Registre Sur Une Plate-Forme en Rotation Uniforme," Le Journal de Physique et le Radium, Serie VIII, Tomé 111, Nr 9, pp 153-161, Sep 1942
 59. Brauser, K.J., and Eichenauer, B.D., "Anordnung Zur Genauen Messung von Winkelgeschwindigkeiten Unter Verwendung des Sagnac Effektes," German Pat 1 298 335, 26.2.1970
 60. Hepner, G., and Pircher, S., "Auf Demprinzip der Interferenz-Messung Beruhendes Laser-Gyrometer," Pat DT-OS1813 463, France 8.12.1978, Germany 3.12.1968
 61. Vali, V., Shorthill, R.W., "Fiber Ring Interferometer," Appl Optics, Vol 15, Nr 5, May 1976
 62. Takahashi, T., and Baierlein, R., "Accelerated Ringlaser," Phys Rev, A, Vol 15, Nr 2, Feb 1977
 63. Fredricks, R.J., and Carrington, W.A., "Sources of Error in a Discrete Component Sagnac Optical Rate Sensor," Proc SPIE, Vol 157, 1978, pp 50-71
 64. Ezekiel, S., Cole, J.A., Harrison, J., and Sanders, G., "Passive Cavity Optical Rotation Sensor," Proc SPIE, Vol 157, pp 68-72, (1978)
 65. Goldstein, R., and Goss, W.C., "Fiber Optic Rotation Sensor (FORS) Laboratory Performance Evaluation," Proc SPIE, Vol 157, pp 122-126 (1978), IEEE/OSA Conference on Laser Eng and Appl Digest; p 39
 66. McLandrich, M.N., and Rast, M.E., "Fiber Interferometer Gyroscope," Proc SPIE, Vol 1-7, pp 127-130 (1978)
 67. Davis, J.,., Ezekiel, S., "Techniques for Shot-Noise-Limited Inertial Rotation Measurement Using a Multiturn Sagnac Interferometer," Proc SPIE, Vol 157, pp 131-136 (1978)
 68. Arditty, H., Shaw, H.J., Chodorow, N., and Kompfner, R., "Re-Entrant Fiberoptic Approach to Rotation Sensing," Proc SPIE, Vol 157, pp 138-148 (1978)
 69. Lin, S.C., "Sensitivity Limits of an Optical Fiber Gyroscope," Proc SPIE, Vol 157, pp 149-163 (1978)
 70. Pirscher, G., Lacombe, M., and Lefeuvre, H., "Preliminary Results Obtained with a Fiber Optic Rotation Sensor (Fors)," Proc SPIE, Vol 157, pp 212-217 (1978)
 71. Papuchon, H., and Fusch, C., "Integrated Optics-A Possible Solution for the Fiber Gyroscope," Proc SPIE, Vol 157, pp 218-223 (1978)
 72. Ezekiel, S., "New Perspectives in Optical Gyroscopes," 1979 IEEE/OSA Conference on Laser Engineering and Applications, Wash DC Digest, p 18
 73. Leeb, W.R., Schiffner, G., Scheitler, K., "Optical Fiber Gyroscopes, Sagnac or Pizeau Effect?", Appl Optics, Vol 18, Nr 9, p 1293, May 1979
- III: TESTING AND APPLICATIONS OF OPTICAL ROTATION SENSING REFERENCES
74. Catherin, J.N., and Dessus, B., "Gyrometres Laser et Applications," Centre de Recherches Compagnie Generale d'Electricite, Dep Rec Phys de Base, Apr 1968
 75. Coccoil, J.D., Helfant, S., "The Intrinsic Stability of Laser Gyro Scale Factor," Proc of the IEEE 1978 National Aerospace and Electronics Conference, May 1968

76. Stowell, W.K., McAdory, R.W., Ziernicki, R., "Air Force Applications for Optical Rotation Rate Sensors," Proc SPIE, Vol 157, pp 166-171 (1978)
77. Eckhardt, D.H., "Surveying and Geophysical Measurements with Inertial Rotation Sensors," Proc SPIE, Vol 157, pp 172-174 (1978)
78. Johnston, J.V., Cantrell, W.G., "New Techniques in Laser Gyro Performance Analysis," Proc SPIE, Vol 157, pp 189-195 (1978)
79. Feldman, J., Helfant, S., "A Laser Gyro Evaluation Plan and Test Results," Proc SPIE, Vol 157, pp 196-204 (1978)
80. Passenheim, B.C., and Mallon, C.S., "Nuclear Radiation Vulnerability of Ring Laser Gyroscope," Proc SPIE, Vol 157, pp 205-211 (1978)
81. Coccoli, J.D., Helfant, S.B., "RLG Evaluation, Complementary Modeling and Testing," C.S. Draper Labs, Rep P-805, Mar 1979

IV. SOME RUSSIAN REFERENCES

82. Khromykh, A.M., "Ring Generator in Rotating Reference Systems," J. Exp Theor Phys, 50, 281-282, Jan 1966, Soviet Physics JETP, Vol 23, Nr 1, pp 185-186, Jul 1966
83. Geljaev, V.P., Devjatkin, I.I., Martinov, V.M., and Fedoro, A.S., "Some Application of Gas Lasers," Seria Radio Elektronika and Swyaje, pp 34-37, Moscow 1970
84. Dotsenko, A.V., and Lariontsev, "Beats in a Solid State Ring Laser," Sov J. Quantum Electron, Vol 7, Nr 5, May 1977
85. Privalov, V.E., and Pilatov, Y.V., "Investigation of the Output Characteristics of a Rotating Ring Gas Laser," Sov J. Quantum Electron, Vol 7, Nr 7, Jul 1977
86. Danileiko, M.V., Danikov, N.K., and Kozubouskii, V.R., "Competition of Orthogonally Polarized Modes in a Ring Laser with a Nonlinear Absorber," Sov J. Quantum Electron, Vol 7, Nr 5, May 1977
87. Andronova, I.A., Kuvatova, "Influence of a Longitudinal Magnetic Field on Nonreciprocal Effects in a Ring Laser," Sov J. Quantum Electron., Vol 7, Nr 6, Jun 1977
88. Sardyko, V.I., "Control of the Emission Spectrum of a Ring Laser by Magnetic-Field-Induced Phase Anisotropy of the Active Medium," Sov J. Quantum Electron., Vol 9, Nr 1, Jan 1979, p 87

V. MRG REFERENCES

89. Slocum, R.E., Reilly, P.M., "Low Field Helium Magnetometer for Space Applications," IEEE Trans Nuc So, NS-10, p 165 (1963)
90. Simpson, J.H., "Nuclear Gyroscope," Astronautics and Aeronautics 2, p 40 (1964)
91. Fairbank, W.M., Hamilton, W.O., Everitt, C.W.F., "Quantized Flux to the Free Precession Nuclear Gyro," Proc OAR Research Appl Conf, Washington DC, p 193 (1966)
92. Simpson, J.H., Greenwood, I.A., "An Optically Pumped Nuclear Magnetic Resonance Gyroscope," AGARD Conf Proc Nr 43, Inertial Navigation-Systems & Components, p 31, May 1968
93. Cohen-Tannoudji, C., Dupont-Roc, J., Haroche, S., Laloe, F., "Detection of the Static Magnetic Field Produced by the Oriented Nuclei of Optically Pumped ^3He Gas," Phys Rev Ltr, 22, 758 (1969)
94. Kanegsberg, E., "NMR Local Field Shift in Gaseous Xenon," Phys Rev Ltr 23, 11, p 57 (1969)
95. Cohen-Tannoudji, C., Dupont-Roc, J., Haroche, S., Laloe, F., "Diverses Resonances de Croisement de Niveaux Sur des Atomes Pompes Optiquement en Champ Null II. Applications a la Mesure de Champs Faibles," Rev de Phys Applique 5, p 102 (1970)
96. Haroche, S., Cohen-Tannoudji, C., "Resonant Transfer of Coherence in non Zero Magnetic Field between Atomic Levels of Different g-Factors," Phys Rev Ltr 24, p 573 (1970)
97. Happer, W., "Optical Pumping," Rev of Mod Phys, 44, p 169 (1972)
98. Happer, W., Svanberg, S., "Power-Series Analysis of Light Shifts in Optical Pumping Experiments," Phys Rev 9A, p 508 (1974)
99. Slocum, R.E., Marton, B.I., "A Nuclear Free Precession Magnetometer Using Optically Polarized ^3He Gas," IEEE Trans Magnetics, MAG-10, Nr 3, Sep 1974

100. Kanegsberg, E., "A Nuclear Magnetic Resonance (NMR) Gyro with Optical Magnetometer Detection," Proceedings SPIE, Vol 157, Laser Inertial Rotation Sensors, p 73-80, Aug 1978
101. McGregor, D.D., Andrychuck, D., Slocum, R.E., "Application of Helium Isotopes to a NMR Gyro," Proceedings SPIE, Vol 157, Laser Inertial Rotation Sensors, pp 81-88, Aug 1978

ACKNOWLEDGEMENT:

The author would like to thank Mr Morris Ostgaard of the Air Force Flight Dynamics Laboratory and my colleagues of the Air Force Office of Scientific Research for the encouragement and support during the preparation of this paper. Ms Stephanie Smaldone deserves my gratitude for her prompt and conscientious secretarial assistance.

APPENDIX A

SUMMARY OF BASIC RELATIONS

$$\Delta t = \frac{2L}{c} \cdot \beta$$

$$\Delta z = \frac{D L}{\lambda_0 c} \cdot \Omega = \frac{\Delta \phi}{2\pi}$$

FRINGE- OR PHASESHIFT-INDEPENDENT OF n , PROPORTIONAL TO L

$$\frac{\Delta t}{T} = \frac{\Delta \phi}{\phi} = \frac{\Delta F}{F} = \frac{D\Omega}{nc}$$

$$\Delta F = \frac{D}{\lambda} \cdot \frac{1}{n} \cdot \Omega = \frac{D}{\lambda_0} \cdot \Omega$$

FREQUENCY SHIFT DEPENDENT ON n , INDEPENDENT OF L

Figure 1. Similarities and differences between frequency and phase shift measurement.

SAGNAC INTERFEROMETER

$$\text{WITH } v = R\Omega; L = 2\pi R N; \Delta t = \frac{4\pi R^2 N}{c^2} \Omega$$

$$\text{GENERALLY } \Delta t = \frac{4AN}{c^2} \Omega \quad \text{A AREA ENCLOSED BY OPTICAL PATH}$$

$$L = \frac{c}{n} \Delta t \quad \text{APPARENT DIFFERENCE IN PATH LENGTH DUE TO ROTATION}$$

$$\Delta \phi = 2\pi f \Delta t \quad \text{OPTICAL PHASE SHIFT}$$

$$\text{FRINGE SHIFT } \Delta z = \frac{\Delta L}{\lambda} = \frac{\Delta \phi}{2\pi} = \frac{c}{\lambda_0} \Delta t = \frac{4AN}{\lambda_0 c} \Omega$$

$$\text{WHERE } \tau = \frac{c}{\lambda_0} = \frac{c}{n\lambda}; \quad \lambda \quad \text{WAVELENGTH IN MATERIAL}$$

$$\lambda_0 = n\lambda \quad \text{FREE SPACE WAVELENGTH}$$

$$\text{EXAMPLE: } \Omega = \Omega_E = 15^\circ/\text{HR} = 7.3 \times 10^{-5} \text{ RAD/SEC}; A = 100 \text{ cm}^2$$

$$\Delta t = 3.2 \times 10^{-20} \text{ SEC.}$$

$$N = 1000; \lambda_0 = 0.63 \text{ } \mu\text{m}$$

$$\Delta \phi = 10^{-6} \text{ RAD.}$$

$$\text{REPORTED DETECTION } \Delta z = 10^{-2} \text{ TO } 10^{-5}$$

$$\Delta z = 1.5 \times 10^{-5}$$

$$\text{PROPOSED USING SYNCHRONOUS DETECTION } \Delta z = 10^{-8}$$

FIGURE 2. Relations and example for the Sagnac Interferometer.

SHOT NOISE LIMITED PHASE SHIFT MEASUREMENT

$$\delta(\Delta \phi) = \frac{\pi}{2\pi N} = \frac{\pi}{(N_p \cdot \eta \cdot \tau)^{1/2}}$$

- * MINIMUM WIDTH OF FRINGE IN RADIANS AT CONTRAST 1
- N_p NUMBER OF PHOTONS DETECTED PER SECOND
- η QUANTUM EFFICIENCY OF DETECTOR
- τ INTEGRATION TIME IN SEC.

MINIMUM UNCERTAINTY $\Delta \Omega$ IN DETECTION OF ROTATION

$$\Delta \Omega = \frac{c \lambda_0}{2\pi N A} \delta(\Delta \phi) = \frac{c \lambda_0}{2\pi N A} \cdot \frac{\pi}{(N_p \cdot \eta \cdot \tau)^{1/2}}$$

$$\text{EXAMPLE: } N_p = 3 \times 10^{15} \text{ (1 mW at } \lambda_0 = 6328 \text{ nm)}; \eta = 0.3; \tau = 1 \text{ sec}$$

$$\Delta \Omega = 7.5 \times 10^{-8} \text{ rad/sec} = 11 \times 10^{-8} \text{ } \mu\text{R/sec}$$

PRESENT MEASUREMENTS BY FACTOR OF AT LEAST 100 SHORT

- PROBLEMS: DETECTION SYSTEM (MODULATION, SYNCH. DETECTION)
- SOURCE QUALITY (JITTER, BANDWIDTH, COHERENCE)
- OPTICAL GUIDES (LOSS, POLARIZATION, MODE CONTROL)

FIGURE 3. Example of the shot noise limit for the interferometer measurement system, with problems under present investigation (11).

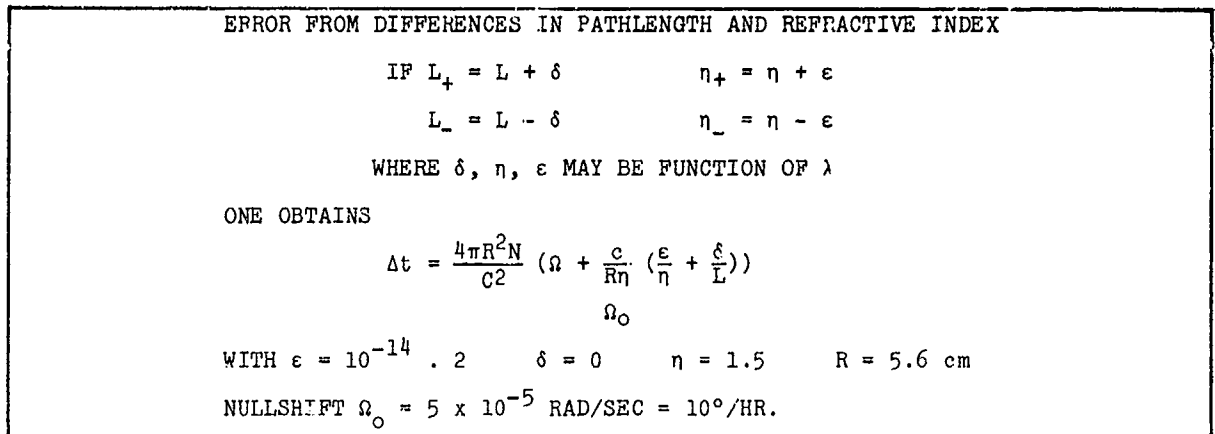


Figure 4. Example of measurement error shift related to optical path nonreciprocities caused by refractive index and mode deviations.

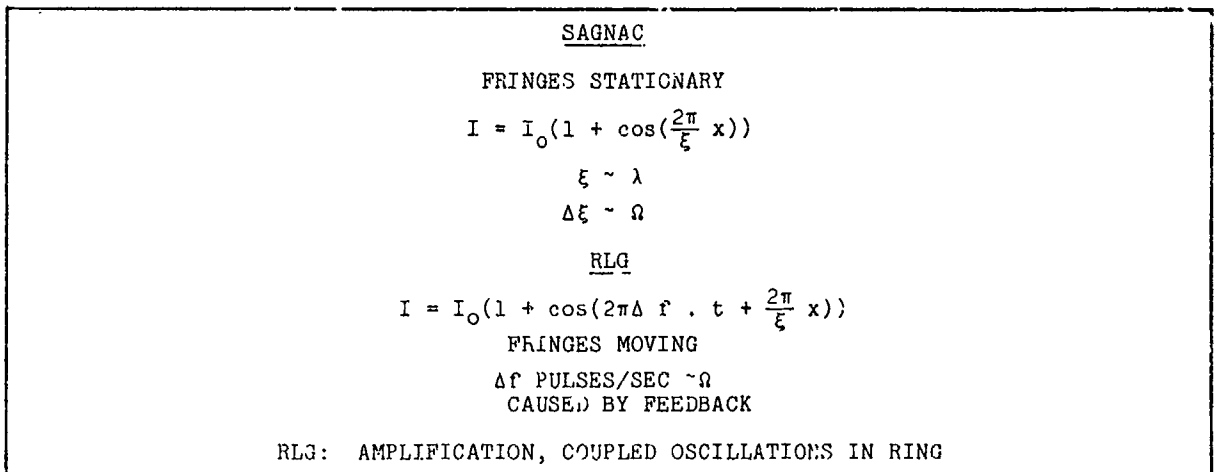


Figure 5. Relation for interference fringe light intensities in case of "passive" and "active" sagnac systems.

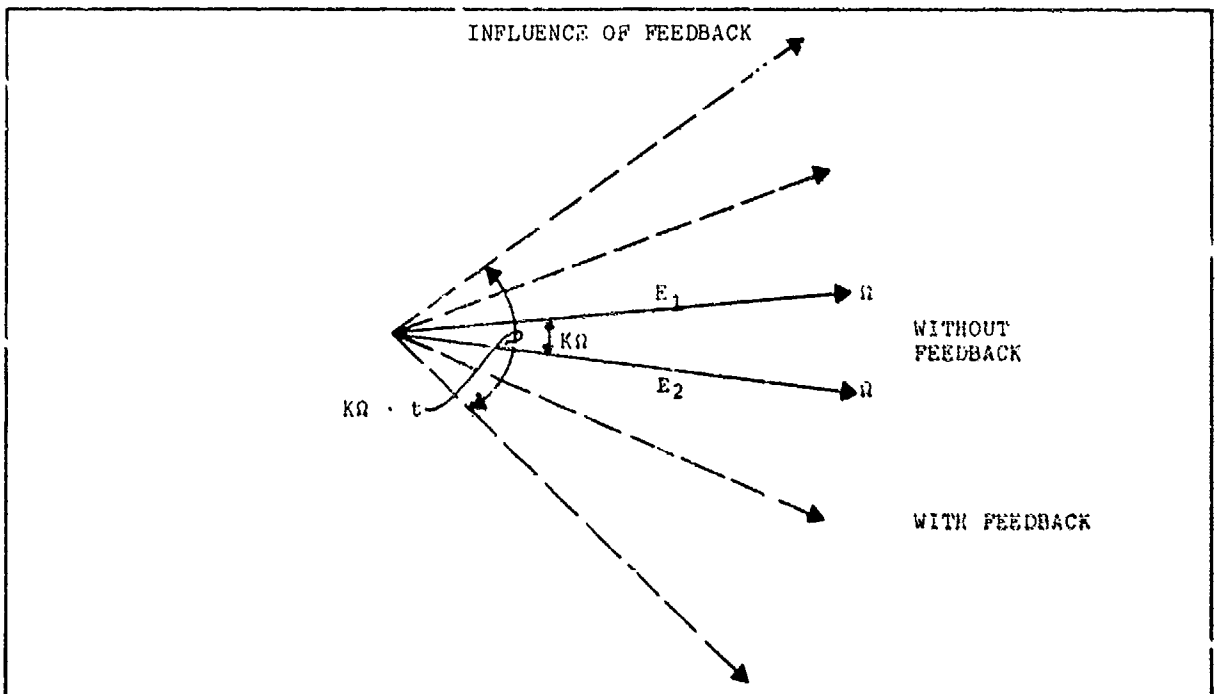


Figure 6. Explanation of active vs. passive system. The wave field vectors are set in motion by the feedback in the regenerative (laser in ring) case. The fringe motion is proportional to rate input.

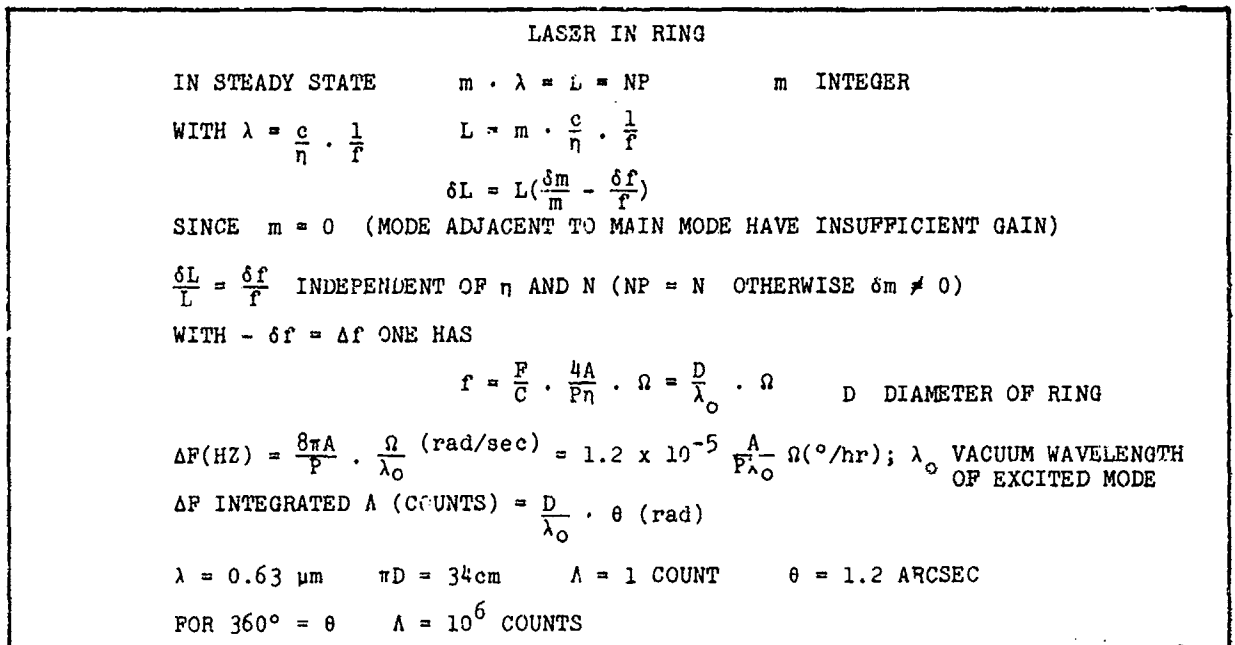


Figure 7. Relations for the frequency or count output in the active case.

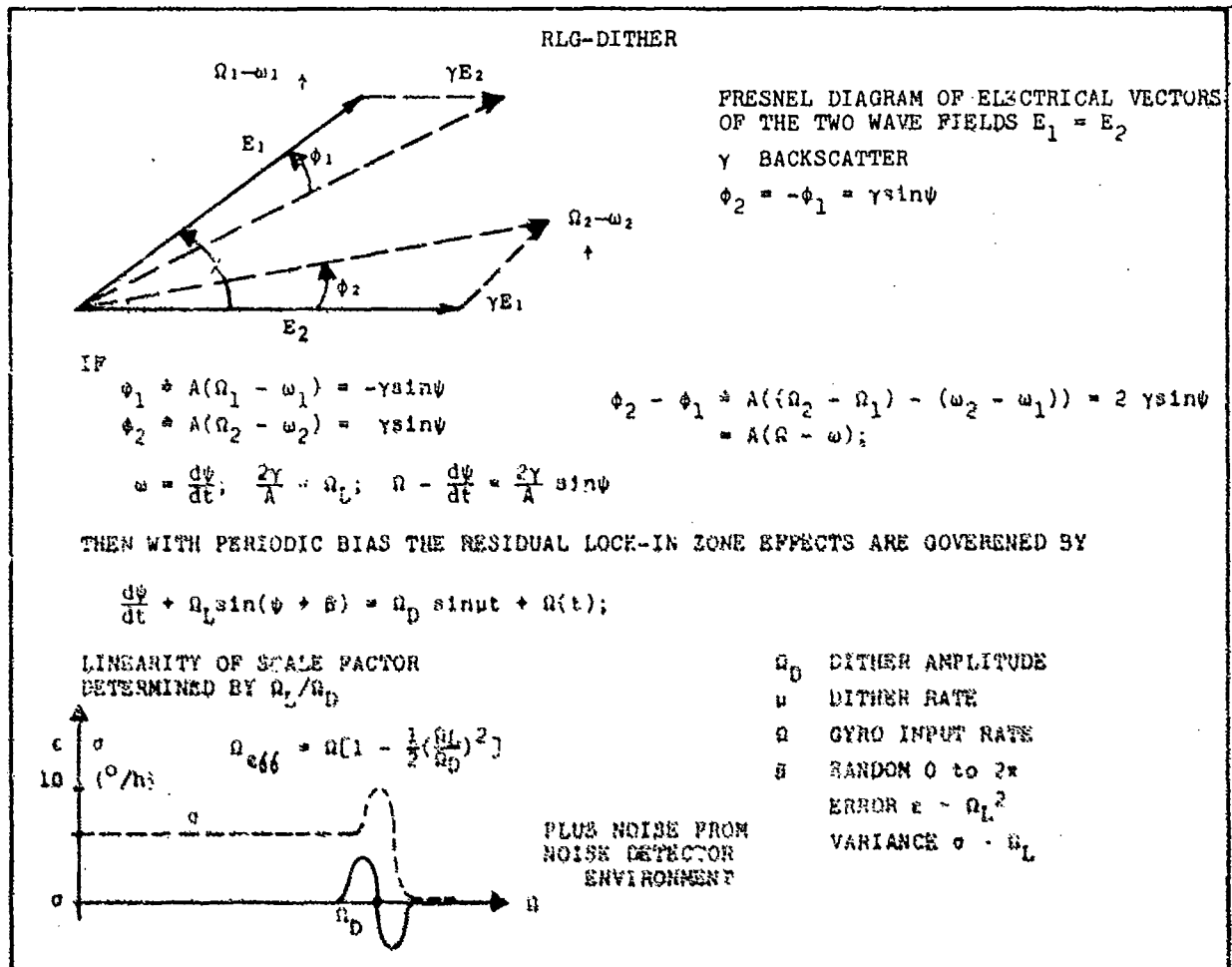


Figure 8. Abbreviated theory of the dithered RLG (Ref I, 642 and #35)

NOISE LIMITS FOR FREQUENCY SEPARATION

$$\delta\nu = \frac{B_R}{S/N} = \frac{B_R}{\sqrt{\gamma \cdot \eta \cdot \tau}}$$

$$\delta\Omega = \delta\nu \times (S_F)^{-1}$$

B_R INSTRUM. LINE WIDTH (Hz)

L PERIPHERY (CM)

$$\delta\Omega = \frac{10^5 \lambda B_R L}{4A \cdot \sqrt{\gamma \cdot \eta \cdot \tau}} (\text{°/hr})$$

FOR λ (CM) SOURCE RADIATION WAVELENGTH

B_R (Hz) INSTRUM. LINEWIDTH

L (CM) PERIPHERY, A RING AREA

γ NUMBER OF PHOTONS/SEC FROM SOURCE

η DETECTOR AND TRANSMISSION EFFICIENCY

τ (SEC) INTEGRATION TIME

FOR $B_R = 1$ MHz, $L = 40$ CM, $A = 10^2$ CM², $\gamma\eta \sim 10^{14}$ /SEC, $\tau = 1$ SEC $\delta\Omega \approx 0.05$ °/HR
 WITH SIZE AND POWER INCREASE: FOR $L = 4 \times 10^3$ CM, 10 WATTS INSTEAD OF 1mW AND
 $\tau = 10^2$ SEC

$$\delta\Omega = 1.5 \times 10^{-8} \text{ °/HR}$$

Figure 9. Shot noise limit for frequency separation (RLG without dither).

DUAL OSCILLATORS (a, b)

$$\omega_a + \Omega_{La}(\sin(\psi_a + \beta_a)) - \Omega_{Ba} = \Omega$$

$$\omega_b + \Omega_{Lb}(\sin(\psi_b + \beta_b)) - \Omega_{Bb} = \Omega$$

$$\omega_a = -\omega_b; \psi_a = -\psi_b; \Omega = 0 \rightarrow$$

$$\text{REQUIRES } \Omega_{Ba} = -\Omega_{Bb}; \Omega_{La} = \Omega_{Lb} = \Omega_L$$

AND IN ADDITION

$$\Omega_L \rightarrow 0; \gamma \rightarrow 0 \text{ AND}$$

$$\Omega_L((\sin\psi(\cos\beta_a + \cos\beta_b) + \cos\psi(\sin\beta_a - \sin\beta_b))) = 0$$

$$\langle\beta_a\rangle \neq \langle\beta_b\rangle = \pi/2; \Omega_L \neq 0$$

UNCOUPLED BEAMS

UNCORRELATED PHASE NOISE

OR PRECISE STATIONARY PHASE RELATION

Figure 10. Symmetry requirements for four mode laser gyro and desirable operational conditions.

SCULLY/SANDERS - OPTICAL DITHER METHOD

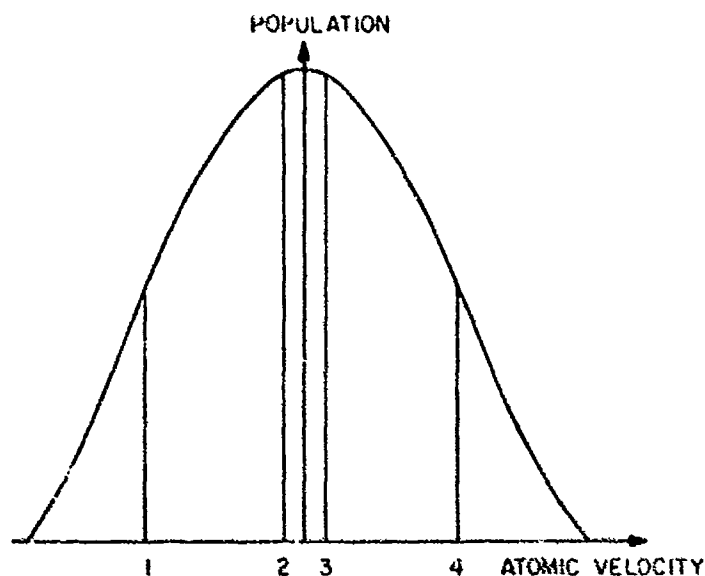


Figure 11a.

SCULLY/SANDERS - OPTICAL DITHER METHOD (CONCL'D)

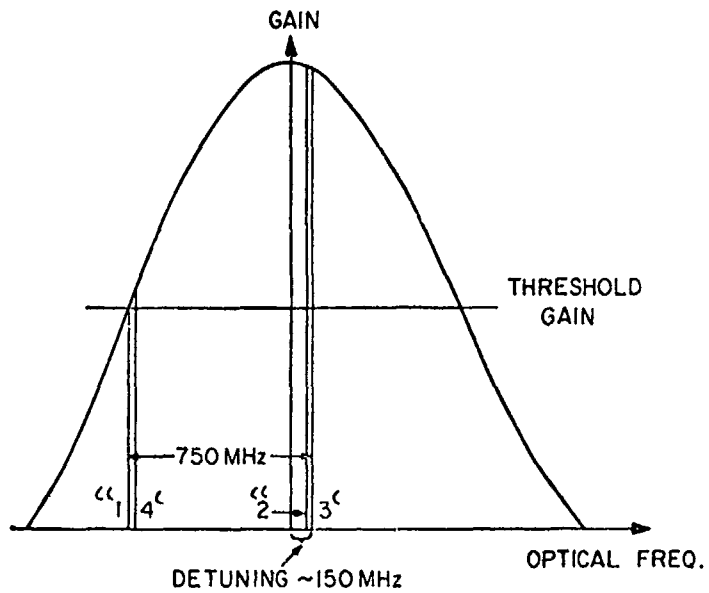


Figure 11b

Figure 11. Suggested "optical dither" method. By using unsymmetric mode location, side modes above threshold gain act to produce oscillatory bias. (I, 45)

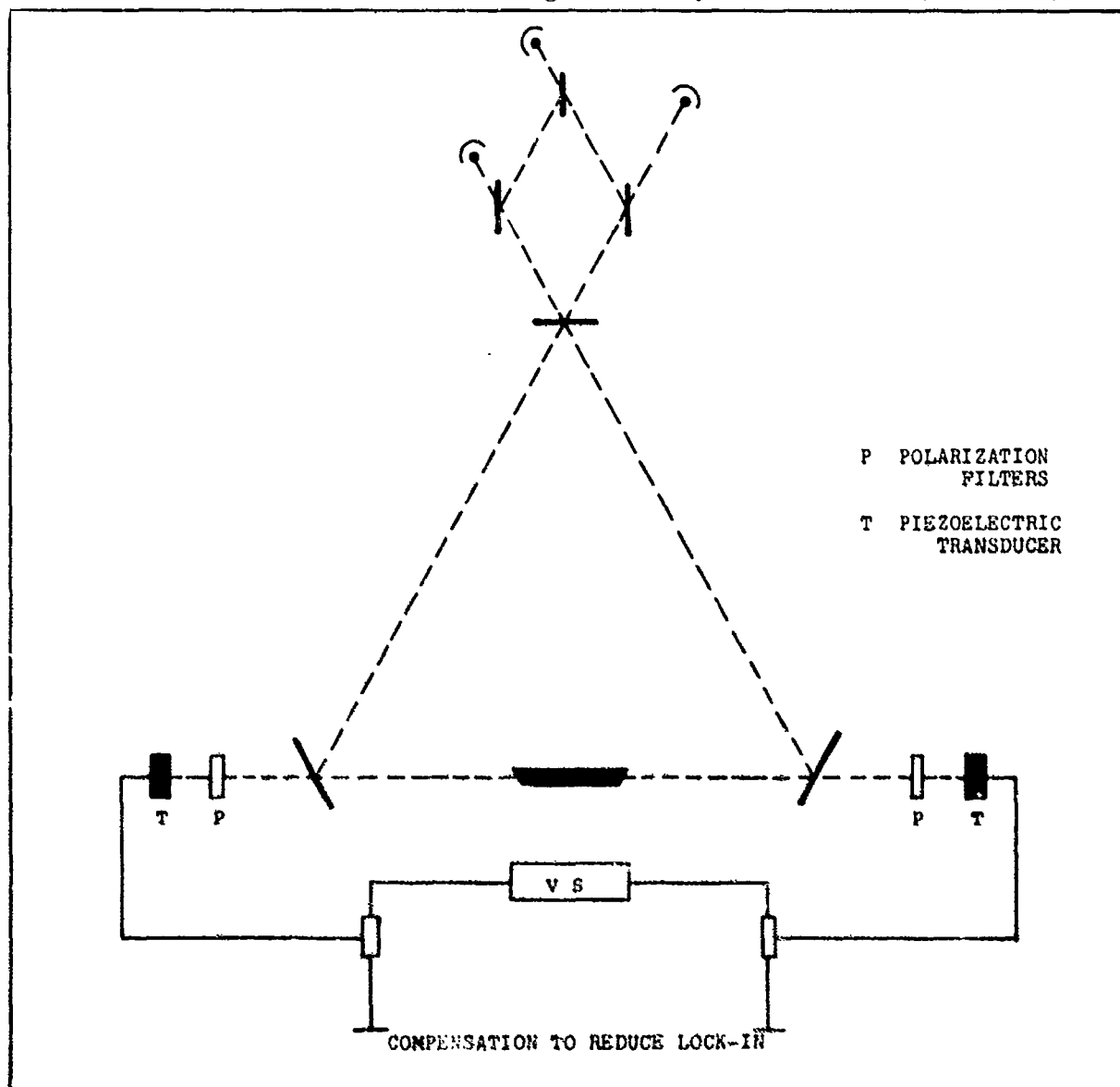


Figure 12. Backscatter compensation suggestion to reduce the lock-in range by secondary movable mirrors; from Russian literature (Ref IV, 085)

A NUCLEAR MAGNETIC RESONANCE GYRO
USING NOBLE GAS ISOTOPES

by

Dr. E. Kanegsberg,
Member of the Technical Staff
Litton Guidance & Control Systems Division
5500 Canoga Avenue, Woodland Hills, CA 91365

SUMMARY

A Nuclear Magnetic Resonance (NMR) Gyro is an inertial angle sensor in which the inertial properties are derived from an intrinsic angular momentum and magnetic moment associated with the nuclei of certain atomic isotopes. Such magnetic moments precess in a magnetic field. A measurement of the shift in precession phase angle is used to obtain the gyro rotation information. The general requirements for NMR gyro operation include the existence of a measurable magnetic moment, the ability to make a continuous high precision measurement of the precession phase of such moments, and a means of distinguishing between rotation effects and magnetic field effects. An approach which satisfies these requirements utilizes two isotopes of the noble gases as the inertial sensors and uses an optically pumped rubidium magnetometer as the readout mechanism. A breadboard NMR gyro utilizing this approach has been tested and is characterized by a high signal-to-noise ratio and a low random bias drift.

I. INTRODUCTION

A Nuclear Magnetic Resonance (NMR) Gyro is an inertial angle sensor in which the inertial properties are derived from an intrinsic angular momentum (spin) associated with the nuclei of certain atomic isotopes. Interest in development of an NMR gyro comes from its potential to have a strapdown gyro sensor with cost, size, performance and reliability advantages over ring laser or conventional gyros. Cost advantages stem from the lack of critical materials or tolerances needed for fabrication. The NMR gyro is expected to be smaller than a ring laser gyro (RLG) for comparable performance and has no fundamental connection between size and angular resolution. Performance potential is to 0.01 deg/hr or better bias drift and, in addition, the NMR gyro can accommodate large input rates and angle ranges, should not be influenced by high acceleration, and should create no reaction torques. Aside from the natural motion of the atoms there are no moving parts.

We shall discuss the general requirements for NMR gyro operation and shall describe an approach to an NMR gyro which utilizes isotopes of the noble gases as the inertial sensors and uses an optically pumped rubidium magnetometer as the readout mechanism.

II. GENERAL REQUIREMENTS FOR AN NMR GYRO

All atoms or atomic nuclei which have a spin angular momentum also have the property of a magnetic moment directed parallel (or anti-parallel) to the spin direction. It is well known (Reference 1) that such a moment will precess about the direction of an applied magnetic field, H , at the Larmor frequency which is given by

$$\omega_L = \gamma H \quad (1)$$

where γ is the ratio of the magnetic moment to the angular momentum and is called the gyromagnetic ratio. If the measurement coordinate system (gyro case) is itself rotating with an angular frequency ω_r about the direction of the magnetic field, then the measured Larmor frequency in the rotating frame will be

$$\omega_m = \gamma H - \omega_r \quad (2)$$

It is the measurement of this shift in observed precession frequency which is fundamental to the NMR gyroscope. If we integrate equation (2) over time we obtain

$$\theta_m = \gamma H t - \theta_g \quad (3)$$

where θ_m is the measured phase angle of the precessing nuclear moment with respect to the gyro case, \bar{H} is the average value of the magnetic field over the time interval, t , and θ_g is the gyro rotation angle. For a practical gyro able to resolve small vehicle rotation angles, θ_m must be measurable to high precision.

There are several general requirements to be satisfied in order to achieve a practical gyro. First, there must be a measurable magnetic moment. Second, it must be precessing and have a well defined frequency. Third, there must be a means of detecting this precessing moment without the measurement contributing significant error. Fourth, the measurement must be continuous in time. Fifth, by reference to equation (3), there

must be a way of distinguishing between magnetic field effects and rotation effects on the measured magnetic moment phase angle.

A sample containing nuclear moments has an almost random distribution of these moments in equilibrium. In order to achieve a measureable moment the individual moments in the sample must be preferentially oriented in one direction to create a macroscopic (vector sum) moment which can be detected with a large signal-to-noise (S/N) ratio. Optical pumping techniques (Reference 2) are usually employed to create such an orientation.

A macroscopic nuclear moment which has been oriented by optical pumping techniques will be directed parallel to the applied magnetic field, H. In order for it to precess it must have a component orthogonal to H. This can be accomplished by applying a small AC magnetic field with a frequency of the Larmor precession in a direction orthogonal to the field, H. This resonant field then acts to torque the net moment and creates a precessing component.

The precessing moment must have a well defined frequency. This requires that the individual moments which comprise the macroscopic moment must all have essentially the same Larmor frequency, which means that they all must experience on the average the same magnetic field. Thus the magnetic field must be homogeneous. The requirement for a well defined frequency means that the nuclear moment orientation which is created in the optical pumping process must be long lived. Processes which tend to destroy this orientation are called relaxation processes and the characteristic time for decay of the orientation is called the relaxation time. Therefore, the requirement for well defined frequency implies that relaxation times must be long. A long relaxation time is also needed for significant nuclear moment orientation to occur since the equilibrium orientation represents a balance between optical pumping rates and relaxation rates.

The precessing net nuclear moment needs to be detectable so that its phase relative to the gyro case can be determined. This implies a process capable of detecting the precessing moment with a high S/N. This measurement process, naturally, must not significantly perturb either the precession frequency or the relaxation times.

For the gyro measurement to be continuous in time, both the nuclear orientation processes and the torquing of the nuclear moment by a resonant field must occur simultaneously with the detection process and also, of course, must not significantly perturb the frequency or relaxation times. Thus the steady-state operation will be one in which the processes of nuclear moment orientation, nuclear moment torquing, and nuclear moment decay are all in equilibrium.

The last general requirement is the need to be able to separate magnetic from rotational effects. This is most easily accomplished by utilizing two kinds of nuclear moments, in other words by using a mixture of two isotopes, each with a nuclear moment characterized by a unique gyromagnetic ratio (Reference 3). Then, letting a and b designate the two isotopes, the measured phase angles are equal to

$$\theta_{ma} = \gamma_a \bar{H} t - \theta_g \quad (4)$$

$$\theta_{mb} = \gamma_b \bar{H} t - \theta_g$$

Where it is assumed that both isotopes experience the same average magnetic field, \bar{H} . From equation (4) we can obtain

$$\theta_g = \frac{\gamma_b \theta_{ma} - \gamma_a \theta_{mb}}{\gamma_a - \gamma_b} = \frac{(\gamma_b/\gamma_a) \theta_{ma} - \theta_{mb}}{1 - (\gamma_b/\gamma_a)} \quad (5)$$

which is independent of the magnetic field, \bar{H} , and

$$\bar{H} = \frac{\theta_{ma} - \theta_{mb}}{t (\gamma_a - \gamma_b)} = \frac{\omega_{ma} - \omega_{mb}}{(\gamma_a - \gamma_b)} \quad (6)$$

which is independent of the rotation angle, θ_g , and where ω_{ma} and ω_{mb} are the measured Larmor precession frequencies of the two isotopes. Using two isotopes means that both must be capable of nuclear moment orientation by either the same or separate optical pumping techniques, that two resonant fields must be applied to torque the respective moments into the precession plane and that the detection process must be able to detect both θ_{ma} and θ_{mb} with high precision.

III. AN NMR GYRO USING NOBLE GASES

An approach to the NMR Gyro has been implemented and tested which uses the noble gases for the two nuclear isotopes. Noble gases were chosen because of their potential for long relaxation times and thus for the precise determination of precession phase angles.

The sample cell containing the noble gases also contains some rubidium vapor which is used for both the nuclear moment orientation process and the measurement technique for detecting the precessing nuclear moments. The Rb is optically pumped by light from a rubidium discharge lamp and the net angular momentum so acquired by the rubidium in the cell is transferred to both noble gas isotopes via a collisional spin exchange process. (References 4 and 5)

The Rb vapor is also utilized for the detection of the precessing nuclear moments. This technique is an adaptation (Reference 6) of a rubidium magnetometer (Reference 7) and senses the weak magnetic fields associated with the nuclear moments. It operates on the principle that the absorption of optical pumping light by rubidium atoms is a function of the direction of the rubidium magnetic moment relative to that of the light beam and that the direction of the rubidium magnetic moment is itself a function of the magnetic field. Thus a magnetic field modulated at the two nuclear Larmor frequencies of the two noble gases can cause modulations in the transmitted optical pumping light at these same frequencies.

In order to implement this magnetometer, an AC magnetic field is applied parallel to the DC field, H. The frequency of this AC carrier field is the Larmor frequency of the rubidium in the field, H. The light transmitted by the cell becomes modulated at this AC frequency, with the nuclear Larmor precession frequencies being manifested as sidebands.

There are several advantages of this Rb magnetometer as a nuclear moment detector. The optically pumped rubidium is already present in the cell for the nuclear moment orientation process. Both the nuclear moment orientation and detection processes are indirect, that is, not directly involving interactions with light. This allows the inherently long relaxation times of the noble gases to be preserved. The magnetometer is a high S/N detector of the precessing nuclear moments. Much of this is due to a strong collisional enhancement effect (Reference 5) which results in the Rb moments sensing a noble gas nuclear moment magnetic field which is, in effect, orders of magnitude larger than would be expected from the nuclear moments alone. In addition, the magnetometer, as a magnetic field detector, can sense and thus control the ambient magnetic field components along the directions orthogonal to the applied field, H, thus preserving the axis stability of H and consequently the gyro.

The principles of operation of this NMR gyro can be summarized by the functional schematic of figure 1. The transmitted light is incident on a photodetector. The resulting signal is then demodulated to remove the carrier AC signal, leaving the Larmor sidebands. These sidebands are then separated to provide the nuclear precession phases, the Larmor precession fields which are used for magnetic moment torquing, and, from equation (6), control of the magnitude of the applied field H. A breadboard gyro model incorporating these techniques has been built and tested. Figure 2 is an assembly drawing of this model. In this model, the magnetic field axis and thus the gyro input axis is vertical. The light is shown passing through the NMR cell at a 45° angle to the magnetic field in order to provide both a parallel (for pumping) and orthogonal (for detection) component of the light beam with respect to the magnetic field. The potential of this gyro is illustrated by the data shown in figure 3 which shows the low bias drifts which have been achieved under favorable conditions during gyro testing. The data, which shows the apparent gyro angle with the gyro mounted on a stationary test stand, is for an 8-hour segment with the average bias removed. Bias repeatability for this model is about 1 deg/hr, limited primarily by systematic effects related to temperature and light intensity. With the gyro mounted on a rate table and rotated about the gyro input axis (vertical), the scale factor was measured and is constant to within experimental measurement accuracy (100 ppm) for all measured rates (up to 70 deg/sec). A S/N of greater than 60 db (1 Hz bandwidth) has been achieved from both nuclear species and relaxation times are in the several hundred second range. This demonstrates the efficiency of the nuclear moment orientation and nuclear moment detection processes as well as the fact that these processes do not severely limit relaxation times.

In summary, we have demonstrated an approach to an NMR gyro which meets the general requirements for continuous, precise measurement of inertial rotation angle and which has the potential for development into a practical gyro. The present research and development program is concerned mainly with obtaining techniques for eliminating the systematic bias drifts and with developing a next generation gyro with significant size reduction and improvement in performance.

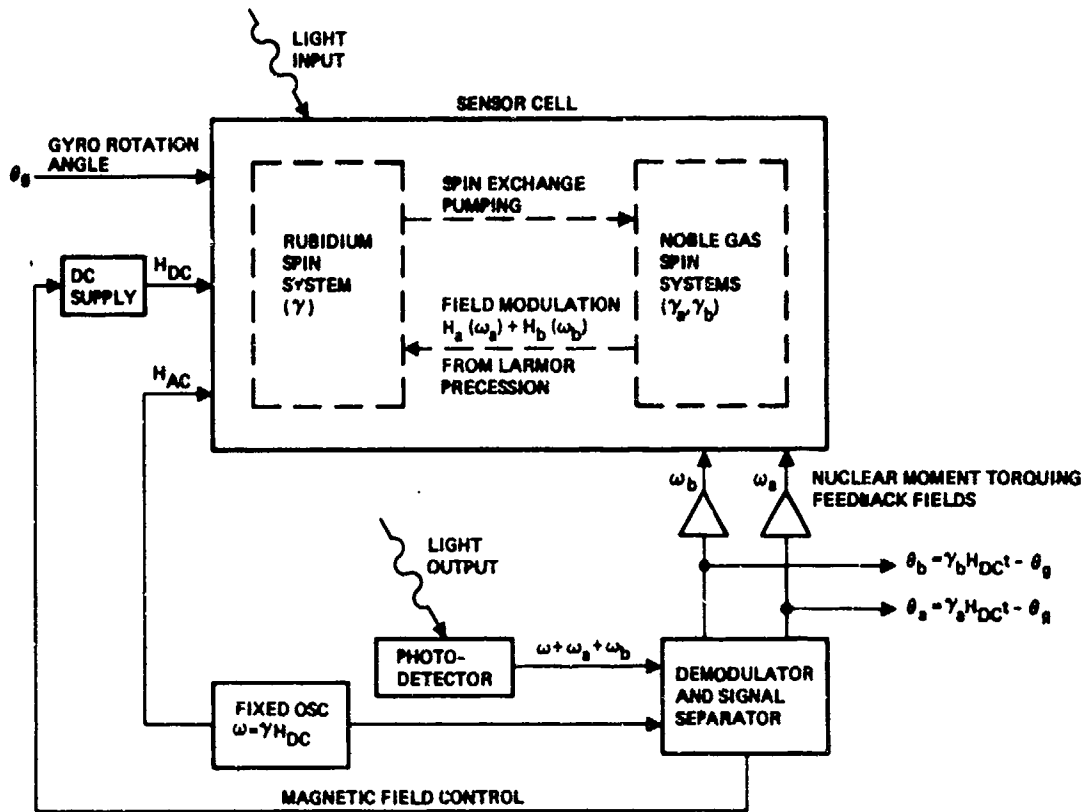


Figure 1. NMR Gyro Functional Schematic

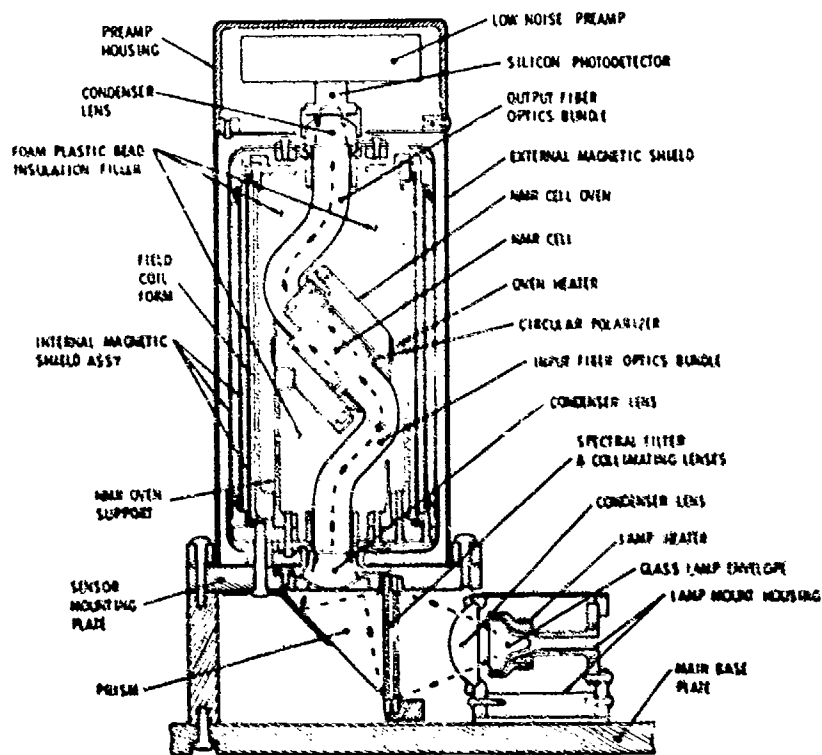
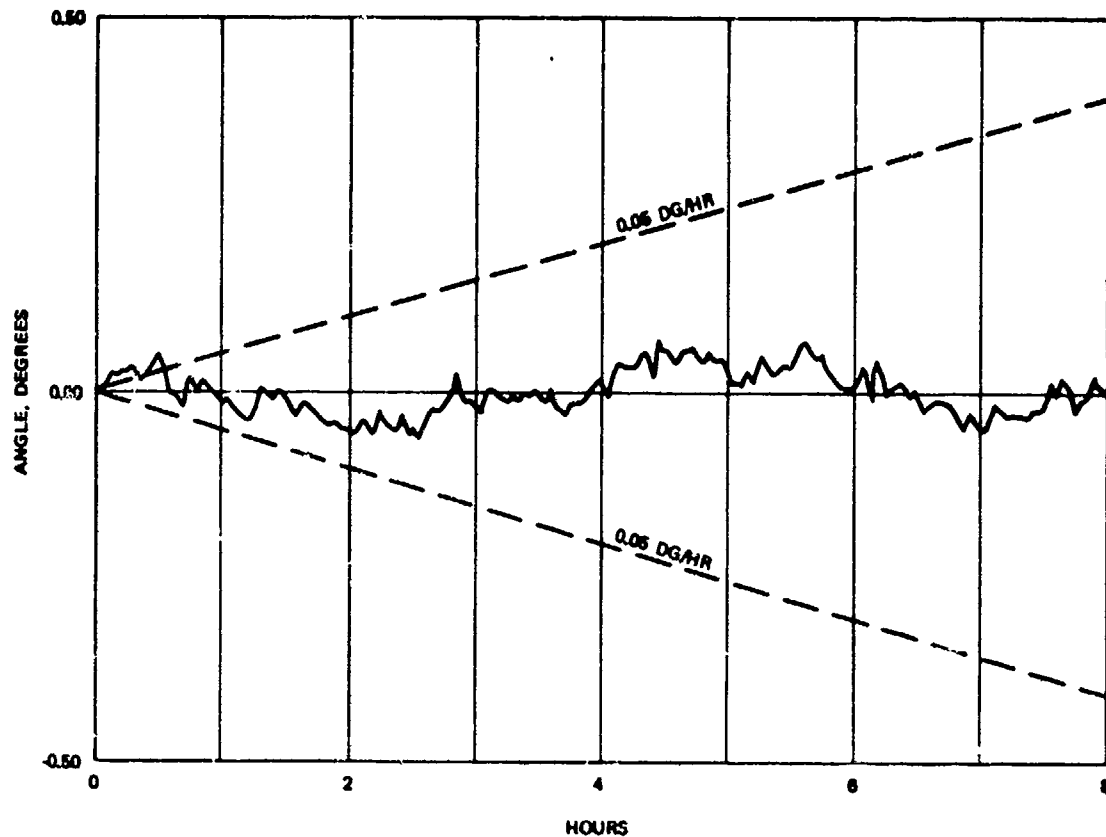


Figure 2. NMR Breadboard Gyro Sensor Assembly Drawing



(3 MINUTE SMOOTHING, AVERAGE BIAS REMOVED)

Figure 3. Breadboard Gyro Output Angle Data

IV. REFERENCES

1. See for instance C.P. Slichter, "Principles of Magnetic Resonance", Harper and Row (N.Y.)
2. For a survey of optical pumping and list of references see: W. Happer, Reviews of Modern Physics, Vol. 44, #2, p 169-249 (April 1972)
3. J. H. Simpson, Astron. and Aeron. 2, #10, p 42 (1964)
4. R. M. Herman, Phys. Rev. 137, A1062 (1965)
5. B. C. Grover, Phys. Rev. Lett. 40, 391 (1978)
6. E. Manegsberg, Proceedings of the SPIE Conference on Laser Inertial Sensors (San Diego, CA, Aug. 28-31, 1978), SPIE Vol. 157, p 73
7. C. Cohen-Tannoudji, J. DuPont-Roc, S. Haroche, P. Laloe; Rev. De Phys. Appliq. 5, 95-108 (1970)

V. ACKNOWLEDGEMENTS

This work has been partially supported by Naval Air Systems Command, contract # N00019-77-C-0380.

HAMILTON STANDARD
 SUPERJET™ SOLID STATE FLUIDIC RATE SENSOR

Richard E. Swarts - Chief of Inertial Systems

Robert J. Slabinski - Senior Systems Engineer

Mario T. Lopiccio - Senior Sensor Design Engineer

Hamilton Standard Division, 1690 New Britain Avenue, Farmington, Connecticut 06032

SUMMARY

The Hamilton Standard Superjet™ Sensor is a solid state fluidic rate sensor replacing conventional inertia wheel gyroscopes in applications where high-shock loading, rapid turn-on and long storage life are important. Applied angular rates are measured by means of the Coriolis acceleration generated deflection of a recirculated gas jet flow. This gas jet flow is used to differentially cool a precision temperature sensitive wire pair located downstream in the jet flow. The instrument contains no rotating or mating sliding parts. The sensor is a small, lightweight, low-power consumption device which is capable of extreme over-ranging without degradation of performance upon recovery.

This paper presents a description of the Superjet™ Sensor and its associated supporting electronics. Presented herein are discussions of the theory of operation, design implementation and test results substantiating the performance capability of the unit. Data are presented which demonstrate capabilities of $0.3^\circ/\text{sec}$ null offset over temperature, $0.02^\circ/\text{sec}$ resolution and 1.0 percent scale factor linearity for rates up to $150^\circ/\text{sec}$.

1.0 INTRODUCTION

Initial development of the Superjet™ Solid State Fluidic Rate Sensor as a promising device with potential commercial and military value can be traced to work performed in 1966 by Hercules Incorporated on an experimental angular rate sensor for use in sailplanes. Improvements implemented by Hercules and subsequently by Hamilton Standard following the execution of a formal licensing/manufacturing agreement in 1972, has resulted in the evolutionary development of the instrument from the original Hercules fluidic angular rate sensor concept to the practical, highly producible rate sensor package currently being supplied by Hamilton Standard for the U.S. Army Copperhead Cannon Launched Guided Projectile program.

The principle of operation of the Fluidic Rate Sensor has not been modified since its inception although numerous design changes have been made to improve the design and establish the present Hamilton Standard Superjet™ Sensor Configuration.

The original sensor device utilized a bidirectional flowmeter to detect jet position by measuring dynamic pressure differences between two adjacent Pitot-static tubes placed symmetrically in the jet flow stream. The laminar fluid jet flow was generated by a centrifugal fan, the rotor of which was the only moving part in the sensor. In the next generation sensor design, the Pitot tubes were replaced by thermistor beads which afforded an improvement in rate detection and response time. The fan powered centrifugal pump was also replaced by an electromagnetic speaker which provided a pulsating air supply which, in turn, was rectified to a smooth airflow within the sensor prior to being directed onto the thermistor sensing elements. The third generation sensor design replaced the electromagnetic speaker with a laminated piezoelectric disc to provide the pulsating airflow. This served to increase frequency response and improve the ability to detect low angular rates. A fourth generation design was successful in miniaturizing the sensor and further increasing frequency response. This later characteristic was achieved by replacing the thermistor beads with thermally sensitive resistance wires and changing the composition of the recirculated gas used to generate laminar fluid jet flow.

The latter basic configuration is still in use today, however, Hamilton Standard has since made several improvements to the internal structure of the Superjet™ Sensor to minimize fluid turbulence, hence improving the laminar flow characteristics of the instrument. Manufacturing/process changes have also been incorporated to ruggedize the sensor affording the ability to withstand severe shock without performance degradation. A unique electronics package has also been developed by Hamilton Standard, which when used in conjunction with the Superjet™ Sensor, forms a functionally complete rate sensor package.

2.0 THEORY OF OPERATION

Hamilton Standard's Superjet™ Solid State Fluidic Rate Sensor utilizes Coriolis acceleration to sense angular rates applied to the instrument. Coriolis acceleration is an acceleration generated in an angular motion environment which causes a mass traveling with a linear velocity to be deflected from its nominal straight line path. This is quickly visualized using, as an example, water emanating from a garden hose. As the hose is spun about an axis perpendicular to the nozzle flow axis, the stream is caused to "bend" (i.e., a force resulting from the applied angular rate motion causes the jet to be deflected from its nominal "at rest" trajectory). The deflection experienced is directly proportional to the magnitude of the applied rate: the greater the applied rate, the greater the deflection experienced. Thus, in a controlled environment, jet deflection at any general downstream position in the jet flow may be used as a direct measure of the applied rate. This principle has been utilized in the mechanization of the Hamilton Standard solid state fluidic rate sensor.

2.1 JET DYNAMICS

The jet flow in the Hamilton Standard Superjet™ Rate Sensor is a gaseous laminar jet stream which is highly sensitive to Coriolis acceleration. As schematically shown in Figure 1, the jet stream moves at a constant jet velocity V_j . In the presence of an angular rate, ω_i , applied along the input axis of the sensor case, the jet stream will be deflected from its nominal center position.

The magnitude and sense of deflection are dependent on the vector characteristics of the applied angular rate. Deflection magnitude is readily calculated using the conventional mathematical expression for Coriolis acceleration. Written along the direction of deflection, y , the equation for Coriolis acceleration is

$$\ddot{y} = 2\omega_i V_j$$

Double integration provides the expression for deflection.

$$y = \omega_i V_j T^2$$

Referring to Figure 1, a sensing element (i.e., wire pair) is inserted into the flow stream at a distance, L , from the jet stream source (i.e., nozzle). This distance can be expressed as the product of the velocity of the jet (V_j) and the time (T) required for a particle in the flow to travel from the nozzle to the sensing wire pair. Using $L = V_j T$, the expression for Coriolis jet stream deflection can be written in three forms.

$$y = \omega_i V_j T^2 \quad (1)$$

$$y = \omega_i L T \quad (2)$$

$$y = \omega_i \frac{L^2}{V_j} \quad (3)$$

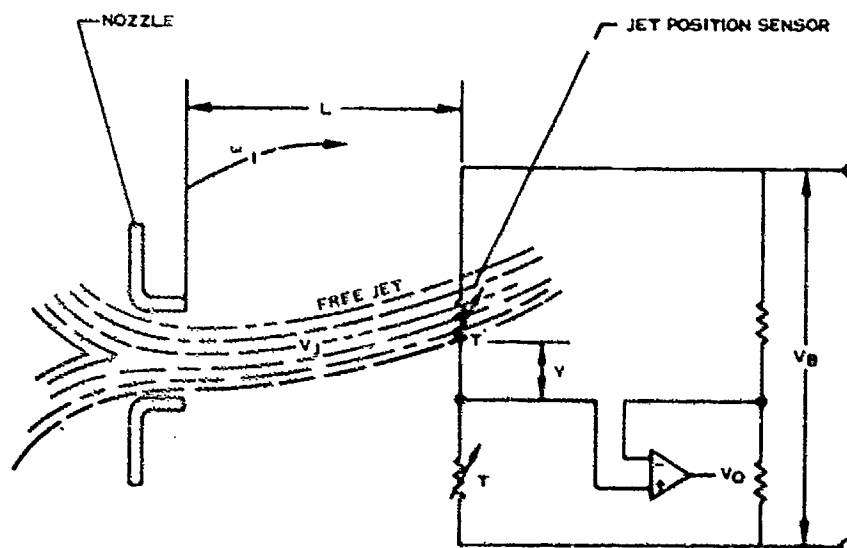


FIGURE 1 SUPERJET™ ANGULAR RATE SENSOR SCHEMATIC F-587

Examination of these equations shows that gas deflection is directly proportional to the magnitude of the input angular rate applied perpendicular to the direction of jet flow (i.e., jet axis). Study of the alternate forms of the equation also identifies the other sensor design parameters which govern jet deflection. Under constant jet velocity and input angular rate conditions, jet deflection is proportional to the product of the length of the jet and jet transport time (Eq. 2). Conversely, equation 3 shows that for a given length jet, deflection is inversely proportional to jet velocity, (i.e., the greater the velocity, the smaller the deflection).

In order to maintain gas jet flow stability and produce a low noise signal, the jet flow must be kept within the streamline laminar flow regime. This condition is achieved by limiting the jet Reynolds Number ($\rho V_j D$). Laminar flow is more readily produced with a gas having low density and high viscosity since, as indicated above, Reynolds Number is directly proportional to density and inversely proportional to the viscosity of the gas. In addition, from the standpoint of obtaining maximum frequency response, it is desirable to set the gas jet velocity as high as possible within the constraints established by the laminar flow criteria. Conversely, as seen in the equations the lateral deflection is inversely proportional to jet velocity. The selected design flow velocity, thus, represents a compromise between frequency response and instrument sensitivity.

2.2 RATE MEASUREMENT

The mechanism used in the Superjet™ Sensor to detect an applied angular rate utilizes the combined effects of the jet deflection and the convective cooling caused by the flow of the gas moving over a stationary element. Using these principles, conversion of the jet deflection into an electrical signal proportional to the input rate is accomplished by symmetrically positioning two temperature sensitive wire resistors on either side of the nominal center of the jet stream at a selected downstream location. These wires are electrically connected by means of a conventional bridge circuit. As the jet deflects to one side or the other of the undisturbed center position, the differential cooling of the temperature sensitive resistors produces an output voltage which varies linearly with input rate. Figure 1 is a diagrammatic representation of this implementation.

The jet deflection/bridge wire sensing principle is insensitive to linear applied motion environments. A constant velocity translation of the sensor in any direction will not cause the jet to be deflected relative to the sensor wire set. Translational acceleration does not introduce a first order error since the laminar gas flow jet is, in effect, buoyantly supported within the free gas space. Acceleration does produce density gradients, however, which may cause second order errors. These are an order of magnitude smaller than comparable errors in an equivalent mechanical gyro.

2.3 PUMP OPERATION

The constant velocity, laminar jet flow within the Superjet™ Sensor is generated by means of a vibrating pump diaphragm functioning to continuously recirculate the gas encapsulated in the sensor through a precision nozzle block. The pump diaphragm is a ceramic piezoelectric crystal mounted around the periphery and electrically excited on its primary surfaces (i.e., perpendicular to the mounting plane). This element is the only "moving" mechanical part in the Superjet™ Sensor and is designed for infinite life.

The internal flow pattern created by the diaphragm pump action is shown in Figure 2. Upon leaving the pump chamber area, the increased pressure gas is forced through the nozzle block orifice into a radial accumulator chamber. Directed by longitudinal plenum chambers the gas flows to the far end of the instrument into another radial accumulator chamber. After traversing the length of the instrument and entering an inlet manifold area, the flow direction is reversed and directed through the jet nozzle orifice. The flow pattern created by this orifice is propagated toward the pump end of the jet via an open duct located in the center of the instrument. The central laminar flow jet is then directed over the sensing wires mounted in the sensor plug assembly. The total laminar flow is then passed back into the pump area through a series of holes located in the base of the sensing plug assembly to complete the jet flow circulation cycle.

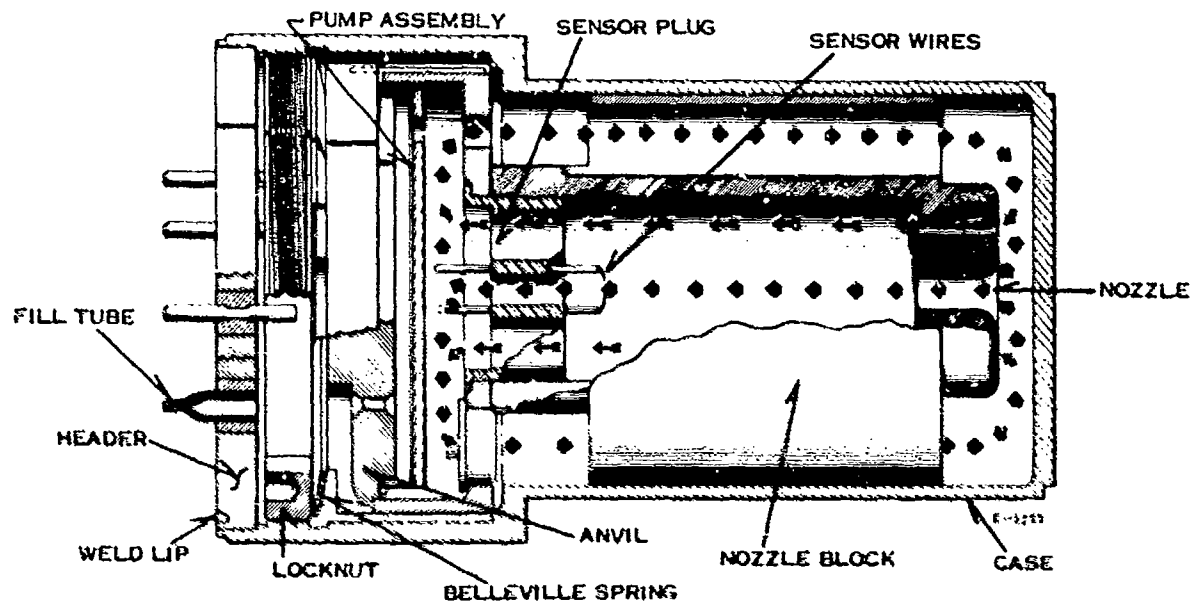


FIGURE 2 SUPERJET™ SENSOR—CROSS SECTION VIEW

The pumping action of the piezoelectric diaphragm creating the jet flow motion is illustrated in Figure 3. The installed positions of the nozzle block, pump support ring and anvil create a thin cylindrical working pump volume immediately aft of the sensor plug. The pump diaphragm is suspended approximately in the center of this volume. On the initial inlet stroke during pump startup (Ref. Part A, Figure 3), the diaphragm is deflected toward the main body of the instrument (i.e., toward the nozzle block). This creates a low pressure region behind the diaphragm (i.e., header side) and gas is drawn into this volume through a small hole in the diaphragm.

On the first compression stroke, (Part B, Figure 3), the diaphragm is deflected toward the header end of the instrument causing a high pressure region to be generated behind the diaphragm. The gas in this volume is subsequently expelled through the single hole in the diaphragm and into the primary instrument flow path. The concentric placement of the diaphragm hole with a matching hole in the nozzle block, coupled with the velocity profile and momentum of the moving gas cause the bulk of the gas expelled by the pump to be carried through the nozzle block entrance orifice and into the primary flow feed plenum. On the next intake stroke (Part C, Figure 3), gas is again drawn into the rear chamber of the pump. In this instance, however, due to 1) the combined effects of the lower flow resistance created by the larger openings in the sensor plug, as compared to the inlet plenum feed orifice, 2) the forward momentum of the gas moving through this orifice and 3) the viscous shear on the walls of the orifice, the gas entering the pump chamber is drawn primarily from the region around the sensor plug. On the following compression stroke (Part D, Figure 3), the newly drawn volume of gas is expelled through the pump exit hole and into the inlet manifold. This process is repeated with each oscillatory pump cycle creating a continually recirculated flow of gas within the sensor.

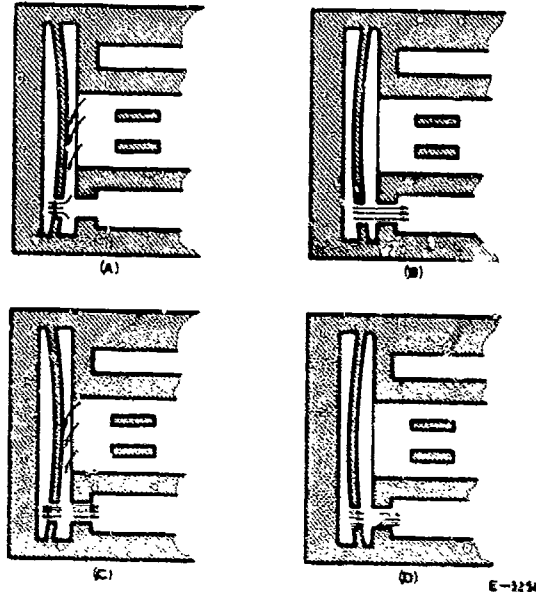


FIGURE 3 SUPERJET™ PUMP OPERATION

3.0 SUPERJET™ SENSOR CONSTRUCTION

The Superjet™ Solid State Angular Rate Sensor concept has been reduced in practice to a simple mechanical configuration specifically developed for ease of manufacture (Ref. Figure 2). The simplicity of the sensor, consisting of only eight mechanical parts/assemblies, is further illustrated by the exploded view shown in Figure 4.

Referring to Figure 4, the pump assembly consists of two elements; a thin piezoelectric crystal and a crystal and a circumferential flexible mounting ring. The crystal element itself is used as the tuning element in an equivalent LCR pump drive analog circuit which causes the pump to vibrate at its natural resonant frequency.

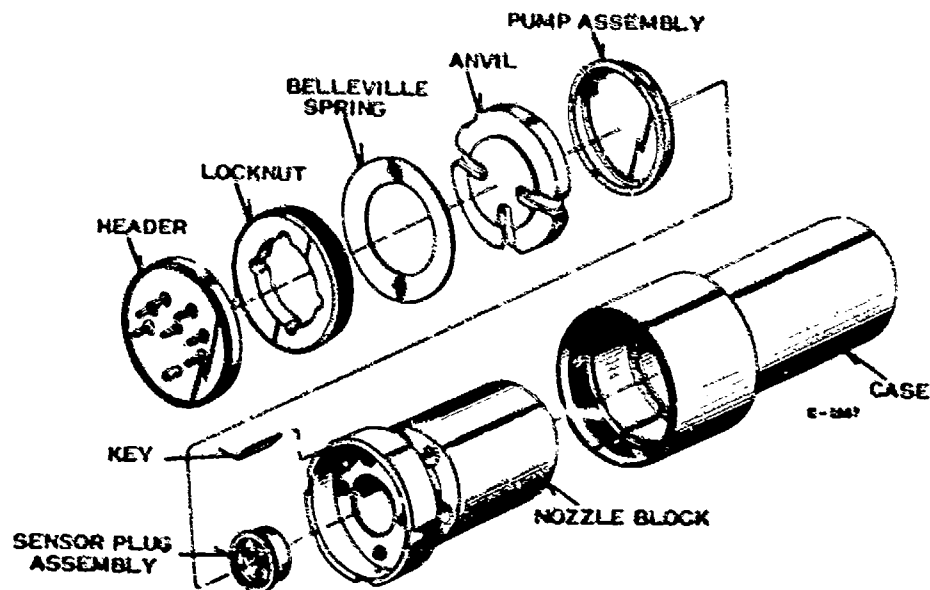


FIGURE 4 SUPERJET™ SENSOR - EXPLODED VIEW

A circular anvil is used to provide the reactive structure needed to support the pump assembly during operation. The anvil is seated directly against the support rim of the pump assembly crystal support flexure. The thickness of the anvil is designed to withstand the pressure pulsations which occur within the pump chamber at the crystal/anvil interface.

A Belleville spring and locknut are used to securely position the pump/anvil against an internal flange in the nozzle block.

The nozzle block is the largest mechanical element in the SuperjetTM Sensor. Its two-fold functions are to 1) channel the recirculated gas flow path within the instrument and 2) provide the internal mechanical structure to position the sensor plug and pump assemblies in the instrument. The nozzle block is basically cylindrical in shape. The outer surface of the piece has a broad annular depression which, when mated with the case of the instrument, forms the feed manifold which receives the pressurized gas generated by the pump assembly.

A nozzle designed to promote laminar flow is formed in the center of one end of the nozzle block. The instrument case is used in conjunction with the nozzle block to form an enclosed flow area. The installation clearance between the end of the nozzle block and the instrument case form an inlet manifold used to divert (i.e., reverse) the direction of the gas flow into the jet nozzle. Both the feed and inlet manifolds serve as "reservoirs" which are designed to attenuate the pressure pulsations generated by the pump providing a more uniform flow over the instrument sensing wires.

The sensor plug assembly is seated in the nozzle block immediately upstream of the pump assembly and contains the sensing elements of the instrument. The sensor plug assembly is comprised of a parallel pair of thin temperature sensitive wire filaments mounted to vertical posts. The posts are secured to the plug assembly by means of feed through glass insulators. Electrical contact with the sensor wires is achieved by means of wires welded to the downstream side of the posts. Prior to final assembly of the SuperjetTM Sensor, the finished plug assembly is trimmed to enhance the resistance tracking characteristics of the wire pair over the full operating temperature spectrum. This trim is performed to improve subsequent instrument null accuracy performance.

The base of the sensor plug is fitted with a series of through holes permitting the jet to flow past the plug into the pump area to be recirculated.

In addition to the above described internal parts, the remaining pieces of the instrument consist of a stainless steel outer case and a header cap through which all electrical contacts to the instrument are made and the instrument is backfilled with gas.

Final assembly of the unit proceeds briefly as follows. The resistance balanced sensor plug assembly is first precisely positioned and attached to the nozzle block. Precision resistors are then mounted at the rear of the sensor plug to complete the bridge circuit.

The pump assembly and anvil are next positioned in the nozzle block behind the sensor plug assembly, and the entire assembly placed in the instrument case. The conical Belleville spring is next positioned behind the anvil using a circular alignment flange located on the anvil. Pressure is then applied to the Belleville spring by means of the annular locknut which screws into the aft portion of the sensor case. The preload pressure applied to the Belleville spring by the locknut permits a large force to be applied to the anvil, firmly securing the anvil/pump assembly to the nozzle block. Thus, the locknut and conical spring provide the means to secure all internal sensor components to the case.

In the final phase of assembly, electrical interconnections are made to the header. The header is then attached and welded to the case. The completed instrument is then backfilled with gas and the fill tube sealed.

4.0 RATE SENSOR PACKAGE ELECTRONICS

In mission applications, the SuperjetTM Rate Sensor is used as an integral element of a Rate Sensor Package consisting of the fluidic sensor and a supporting electronics module developed by Hamilton Standard. The functional characteristics of the complete SuperjetTM Rate Sensor Package are, to a large extent, governed by the operation of the electronics module. Although the generic electronics module contains the same basic elements, the design of each module is tailored to satisfy specific vehicle interface and operational usage mission requirements. The discussion which follows presents a description of the electronic modules developed for the current Copperhead Ball Rate Sensor Program. The operational function of this package, as used in the Copperhead application, is presented in paragraph 5.3.

4.1 FUNCTIONAL DESCRIPTION

The electronics module consists of three printed circuit board assemblies: the processor board, the bridge amplifier board, and the pump oscillator board, and supporting power supply and signal conditioning electronics. The function of the board assemblies is as follows:

- Processor Board - The Processor Board contains a microcomputer which performs sensor compensation, and null store bias correction functions. The microcomputer accepts data from the SuperjetTM Sensor and outputs controlling information to the other electronic functional elements within the RRS.
- Bridge Amplifier Board - The Bridge Amplifier Board supplies the SuperjetTM Sensor bridge sensing resistors with the regulated voltage, constant power required to maintain scale factor performance requirements.

- Pump Oscillator Board - The Pump Oscillator Board supplies the excitation voltage to the pump piezoelectric crystal assembly in a closed loop oscillator circuit.

The Hamilton Standard roll rate sensor electronics assembly performs several functions as described in the following paragraphs.

4.1.1 INPUT POWER CONDITIONING

Input Power Conditioning encompasses the responsibility assigned to a conventional power supply. This function consists of the generation, regulation and distribution of the various DC voltages required to operate the unit using input power provided from a single DC battery supply. Because of the low voltage DC characteristics of the rate sensor power requirements, the power supply is a particularly simple, passive resistive network implementation which does not rely on the use of inverters, converters, etc., to generate intermediate AC and/or higher DC voltages for internal use.

4.1.2 SIGNAL CONDITIONING

Signal Conditioning is provided at two important functional stations in the rate sensor electronics package. The first signal conditioning function consists of the isolation, filtering and amplification of the sensing signal obtained from the bridge circuit to levels compatible with the operating characteristics of the standard analog and digital logic elements used throughout the unit. The second major signal conditioning function consists of the integration, filtering and level adjustment of the rate sensor output signal to satisfy vehicle autopilot interface requirements.

4.1.3 AUTOMATIC SEQUENCING

Automatic Sequencing of the rate sensor package achieves compatibility with mission flight scenarios while implementing self-contained null store functions. It is accomplished by means of preprogrammed logic contained in the rate sensor electronics.

4.1.4 STATIC NULL COMPENSATION

Static Null Compensation in the form of a constant electrical null offset is generated by the rate sensor electronics to compensate for electronics long term aging and related instability effects in order to enhance absolute null accuracy performance. This is accomplished by electrically energizing the electronics and bridge wire pair prior to pump turn-on and noting the net current unbalance between the two elements of the bridge. In the absence of a sensed inertial input motion created by the pump-off condition (even in the presence of an actual applied motion) the unbalance is attributed to the total accumulated shift in electronic parameters at the time of turn-on. The null offset is then electrically readjusted to zero by means of feedback loop logic. This procedure virtually eliminates error parameters attributed to long term electronic component stability.

4.1.5 DYNAMIC NULL COMPENSATION

Dynamic Null Compensation provided by the rate sensor electronics is an additional null offset correction factor applied after pump turn-on to compensate for temperature dependent jet flow/wire plug geometry misalignments remaining after final assembly of each sensor. The magnitude of this correction is based on the initial laboratory calibration of the sensor performed at the time of manufacture and is assumed to remain constant during the life of the unit.

4.1.6 SCALE FACTOR COMPENSATION

Scale Factor Compensation for operating temperature variations is automatically generated by the rate sensor electronics. The gain changes are developed by the direct reading of the temperature sensitive wire bridge circuit and are designed to offset the natural variation of sensor plug/bridge network resistive experienced with temperature change. Scale factor voltage compensation is determined during the calibration and trim of the unit during the final phase of manufacture.

Figure 5 presents a functional block diagram of the rate sensor/electronics package. The unit consists of three major functional elements: the Superjet™ Rate Sensor; the primary analog signal processing electronics; and a supportive digital compensation network. The compensation network is operated in a feedback mode during initial turn-on to provide the null store function as described in further detail below.

During flight operation, the output of the Superjet™ Rate Sensor is combined with static and dynamic null compensation signals and processed in an analog gain stage. The output of the gain stage is then adjusted to compensate for variations in scale factor incurred with local ambient temperature changes. The scale factor temperature compensated rate output signal is then used for two purposes: 1) as a direct input rate signal to the vehicle autopilot and 2) as input to an analog integration stage to derive roll angle data which, in turn, is also input to the autopilot.

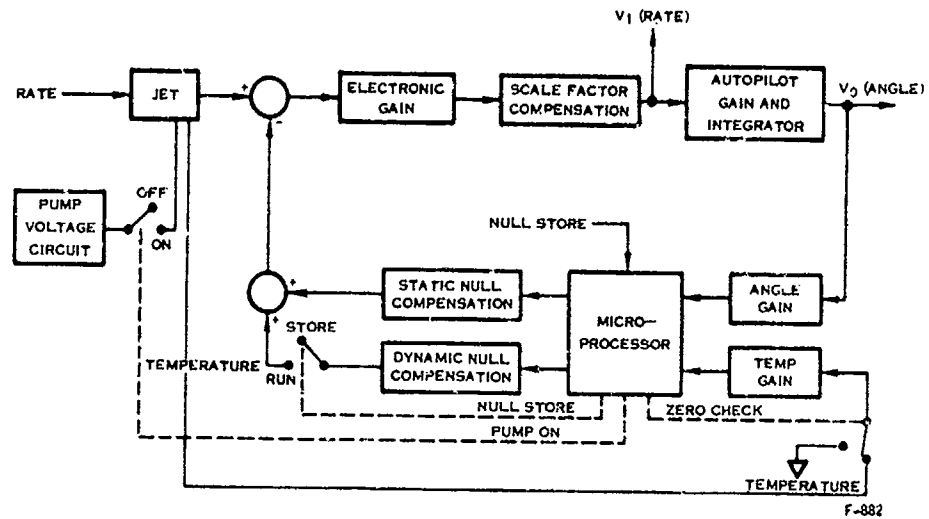


FIGURE 5 ROLL RATE SENSOR FUNCTIONAL BLOCK DIAGRAM

5.0 COPPERHEAD ROLL RATE SENSOR PACKAGE

Hamilton Standard is presently supplying the Roll Rate Sensor (RRS) package for the U.S. Army/Martin Marietta Corporation Copperhead program. Copperhead is a laser guided projectile which is launched from an armored vehicle mounted 155 mm cannon. The Roll Rate Sensor package operates during flight to provide initial round despun and subsequent zero rate roll stabilization functions. These functions are performed after rapid turn-on in the post launch high spin rate environment created when the round is fired from the cannon bore.

Hamilton Standard's Copperhead Roll Rate Sensor program began in 1975 with an initial award to build and evaluate six engineering brassboard units to demonstrate the suitability of the Superjet™ Sensor concept for the Copperhead application. The success of this program led to Hamilton Standard's selection to perform the Engineering Development (ED) Phase program in 1976. A total of 470 preproduction prototype engineering units have been delivered with the program formally completed in fourth quarter 1979. During this program, the unit was successfully qualification tested in the laboratory, simulating the severe Copperhead mission flight environments and in a series of 9,000 g shock environment cannon cannister launches.

Based on its Engineering Development phase program performance, in 1978 Hamilton Standard was awarded a contract to develop the computerized Initial Production Facility (IPF) required to automatically assemble and test the RRS in high volume production quantities. This program is scheduled for completion in 1980.

An Initial Production (IP) program will begin in early 1980. This program, for the manufacture of Roll Rate Sensor Units, will serve to verify the production design of the unit, as well as the IP production facilities developed for its high volume production. The IP program is scheduled for completion in 1982. Full Copperhead RRS production will be initiated in 1982 and will continue through the 1980's with follow-on procurements anticipated in the post 1990 time period.

5.1 PHYSICAL CHARACTERISTICS

The Copperhead Roll Rate Sensor (RRS) is a single axis unit consisting of the Hamilton Standard Superjet™ Sensor and supporting electronics mounted in a common housing. The unit occupies a total volume of less than 10.5 in³ (172 cm³) and weighs 12.0 ounces (340 gm). The unit consumes approximately 2.4 watts of total operating power. The Superjet™ Roll Rate Sensor package has been successfully qualification tested for use on the Copperhead Common Launched Guided Projectile Program and has demonstrated its ability to operate after withstanding launch loads of:

Longitudinal Shock	9000 g's
Lateral Shock (2 Axes)	800 g's
Roll Acceleration	93,750 rad/sec ²

Figure 6 is a photograph of the Copperhead Roll Rate Sensor assembly presently being delivered under the current Engineering Development Phase contract. Figures 7 and 8 present the installation outline drawing and an exploded internal view of the complete RRS sensor package, respectively. Table 1 presents a more complete summary of the major physical and performance specifications of the unit.

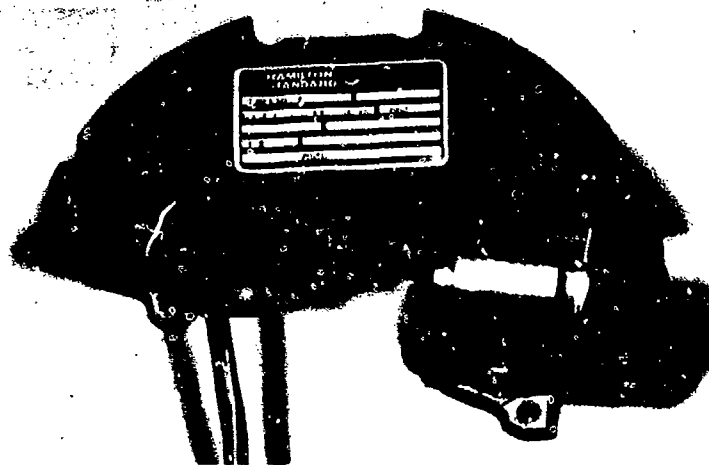


FIGURE 6 COPPERHEAD ROLL RATE SENSOR PACKAGE

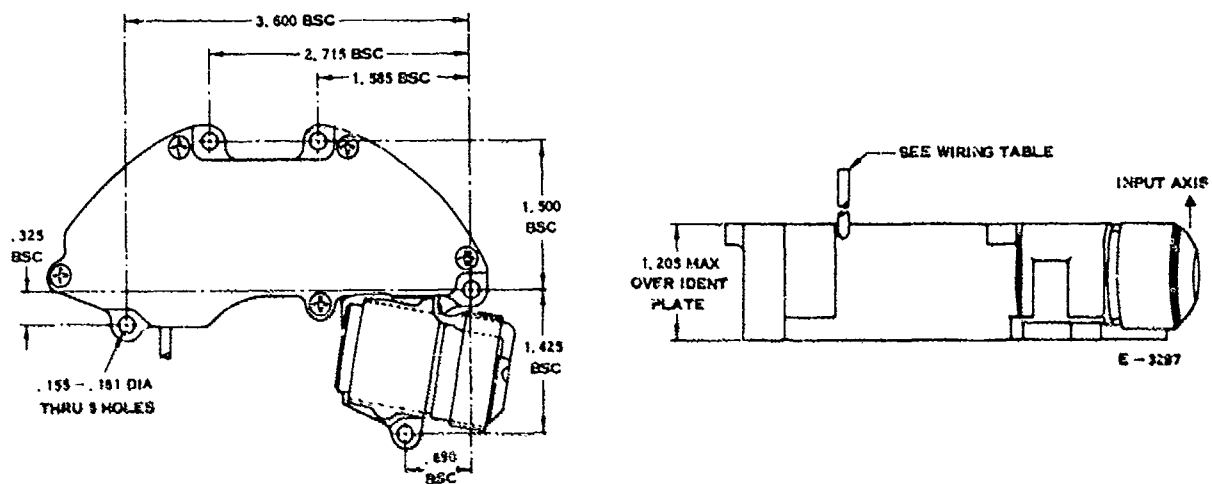


FIGURE 7 COPPERHEAD ROLL RATE SENSOR INSTALLATION DRAWING

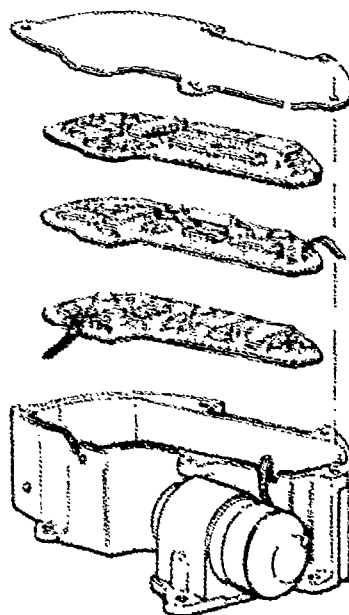


FIGURE 8 COPPERHEAD ROLL RATE SENSOR ASSEMBLY - EXPLODED VIEW

TABLE I
COPPERHEAD RRS CHARACTERISTICS SUMMARY

Weight of Jet:	- 3.8 oz.
Weight of Total Package:	- 12.0 oz.
Volume of Total Package:	- 10.5 in. ³
Input Voltage:	- $\pm 15V @ 22 \text{ ma}$ +11.5V @ 120 ma
Rate Range:	- 120 ⁰ /sec.*
Scale Factor:	- Rate - 6 mvolts/degrees/sec - Angle - 120 mv/degree - Null Stability (Absolute, Environment) - $\pm 0.6^0$ /sec (when null compensation performed in high rate environment) - $\pm 0.3^0$ /sec (when null compensation performed in benign environment) - Scale Factor - 15% (Absolute, Environment and Symmetry) - Scale Factor Linearity - 1% to 120 ⁰ /sec - 2% to 500 ⁰ /sec
Linear Acceleration Sensitivity:	- .02 ⁰ /sec/g
Frequency Response:	- 40 Hz
Input Axis Alignment:	- 1/2 deg. (.25 ⁰ on Copperhead IA to roll reference 1.5 ⁰ IA wrt jet axis)
Environmental Capability:	- Temp: -25 ⁰ F to +155 ⁰ F Vibration: 7.6 g RMS Shock: 10,000 g's

*Modification to existing packages will increase rate range to 500⁰/sec

(Scale factor linearity will degrade.)

5.2 POWER REQUIREMENTS

The power consumed by a SuperjetTM Rate Sensor/electronics channel is very low. In the Copperhead application, required DC voltages are derived from a single battery supply greatly simplifying the complexity (and weight and cost) of the power supply required to support the operation of the unit. Table II lists the DC voltages used in the operation of the present Copperhead RRS design and the corresponding current and power consumed at each voltage. As shown in Table II, a total of only 1.26 watts at the desired voltages is required to operate the complete sensor channel. Of this total, the largest single element is the $\pm 15 \text{ VDC}$, 0.63 watts required to operate the analog electronics including operational amplifiers, A/D's, O/A's etc. The second largest requirement is the +5VDC, 0.45 watts required to supply the micro-computer.

Power distribution in the Copperhead RRS is accomplished by means of a simple resistive dropping network designed to generate the above required internal working voltages from the vehicle $\pm 15 \text{ VDC}$ center tapped 30 VDC battery supply. The complete supply consists of a simple regulation circuit and the dropping network shown in Figure 9. The penalty paid for the use of the dropping network as opposed to the direct input of the required voltage levels is the power dissipated in the resistive network. As shown in Figure 9, the true total power consumed by the Copperhead RRS is 2.473 watts, approximately twice that actually required by the sensor and electronics.

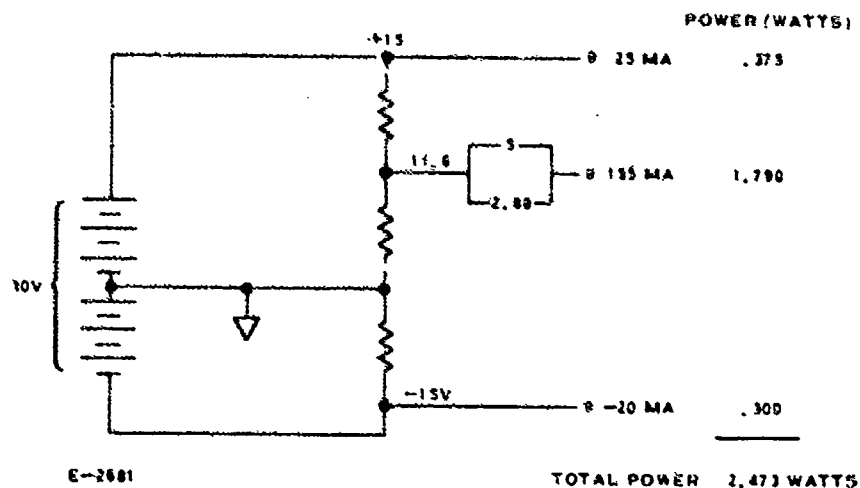


FIGURE 9 COPPERHEAD POWER DISTRIBUTION

TABLE II
SUBASSEMBLY POWER REQUIREMENTS

<u>FUNCTIONAL ELEMENT</u>	<u>VOLTAGE (V)</u>	<u>CURRENT (MAMPS)</u>	<u>POWER (WATTS)</u>
Wire Pair	+2.88	55	.158
	+15	22	.3
Electronics	-15	20	.3
	+5	90	.45
Pump	+5	5	.025
Total			<u>1.263</u>

5.3 FUNCTIONAL OPERATION

The functional operation of the Copperhead Roll Rate Sensor package and, in particular, the null store and compensation functions is, perhaps, best understood while considering the overall operating sequence of the Roll Rate Sensor (RRS) package during the Copperhead mission.

The RRS package is launched in a completely inert state and emerges from the rifled cannon bore in a high roll rate spin stabilized condition. Approximately 400 milliseconds after firing, an 11.6 volt battery in the round is activated. Battery activation causes 2.88 VDC warmup power to be automatically applied to the RRS Superjet™ Sensor wires and bridge circuit, and a Null Store discrete to be applied to the compensation electronics. The early application of power to these elements permits the complete bridge circuit to become thermally stabilized prior to initialization of the null store function. As explained below, this enhances null store accuracy and subsequent mission performance. The applied null store discrete is not used at this time.

At a mission range dependent preselected point during the flight of the round, a ± 15 volt vehicle battery supply is activated by the vehicle master sequencer. This causes the primary supply voltage to be applied to the remaining RRS electronics and, consequently, both primary analog and digital compensation circuits to become activated.

Figure 5 presents a functional block diagram of the Roll Rate Sensor package and indicates the compensation which is performed during the initial turn on and subsequent operation of the unit. The heart of the compensation network is an Intel Model 8748 microcomputer. This device, housed in a 40-pin dual in-line package, is a self-contained programmable 1K-byte by 8-bit parallel microcomputer. This microcomputer sequences and performs the computations needed to support the RRS static and dynamic null store functions.

The first functions performed by the microcomputer under software control are a series of housekeeping chores which are initiated by the "Power Reset" indication generated when power is applied to the microcomputer. These housekeeping tasks include; 1) discharge of capacitors in the analog circuit and initialization of null conditions, and 2) BITE checkout of the Superjet™ Sensor (i.e., bridge resistance reading) and register of the output of the "Temp Gain" circuit element identified in Figure 5.

The Temp Gain circuit consists of an analog amplifier stage and an A/D converter which is used to format the temperature data used by the microcomputer. In a grounded input signal state, the digital output from the "Temp Gain" circuit should be zero valued. In the event a nonzero value is registered due to a shift in electronics characteristics, this bias value is recorded in the computer and used to adjust subsequent temperature readings to the correct level.

After the Temp Gain and BITE checks have been completed, the microcomputer recognizes the presence of the "null store" discrete and places the Null Store Mode and Temperature Measurement switches in the "ON" position, while maintaining the pump in an inoperative state. This sequence of events initiates the null store cycle. The microcomputer begins reading the integrated angle output of the analog circuit after the data is properly scaled and converted from analog to digital format by the "Angle Gain" circuit.

The static null store compensation function is divided into two parts: Coarse Null Compensation, and Fine Compensation. The coarse null is implemented by using the microcomputer as part of a feedback loop. The output signal from the microcomputer is converted to analog format, scaled and combined with the input signal from the Superjet™ Rate Sensor (pump nonoperating) to drive the integrated output of the assembly to zero. It takes approximately 400 milliseconds for the coarse null algorithm to converge to within one data element (bit) of true null. The remainder of the 1.3 second interval assigned to the null store function (for the Copperhead mission) is spent in an interactive fine null compensation mode. During this interval, a filtered averaging technique is used to continuously refine and update the null value derived during the coarse null mode. The zero output feedback mechanism is employed to establish the fine null value. The filtering/update process is continued throughout the null store function as dictated by Copperhead overall mission scheduling constraints. The filtering process is weighted to reflect the most recently acquired data in order to extract the highest possible accuracy. The value converged upon at the end of the assigned null store interval is stored for use as a constant correction value during pump-on RRS operation.

The static null store function is completed by microcomputer recognition of the removal of the null store discrete by the Copperhead round master sequencer. Removal of this signal causes power to be applied to the Superjet™ Sensor pump and the RRS to be placed in the Run mode. The feedback loop used during null store is then broken and a temperature reading stored for later use. During the remainder of the mission, the microcomputer functions to continue to input null compensation values, after D/A conversion, into the

primary autopilot analog processing circuit. As indicated above, the static null compensation is a constant offset value added throughout the remaining portion of the mission. Prior to being combined with the sensor output signal for analog processing, the static null compensation is continually supplemented by an additional dynamic null compensation factor designed to compensate for sensor wire/jet flow misalignment effects. As previously indicated, this later compensation term is a temperature dependent parameter. It is, consequently, updated periodically during the mission under microcomputer software control. This is accomplished by means of a table look up/interpolation routine programmed in the microcomputer using dynamic alignment compensation data taken over the full operating temperature range of the unit. During factory calibration, recorded calibration values are "burned" into the PROM memory elements of the microcomputer. The initial dynamic compensation table "look up" performed during pump-on operation is executed using the averaged temperature data taken at the beginning of the static null store period. Subsequent updates made during the remainder of the flight are performed at a 4 Hz rate under program control. The temperature measurements used for these updates are instantaneous values sampled from the Superjet™ Sensor and preconditioned by the Temp Gain electronics.

After pump turn-on, the RRS operates throughout the remaining portion of the Copperhead mission to provide roll despinn and stabilization functions. The despinn function is performed immediately after pump turn on to cancel the residual high roll rate created during the travel of the round in the rifled cannon bore. The decision to enter a despinn operating mode is made by comparing the fully compensated output of the RRS against a preset threshold (Figure 10). A reading below the threshold, caused by the gross deflection of the sensor jet flow across the sensing wire pair (in a very high angular rate environment), causes the output signal to be latched and held in a saturated maximum command signal condition to produce a maximum command signal condition to produce a maximum vehicle despinn torque through the vehicle control fins. The latched condition is maintained until the threshold is exceeded (i.e., the jet flow approaches a central position relative to the sensing wires) and proportional control can be initiated. Despinn is then completed using proportional control, and the round is maintained in a zero rate roll stabilized attitude until target impact.

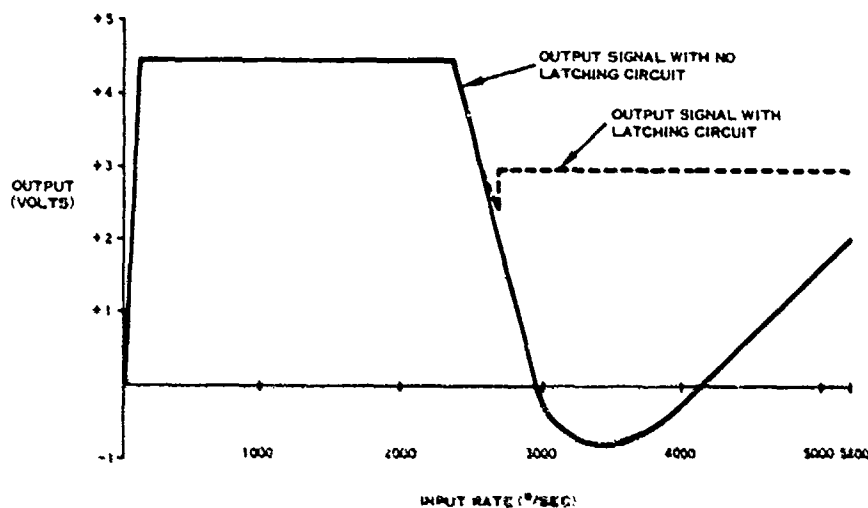


FIGURE 10 COPPERHEAD RRS LATCHING FUNCTION

5.4 LIFE/RELIABILITY

The reliability of the Roll Rate Sensor is inherently high due to its design simplicity. The predicted failure rate of the complete RRS Superjet™ Sensor and supporting electronics package is approximately forty failures per million operating hours ($\lambda = 40 \times 10^{-6}$) or an equivalent MTBF of 25,000 hours. This failure rate is based on conservative component failure rates derived from MIL-HDBK-217B, using 65°C ambient temperature conditions and environment stress factors for a missile launch environment. In a less hostile environment, the effective predicted MTBF of the unit would be considerably higher.

Life tests on five experimental Superjet™ Rate Sensors have exceeded 34,000 hours each or a cumulative total of over 170,000 hours without failure. The elimination of wear limited components in both the jet sensor and supporting electronics has made it possible to attain virtually unlimited unit life.

The environmental resistance of the sensor assembly has been analyzed and experimentally demonstrated for a broad spectrum of vibration, shock and acceleration dynamic conditions. The Superjet™ Angular Rate Sensor is exceptionally tolerant to angular rate overranging. This is a consequence of the fact that overranging does not produce an internal mechanical force on stops, gimbal suspensions, or spin bearings as in conventional rate gyroscopes. Thus, the unit will recover from a large overrange condition without damage or degradation of performance.

6.0 PERFORMANCE

Figure 11 presents Acceptance Test null performance data taken on a sample of 16 Roll Rate Sensor units for the Copperhead program. The data presented illustrates the ability to trim null offset over the full Copperhead -25°F to +155°F operating temperature range. Factors influencing this data are, the specified operating temperature range, word size of the A/D converters used in the present circuit which determines the resolution of the temperature monitor and integrated angle error signals read by the microcomputer during the null store sequence.

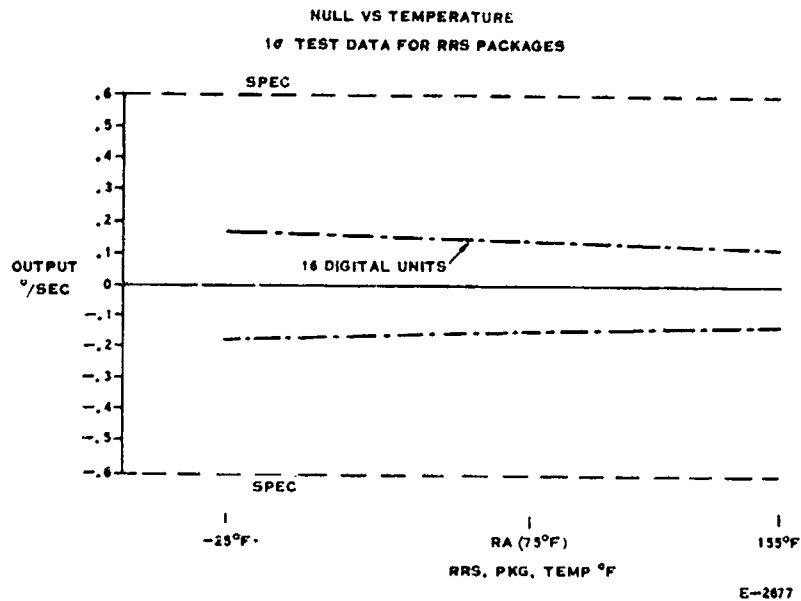


FIGURE 11 COPPERHEAD RRS NULL TRIM PERFORMANCE

Other performance factors of interest are linearity, asymmetry and absolute scale factor. Linearity is defined as the deviation from the least squares straight line fit of the input-output transfer function taken over full operating rate range of the instrument. Figures 12 and 13 present the linearity performance characteristics of two Copperhead RRS units based on data taken following completion of the Qualification Test program. The data taken shows turn on-to-turn on repeatability performance over a period of approximately one week under laboratory ambient conditions (Figure 12) and over the full operating temperature range (Figure 13). The data presented is expressed in terms of percent of point and, as such, is undefined at a zero angular rate condition.

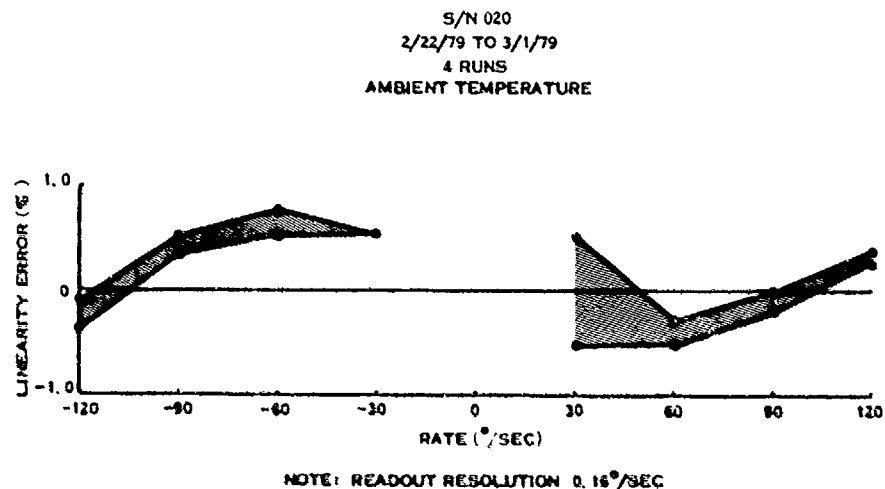
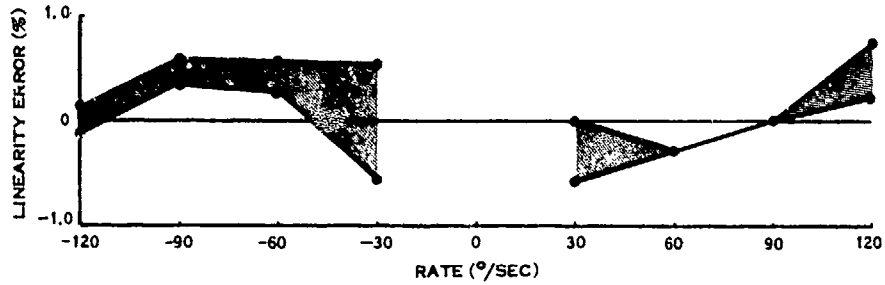


FIGURE 12 LINEARITY REPEATABILITY PERFORMANCE - S/N 020

Data obtained on both units indicate linearity performance better than ± 1.0 percent of point over the rate range between $\pm 120^\circ/\text{sec}$, exclusive of the zero rate singularity point. A run-to-run repeatability (peak-to-peak) capability on the order of 0.25 percent over the 7 and 10-day test intervals and operating temperature range is also indicated by this data. It should be noted that the data at the $\pm 30^\circ/\text{sec}$ point is colored by the $0.16^\circ/\text{sec}$ readout resolution capability of the laboratory instrumentation used to obtain this data which accounts for the disproportionate spread shown.

S/N 026
 2/28/79 TO 3/9/79
 6 RUNS
 TEMPERATURE, -25°F TO 155°F



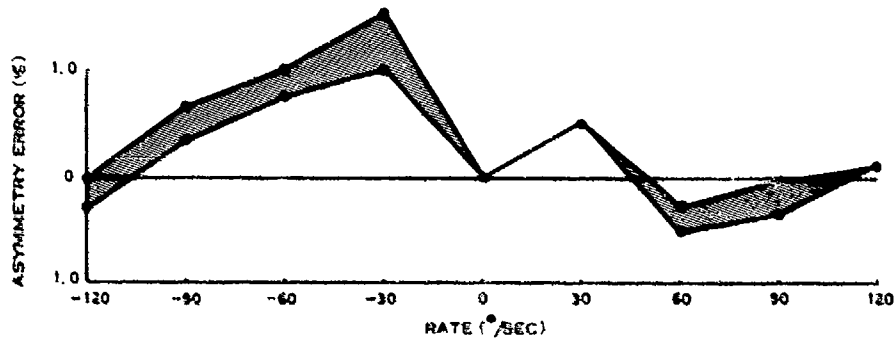
NOTE: READOUT RESOLUTION 0.16°/SEC

E-3226

FIGURE 13 LINEARITY TEMPERATURE/REPEATABILITY PERFORMANCE -S/N 026

Scale factor asymmetry is the deviation from the straight line least square approximations for positive and negative rates, each normalized through the zero point. Scale factor asymmetry data taken on Copperhead units during the above referenced post qualification test program is presented in Figures 14 and 15. Once again, the data is expressed in terms of percent of point. The data presented shows a performance level of better than ± 1.5 percent, with the above mentioned laboratory instrumentation error at $\pm 30^\circ/\text{sec}$ adversely affecting this value. A turn on-to-turn on repeatability capability over the test period of approximately 0.5 percent, including full operating temperature variation effects, is demonstrated.

S/N 020
 2/22/79 TO 3/1/79
 4 RUNS
 AMBIENT TEMPERATURE

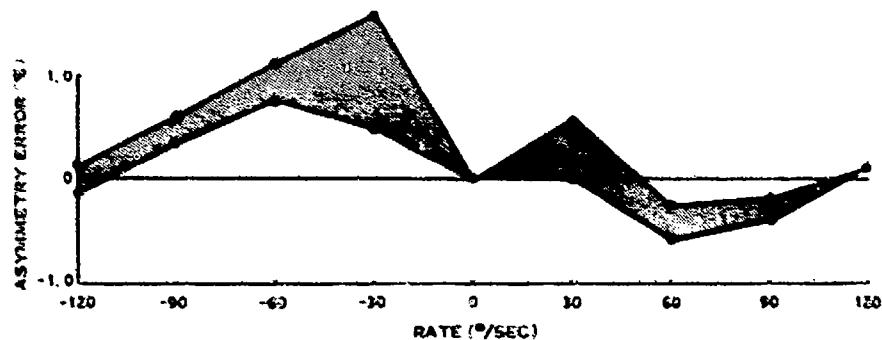


NOTE: READOUT RESOLUTION 0.16°/SEC

E-3189

FIGURE 14 ASYMMETRY REPEATABILITY PERFORMANCE

S-N 026
 2/28/79 TO 3/9/79
 6 RUNS
 TEMPERATURE, -25°F TO 155°F



E-1166

FIGURE 15 ASYMMETRY TEMPERATURE/REPEATABILITY PERFORMANCE

The scale factor magnitude stability performance of a Copperhead qualification unit is summarized in Figure 16. The data presented is expressed in terms of both absolute magnitude (MV/deg/sec) of the analog output device and the percentage deviation from the mean scale factor value taken over the total rate range of the instrument. In examining the data presented in Figure 16, the following important consideration should be noted. This is that scale factor magnitude and scale factor variation with temperature and/or rate are trimmable parameters in the rate sensor design. Variations between the units and closer absolute agreement can be achieved with finer calibration trim. Thus, the pertinent characteristic of the data shown in Figure 16 should be limited to stability considerations. The data presented substantiates a 0.75 percent turn on-to-turn on stability capability over the complete rate range of the instrument at room ambient conditions for an 8-day period.

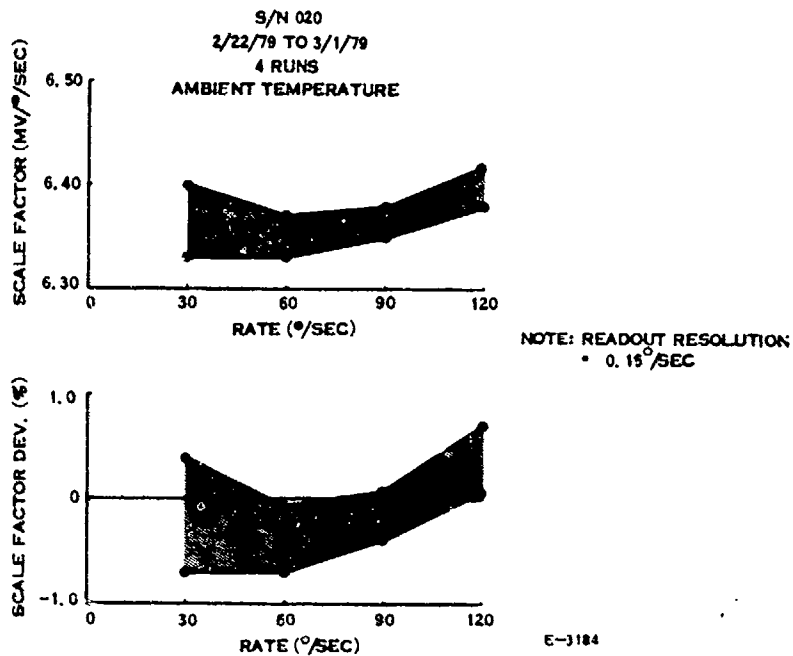


FIGURE 16 ABSOLUTE SCALE FACTOR REPEATABILITY PERFORMANCE

7.0 DESIGN TRADEOFFS/GROWTH POTENTIAL

7.1 REACTION TIME

As illustrated by the Copperhead turn-on sequence schematically shown in Figure 17, the time required to bring the Superjet™ Rate Sensor/electronics module from an unpowered dormant state to a mission ready fully operating condition can be divided into the following segments:

- The time required to achieve thermal stabilization of the Superjet™ Sensor plug wires after initial application of power,
- The time required to perform the null store function, and
- The time required to activate the pump and achieve stable flow conditions.

Beginning with the last item above, pump/flow activation time is dictated by parameters including; the flexure stiffness/resonant frequency characteristics of the piezoelectric pump diaphragm, the applied pump voltage (i.e., design jet flow speed) and the internal flow geometry of the sensor. These are fixed design parameters for the existing Copperhead Superjet™ Rate Sensor configuration.

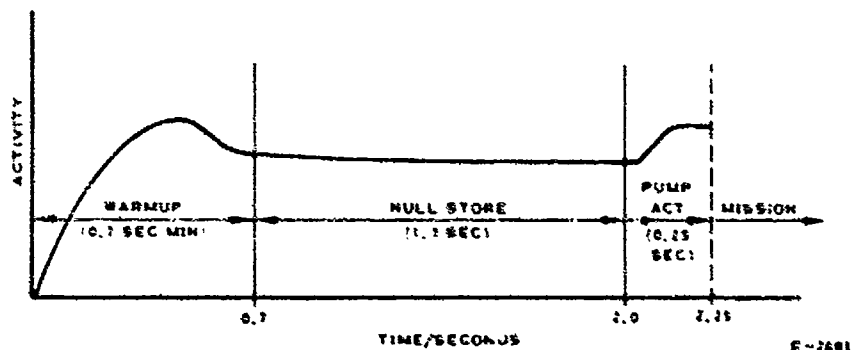


FIGURE 17 COPPERHEAD ACTIVATION SEQUENCE

Figure 18 presents a photograph of an oscilloscope trace showing the analog output of the sensor electronics as a function of time when the sensor is turned on in the presence of $1000^{\circ}/\text{sec}$ CW and CCW rates. The sudden change in output level shown in Figure 18 represents the onset of stable flow conditions. The application of power at the pump site is indicated by the "tick" marks at the lefthand side of the trace. Each major horizontal division represents a 5 msec interval. This data clearly shows that pump startup is accomplished in a 25-30 msec period. The time interval between the end of null store and the application of power at the pump represents the time required for the system software to execute the pump on command based on the current software executive/programming mechanization.

V₁ TURN ON VS. NULL STORE END

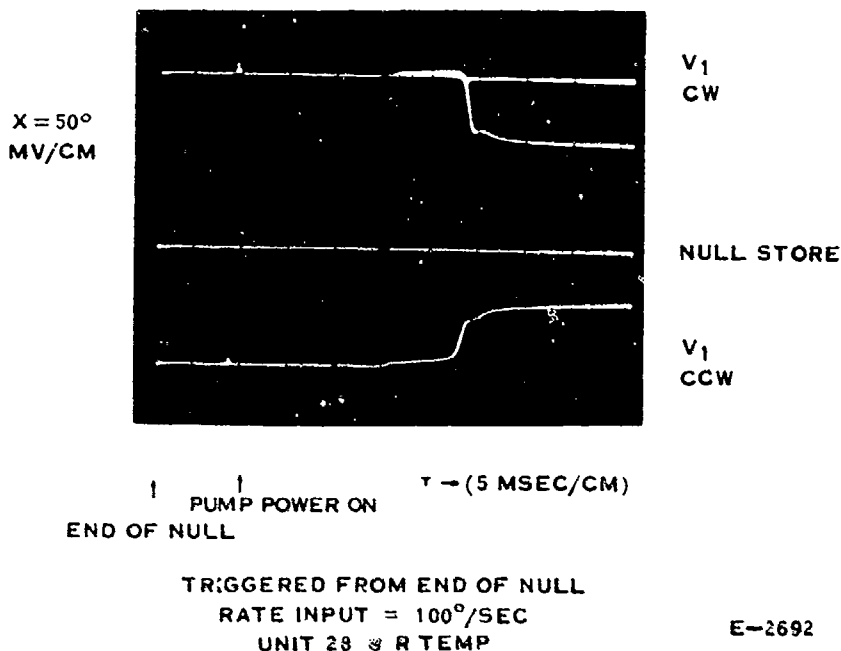


FIGURE 18 SUPERJET™ PUMP TURN ON PERFORMANCE

The remaining two elements of the turn on cycle are interrelated. The time required to perform the null store function is governed by the following factors:

- The ability to establish and maintain stable operation conditions during the null store,
- The noise level present in the circuit,
- The ambient motion environment present at the time of null store,
and
- The algorithms and processing cycle time required to execute the null store computations.

The establishment of stable operating conditions after the initial application of power to the Superjet™ Sensor is principally determined by the transient response of the sensor plug wires in reaching steady state operating temperature.

The current Copperhead turn on time profile specification shown in Figure 17 strongly reflects Copperhead mission imposed operating sequence constraints rather than the true performance capabilities of the assembly as dictated by the physical design of the unit. For example, in the Copperhead application warmup power is applied to the sensor wires for a minimum 0.7 sec period prior to the application of power to the electronics and the initiation of the null store function. The allocated 1.3 sec null store time again reflects the Copperhead mission operating sequence. The 0.25 sec pump activation time is also a conservatively stated Copperhead dictated mission requirement.

An alternate startup procedure with a faster reaction time capability than the present Copperhead hybrid analog/digital circuit has been demonstrated in engineering development tests performed in support of other advanced application programs. In these tests, the warmup and null store functions were initiated simultaneously using units which were specifically sequenced and trimmed to perform the composite warmup/null store function in period ranging from 0.25 to 2.0 seconds. The data obtained indicated the ability to achieve a Copperhead static null accuracy level ($0.3^{\circ}/\text{sec}$) using a total 0.5 to 0.75 sec null storage period under laboratory ambient conditions.

Early initiation of the null store function as performed in the above tests, means that the null store function is being performed before thermal stabilization of the sensor wires has been achieved. The process must, consequently, rely on a functional extrapolation to steady state conditions. The success of this process is, in turn, dependent on the predictability and repeatability of the wire warmup process.

Two fundamental approaches can be made to lower the sensitivity of this technique to externally induced variations while reducing overall reaction time.

These are:

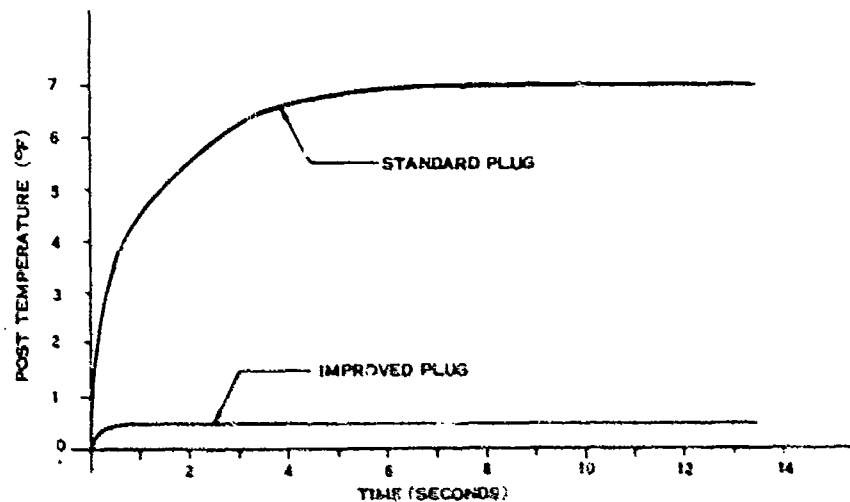
Reduction of warmup time requirements, and

Reduction of the time required to perform null store.

Improvement of the thermal response characteristics of the sensor plug can be used to either maintain the functional separation of warmup and null store functions or, alternately at a minimum, to reduce the range of extrapolation required during fast reaction turn on.

7.1.1 REACTION TIME IMPROVEMENTS

As an element of its on-going Superjet™ Sensor product improvement program, Hamilton Standard is developing an improved thermal characteristic sensor plug. The analytical design of the plug has been completed and several prototypes are currently being fabricated. It is anticipated that normal evaluation tests of this device, first as a separate subassembly and then as an element of a complete sensor, will begin soon. The predicted thermal response of the improved plug, expressed as the variation of wire support post temperature with time from power turn on, is presented in Figure 19.



* POST TEMPERATURE CHANGE ABOVE AMBIENT AT TIP OF POST

6-3184

FIGURE 19 SENSOR PLUG THERMAL RESPONSE

THE CACTUS ACCELEROMETER

by Alain Bernard*, Michel Gay** and Rémy Juillerat***

Office National d'Etudes et de Recherches Aérospatiales (ONERA)
92320 Châtillon (France)

ABSTRACT

The functioning of Cactus is based on the measurement of the force necessary to maintain a reference, or proof mass within a cage, without any material contact. This force is the resultant of three orthogonal, electrostatic attraction forces. Each of them is generated by an electronic circuit fed with the measure of the relative position of the proof mass within the cage. Each of these circuits thus ensures a servo-positioning function of the proof mass.

The whole apparatus being mounted on board a spacecraft, the forces that can create a relative movement of the proof mass within the cage are, on the one hand, the surface forces acting on the spacecraft and, on the other hand, the inertial forces resulting from the spacecraft movement about its centre of mass. The forces of the first kind are due to radiation pressure (of Sun and Earth), and to the drag resulting from the impact of gas molecules on the spacecraft surfaces. Those of the second kind can be minimized by a thorough centering and a sufficiently small amplitude of the spacecraft movement.

The apparatus permits the measurement of the resultant of these surface forces, this resultant being measured in terms of force per unit mass, or acceleration.

The resolution is 2×10^{-10} G and the bias 10^{-9} G

The overall qualification has been ensured in orbital flight by the Castor satellite launched by CNES, the French Space Agency, in June 1975.

1 - INTRODUCTION

The accelerometer called Cactus/a French acronym meaning Ultra-Sensitive, Three-axis, Capacitive Accelerometric Transducer) has been developed at ONERA with a view to space applications. It is a three-axis accelerometer, electrostatically suspended, whose resolution is of the order of 10^{-10} G (10^{-9} m/s²). It permits the measurement of all the forces, of an origin other than gravitational, acting on an artificial satellite, these forces being expressed in terms of accelerations sustained by the satellite.

Cactus has been qualified in 1975 [1]. It constituted the payload of the French satellite Castor, realized and launched by CNES, the French Space Agency. The lifetime in orbit of this satellite has been 45 months, during which the permanent operation of Cactus yielded a large number of scientific results.

The detailed observation of the operation of Cactus improved the knowledge of several parameters, of physical nature, which condition the instrument resolving power and bias. These results, and ensuing work on them, allowed the design of two new versions of this type of accelerometer :

- an accelerometer with higher resolution (project Super-Cactus).
- an accelerometer with linear response and shorter response time.

2 - WORKING PRINCIPLE OF ELECTROSTATIC ACCELEROMETERS

2.1 General

The principle consists in measuring the force developed by a three-axis electrostatic suspension to maintain a spherical proof mass (called "ball") at the centre of a cage, also spherical, solid with the satellite.

Considering the notations defined on figure 1, and calling :

m the ball mass,

$M-m$ the satellite mass,

\vec{F}_s the resultant of the surface forces acting on the satellite,

\vec{F}_a the resultant of the forces applied to the ball by the satellite,

\vec{g}_s and \vec{g}_b the accelerations imparted to the satellite and the ball by gravitational attraction, the equations governing the relative motion of these two bodies write, in the Galilean reference frame X, Y, Z :

$$\frac{d^2 \vec{r}_s}{dt^2} = \frac{\vec{F}_s - \vec{F}_a}{M-m} + \vec{g}_s$$

$$\frac{d^2 \vec{r}_b}{dt^2} = \frac{\vec{F}_a}{m} + \vec{g}_b$$

i.e.

$$\frac{d^2 \vec{GB}}{dt^2} = \frac{M \vec{F}_b - m \vec{F}_s}{m(M-m)} + \vec{g}_b - \vec{g}_s$$

*Research Subdivision Head, ONERA, **Research Group Head, ONERA, ***Research Division Head, ONERA

The distance GB is small enough for the difference $\vec{g}_B - \vec{g}_s$ to be negligible so that, in steady regime (GB constant), we only have :

$$\frac{\vec{F}_B}{m} = \frac{\vec{F}_E}{M} \quad (1)$$

So, the knowledge of \vec{F}_B makes it actually possible to determine, in these conditions, the resultant of the forces of non-gravitational origin acting on the satellite. It should however be noted that in reality the resultant of the force \vec{F}_U due to the electrostatic suspension and of disturbing or parasitic forces \vec{F}_P :

$$\vec{F}_B = \vec{F}_U + \vec{F}_P \quad (2)$$

Moreover, in the general case where the acceleration $\frac{d^2\vec{GB}}{dt^2}$ is not strictly negligible, it is convenient to express the ball-satellite relative motion in the G_{xy} reference frame related to the latter. Noting $\vec{\Omega}$ the instantaneous rotation of the satellite, and defining the following accelerations :

- inertial acceleration $\vec{\Gamma}_I$:

$$\vec{\Gamma}_I = \frac{M-m}{M} \left[\vec{g}_B + \vec{\Omega} \wedge (\vec{\Omega} \wedge \vec{GB}) + 2\vec{\Omega} \wedge \dot{\vec{GB}} + \ddot{\vec{GB}} \right] \quad (3)$$

- control acceleration $\vec{\Gamma}_U$:

$$\vec{\Gamma}_U = \frac{\vec{F}_U}{m}$$

- parasitic acceleration $\vec{\Gamma}_P$:

$$\vec{\Gamma}_P = \frac{\vec{F}_P}{m}$$

- external acceleration (to be measured) :

$$\vec{\Gamma}_E = \frac{\vec{F}_E}{M}$$

The measured acceleration finally writes :

$$\vec{\Gamma}_E = \vec{\Gamma}_U + \vec{\Gamma}_P - \vec{\Gamma}_I \quad (5)$$

The error $\Delta\vec{\Gamma}_E$ on the accelerometric measurement results from the uncertainty $\Delta\vec{\Gamma}_U$ on the calculation of the control accelerations (from the data transmitted to the ground), and on the estimation errors of accelerations $\vec{\Gamma}_P$ and $\vec{\Gamma}_I$:

$$\Delta\vec{\Gamma}_E = \Delta\vec{\Gamma}_U + (\vec{\Gamma}_P - \hat{\vec{\Gamma}}_P) - (\vec{\Gamma}_I - \hat{\vec{\Gamma}}_I)$$

2.2 Electrostatic force exerted on a conducting proof mass

The fundamental results concerning the charges, potentials and the electrostatic force exerted on an insulated conductor (the ball) by a system of electrodes set at various potentials are recalled below, using the notations of figure 2.

The cage, considered as the electrode of order zero, is the reference of the potentials ($V_i = 0$ for $i = 0$). Noting C_B the total capacitance of the ball relative to the cage and the electrodes :

$$C_B = C_0 + \sum_{i=1}^n C_i$$

the potential V is given by :

$$V = \frac{Q + \sum_{i=1}^n C_i V_i}{C_B} \quad (6)$$

and the electrostatic force exerted on the ball writes :

$$\vec{F}_U = \frac{1}{2} \sum_{i=1}^n (V - V_i)^2 \vec{\nabla} C_i \quad (7)$$

The only data available for calculating \vec{F}_U are, on the one hand, the voltages V_i transmitted by telemetry and, on the other hand, the values $\vec{\nabla} C_i$ of the gradients of the ball-electrodes capacitances resulting from the calibrations. As a consequence, the ball potential V , whose value can not be directly determined from these data, is subject to uncertainties that are to be minimized. To this end, the electrode arrangement must be such that the virtual charges ($\sum C_i V_i$) be zero, and that charge Q have a low value ($\approx 10^{-11}$ C). The latter condition leads to the choice of ball and cage materials presenting only a small contact potential difference, in order to limit the charge acquired at the rupture of electric contact between the two bodies. It is moreover necessary to periodically discharge the ball, by bringing it into contact with the cage, so as to eliminate the extra charges due to cosmic radiations whose energy is sufficient to cross the satellite and reach the ball [2].

2.3 Constitution of a servocentral channel

The electrostatic suspension of the proof mass is realized by three identical servocentral channels acting along the three axes of the instrument. Figure 3 represents the block diagram of one channel.

The cavity surrounding the proof mass is put in communication with free space in order to eliminate the damping action due to the presence of a gas in the ball-cage gap, as well as the pneumatic perturbations due to the presence of pressure gradients. In these conditions it is necessary, to obtain a stable suspension, that the values V_i of the potentials of the action electrodes be functions of the ball position and velocity relative to the cage. In this end, a capacitive transducer D provides, along each axis, a voltage proportional to the distance X of the ball to a reference point (origin O of the transducer), located as close as possible to the geometric centre of the cage and the electrodes. Damping is introduced into the feedback loop by the RC correcting circuit, whose output voltage is proportional to $(X + Y\dot{X})$. The time constant T is determined in such a way as to obtain the desired damping ratio.

The set of amplifiers AM finally delivers the voltages V_i to the action electrodes, and makes it possible :

- either to select, according to the sign of the signal ($\pm \tau \dot{z}$), the system of electrodes that should be polarized (the solution adopted on Cactus - see section 5);
- or to apply to the two opposed systems of electrodes voltages V_i whose amplitudes vary in opposite senses around a fixed polarization value V_0 (a solution envisaged for future projects - section 5) :

$$V_i = V_0 \pm K (\pm \tau \dot{z}) \tag{8}$$

K being a constant.

In all cases, the information delivered by the accelerometer (though the measuring amplifiers AM) is the values of the voltages V_i of the various action electrodes.

2.4 Precision of electrostatically suspended accelerometers

Considering the rough measurements only, the error writes :

$$\Delta \vec{\Gamma}_E = \vec{\Gamma}_p - \vec{\Gamma}_z + \Delta \vec{\Gamma}_0 \tag{9}$$

2.4.1 Contribution of the accelerometer to $\vec{\Gamma}_p$ (see Eqs. 2, 4).

Physical phenomena likely to provoke noticeable disturbances are many, if we consider the very high sensitivity expected for these accelerometers, and their measuring range [3]. That is why the assembly comprising the ball, the cage and the electrodes has been designed with a view to minimize these disturbances. In these conditions, experience showed that $\vec{\Gamma}_p$ results mainly from the residual of gravitational attraction of the ball by the masses of the accelerometer itself and the satellite as a whole. This residual, which corresponds to the defect of spherical symmetry of the distribution of these masses, can hardly be limited to less than $10^{-10}g$.

It should be noted that this acceleration is constant in a satellite-related reference frame, so that it is easy to have a precise estimate of it through observations in orbit.

2.4.2 Contribution of the accelerometer to $\vec{\Gamma}_z$ (see Eq. 3).

Remembering the definition of this acceleration, it is possible to separate it into two independent parts if we note that :

$$\vec{OB} = \vec{GO} + \vec{OB} = \vec{\lambda} + \vec{x}$$

which leads to setting :

$$\vec{\Gamma}_z = \vec{\Gamma}_{I\lambda} + \vec{\Gamma}_{Ix}$$

The inertial acceleration $\vec{\Gamma}_{I\lambda}$ is due to the off-centering $\vec{\lambda}$ and the angular motion $\vec{\Omega}$ of the satellite. To reduce this acceleration to low values, we must perform a strict centering of the satellite in orbit ($\vec{\lambda} \rightarrow 0$) and limit its spinning rate to values lower than 10^{-2} rad/s.

On the other hand, the inertial acceleration $\vec{\Gamma}_{Ix}$ is only due to the accelerometer. However, it is possible to show that in permanent regime ($\vec{\Omega}$ and \vec{V}_c constant in the absolute reference frame), the acceleration $\vec{\Gamma}_{Ix}$ is zero if the accelerometer presents three identical linear servocontrol channels. In case the servocontrols are not linear, $\vec{\Gamma}_{Ix}$ can always be brought back to acceptable values by lowering the satellite spinning rate Ω of the order of 10^{-3} rad/s). Thus, the dynamic perturbation $\vec{\Gamma}_{Ix}$ takes noticeable values only during the transient regimes corresponding to rapid variations of the acceleration $\vec{\Gamma}_0$ to be measured.

2.4.3 Uncertainty on the calculation of acceleration $\vec{\Gamma}_0$ developed by the electrostatic suspension :

The previously given expression of acceleration $\vec{\Gamma}_0$ (Eq. 1) :

$$\vec{\Gamma}_0 = \frac{1}{2m} \sum_{i=0}^2 (v-v_i)^2 \vec{V}C_i$$

can be developed so as to bring to light three terms :

$$\vec{\Gamma}_0 = \vec{\Gamma}_v + \vec{\Gamma}_{v^2} + \vec{\Gamma}_c$$

with

$$\vec{\Gamma}_v = -\frac{v}{m} \sum_{i=0}^2 v_i \vec{V}C_i$$

$$\vec{\Gamma}_{v^2} = \frac{v^2}{2m} \sum_{i=0}^2 \vec{V}C_i$$

$$\vec{\Gamma}_c = \frac{1}{2m} \sum_{i=0}^2 v_i^2 \vec{V}C_i$$

Accelerations $\vec{\Gamma}_v$ and $\vec{\Gamma}_{v^2}$ represent electrostatic perturbations, respectively linear and quadratic functions of the ball potential V. The last term, $\vec{\Gamma}_c$, represents the control acceleration actually calculated (from the voltages V_i transmitted by telemetry and the values of gradients $\vec{V}C_i$ provided by the calibrations).

Thus, the uncertainty on $\vec{\Gamma}_0$ is given by :
$$\Delta \vec{\Gamma}_0 = \vec{\Gamma}_v + \vec{\Gamma}_{v^2} + \Delta \vec{\Gamma}_c \tag{10}$$

i - Perturbation linear with the ball potential, \overline{V}

As far as the arrangement adopted for the accelerometer makes it possible to cancel out the virtual charges $\sum C_i V_i$ (Eq. 6), the ball voltage V is independent of the voltages V_i applied to the action electrodes. To get free of the disturbance \overline{V} , it then suffices :

- either to maintain at zero the sum $\sum V_i \overline{\nabla C_i}$ by using, on each half axis, two action electrodes supplied by continuous voltages of opposite signs (the arrangement adopted for Cactus),
- or to use action voltages V_i at high frequency and zero mean value (a solution envisaged, for instance, for Super-Cactus).

ii - Perturbation quadratic with the ball potential, $\overline{V^2}$:

The ball potential being practically :

$$V \approx \frac{Q}{C_B} \quad (\sum C_i V_i = 0)$$

this perturbation writes simply :

$$\overline{V^2} = \frac{1}{2m} \frac{Q^2}{C_B^2} \overline{\nabla C_B}$$

C_B being the ball capacitance relative to the cage and electrodes assembly, which almost possesses a spherical symmetry, the perturbation is zero ($\overline{\nabla C_B} = 0$) when the ball centre is at a point O_F , called force zero, and located close to the geometric centre of the cavity.

Noting $\vec{s} = \overrightarrow{OO_F}$, the linearization of the perturbation expression leads to :

$$\overline{V^2} = \beta Q^2 (\vec{x} - \vec{s}) \quad (11)$$

The scalar β , representative of the system geometry, is of the order of $4 \times 10^{13}/e$, where e is the ball-cage gap.

To minimize the electrostatic perturbation obtained for low acceleration levels ($\vec{x} \rightarrow 0$), a careful positioning of the detector's centre at the force zero must be ensured ($\vec{s} \rightarrow 0$).

iii - Uncertainty on the control acceleration : $\Delta \overline{a_c}$

In the absence of errors on the measurement of voltages V_i , the uncertainty $\Delta \overline{a_c}$ is given by :

$$\Delta \overline{a_c} = \frac{1}{2m} \sum_{i=1}^m V_i^2 (\overline{\nabla C_i} - \overline{\nabla C_{i,m}}) \quad (12)$$

where $\overline{\nabla C_{i,m}}$ are the values provided by the calibrations.

In reality, the noise of electronic origin issued from the detectors (circuits functioning at the lowest levels of voltage and intensity) propagates to the servoloops, and thus is responsible for an acceleration noise whose r.m.s. value σ_{a_c} determines the resolving power of the rough acceleration measurements. The evaluation of σ_{a_c} does not present any difficulty, account being taken of the detectors resolving power and of the transfer functions of the circuits. For the noise at low frequencies, the servocontrol can be represented by the diagram of figure 4.

The closed loop gain $\sigma_{a_c} / \sigma_{a_e}$ tends towards ω^2 when $\omega \rightarrow 0$ so that the noise spectral density intervenes essentially at the higher frequencies within the electronic circuits bandwidth. That makes this noise easy to filter during data processing, and makes it possible to exploit position measurements within less than $10^{-3} \mu\text{m}$ in spite of the low frequency noise generated by the sphericity defects of the ball ($10^{-1} \mu\text{m}$) in the presence of slow rotations of the ball relative to the cage.

2.4.4 Conclusion

We have seen that electrostatically suspended accelerometers make it possible to obtain, without any statistical processing, measurements of slowly variable accelerations ($\overline{a_c} \rightarrow 0$) with a very low bias (10^{-9} G for Cactus), and a resolving power of the order of 10^{-5} of the measuring range. As regards precision, it essentially depends on the calibration means implemented.

3 - CALIBRATION METHODS

3.1 Ground calibration of accelerometers

3.1.1 Ground measurement of capacitance gradients (fig. 5)

The ball is positioned in front of the system of electrodes to be calibrated, which is mounted on a support simulating the cage. The positioning bench allows in particular the ball displacement along the electrodes axis, ensuring a great stability of the ball electrode distance for all successive positions. For each position, the distance measurements (d along the displacement direction \vec{s}) are performed by a high resolution laser interferometer.

For each value of d , two capacitances are measured :

- one, noted C_M , is that of the electrode relative to the ball, the cage and the screen electrode taken together ;

- the other, noted C_I , is that of the electrode relative to the ball only advantage being taken of using a screen electrode to implement an "in situ" measuring technique.

These two sets of measurements allow the definition, by identification, of two functions :

$$C_n = f_n(d) \quad \text{and} \quad C_I = f_I(d)$$

As there is not, strictly speaking, a total influence between electrode and ball, $\vec{\nabla} C_n$ is the capacitance gradient to be considered for the calculation of the electrostatic force. The function allows the calculation of this gradient :

$$\vec{\nabla} C_n = g_n(d)$$

Furthermore, to use these results it is necessary to be able to identify with great precision the value of d corresponding to the operational arrangement of the ball-cage-electrodes assembly, and to the positioning of the origin of the position detector in this assembly. This possibility is provided by the measurements of $C_I (= f_I(d))$, that are independent of the spurious capacitance values obtained in the various mountings.

The distance d is defined by the inverse function of f_I :

$$d = f_I^{-1}(C_I)$$

It is difficult to evaluate the error on the gradient measurement, as this is essentially conditioned by the choice of the models (functions f_n and f_I). For Cactus, designed before 1975, this error was lower than 10^{-2} ; but, considering the improvements brought to this method since then [4], a precision of 10^{-3} can reasonably be expected.

3.1.2 Overall tests of accelerometers in the ONERA weightlessness facility

ONERA has at its disposal, at Chatillon near Paris, a vertical tube 40 m high and 0.75 m in diameter, where the drop duration is 2.9 seconds [5]. A set of primary and diffusion pumps makes it possible to reduce the pressure inside this tube to 10^{-5} mbar, which limits at $10^{-7}G$ the aerodynamic drag of the capsule during the drop.

The accelerometer to be tested is mounted inside the capsule so that two of its axes are horizontal. The external disturbances acting along these two axes are then very small, of the order of a few $10^{-9}G$.

The weightlessness facility is the only means for testing the operation of ultra-sensitive accelerometers, because the maximum measurable acceleration is very small as compared to the Earth gravity.

A test consists in analyzing the operation of the electrostatic suspension during the drop duration. The main difficulty results from the limitation at 2.9 seconds of the test duration, while accelerometers such as Cactus have response times of the order of 5 seconds. This difficulty can be somewhat overcome by equipping the accelerometer with electronic circuits delivering higher voltages, so that testing takes place within a less sensitive range (e.g. $10^{-4} - 10^{-9}G$) within which response times are much smaller.

The test capsule is also equipped with a device for positioning the accelerometer proof mass at the cage centre from the beginning of the test : for this, it suffices to provoke, by displacement of a small mass inside the capsule, a rapid translation of the capsule centre of mass in the drop direction. The proof mass which, at the start, was resting on the cage, is thus brought to the cage centre if the device is so designed that the translation amplitude is equal to the ball-cage gap of the accelerometer under test.

In spite of these arrangements, the accelerometer can only be tested in transient regime. The recording of all measurements provided by the instrument during the test makes it possible, by comparison with results of numerical simulations taking into account all the test conditions, to make sure of the coherence of its operation. This method permits the discovery of any defect likely to affect the operation of the instrument, and expressed by perturbing accelerations as low as $5 \cdot 10^{-9}G$.

3.2 In-orbit overall calibration of the accelerometer

The in-orbit characterization of the accelerometer aims at :

- checking the value of the calibration coefficients (coefficients corresponding essentially to the values of the gradients $\vec{\nabla} C_i$ of the electrode-ball capacitances),
- estimating of the biases of the instrument : the estimation error of these biases constitutes the threshold of the accelerometer.

The principle adopted for the calibration consists in creating a known inertial acceleration $\vec{\Gamma}_{I\lambda}$, by imposing to the satellite a high spinning rate Ω and creating a known off-centering $\vec{\lambda}$ along the axis to be calibrated.

To calibrate the axis \vec{x} for instance (fig. 6), the rate Ω is imposed by the start of the rotation of a wheel around axis \vec{z} (or \vec{y}), and off-centering $\vec{\lambda}$ is obtained by displacement of a small mass along \vec{x} over a known distance.

Supposing Ω and $\vec{\lambda}$ constant, we have :

$$\vec{\Gamma}_{I\lambda} \approx \frac{M-m}{M} [\Omega^2 \lambda] \vec{x}$$

This acceleration can be calculated with a good precision, knowing $\vec{\lambda}$ by measurement of the small mass position, and $\vec{\Omega}$ from the values provided by the satellite attitude restitution. However, the calibration is carried out in the presence of accelerations other than \vec{V}_A :

$$\vec{V}_0 = (\vec{V}_E + \vec{V}_{I_x} - \vec{V}_P) + \vec{V}_{I_A}$$

The principal errors are due to the variations of acceleration \vec{V}_E , of which we have precise measurements only before and after the calibration operation.

So, to minimize calibration errors, it is advisable to carry out these operations when \vec{V}_E is minimum (at apogee, in the Earth Shadow), and to choose Ω and λ in such a way that acceleration \vec{V}_{I_A} is close to the maximum value allowed to the accelerometer.

Estimation of the biases is obtained by statistical processing of the measurements. The principle rests on the fact that, in the accelerometer frame of reference, the biases are expressed by constant accelerations, while the external acceleration \vec{V}_E rotates, in this reference frame, at the satellite spinning rate. Whatever the method used, it is thus mandatory to have available batches of measurements which, for a same value of external acceleration (e.g. at apogee in the shadow), correspond to sufficiently varied attitudes of the satellite.

These principles have been applied for the in-orbit calibration of Cactus. Obviously, they can only be used if the satellite carrying the accelerometer has been designed accordingly.

4 - THE CACTUS ACCELEROMETER

4.1 Description and performance

The inertial mass, of spherical shape, is made of platinum-rhodium alloy; it has a diameter of about 4 cm, a mass of 600 g, and is coated with a 2- μ m thick gold deposit. The shape defects, expressed in difference of sphericity, are lower than 0.1 μ m.

The cage surrounding this ball is made of a stainless alloy, also gold plated. The gap between ball and cage is 85 μ m wide, and their maximum relative displacement, corresponding to the highest accelerations applied, is 10 μ m.

This displacement is measured, on each of the three orthogonal axes, by a pair of electrodes making up, with the ball, a capacitive bridge. The resolution of the position transducer is 10^{-3} μ m, and its stability 7.10 $^{-3}$ μ m per degree C of temperature variation. The position detection electrodes are concentric with the electrodes developing the control forces of electrostatic nature, called "action" electrodes (fig. 7). For reasons of electrostatic balance (see section 2.2 and Eq. 6), these latter electrodes are supplied, on each half-axis, by two equal voltages of opposite sign.

The two electrodes of each half-axis being supplied or not according to the sense of displacement of the ball, there results that the relation between the component along the axis considered (e.g. x) of the control acceleration, \vec{V}_{C_x} , and the value of the two voltages applied, $+V_x$ and $-V_x$, is of quadratic form. This conformity law leads to a dynamic response which depends on the level of acceleration applied. Figure 8 gives the responses of the instrument, expressed as the ratio between the instantaneous value of the measured acceleration \vec{V}_S and that of the applied acceleration \vec{V}_E , for three steps of applied acceleration, equal respectively to 10^{-8} , 10^{-7} and 10^{-6} G.

Cactus presents itself as a self-contained assembly, comprising the cage with the ball, the servocontrol electronic circuits, those for conditioning the measuring signals, and the tubes connecting the inside of the cage to the space vacuum. A mechanical support used as a reference makes it possible to place, during its mounting, the ball centre reference as close as possible to the satellite centre of mass.

The nominal characteristics of Cactus are as follows:

. Measuring range (modulus of acceleration vector)	10 $^{-5}$ G
. Bias	lower than 10 $^{-9}$ G
. Resolution (at low accelerations)	2x10 $^{-10}$ G
. Conformity law	quadratic
. Precision of sensitivity coefficient (error from conformity law)	10 $^{-2}$
. Response time at 5% :	
- at low accelerations	6 sec
- at high accelerations	2 sec
. Domain of no damage	5 G
. Electric consumption	2 W
. Operating temperature	- 20 to + 40°C
. Mass	10 kg
. Volume	10 dm 3

4.2 Scientific results obtained on board the Castor satellite

The orbit of the Castor satellite had a perigee of 270 km and an apogee of 1200 km, with an inclination of 30° on the equatorial plane. The forces acting on the satellite, and measured by Cactus in terms of acceleration, comprised on one hand the atmospheric drag and, on the other hand, radiation

pressures, viz. those due to the direct solar radiation, the solar radiation backscattered by the Earth, the thermal radiation of Earth, and the anisotropic thermal radiation of the satellite, whose surface temperatures were widely different between the lighted zone and the opposite side.

From the knowledge, at any time, of the satellite position along its orbit, as well as of its attitude, it has been possible to separate the components of these various accelerations, as well as those due to the biases of the instrument. The data processing method, developed by the Centre for Geodynamic and Astronomic Studies and Research, Grasse, Southern France, made it possible to exploit a resolution of :

- 10^{-10} G for any individual measurement of low acceleration (lower than 10^{-8} G),
- 10^{-11} G by statistical processing of a large number of measurements (also for accelerations lower than 10^{-8} G).

The few following results are given as examples :

- Atmospheric density [6]. Figure 9 represents the curves of equal value of the ratio : observed density/theoretical density, the latter being that given by the Jacchia model 74 [7]. The measurements revealed density variations as a function of longitude, that the theoretical models did not mention.

- Earth infrared radiation [8]. Figure 10 presents a histogram traced from the mean values from the acceleration due to this radiation, and taken on 211 arcs of orbit, of 5 minutes duration each. The dispersion observed results not only from the measurement uncertainties, but above all from the differences of thermal emission of the overflow zones (oceans, continents, cloud covers). More detailed processings revealed systematic differences between oceans and continents, or between equatorial and tropical zones, and these differences are in good agreement with radiometric measurements from space.

- Own thermal radiation of the satellite [8]. The anisotropy of this radiation is emphasized on figure 11, which presents the decrease of the corresponding acceleration when the satellite enters the Earth shadow. This decrease is due to the re-equilibration of the surface temperatures following the disappearance of solar radiation.

5 - FURTHER PROJECTS

5.1 The Super-Cactus project

A study carried out on request from the European Space Agency showed the feasibility of a new generation of this type of accelerometer-called Super-Cactus- , with a precision improved tenfold [9]. Its main expected characteristics are as follows :

. Measuring range	10^{-7} G
. Bias	10^{-11} G
. Resolution	$2 \cdot 10^{-11}$ G
. Response time at 1%	17 sec
. Electric consumption	3 W

The structure planned for Super-Cactus is very similar to that of Cactus, the sensitivity increase being obtained by :

- new electronic circuits for the capacitive measurement of the relative position of the ball, characterized by a better thermal and temporal stability ;
- a new technology for the construction of the cage, increasing its dimensional stability ;
- an optimization of the characteristics of the position servocontrol for a measuring range shifted towards lower accelerations.

Super-Cactus has been designed with a view to constitute the payload of a satellite measuring the Earth radiation budget (project Biramis, of ESA). It is shown that, if the satellite has a spherical shape and if its surface displays certain thermo-optical properties, the acceleration imparted on it under the influence of the radiation pressures of various sources constitutes a vector measurement of the local resultant of the energy fluxes emitted respectively by these sources. An appropriate processing of this vector would yield the determination of the energy exchange between Earth and space at all points of the orbit. Moreover, a statistical processing of measurements issued from several satellites of the same nature would make it possible to calculate the global radiation budget of the Earth, a fundamental value in climatology [10].

5.2 Projects of accelerometers with linear response

The experience acquired with Cactus and the progress achieved at ONERA in the field of capacitive metrology open the way to the concept of three-axis electrostatic accelerometers with a linear response, adapted to the measurement of accelerations lower than 10^{-3} G.

A measuring range from 10^{-3} G to 10^{-7} G can be envisaged, in particular for space applications, as, on one hand, these values correspond to the accelerations obtained in "laboratory satellites" and, on the other hand, the accelerometers developed for inertial navigation are poorly adapted to operate in this range, where their precision and their resolution are insufficient. For the electrostatically suspended accelerometer, the expected precision is 10^{-3} , which corresponds to the present possibilities for measuring the gradients of the ball-electrode capacitances. The resolution depends on the filtering performed on the measurements, but would any way be better than 10^{-7} G.

In spite of the polarization voltages V_0 to be applied to the action electrodes in order to obtain a linear characteristic, the resulting bias is expected to be lower than $3 \times 10^{-6}g$, with a stability of $10^{-7}g$. As compared with Cactus, the sensitivity of these accelerometers would be lower, but on the other hand their responses would be faster : 0.2 sec for the response time at 1% to an acceleration step (which corresponds to a natural frequency of the order of 5 Hz).

REFERENCES

- 1 J. Bouttes, M. Delattre, R. Juillerat
Qualification in Orbital Flight of the Cactus High Sensitivity Accelerometer - ONERA T.P. 1976-66E.
- 2 R. Juillerat, J.P. Philippon
Electrification of the proof mass of a drag free or accelerometric satellite - Spacecraft Charging Conference - Colorado Springs (Oct. 76). ONERA T.P. 1976-150
- 3 R. Juillerat
Analyse des limitations physiques des accéléromètres pour sonde spatiale et des détecteurs de sonde à traînée compensée.
(Analysis of the Physical limitations of accelerometers for space probe and of detectors of drag - free probes) Proceedings of the International school of physics - Varenne, Italy, July 1972. Academic press - 1974 - pp. 449-487.
- 4 M. Gay
La métrologie mécanique de précision par moyens capacitifs.
(High precision mechanical metrology by capacitive means) - Revue Française de Mécanique n° 64-1977 pp. 9-18 T.P. 1978-115.
- 5 J. Beaussier
Essais en Impesanteur effectués à l'ONERA
(Weightlessness tests carried out at ONERA) Aéronautique et Astronautique n° 56 - 1976-1 pp. 41-45 T.P. 1975-126.
- 6 F. Barlier, C. Berger, J.L. Falin, G. Kockarts, G. Thuillier
Atmospheric Models based on Satellite Drag Data - Annales de Géophysique n° 34 (1978) p.9.
- 7 L.G. Jacchia
Models of atmospheric - SAO Report n°332 (1971).
- 8 Y. Boudou, F. Barlier, A. Bernard, R. Juillerat, A.M. Mainguy, J.J. Welch
Synthèse des résultats en vol de l'accéléromètre Cactus pour des accélérations inférieures à $10^{-9}g$.
(Synthesis of in-orbit results of the Cactus accelerometer for accelerations lower than $10^{-9}g$) - Acta Astronautica, Vol. 6 n° 11, p. 1387-1398 (1979) - Also Rech. Aerosp. n° 19/8-6, p. 335-342.
- 9 A. Bernard, M. Gay, A.M. Mainguy
Super-Cactus Project of $10^{-11}g$ Three-axis accelerometer - XXX IAF Congress Munich 16-22 Sept. 1979) T.P. 1979-124.
- 10 A.M. Mainguy, A. Bernard, M. Romero, J. Bouttes and F. Barlier
Biramis : mesure du bilan radiatif de la terre par microaccélérométrie spatiale (Biramis : Direct measurement of the Earth radiation budget by means of an accelerometer). La Recherche Aérospatiale n° 1979-6, p. 349-354. English translation ESA-TT, to appear.

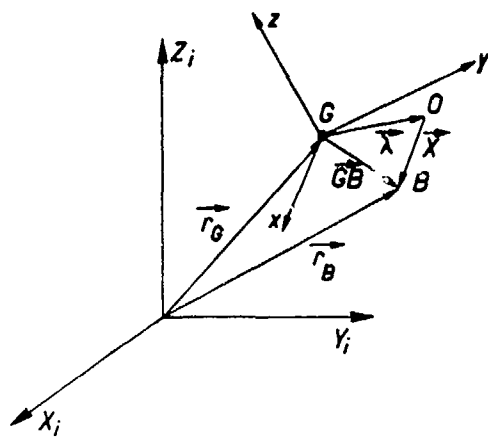


Fig. 1 - Definition of the geometric variables
 X_i, Y_i, Z_i : Galilean reference frame
 $G \approx y_B$: satellite-related reference frame
 G : satellite centre of mass
 O : origin of position detector
 B : ball centre of mass
 $\lambda = \overrightarrow{GO}$: off-centering
 \overline{X} : measured position of the ball.

Fig. 2 - Electrostatic force : notations

- C_0 : ball-cage capacitance
- C_i : capacitance of electrode relative to the ball
- V_i : potential of electrode
- ∇C_i : gradient of capacitance
- Q and V : charge and potential of the ball.

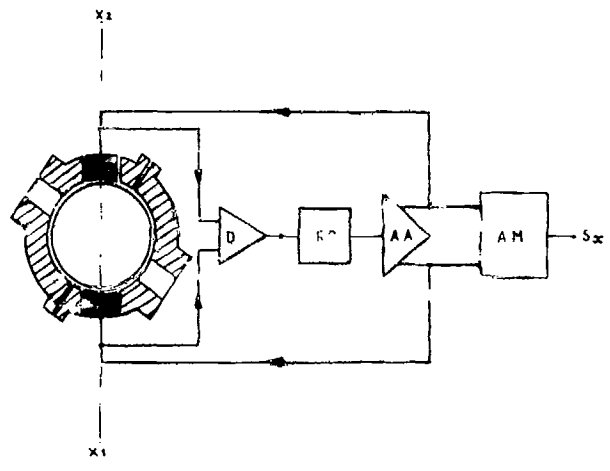
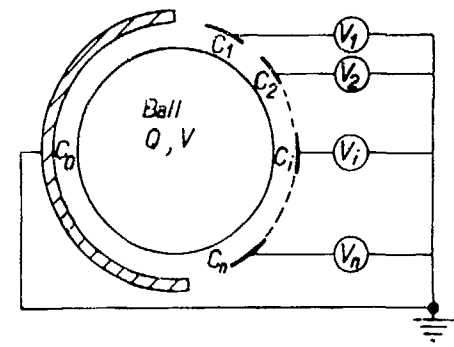


Fig. 4 - Servocontrol diagram for low frequencies

Fig. 3 - Block diagram of one servo-control channel

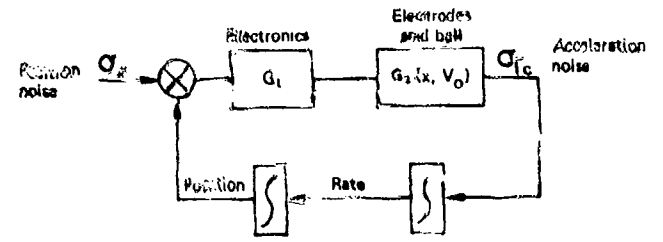
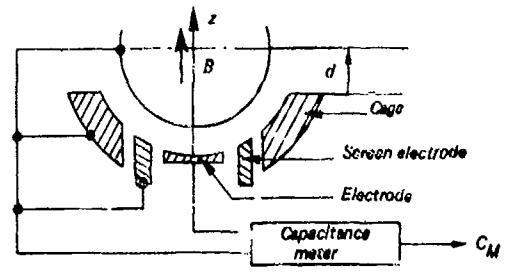


Fig. 5 - Measurement of gradients



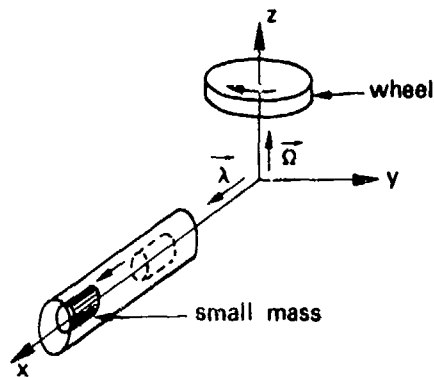


Fig. 6 - Principle of in-orbit calibration.

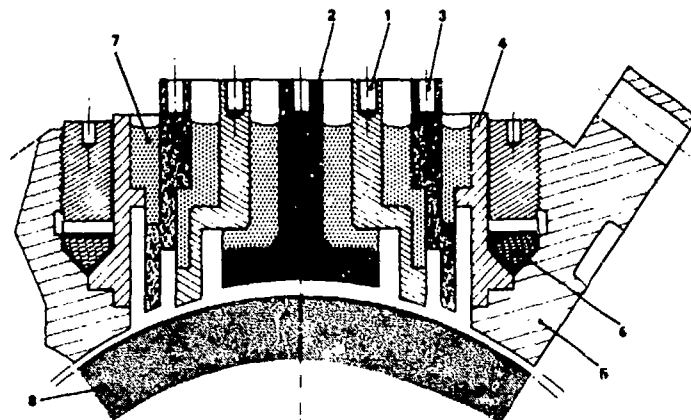


Fig. 7 - Cross-section of a system of electrodes

- 1 - Detection electrode
- 2, 3 - Action electrodes
- 4 - Body of supporting plug
- 5 - Body of cage
- 6 - Air tightness joint
- 7 - Insulation
- 8 - Inertial mass (ball)

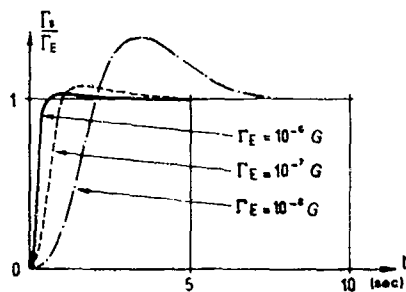


Fig. 8 - Responses to acceleration steps

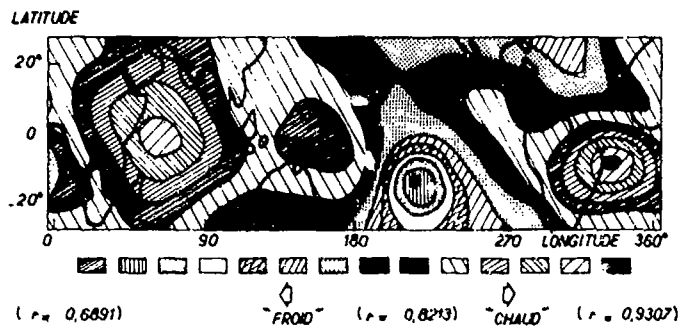


Fig. 9 - Measurements of atmospheric density between 30° latitude South and 30° latitude North, and comparison with a theoretical model of atmosphere

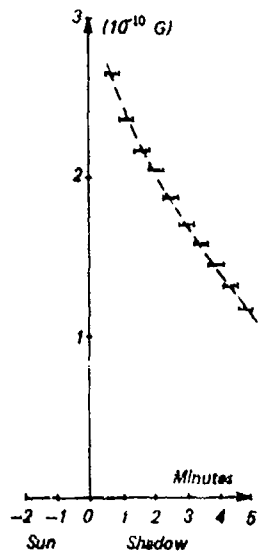


Fig. 11 - Component of the measured acceleration, along the axis of thermal thrust, when the satellite enters the Earth shadow (measurements averaged over short time intervals)

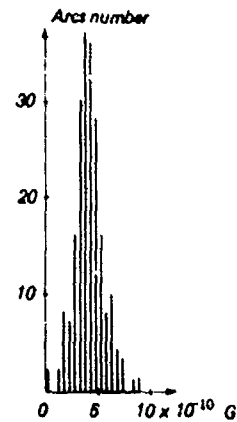


Fig. 10 - Histogram of the accelerations applied to the satellite and due to the Earth infrared radiation. Statistics on 211 arcs of orbit

INERTIAL SYSTEM ALIGNMENT AND CALIBRATION
ON A MOVING BASE

Mario B. Ignagni
Honeywell Inc.
Systems and Research Center
2600 Ridgway Parkway
Minneapolis, Minnesota, USA 55413

SUMMARY

The problem of optimally aligning and calibrating an inertial navigation system on a moving base is addressed. A comprehensive solution to this class of problems is given and shown to be optimal, subject only to structural constraint normally imposed by practical implementation limitations.

1. INTRODUCTION

The alignment and calibration of an inertial navigation system, while on a moving base, represents an important class of problems encountered in both air-launched and ship-launched vehicle applications. The problem of interest is that of optimally establishing a slave inertial system's attitude, velocity, and position relative to a geographic navigational reference frame, and an estimate of its sensor calibration errors, by means of information obtained from a master navigation system aboard the transport vehicle. The master navigation system may, in general, be aided from some external source of navigation information and may also be of a different generic type than the slave (such as a platform master system and a strapdown slave system). Aiding of the master system and transfer-alignment/calibration of the slave system are assumed to be carried out utilizing Kalman estimation techniques.

The solution to be developed assumes that the aided master system is completely independent of the slave system during the transfer-alignment/calibration process. This is a reasonable assumption from two points of view. First, the slave system is generally of lower precision than the master and, hence, would contribute little or no improvement to the estimation accuracy of the master's errors. Second, if the master system's Kalman estimator were generalized to include information from the slave system, the dimension of the resultant estimator would be prohibitively large, since all of the slave's error states would of necessity have to be augmented to those of the master.

The solution given is based on the idea that, as a first step, the alignment and calibration of the slave system can be carried out as though the master system were error free. Then, as a second step, the alignment and calibration of the slave can be refined by introducing the master system's estimate of its own errors into the process. This two-step procedure is shown to yield an optimal result subject to the structural constraint defined above.

The transfer-alignment/calibration process is specifically defined, in the development to follow, for the case of velocity matching. However, this is not an inherent limitation since, in general, the method allows both attitude and position matching to be incorporated as well, either singly or in combination with velocity matching.

2. NAVIGATION ERROR MODEL

The navigation error model assumed in the development is a "†-angle" formulation, which is a classic set of navigation error equations applicable to all mechanization options (Reference 1). The † angle error model may be expressed in the following form

$$\dot{\dagger} = \epsilon_g - (\rho + \Omega) \times \dagger \quad (1)$$

$$\begin{aligned} \delta \dot{V} = \epsilon_a - \dagger \times A^L - (2\Omega + \rho) \times \delta V - \omega_g^2 \delta R \\ + 3\omega_g^2 (\delta R \cdot R / |R|) R / |R| + \delta g \end{aligned} \quad (2)$$

$$\delta \dot{R} = \delta V - \rho \times \delta R \quad (3)$$

where

- † = attitude error vector
- δV = velocity error vector
- δR = position error vector
- ρ = angular velocity vector of local-vertical reference frame relative to an earth-fixed frame

- Ω = angular velocity vector of the earth relative to an inertial frame
 A^L = vehicle non-gravitational acceleration
 R = radius vector from earth's center to vehicle
 ω_g = schuler frequency = $\sqrt{g/R}$
 ϵ_g = angular rate error due to gyro errors
 ϵ_a = acceleration error due to accelerometer errors
 δg = error in computed plumb-bob gravity vector

It is assumed that all vectors are expressed with components in the local-vertical navigation reference frame.

The vectors ϵ_g and ϵ_a may be further expressed in terms of individual sensor errors as

$$\epsilon_g = T_g M_g \delta \omega_g$$

$$\epsilon_a = T_a M_a \delta A_a$$

where

$\delta \omega_g$ = vector of gyro errors (bias plus random noise)

δA_a = vector of accelerometer errors (bias plus random noise)

T_g = transformation matrix relating gyro reference axes to the local-vertical frame

T_a = transformation matrix relating accelerometer reference axes to the local-vertical frame

M_g = coefficient matrix which transforms the collection of gyro errors into a net angular rate error in the gyro reference axes

M_a = coefficient matrix which transforms the collection of accelerometer errors into a net acceleration error in the accelerometer reference axes

For the purposes of the discussion to follow, the generalized navigation error model will be written in the following discretized form [Reference 2]:

$$x_n = A_n x_{n-1} + B_n b_n + \delta g_n + \xi_n \quad (4)$$

$$b_n = F_n b_{n-1} + \mu_n \quad (5)$$

where x is the vector of navigation errors defined by

$$x = (\delta V \ \delta R)^T$$

and

b = vector of sensor bias errors

ξ, μ = random vector sequences uncorrelated in time and with respect to each other

n = iteration designator

with A , B , and F being time-variant coefficient matrices. An important property of the error model which will be utilized to advantage is that, regardless of the mechanization option (i. e., strapdown, platform, ESG), the coefficient matrix A is always the same. This is, however, not true of the matrix B , which is strictly determined by the particular mechanization option. These properties, which may be inferred directly from equations (1), (2), and (3), are discussed at length in Reference 3. It will also be noted from (5) that in the general case, provision is made for time-correlated sensor biases (i. e., Gauss-Markov process).

The generic error model given by (4) and (5) will be utilized in the treatment of both the master and slave systems which follow.

3. THE AIDED MASTER NAVIGATION SYSTEM

The master navigation system is assumed in general to have access to external aiding information, such as that provided by the Global Positioning System (GPS) or LORAN, and to possess the computational capability to optimally utilize this aiding information, which means, in the latter instance, that the master navigation system has its own dedicated Kalman estimator to allow continual update of its navigational states and sensor calibration coefficients.

The navigational error model for the master system is taken from (4) to be defined by

$$x_n^m = A_n^m x_{n-1}^m + B_n^m b^m + \delta g_n \quad (6)$$

where it is assumed that the master's bias vector (b^m) is essentially constant and that the vector ξ (arising from sensor random noise) is absent or ignorable. Both of these restrictions are generally satisfied in high-precision navigation systems, and it may be presumed that the master navigation system would normally be a member of such a class of systems.

The measurement equation for the master navigation system can be written in the following generalized form

$$y_n^m = H_n^m x_n^m + H_n^r r_n + \eta_n^m \quad (7)$$

where

y^m = measurement vector for the master system

x^m = vector of master system's navigational errors

r = vector of error states associated with the external aid and gravity error model

H^m, H^r = observation matrices

η^m = observation noise vector

All of the states associated with the aided master system can be adjoined to form the state vector, z , defined by

$$z = (x^m \ b^m \ r)^T$$

which may be recursively estimated by means of the conventional Kalman estimator (Reference 4):

$$\hat{z}_n^- = \Phi_n \hat{z}_{n-1} \quad (8)$$

$$P_n^- = \Phi_n P_{n-1} \Phi_n^T + Q_n \quad (9)$$

$$K_n = P_n^- L_n^T (L_n P_n^- L_n^T + R_n)^{-1} \quad (10)$$

$$\hat{z}_n = \hat{z}_n^- + K_n (y_n^m - L_n \hat{z}_n^-) \quad (11)$$

$$P_n = (I - K_n L_n) P_n^- \quad (12)$$

where

\hat{z}_n^-, \hat{z}_n = a priori and a posteriori estimates of z at the n th update point

P_n^-, P_n = a priori and a posteriori estimation error covariance matrices at the n th update point

Φ_n = state transition matrix from $(n-1)$ th to n th update points

K_n = gain matrix

L_n = observation matrix

Q_n = process noise covariance matrix

R_n = observation noise covariance matrix

The estimation error covariance matrix of z is defined in partitioned form as

$$P = \begin{bmatrix} P_{xx}^m & P_{xb}^m & P_{xr}^m \\ P_{xb}^{mT} & P_b^m & P_{br}^m \\ P_{xr}^{mT} & P_{br}^{mT} & P_r^m \end{bmatrix}$$

with the matrices Φ , L , Q , and K being partitioned in like manner.

The Kalman estimator for the master system will, as noted earlier, be taken as completely independent of the slave system; that is, no information from the slave system will be assumed to enter into the estimation of the master system's states.

4. TRANSFER-ALIGNMENT/CALIBRATION OF THE SLAVE NAVIGATION SYSTEM

4.1 Initialization of the Slave System

The slave navigation system is normally initialized by a direct transfer of navigational information derived from the master system. The master's velocity and position components in the local-vertical reference frame are transferred directly into the slave, after being suitably adjusted for the known separation between the two systems. The initial attitude of the slave system is derived from the master's knowledge of vehicle attitude and the approximately-known attitude of the slave system relative to the vehicle frame. The initialization process defined results in initial slave velocity, position, and attitude errors which are equal to the corresponding errors in the master system, plus the relative errors arising from vehicle flexure, the uncertainty in the slave's attitude relative to the vehicle frame, and the uncertainty in the displacement between the master and slave systems.

4.2 The Measurement Process

The slave navigation system is assumed to be aligned and calibrated by velocity matching with the master system, utilizing its own dedicated Kalman estimator. The measurement equation for the slave system is defined for the velocity-match process as follows

$$y^s = V^m + \hat{V}_L - V^s \quad (13)$$

where

V^m = velocity vector computed by master navigation system

V^s = velocity vector computed by slave navigation system

\hat{V}_L = lever-arm velocity correction

= $\omega \times \ell$

and

ω = vehicle angular velocity vector

ℓ = displacement vector between master and slave navigation systems

The measurement equation may be expanded by utilizing the following relationships

$$V^m = V_o + \delta V^m \quad (14)$$

$$V^s = V_o + V_L + V_d + \delta V^s \quad (15)$$

where

V_o = true vehicle velocity at master navigation system location

V_d = extraneous velocity at slave navigation system location due to vehicle flexure

δV^m = velocity error of master navigation system

δV^s = velocity error of slave navigation system

Utilizing Equations (14) and (15) in (13) yields the following form for the velocity-match measurement equation processed by the slave Kalman estimator (assuming a perfect V_L correction):

$$y^s = \delta V^m - \delta V^s - V_d$$

Before differencing master and slave velocities, and processing through a Kalman estimator, it is possible to prefilter each set of velocity measurements to remove, to a large degree, the effect of the flexure-induced velocity (V_f). Prefiltering is commonly utilized to advantage in Kalman estimator designs when measurements are available at a much higher rate than it is possible or desirable to process them. A convenient type of prefilter to employ, when the measurement is corrupted primarily by high-frequency noise, is a first-order lag. The time constant of the lag can be chosen to produce a desired degree of attenuation of the noise in the measurement, while leaving the signal component essentially unaltered. Furthermore, if the Kalman estimator update interval is on the order of two or more times greater than the natural period of the flexure motion, the prefiltered measurement noise may be accurately represented at the Kalman estimator update points by an uncorrelated random sequence [Reference 5]. Therefore, it will be assumed that the series of measurements utilized in the velocity-match Kalman estimator can be faithfully represented by

$$y_n^s = \delta V^m - \delta V^s + \eta_n^s \quad (16)$$

where η_n^s is an uncorrelated random sequence.

4.3 The Differential-State Estimator

From the generic form of the navigation error model given by (4) and (5), error propagation in the slave system is taken to be defined in general by

$$x_n^s = A_n x_{n-1}^s + B_n^s b_n^s + \delta g_n + \xi_n^s \quad (17)$$

$$b_n^s = F_n^s b_{n-1}^s + \mu_n^s \quad (18)$$

It is clear, therefore, that the difference between the master's and slave's navigational errors, defined by

$$\Delta x = x^m - x^s$$

can be completely determined by subtracting equation (17) from (6), to yield the result

$$\Delta x_n = A_n \Delta x_{n-1} - B_n^s b_n^s + B_n^m b_n^m - \xi_n^s \quad (19)$$

in which the absence of the gravity error, δg , will be noted.

Returning to the velocity-match measurement equation, it is evident that the following alternate formulation is possible

$$y_n^s = H (\Delta x \ b_n^s)^T + \eta_n^s \quad (20)$$

where H is the observation matrix defined by

$$H = [H_x \ 0]$$

and

$$H_x = [0 \ 1 \ 0]$$

A velocity-match Kalman estimator can be predicated on the basis of (18) and (19) defining the state equations, and (20) providing the measurement relationship. A complication arises, however, due to the presence of the master's bias vector, b^m , in the state equations. A unique method of dealing with biases in Kalman estimators has been suggested by Friedland in Reference 6, and some essential elements of this method can be incorporated into the transfer-alignment problem. The following development utilizes the central idea of Friedland's method in a modified form more suited to the problem at hand.

4.4 The Bias-Free Estimator of Δx and b^s

Suppose that the master's bias vector b^m is ignored (that is, assumed to be zero) in (19), and that a Kalman estimator is defined which produces estimates of Δx and b^s utilizing the process equations

$$\Delta x_n = A_n \Delta x_{n-1} - B_n^s b_n^s - \xi_n^s$$

$$b_n^s = F_n^s b_{n-1}^s + \mu_n^s$$

and the velocity-match measurement equation given previously. The estimate of Δx and b^s will then be defined by the following Kalman estimator recursive sequence

$$\tilde{z}_n^{s-} = A_n \tilde{z}_{n-1}^s \quad (21)$$

$$\tilde{P}_n^{s-} = A_n \tilde{P}_{n-1}^s A_n^T + Q_n^s \quad (22)$$

$$\tilde{K}_n^s = \tilde{P}_n^{s-} H^T (H \tilde{P}_n^{s-} H^T + R_n^s)^{-1} \quad (23)$$

$$\tilde{z}_n^s = \tilde{z}_n^{s-} + \tilde{K}_n^s (y_n^s - H \tilde{z}_n^{s-}) \quad (24)$$

$$\tilde{P}_n^s = (I - \tilde{K}_n^s H) \tilde{P}_n^{s-} \quad (25)$$

where

$$z^s = (\Delta x \ b^s)^T$$

and

$\tilde{z}_n^{s-}, \tilde{z}_n^s$ = a priori and a posteriori estimates of z^s when the master's bias is assumed to be zero

$\tilde{P}_n^{s-}, \tilde{P}_n^s$ = computed a priori and a posteriori estimation error covariance matrices of z^s when the master's bias is assumed to be zero

\tilde{K}_n^s = gain matrix

The matrices Q^s and R^s are the slave system's process and measurement noise covariance matrices, defined by

$$Q^s = \begin{bmatrix} E(\xi^s \xi^{sT}) & 0 \\ 0 & E(\mu^s \mu^{sT}) \end{bmatrix}$$

$$R^s = E(\eta^s \eta^{sT})$$

and \tilde{P}^s is defined in partitioned form as

$$\tilde{P}^s = \begin{bmatrix} \tilde{P}_{\Delta x}^s & \tilde{P}_{\Delta x b}^s \\ \tilde{P}_{\Delta x b}^{sT} & \tilde{P}_b^s \end{bmatrix}$$

The initial value of \tilde{P}^s is chosen as

$$\tilde{P}_0^s = \begin{bmatrix} P_{\Delta x}^s(o) & 0 \\ 0 & P_b^s(o) \end{bmatrix}$$

where $P_{\Delta x}^s(o)$ is the covariance matrix of the initial estimation error in Δx_o , and $P_b^s(o)$ is the error covariance matrix for the initial estimate of the slave's sensor biases.* The initial error covariance matrix $P_{\Delta x}^s(o)$ is, as a result of the initialization process defined, determined entirely by the relative errors originating from vehicle flexure, the uncertainty in the slave's attitude relative to the vehicle frame, and the uncertainty in the displacement between the master and slave systems. This follows from

$$x_o^s = x_o^m + x_o^r$$

*The designator "o" is used throughout to indicate the time point at which the transfer-alignment process begins.

where

x_0^m, x_0^s = initial master and slave navigational error states

x_0^r = initial error in correction for relative effects

which leads to

$$P_{\Delta x}^s(0) = E \left[(\Delta \hat{x}_0 - \Delta x_0)(\Delta \hat{x}_0 - \Delta x_0)^T \right] \\ E \left\{ \left[\hat{x}_0^m - \hat{x}_0^s - (x_0^m - x_0^s) \right] \left[\hat{x}_0^m - \hat{x}_0^s - (x_0^m - x_0^s) \right]^T \right\}$$

and, because the initial estimates of the master and slave navigational errors are equal (i. e., $\hat{x}_0^s = \hat{x}_0^m$),

$$P_{\Delta x}^s(0) = E \left[(x_0^m - x_0^s)(x_0^m - x_0^s)^T \right] \\ = E(x_0^r x_0^{rT})$$

Also, since the relative errors are independent of the master system, the initial estimation error in Δx is uncorrelated with all errors of the master. This is a key fact to be utilized in the later development.

4.5 The Perfectly-Known-Bias Estimator of Δx and b^s

The bias-free case is closely related to the case where the master's bias vector is perfectly known. Even though, in the context of the present problem, this is strictly a fictitious situation, consideration of this case allows a natural and simple exposition of the solution to the transfer-alignment/calibration problem.

If the master's bias vector were perfectly known (that is, with zero variance), the optimal estimate of b^m would be one and the same value, and the recursive estimate of z^s would take the form

$$\hat{z}_n^{s-} = A_n \hat{z}_{n-1}^{s-} + B_n^m b^m \quad (26)$$

$$\hat{P}_n^{s-} = A_n \hat{P}_{n-1}^{s-} A_n^T + Q_n^s \quad (27)$$

$$\hat{K}_n^{s-} = \hat{P}_n^{s-} H^T (H \hat{P}_n^{s-} H^T + R_n^s)^{-1} \quad (28)$$

$$\hat{z}_n^{s+} = \hat{z}_n^{s-} + \hat{K}_n^{s-} (y_n^s - H \hat{z}_n^{s-}) \quad (29)$$

$$\hat{P}_n^{s+} = (I - \hat{K}_n^{s-} H) \hat{P}_n^{s-} \quad (30)$$

where \hat{z}_n^{s-} and \hat{P}_n^{s-} are the a priori and a posteriori estimates of z^s when b^m is perfectly known, and b^m is the true value of the master's bias vector. The gain matrix (\hat{K}_n^{s-}) for this estimator is identical to that of the bias-free case, as are the a priori and a posteriori error covariance matrices (\hat{P}_n^{s-} , \hat{P}_n^{s+}), with only the state estimation equations being different. However, the important distinction to be noted is that when b^m is perfectly known, the resultant estimator produces a true minimum variance estimate of z^s , with \hat{P}_n^{s+} being a true statistical measure of the error in the estimate; whereas, when the bias is simply ignored, the estimate of z^s is not minimum variance in nature, and \hat{P}_n^{s+} is not a true measure of the statistical error in the estimate.

The initial estimation error and covariance matrix for the estimator having perfect knowledge of the master's bias are exactly the same as for the bias-free estimator, since both estimators are initially identical in all respects.

4.6 Relationship Between the Bias-Free and Perfectly-Known-Bias Estimates of Δx and b^s

The recursive estimate \hat{z}_n^{s+} , as defined by (21) and (24), will differ from \hat{z}_n^{s-} , as defined by (26) and (29), due only to the presence of b^m in the latter equation set. Since equation set (26) and (29) is strictly linear in nature, its solution can be decomposed into two parts: that part due to b^m alone and the remaining part due to the forcing function y^s . The component of \hat{z}_n^{s+} , due to the forcing function y^s , is clearly identical to the solution \hat{z}_n^{s-} obtained from (21) and (24), which allows the following relationships between the two estimates to be written immediately as

$$\hat{z}_n^{s-} = \tilde{z}_n^{s-} + U_n b^m \quad (31)$$

$$\hat{z}_n^s = \tilde{z}_n^s + V_n b^m \quad (32)$$

where U and V are sensitivity matrices which are to be defined. From (21), (26), (31), and (32) the following is easily seen to be true

$$\begin{aligned} \hat{z}_n^{s-} - \tilde{z}_n^{s-} &= U_n b^m = A_n (\hat{z}_{n-1}^s - \tilde{z}_{n-1}^s) + B_n^m b^m \\ &= A_n V_{n-1} b^m + B_n^m b^m \\ &= (A_n V_{n-1} + B_n^m) b^m \end{aligned}$$

Therefore, the sensitivity matrix relating the a priori estimates, \tilde{z}_n^{s-} and \tilde{z}_n^s , is given by the relationship

$$U_n = A_n V_{n-1} + B_n^m \quad (33)$$

Similarly, from (24), (29), (31), and (32) one finds that

$$\begin{aligned} \hat{z}_n^s - \tilde{z}_n^s &= V_n b^m = \hat{z}_n^{s-} - \tilde{z}_n^{s-} + K_n^s \left[-H (\hat{z}_n^{s-} - \tilde{z}_n^{s-}) \right] \\ &= U_n b^m - K_n^s H U_n b^m \end{aligned}$$

from which it is clear that the sensitivity function relating the a posteriori estimates, \hat{z}_n^s and \hat{z}_n^{s-} , is given by

$$V_n = U_n - K_n^s H U_n = (I - K_n^s H) U_n \quad (34)$$

Equations (33) and (34) taken together provide a recursive algorithm for computing the sensitivity functions appearing in (31) and (32).

4.7 The Adjusted Estimates of x^s and b^s

The estimate of b^m , as obtained from the master system's independent Kalman estimator, can be utilized to correct the bias-free estimate \tilde{z}^s , as defined by (28) through (30), by means of the following

$$\hat{z}_n^{s-} = \tilde{z}_n^{s-} + U_n \hat{b}_{n-1}^m \quad (35)$$

$$\hat{z}_n^s = \tilde{z}_n^s + V_n \hat{b}_n^m \quad (36)$$

where \hat{z}^{s-} and \hat{z}^s are the a priori and a posteriori adjusted estimates of z^s , and \hat{b}^m is the master system's estimate of its own bias vector.

The a priori and a posteriori adjusted estimates of Δx and b^s follow directly as

$$\Delta \hat{x}_n^- = \Delta \tilde{x}_n^- + U_x(n) \hat{b}_{n-1}^m \quad (37)$$

$$\hat{b}_n^{s-} = \tilde{b}_n^{s-} + U_b(n) \hat{b}_{n-1}^m \quad (38)$$

$$\Delta \hat{x}_n^s = \Delta \tilde{x}_n^s + V_x(n) \hat{b}_n^m \quad (39)$$

$$\hat{b}_n^s = \tilde{b}_n^s + V_b(n) \hat{b}_n^m \quad (40)$$

which utilize the partitions inherent in \tilde{z}^s , U , and V

$$\tilde{z}^s = (\Delta \tilde{x} \tilde{b}^s)^T, \quad U = \begin{bmatrix} U_x & U_b \end{bmatrix}, \quad V = \begin{bmatrix} V_x & V_b \end{bmatrix}$$

The efficacy of adjusting the bias-free estimates in the manner given is apparent from the relationship between the bias-free and perfectly-known-bias estimates given in (31) and (32). Since the master system's estimate of its own bias vector is taken to be completely independent of the slave system and

because \hat{b}^m is by definition an optimal estimate of the master's bias, one may conclude that the adjusted estimate of b^s is also optimal.

Finally, from the definition of Δx , the a priori and a posteriori estimates of \hat{x}^s are determined from

$$\hat{x}_n^{s-} = \hat{x}_n^{m-} - \left[\Delta \tilde{x}_n^- + U_x(n) \hat{b}_{n-1}^m \right] \quad (41)$$

$$\hat{x}_n^s = \hat{x}_n^m - \left[\Delta \tilde{x}_n + V_x(n) \hat{b}_n^m \right] \quad (42)$$

where \hat{x}^{m-} and \hat{x}^m are the corresponding estimates of the master's bias.

4.8 Error Covariance Matrices for \hat{x}^s and \hat{b}^s

The estimation errors for the slave system a posteriori estimates defined by (40) and (42) are derived in the following manner. The estimation error for \hat{x}^s is first determined as

$$\begin{aligned} \hat{x}_n^s - x_n^s &= \hat{x}_n^m - \left[\Delta \tilde{x}_n + V_x(n) \hat{b}_n^m \right] - x_n^s \\ &= \hat{x}_n^m - x_n^m + x_n^m - x_n^s - \left[\Delta \tilde{x}_n + V_x(n) \hat{b}_n^m \right] - V_x(n) (\hat{b}_n^m - b^m) \\ &= \hat{x}_n^m - x_n^m - (\Delta \tilde{x}_n - \Delta x_n) - V_x(n) (\hat{b}_n^m - b^m) \end{aligned} \quad (43)$$

where, as recalled, $\Delta \tilde{x}$ is the estimate of Δx which would be obtained were the master's bias known perfectly (see equations (26) through (30)). The a posteriori error covariance matrix for the estimate \hat{x}^s is then determined directly from (43) as

$$\begin{aligned} P_{\hat{x}}^s(n) &= E \left[(\hat{x}_n^s - x_n^s) (\hat{x}_n^s - x_n^s)^T \right] \\ &= P_x^m(n) + \tilde{P}_{\Delta x}^s(n) + V_x(n) P_b^m(n) V_x^T(n) - P_{xb}^m(n) V_x^T(n) - V_x(n) P_{xb}^{mT}(n) \quad (44) \end{aligned}$$

where the following definitions apply

$$\begin{aligned} P_x^m(n) &= E \left[(\hat{x}_n^m - x_n^m) (\hat{x}_n^m - x_n^m)^T \right] \\ P_b^m(n) &= E \left[(\hat{b}_n^m - b^m) (\hat{b}_n^m - b^m)^T \right] \\ P_{xb}^m(n) &= E \left[(\hat{x}_n^m - x_n^m) (\hat{b}_n^m - b^m)^T \right] \\ \tilde{P}_{\Delta x}^s(n) &= E \left[(\Delta \tilde{x}_n - \Delta x_n) (\Delta \tilde{x}_n - \Delta x_n)^T \right] \end{aligned}$$

The following identities were also utilized in obtaining (44)

$$\begin{aligned} E \left[(\hat{x}_n^m - x_n^m) (\Delta \tilde{x}_n - \Delta x_n)^T \right] &= 0 \\ E \left[(\hat{b}_n^m - b^m) (\Delta \tilde{x}_n - \Delta x_n)^T \right] &= 0 \end{aligned}$$

which simply express the fact that the estimate $\Delta \tilde{x}$ is initially, and at all subsequent times, uncorrelated with the estimates produced by the master system's Kalman estimator.

In a similar manner, the estimation error in \hat{b}^s is found to be

$$\begin{aligned} \hat{b}_n^s - b_n^s &= \hat{b}_n^s + V_b(n) \hat{b}_n^m - b_n^s \\ &= \hat{b}_n^s + V_b(n) b^m + V_b(n) (\hat{b}_n^m - b^m) - b_n^s \\ &= \hat{b}_n^s - b_n^s + V_b(n) (\hat{b}_n^m - b^m) \end{aligned} \quad (45)$$

from which the a posteriori error covariance matrix is determined as

$$\begin{aligned} P_b^s(n) &= E \left[(\hat{b}_n^s - b_n^s) (\hat{b}_n^s - b_n^s)^T \right] \\ &= \tilde{P}_b^s + V_b(n) P_b^m(n) V_b^T(n) \end{aligned} \quad (46)$$

and the fact that the estimate \hat{b}^s is uncorrelated with \hat{b}^m has been utilized.

The a priori estimation error covariance matrices are obtained directly from (44) and (46) with the substitution of the a priori values of P_x^m , P_b^m , P_{xb}^m , $P_{\Delta x}^s$, and P_b^s for the corresponding a posteriori values, and with U_x and U_b substituting for V_x and V_b .

A block diagram of the transfer-alignment scheme is shown in Figure 1. It will be noted that, for both the master and slave systems, the navigational states are output-corrected rather than by direct reset of the internal navigational states. It is clear that this is an essential requirement during the transfer-alignment process, since access to the unaided velocities of both the master and slave systems is required in the implementation of the slave Kalman estimator. Preceding the transfer-alignment process, it could normally be presumed that the aided master system is corrected by a direct reset of its navigational and bias (sensor calibration coefficient) states and, consequently, at the initiation of transfer-alignment the master's estimate of the errors in these states would be zero.

It should also be noted that, even though the scheme given is generalized to include an estimate of the slave's positional errors, these states can usually be made equal to those of the master system with little or no degradation of overall performance.

4.9 A Special Case

Suppose that, to promote computational simplicity, the correction of the slave states for the master's bias is omitted. It is of interest to establish the estimation accuracy associated with this case.

To begin, it is noted that the omission of the correction to the slave's states, for the master's bias, is equivalent to assuming that the master's bias is identically zero - which, in fact, is the master system's estimate of its own bias at the initiation of transfer-alignment. Therefore, following the development which leads to (43), and substituting \hat{b}_0^m for \hat{b}_n^m , results immediately in the modified estimation error equation

$$\hat{x}_n^s - x_n^s = \hat{x}_n^m - x_n^m - (\Delta \bar{x}_n - \Delta x_n) - V_x(n) (\hat{b}_0^m - b^m)$$

The estimation error covariance matrix is then determined as

$$P_x^s(n) = P_x^m(n) + P_{\Delta x}^s(n) + V_x(n) P_b^m(o) V_x^T(n) - G_x(n) - G_x^T(n) \quad (47)$$

where

$$G_x(n) = E \left[(\hat{x}_n^m - x_n^m) (\hat{b}_0^m - b^m)^T \right] V_x^T(n)$$

Returning to the generalized recursive form of the Kalman estimator given by (8) through (12), it is a straightforward matter to show that the estimation error at the n th update interval may be expressed in the form

$$\hat{x}_n - z_n = W_n (\hat{x}_0 - z_0) + \dots$$

where the missing terms are a function only of the process and measurement noise, and W is defined recursively by

$$W_n = (I - K_n) W_{n-1} \quad W_0 = I$$

Therefore it is clear that the estimation error in \hat{x}_n^m can be expressed in terms of initial estimation errors as

$$\hat{x}_n^m - x_n^m = W_{11}(n) (\hat{x}_0^m - x_0^m) + W_{12}(n) (\hat{b}_0^m - b^m) + \dots$$

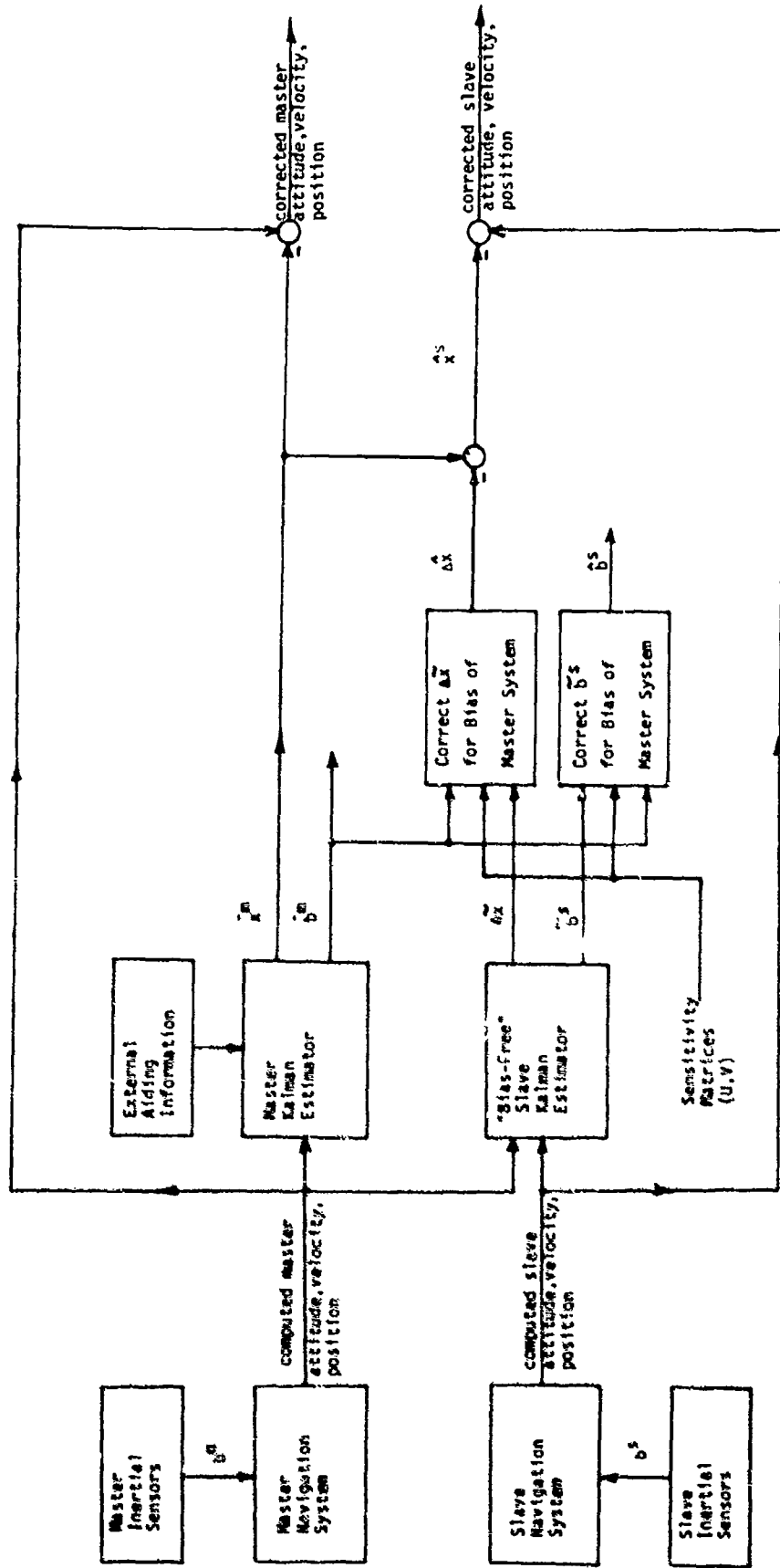
where W_{11} and W_{12} are the appropriate matrix partitions of W , as defined above. This expansion of the estimation error in \hat{x}_n^m allows $G_x(n)$ to be evaluated as

$$G_x(n) = \left[W_{11}(n) P_{xb}^m(o) + W_{12}(n) P_b^m(o) \right] V_x^T(n) \quad (48)$$

which completes (47).

In a similar manner the estimation error equation for the slave's bias is, from a modification of (45),

$$\hat{b}_n^s - b_n^s = \hat{b}_n^s - b_n^s + V_b(n) (\hat{b}_0^m - b^m)$$



\hat{x}^M = estimated error in the master's navigation states
 \hat{b}^M = estimated value of the master's bias vector
 $\hat{\Delta x}$ = bias-free estimate of the differential-state error
 $\hat{\Delta x}$ = adjusted estimate of the differential-state error
 \hat{b}^S = bias-free estimate of the slave's bias vector
 \hat{b}^S = estimated value of the slave's bias vector
 \hat{x}^S = estimated error in the slave's navigation states

Figure 1. Block Diagram of Transfer-Alignment/Calibration Scheme

which leads directly to the estimation error covariance matrix

$$P_b^s(n) = \hat{P}_b^s(n) + V_b(n) P_b^m(o) V_b^T(n) \quad (49)$$

4.10 Effect of Lever-Arm Correction Uncertainties

Consider the case where the separation between the master and slave systems is not perfectly known but is subject to a finite error. It is of interest to establish the effect of such an error on the alignment and calibration process for the slave system.

The error in the lever-arm velocity correction, \hat{V}_L , due to an uncertainty, δl , in the lever arm is defined by

$$\delta \hat{V}_L = \omega \times \delta l$$

where ω is the angular velocity of the transport-vehicle frame. The error $\delta \hat{V}_L$ may also be written in the form

$$\delta \hat{V}_L = H_L \delta l$$

where

$$H_L = \begin{bmatrix} 0 & -\omega_3 & \omega_2 \\ \omega_3 & 0 & -\omega_1 \\ -\omega_2 & \omega_1 & 0 \end{bmatrix}$$

and the ω_i are the components of ω . Therefore, repeating the steps which lead to the measurement relationship given by (16), the following modified result is obtained

$$y_n^s = \delta v^m - \delta v^s + H_L \delta l + \eta_n^s \quad (50)$$

The introduction of the term due to δl does not require a modification of the generalized computational format for the slave estimator, since it is always possible to augment the differential-state error (δx) with the three states associated with δl , and to redefine the slave's measurement matrix as

$$H_x = \begin{bmatrix} 0 & I & 0 & H_L \end{bmatrix}$$

In the event that the value of ω utilized in computing \hat{V}_L is also in error, a second component of $\delta \hat{V}_L$ can be defined as

$$\delta \hat{V}_L = \delta \omega \times l$$

where $\delta \omega$ is the uncertainty in the value of ω determined by the master navigation system. If the master system is a platform or ESG navigator, ω is determined by differentiating the attitude readout angles, in which case $\delta \hat{V}_L$ can be approximated by a white noise function that can be lumped with the random measurement noise η^s originating from vehicle flexure. If the master navigator were strapdown in nature, the value of ω would be available directly from sensor outputs and could be taken, for the purpose of computing \hat{V}_L , to be essentially error free.

5. CONCLUSION

A methodology for alignment and calibration of an inertial navigation system on a moving base has been defined which provides an optimal result for the assumed restriction that the aided master navigation system operate independently of the slave system--a restriction that is enforced by practical implementation constraints.

It was shown that, in the general case considered, the slave system's navigational and sensor bias states can be optimally estimated by utilizing all of the information available from the aided master's Kalman estimator. In the special case considered, only the aided master's estimate of its navigational errors enters into the estimation of the slave errors. In both cases, the estimation error covariances can be rigorously and completely defined. The estimation error covariance computations defined are, with the exception of those required in the estimators for the master system and the bias-free slave system, intended only for offline performance analyses - and are not required in the actual implementation of the scheme.

Even though the treatment of the slave Kalman estimator was based on the optimal form for this type of estimator, the results given are also applicable if the slave estimator is, in reality, suboptimal; that is, if one or more of the slave's error states is totally ignored. In this case it is only necessary that the covariance matrices $\hat{P}_{\Delta x}^s$ and \hat{P}_b^s (required in computing P_x^s and P_b^s) be obtained from the full-state slave error model utilized in conjunction with the gain matrix \hat{K}^s computed by the bias-free slave estimator.

REFERENCES

- [1] Leondes C. T. (editor), Guidance and Control of Aerospace Vehicles, McGraw-Hill, 1963.
- [2] Ignagni M. B., "Discretization of Nav Error Equations," Appendix D in Unaided Tactical Guidance, Air Force Armaments Laboratory Report AFATL-TR-78-38, H. T. Gaines et al, March 1978.
- [3] Britting K. R., Inertial Navigation System Analysis, Wiley-Interscience, 1971.
- [4] Morrison N., Introduction to Sequential Smoothing and Prediction, McGraw-Hill, 1969.
- [5] Ignagni M. B., "Wing Bending and Prefiltering," Appendix C in AFATL-TR-78-38 (see Reference 2).
- [6] Friedland B., "Treatment of Bias in Recursive Filtering," IEEE Transactions on Automatic Control, August, 1969.

IDENTIFICATION AND DETERMINATION OF STRAPDOWN
ERROR-PARAMETERS BY LABORATORY TESTING

by
Dr.D.K.Joos
U.K.Krogmann

Bodenseewerk Gerätetechnik GmbH
Postfach 1120
D-7770 Überlingen, Germany

SUMMARY

The performance of an inertial navigation system (INS) is largely affected by a number of important error-sources, where most of which are related to the instruments used. This particularly applies to strapdown-systems.

The paper describes laboratory test procedures to determine static and dynamic parameters of the gyro and accelerometer measurement model.

It is shown, that a proper rate-test and a multiposition test with respect to earth-rate and gravity-vector are well suited to ascertain static parameters with sufficient accuracy. Optimal parameter values are retrieved from measured test-data applying regression analysis techniques. It is shown, how uncertainties in parameter estimates can be determined from actual measurement residues.

The verification of major dynamic performance parameters of interest (i.e. anisoinertia torque, angular acceleration term) by appropriate test procedures utilizing a 3-axes test-table is shown.

Applicability and feasibility of the proposed test-procedures is demonstrated utilizing the Modular-Strapdown-System (MSS).

Test-configuration and sequence as well as processing of test-data including collection and reduction are described. Significant MSS error-parameters are extracted and evaluated applying iterative linear regression techniques. The corresponding software-structure is described.

The results obtained confirm the usefulness of the developed test-procedures and software for calibrating a strapdown-system with sufficient accuracy. Moreover it can be stated that the software-package exceeds its pure calibration function. It proved to offer a considerable potential to analyse a strapdown-system as well as the test-equipment.

1. Introduction

The objective of INS-Testing is usually devoted to demonstrate basic system navigation accuracy.

The performance of an inertial navigation system is largely affected by a number of important error sources, where most of which are related to the instruments used. This particularly applies to strapdown-systems. Recent advances in sensor technology have provided instruments capable of determining angular rates and acceleration with high accuracy over a broad spectrum of dynamic conditions.

To fully utilize this potential requires accounting for several instruments- and system effects, which otherwise would cause considerable navigational errors. To accomplish this, precise laboratory measurement and identification of important parameters are necessary. Such sensor performance information represents the basis for the calibration or error-compensation algorithms included in the Strapdown-Inertial-System software.

2. Brief comparison of gimballed versus strapdown inertial system

Figure 1 shows the block diagram of an INS realization with a "local-level-north" reference system.

The basic item of this system is the inertial measuring unit which is realized as a gyro-stabilized platform. Three accelerometers and three gyros are arranged on the stabilized element with their input axes mutually vertical. The stabilized element is isolated from the aircraft motions by means of a gimbal system. Deviations from the reference attitude are detected by the gyros and corrected by a corresponding rotation of the gimbal.

Prior to the start the stabilized element of the platform has to be so aligned that the input axes of the accelerometers coincide with those of the reference system.

In order to maintain the alignment of the input axes of the accelerometers to the reference system also during flight, the stabilized element is slaved by corresponding signals for the torquers of the gyros ($\omega_N, \omega_E, \omega_V$); the respective loops represent the well known Schuler-loops of an INS with earth-fixed reference coordinates.

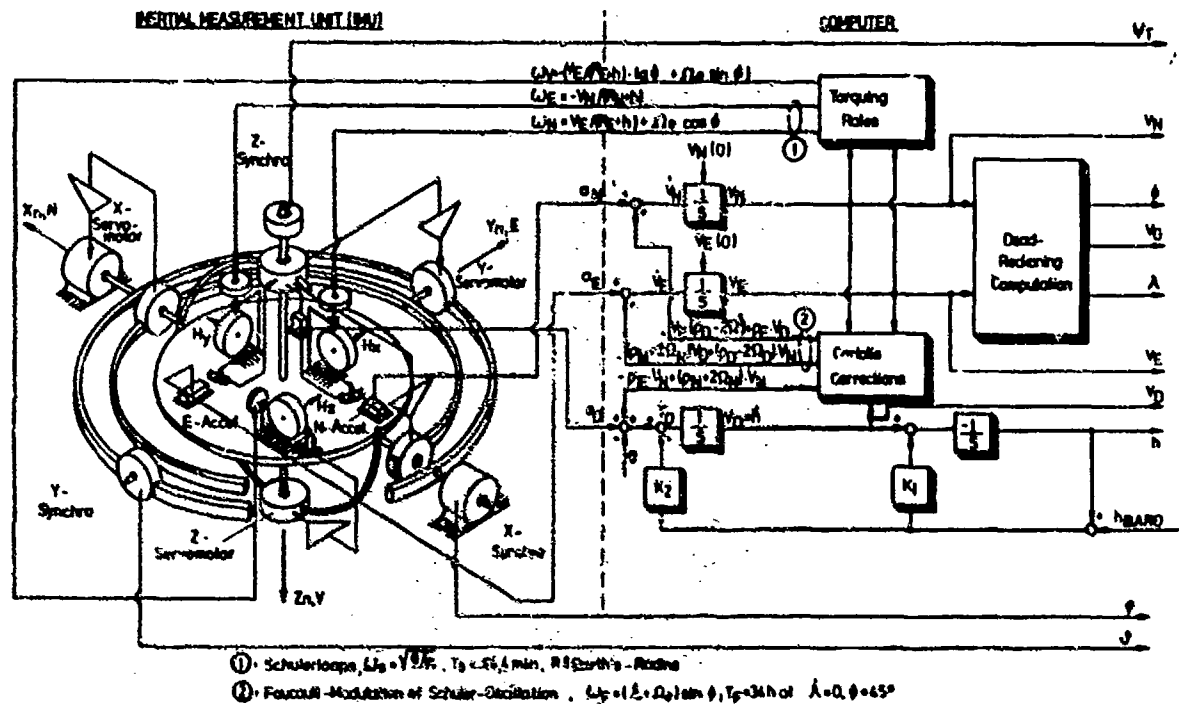


Fig. 1: INERTIAL SYSTEM MECHANIZATION WITH GIMBALED IMU

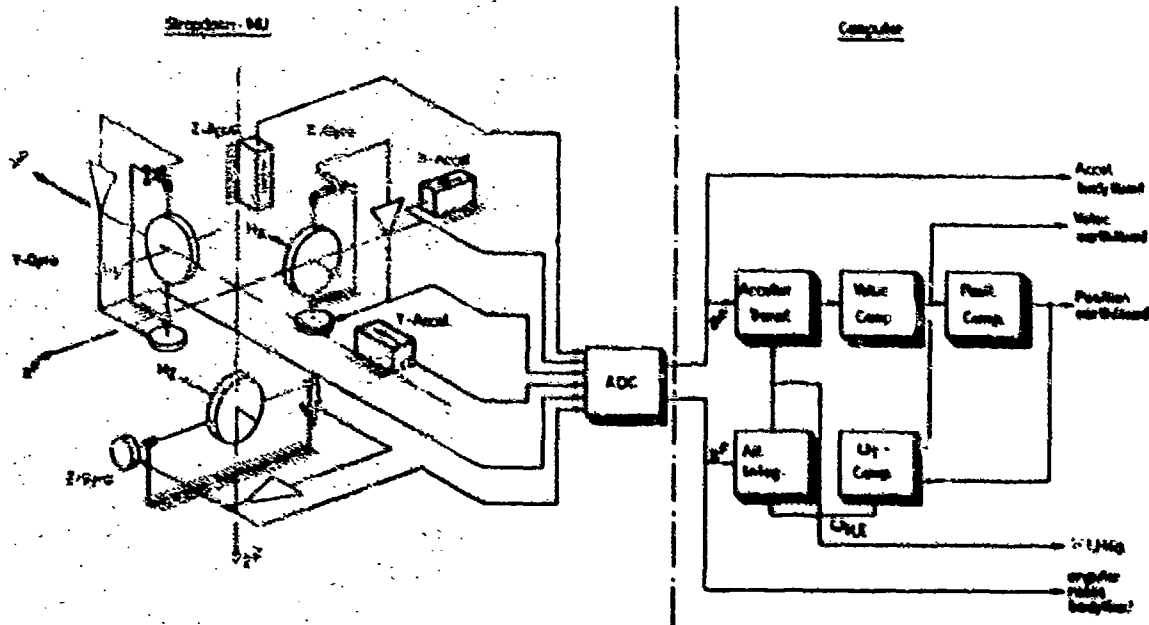


Fig. 2: INERTIAL SYSTEM MECHANIZATION WITH STRAPDOWN IMU

The computer calculates besides these feedback signals also the Coriolis-corrections for the output signals of the accelerometers (Poucault-modulation of the Schuler-oscillation). The pitch and roll angles ($\Delta\theta, \Delta\psi$) as well as the "true heading" (Ψ_T) can be read off directly on the synchros of the platform gimbal system.

The inertial measuring units in "strapdown configuration" are characterized by the fact that the sensors are directly mounted to the vehicle frame (Figure 2). Since there is no isolation from vehicle motions the sensors are subjected to both full translatory and rotational dynamics of the vehicle.

As shown in Figure 2 the output signals of the gyros (angular rate) and the accelerometers (linear acceleration) are transferred to the computer after analogue/digital conversion. This computer transforms the measured acceleration-vector into the reference coordinate frame (local-level-north). To accomplish this the transformation parameters representing the mutual attitude of the reference coordinate frame and the aircraft-related sensor-input-axes system are continuously determined through integration of the angular rates measured by the gyros.

The 9 elements of the direction cosine matrix, the 4 elements of a rotational quaternion or the 3 Euler-angles can be used as transformation parameters.

Due to rotation of the earth with respect to the inertial space, on the one hand, and the motion of the vehicle with respect to the earth, on the other hand, the transformation parameters are "slaved" in the computer in the same way as the platform cluster is torqued at the corresponding rate in the gimballed configuration.

When the components of the acceleration are determined in the earth-fixed reference system in the computer the inertial navigation computations are performed in principle in the same way as in the gimballed configuration system.

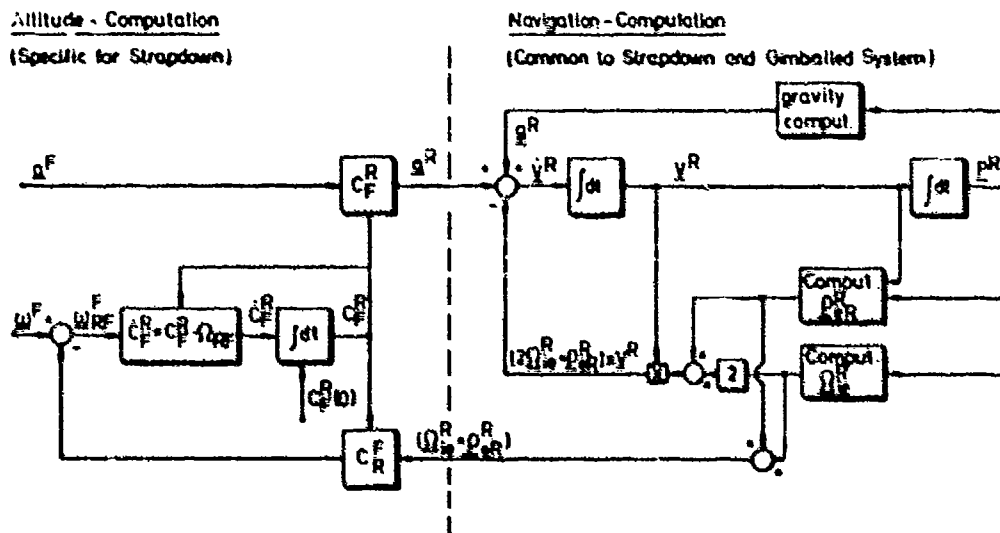


Fig. 3: BLOCKDIAGRAM OF STRAPDOWN-INERTIAL COMPUTATIONS

Figure 3 shows a vectorial block diagram of the attitude and navigation equations with the left part of the figure (attitude computation and acceleration transformation) representing the function of the gyro-stabilized platform for gimballed configuration systems.

In conclusion it can be stated, that strapdown-systems offer advantages over gimballed systems for a number of applications. However, to realize their potential it is necessary to compensate for several sensor effects which otherwise would obscure vehicle motions.

3. Strapdown sensor-error-models

The most critical problem in strapdown systems arises within the scope of computation of rotational dynamics (left part of Figure 3).

As mentioned before, recent advances in sensor technology have made available instruments capable of determining angular rate and linear acceleration with high precision over a broad spectrum of dynamic conditions.

Utilization of these inherent capabilities requires accounting for several sensor- and system-effects, which otherwise would cause considerable navigational errors.

The extent of the parameter compensation becomes evident considering the sensor-error-models. The procedures described in the following are used for the calibration of a system containing two-axes dynamically tuned gyros with electrical caging as sensors for the angular rate.

In Figure 4 the sensor arrangement of the strapdown inertial measuring unit (IMU) with respect to vehicle-axes is shown. Furthermore the measurement equations for the two sensitive axes of the Z-gyro (1) are represented in tabulated form. Beside the desired rate term these equations contain a number of perturbing signal components. Some are determined by the imperfection of the sensors and their mounting (e.g. bias, mass-unbalance, misalignment etc.) and others are due to physical reasons (anisoinertia, angular acceleration etc.).

In order to extract the useful information $\omega_x, \omega_y, \omega_z$ from the measurable torquer signals M_y/H and M_x/H a compensation of static and dynamic error components in the measuring equations is necessary as shown in Figures 5 and 6 for gyro 1.

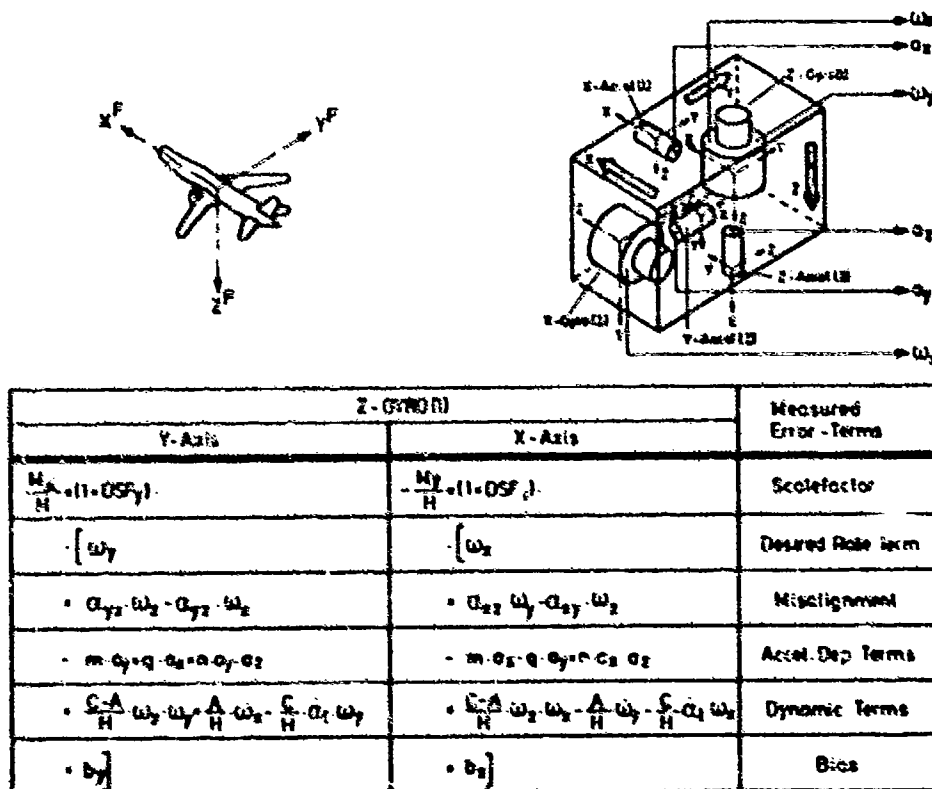


Fig. 4: ERROR-MODEL OF A DRY TUNED 2-AXES STRAPDOWN-GYRO

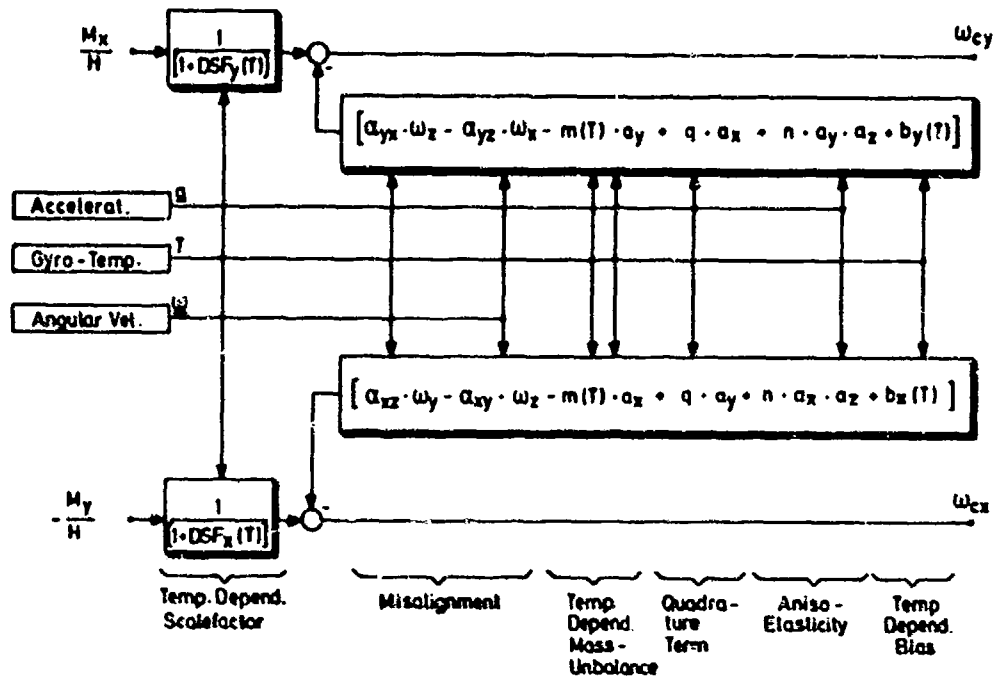


Fig. 5: COMPENSATION OF STATIC GYRO-ERRORS

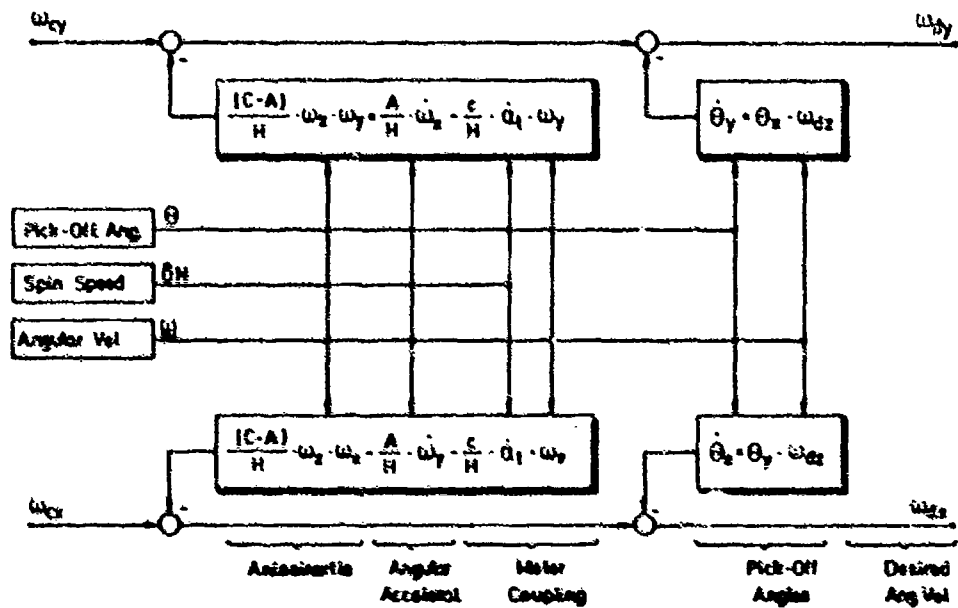


Fig. 6: COMPENSATION OF DYNAMIC ERRORS

For compensating the unwanted terms the parameters of the error-model and the exact inertial rates as well as the acceleration components of the sensor block must be known.

The parameters of the error-model are determined by appropriate tests as described in the following. Due to the fact that some parameters are temperature-dependent, these tests have to be performed at various sensor temperatures.

The exact inertial angular rates and accelerations will only be determined through the compensation. For this reason only the uncompensated sensor signals can be used for the error compensation.

For the compensation of the dynamic components (Figure 6) the pickoff angles of the axes and the rotor speed are also measured.

Regarding single-axis pendulous accelerometers considered here the corresponding linearized error-model for the x-accelerometer as well as the corresponding compensation block diagram is shown in Figure 7. Fortunately full compensation of all error terms is not necessary in any application. Depending on the individual requirements means for proper compensation have to be implemented after careful analysis.

$$\frac{U_x}{SF_x} = (1 + DK_x(T)) [a_x + \epsilon_{xz} \cdot a_y - \epsilon_{xy} \cdot a_z + KQ_x \cdot a_x^2 + B_x(T)]$$

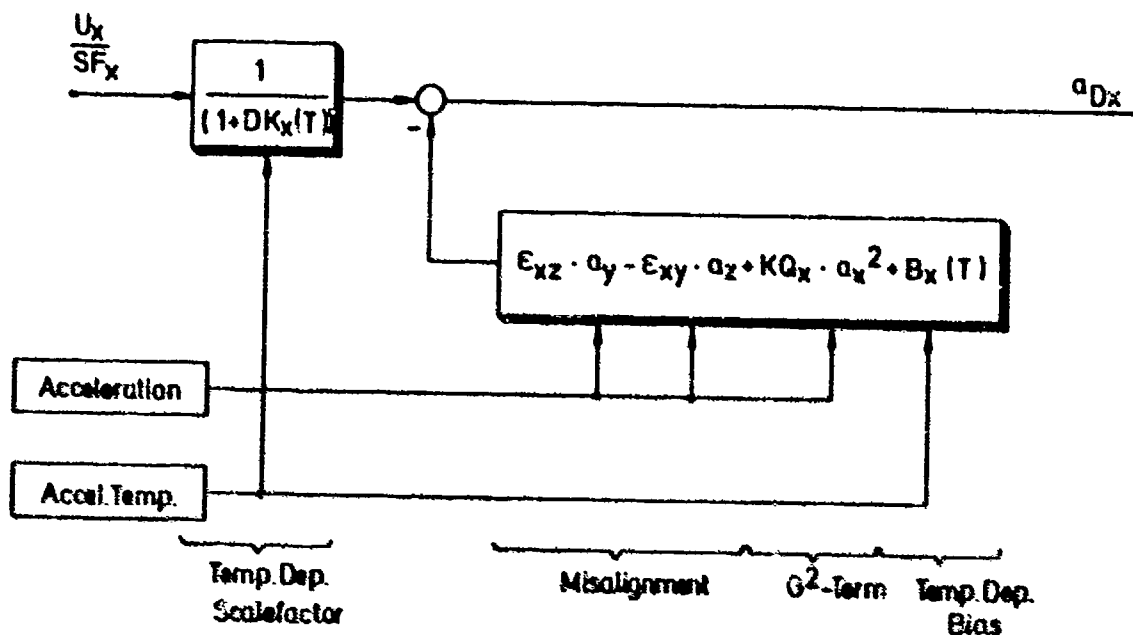


Fig. 7: COMPENSATION OF ACCELEROMETER-ERRORS

4. Determination of gyro-parameters

4.1 Test-objective

The objective of laboratory tests to be performed is twofold:

- determination of static parameters
- verification of dynamic parameters

With respect to the first item two different types of tests have to be distinguished:

- rate-test to determine those parameters excited by external rates
- multi-position static test to determine all remaining parameters excited by external acceleration.

To accomplish this, a three-axis test-table is considered here as the main test-equipment.

4.2 Parameters for the compensation of static errors

4.2.1 Rate-Test

The objective of the rate test is to determine

scale-factor

and

misalignment-errors.

Performing this task requires commencing through the following sequence of steps:

- adjust test-table sequentially in 3 positions, where in each position one of the three IMU main-axes is aligned to the local vertical
- rotate test-table CW and CCW about the vertical axis of the table with constant rate by 360°
- in each position integrate measured torquing-signals over a full period for CW- and CCW-rotations
- compute the differences of integrated signals for CW and CCW rotations. These differences are proportional to scale-factor and misalignment errors.

As shown in Figure 8 the sensor block is arranged in test-position 1 on a test-table with respect to earth-rate and gravity-vector.

The following applies then to the driving components of angular rate and acceleration in direction of the sensor Block axes due to earth rate, introduced table-rate and gravity-vector.

$$\begin{bmatrix} \omega_x^F \\ \omega_y^F \\ \omega_z^F \end{bmatrix} = \begin{bmatrix} \cos \varphi_3(t) & \sin \varphi_3(t) & 0 \\ -\sin \varphi_3(t) & \cos \varphi_3(t) & 0 \\ 0 & 0 & 1 \end{bmatrix} \begin{bmatrix} \Omega_c \\ 0 \\ \dot{\varphi}_3 - \Omega_s \end{bmatrix} \quad (4.1)$$

$$\begin{bmatrix} a_x^F \\ a_y^F \\ a_z^F \end{bmatrix} = \begin{bmatrix} \cos \varphi_3(t) & \sin \varphi_3(t) & 0 \\ -\sin \varphi_3(t) & \cos \varphi_3(t) & 0 \\ 0 & 0 & 1 \end{bmatrix} \begin{bmatrix} 0 \\ 0 \\ -g \end{bmatrix} \quad (4.2)$$

Starting from the initial position shown in Figure 6, the test table is rotated through exactly 360° about the vertical axis at $\dot{\varphi}_3 = \Omega_s = \text{const.}$

Taking into account the measurement equations for the gyro 1 (Figure 4) the following torquer signals are generated:

$$\frac{M_x}{H} / (+) = (1 + DSF_y) [-\Omega_c \cdot \sin(\Omega_3 \cdot t) + \alpha_{yx} (\Omega_3 - \Omega_s) - \alpha_{yz} \Omega_c \cos(\Omega_3 \cdot t) - \frac{(C-A)}{H} \cdot (\Omega_3 - \Omega_s) \cdot \Omega_c \cdot \sin(\Omega_3 \cdot t) + b_y] \quad (4.3)$$

$$-\frac{M_y}{H} / (+) = (1 + DSF_x) [\Omega_c \cos(\Omega_3 \cdot t) - \alpha_{xz} \Omega_c \sin(\Omega_3 \cdot t) - \alpha_{xy} (\Omega_3 - \Omega_s) + \frac{(C-A)}{H} \cdot (\Omega_3 - \Omega_s) \cdot \Omega_c \cdot \cos(\Omega_3 \cdot t) + b_x] \quad (4.4)$$

The measurement and integration of these torquer signals over a complete period provide the following signals:

$$J_x (+) = \int_0^T \frac{M_x}{H} / (+) dt; \quad J_y (+) = \int_0^T \frac{M_y}{H} / (+) dt \quad (4.5)$$

The corresponding integration of equation (4.3) and (4.4) eliminates the harmonic contents and leads to the result

$$J_x (+) = (1 + DSF_y) \cdot [\alpha_{yx} (\Omega_3 - \Omega_s) + b_y] \cdot T \quad (4.6)$$

$$-J_y (+) = (1 + DSF_x) \cdot [-\alpha_{xy} (\Omega_3 - \Omega_s) + b_x] \cdot T \quad (4.7)$$

For a negative rotation $\Psi_3 = -\Omega_3$ of the test table through 360° about the vertical axis the following relations result for the integrated torquer signals:

$$J_x (-) = (1 + DSF_y) \cdot [-\alpha_{yx} (\Omega_3 + \Omega_s) + b_y] \cdot T \quad (4.8)$$

$$J_y (-) = (1 + DSF_x) \cdot [\alpha_{xy} (\Omega_3 + \Omega_s) + b_x] \cdot T \quad (4.9)$$

If the differences of the torquer signals integrated over a full period for positive and negative rotation are computed, it results for test position 1:

$$\Delta J_{x1} = J_{x1} (+) - J_{x1} (-) = 2 (1 + DSF_y) \cdot \alpha_{yx} \cdot \Omega_3 \cdot T \quad (4.10)$$

$$\Delta J_{y1} = J_{y1} (+) - J_{y1} (-) = 2 (1 + DSF_x) \cdot \alpha_{xy} \cdot \Omega_3 \cdot T \quad (4.11)$$

From Figure 8 it becomes ultimately evident, that in test position 1 the misalignments α_{xy} and α_{yx} become observable by an introduced table rate Ψ_3 .

Figure 9 shows the three test positions required for the determination of the static parameters of the Z-gyro (1) according to the rate test procedure specified herein. In addition the determining equations for the scale-factor and alignment errors are contemplated.

Further positions and rotations about other axes of the test table provide redundant measuring information for the unknown parameters (see Figure 10b). These can then be determined optimally in a least square sense applying linear regression techniques as described for the following multi-position test.

In order to determine possible non-linearities of the scale factor the tests must be performed at various rotation rates of the test-table.

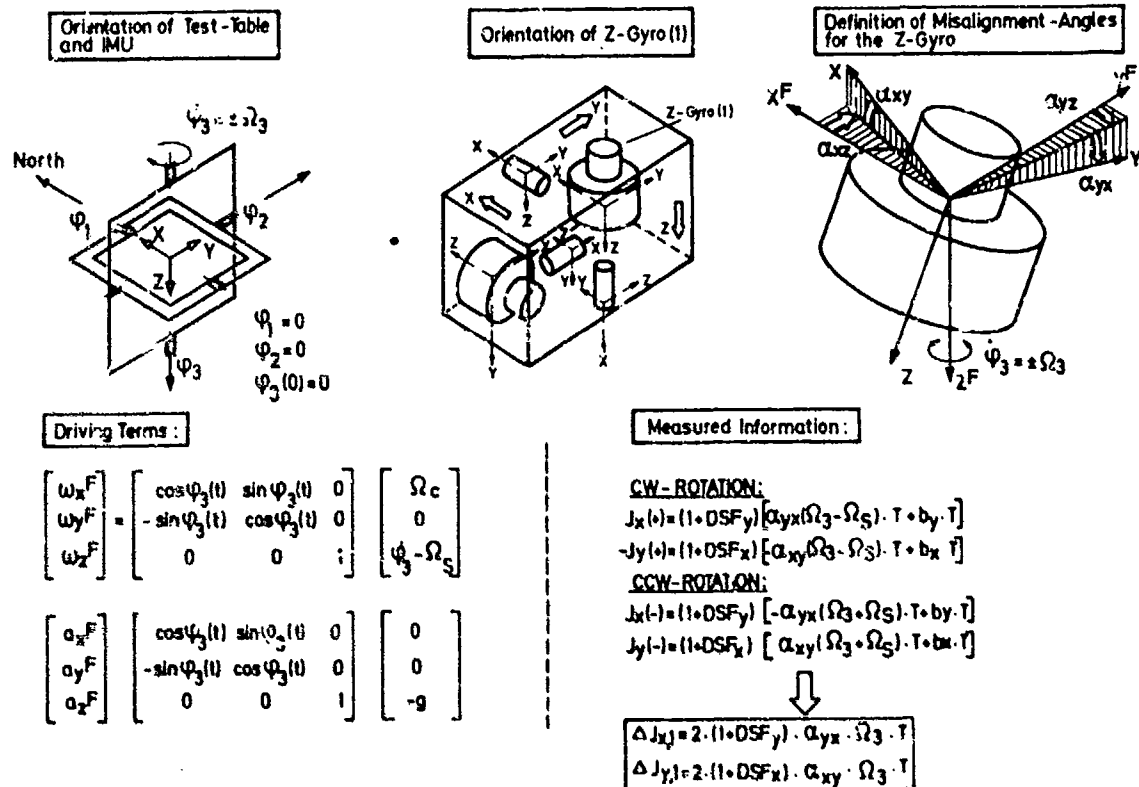


Fig. 8: RATE-TEST-POSITION 1

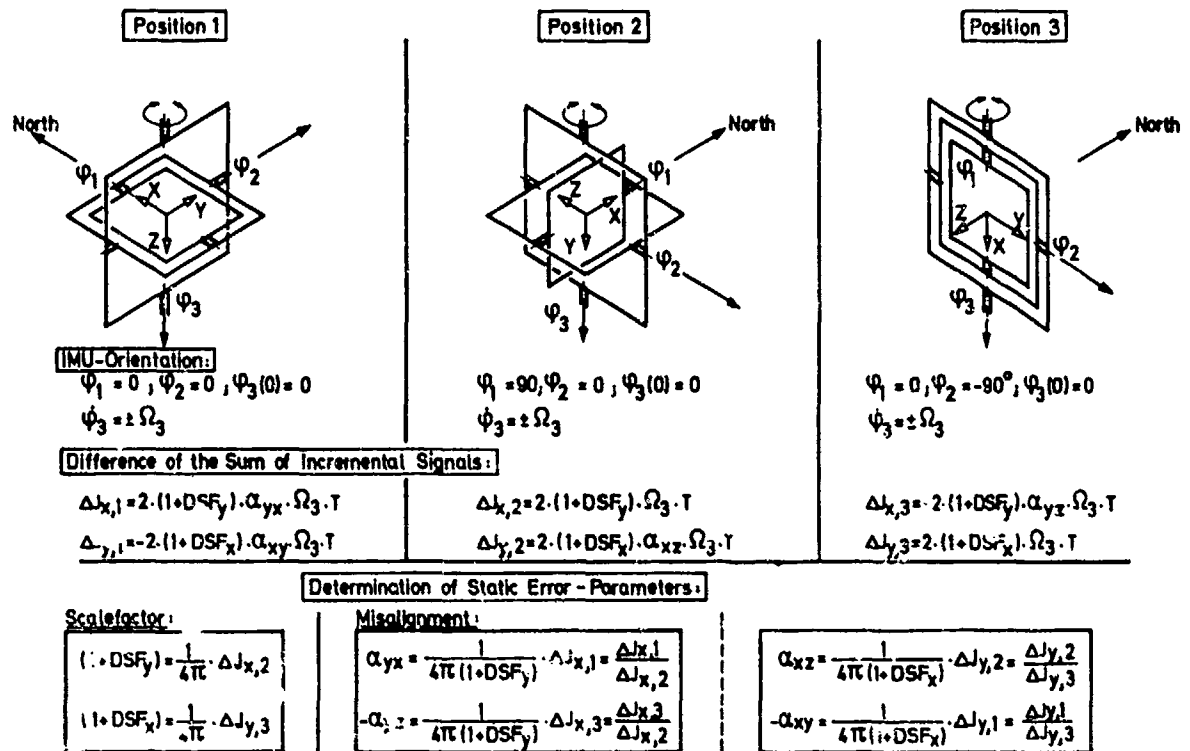


Fig. 9: STATIC ERROR -PARAMETERS FROM A 3-POSITION RATE-TEST

4.2.2 Multi-position static test

As mentioned before, the objective of the multi-position test is to determine the following gyro parameters excited by external acceleration:

- mass-unbalance
- quadrature term
- anisoelectricity

Furthermore the bias drift is determined as well.

To accomplish this, the following test procedure is appropriate:

- perform multi-position test by orienting the IMU in a number of predetermined positions with respect to earth-rotation and gravity-vector
- measure gyro torquer-signals over a predetermined period of time
- perform linear regression analysis to determine the best estimate for the error-parameter vector in a least squares sense.

Again only gyro 1 is considered in the following:

For the multi-position-test it is assumed that the scale-factor-and misalignment-errors have been determined through the rate-test.

Figure 10a shows the individual orientations of the sensor block for the full 24-position-test. The three main positions are identified by the fact that each sensor block axis is oriented once in the north, east and vertical direction.

Each main position includes 8 test positions. They result from the stepwise tilting of the sensor-block by respectively 45° about the axes of the test table as shown in Figure 10a. Different components of the earth-rotation and the gravity-vector are thus always acting along the sensor-block axes (ω_x, y, z resp. a_x, y, z) thus exciting corresponding error-terms in the measurement equations:

If "n" positions are generally considered, the measurement model according to equation (4.12) will result, for instance, for the Y-axis of gyro 1 (see also Figure 4).

$$\begin{array}{c}
 \frac{1}{(1+DSF_y)} \cdot \begin{bmatrix} \frac{M_x}{H} (1) \\ \frac{M_x}{H} (2) \\ \vdots \\ \frac{M_x}{H} (n) \end{bmatrix} - \begin{bmatrix} \omega_y(1) & \omega_z(1) & -\omega_x(1) \\ \omega_y(2) & \omega_z(2) & -\omega_x(2) \\ \vdots & \vdots & \vdots \\ \omega_y(n) & \omega_z(n) & -\omega_x(n) \end{bmatrix} \cdot \begin{bmatrix} 1 \\ \alpha_{yx} \\ \alpha_{yz} \end{bmatrix} = \begin{bmatrix} -\alpha_y(1) & \alpha_x(1) & \alpha_y(1) \cdot \alpha_z(1) & 1 \\ -\alpha_y(2) & \alpha_x(2) & \alpha_y(2) \cdot \alpha_z(2) & 1 \\ \vdots & \vdots & \vdots & \vdots \\ -\alpha_y(n) & \alpha_x(n) & \alpha_y(n) \cdot \alpha_z(n) & 1 \end{bmatrix} \cdot \begin{bmatrix} m \\ a \\ n \\ b_y \end{bmatrix} + \begin{bmatrix} V(1) \\ V(2) \\ \vdots \\ V(n) \end{bmatrix}
 \end{array} \quad (4.12)$$

Known From Rate-Test
Torquer Signals In Diff. Positions
Determined From Test-Table Position
Known From Rate Test
Determined From Test-Table Position
Unknown Parameter-Vector
Noise

Z
A
X
V

Measurement-Vector
Measurement-Matrix
Parameter Vector
Measurement Noise

Assuming that the individual measurements are statistically independent, this is an equation in the form of a linear regression model:

$$\underline{Z} = \underline{A} \cdot \underline{X} + \underline{V} \quad (4.13)$$

with

- measurement vector (n-dimensional)

$$\underline{z} = \frac{1}{(1 + DSF_y)} \cdot \begin{bmatrix} \frac{M_x}{H} (1) \\ \frac{M_x}{H} (2) \\ \vdots \\ \frac{M_x}{H} (n) \end{bmatrix} - \begin{bmatrix} \omega_y(1) & \omega_z(1) & -\omega_x(1) \\ \omega_y(2) & \omega_z(2) & -\omega_x(2) \\ \vdots & \vdots & \vdots \\ \omega_y(n) & \omega_z(n) & -\omega_x(n) \end{bmatrix} \cdot \begin{bmatrix} 1 \\ \alpha_{yx} \\ \alpha_{yz} \end{bmatrix} \quad (4.14)$$

- Measurement matrix (n x 4)

$$A = \begin{bmatrix} -\alpha_y(1) & \alpha_x(1) & \alpha_y(1) \cdot \alpha_z(1) & 1 \\ -\alpha_y(2) & \alpha_x(2) & \alpha_y(2) \cdot \alpha_z(2) & 1 \\ \vdots & \vdots & \vdots & \vdots \\ -\alpha_y(n) & \alpha_x(n) & \alpha_y(n) \cdot \alpha_z(n) & 1 \end{bmatrix} \quad (4.15)$$

- Parameter vector (4-dimensional)

$$\underline{x}^T = [m \quad q \quad n \quad by] \quad (4.16)$$

\underline{v} is the n-dimensional vector of the measurement noise.

Supposing independent individual measurements, an optimal estimate $\hat{\underline{x}}$ of the parameter vector \underline{x} within the meaning of minimum error squares can be determined as follows:

$$\hat{\underline{x}} = [A^T A]^{-1} \cdot A^T \cdot \underline{z} \quad (4.17)$$

If \underline{x} is an m-dimensional vector, it is necessary that A must also include m linear-independent row-vectors to ensure that \underline{x} is fully observable.

The following applies to the variance of the optimally estimated value $\hat{\underline{x}}$ if the individual measurements have equal variances σ^2 :

$$\text{VAR}(\hat{\underline{x}}) = \sigma^2 [A^T A]^{-1} \quad (4.18)$$

An unbiased estimate for σ^2 can be computed from the residues of the measured values:

$$\hat{\sigma}^2 = \frac{\underline{w}^T \underline{w}}{N - M} \quad (4.19)$$

with

$$\underline{w} = \underline{z} - A \cdot \hat{\underline{x}}$$

N = number of positions (measurements)

M = number of unknown parameters

Concerning the accuracy of the optimally estimated parameters it results therefore:

$$\text{VAR}(\hat{\underline{x}}) = \frac{\underline{W}^T \underline{W}}{n-m} [\underline{A}^T \underline{A}]^{-1} \quad (4.20)$$

Another alternative method for determining the accuracy of the estimated parameters is shown in the appendix.

For a subset of 8 positions that are specially marked in Figure 10a the quantitative regression-model is indicated in Figure 11. The acceleration- and rate-values of the test position 4 can for instance be readily explained by means of the gyro orientation shown in Figure 11. In this respect the test position 4 is derived from the main position 1 by the rotation $\psi_4 = 135^\circ$.

The observability of the parameter vector of equation (4.16) by means of the selected 8 positions is ensured because the determinate derived from four arbitrary rows of the A-matrix (Figure 11) is not equal to zero. There exist therefore four linear independent row-vectors of A.

If the measurement matrix A according to Figure 11 is now used in equation (4.18) the variance of the optimally estimated value \hat{x} for the parameter vector \underline{x} is shown in Figure 12 together with that for the full 24-position-test.

Supposing that the torquer signals of the gyros in the individual positions are measured with an accuracy of $0.01^\circ/\text{h}$ (i.e. measurement noise $\sigma^2 = (0.01^\circ/\text{h})^2$) the accuracies of the estimated parameters result as shown in Figure 12.

With the exception of the anisoelectricity coefficient the measurement noise is reduced by the 8-position test concerning the remaining parameters. Moreover a small correlation between mass-unbalance and bias-drift appears with a correlation coefficient of

$$\rho(m, b_y) = -0,25$$

This correlation is spurious. Its reason is the particular selection of the positions, which can be explained as follows:

The A-matrix in Figure 11 shows that in all 8 test positions the measuring signal includes a component due to the bias.

In position 2 and 4 (2nd and 4th row of A) there are further components due to m and n. As the signal components due to m and b_y have the same sign in these two positions, they are not discernable from each other. The bias b_y can however be observed uncorrupted in the positions 1 and 5. With this information about the bias, the mass-unbalance coefficient m is then determined by the regression algorithm from the measurement signals in position 2 and 4. Obviously a correlation is thus computed between m and b_y . The measurement equation for the Y-axis of the gyro 1 (Figure 4) shows that in the positions 2 and 4 of the 8-position test the measurement signal Mx/H includes also a component due to the anisoinertia ($\omega_x \neq 0, \omega_y \neq 0$ in (4.12))

For a typical value of $(C-A)/H = 10^{-3}$ sec this results in a torquer signal contribution of approx. $5 \cdot 10^{-7} \text{h}$ which is of course negligible.

If all 24 positions according to Figure 10a are utilized the same covariance matrix as that shown in Figure 12 will result for each of the four gyro axes.

The gyro parameters are practically no longer correlated. The measurement noise is reduced for all parameters. The accuracy improvement of the 24-position test as compared to the 8-position-test is about $\sqrt{24/8} = 1.7$.

A regression model according to equation (4.12) can be used in principle for each of the four gyro axes.

Main Position Nr.	Initial Position of the Three Axis Test Table	IMU-ATTITUDE			Main Position Nr.	Initial Position of the Three Axis Test Table	IMU-ATTITUDE		
		ψ_1 (Roll)	ψ_2 (Pitch)	ψ_3 (Yaw)			ψ_1 (Roll)	ψ_2 (Pitch)	ψ_3 (Yaw)
1		0°	0°	0°		0°	0°	0°	
		45°	0°	0°		0°	0°	±ψ/2	
		90°	0°	0°		0°	0°	-90°±ψ/2	
		135°	0°	0°		0°	0°	±ψ/2	
		180°	0°	0°		0°	0°	-90°±ψ/2	
		225°	0°	0°		0°	0°	±ψ/2	
		270°	0°	0°		0°	0°	0°	0°
		315°	0°	0°		0°	0°	0°	0°
2		0°	-90°	-90°		0°	-90°	-90°	
		0°	-45°	-90°		0°	-90°	-90°±ψ/2	
		0°	0°	-90°		0°	-90°	-180°±ψ/2	
		0°	45°	-90°		0°	-90°	-90°±ψ/2	
		0°	90°	-90°		0°	-90°	-90°±ψ/2	
		0°	135°	-90°		0°	-90°	-90°±ψ/2	
		0°	180°	-90°		0°	-90°	-90°±ψ/2	
		0°	225°	-90°		0°	-90°	-90°±ψ/2	
3		90°	0°	90°		90°	0°	90°	
		90°	45°	90°		90°	0°	90°±ψ/2	
		90°	90°	90°		90°	0°	±ψ/2	
		90°	135°	90°		90°	0°	90°±ψ/2	
		90°	180°	90°		90°	0°	±ψ/2	
		90°	225°	90°		90°	0°	90°±ψ/2	
		90°	270°	90°		90°	0°	±ψ/2	
		90°	315°	90°		90°	0°	90°±ψ/2	

Measurement: Sum of the Incremental Sensor Signals
 Measur. Time: 10 Min

Measurement: Sum of the Incremental Signals
 Measur. Time: 10 min.
 Const. rate: ± 0,1, 0,3, 1, 3, 10 Jdg/sec

Fig. 10: SUMMARY OF TEST - POSITIONS

Model for the 8-Position-Test:

$\text{Lat} = 45^\circ, \Omega_e = \Omega_E \cdot \cos 45^\circ = \Omega_E \cdot \sin 45^\circ$

$$\frac{1}{(1 - DSE_y)} \begin{bmatrix} M_x(i) \\ H_x(i) \end{bmatrix} - \Omega_e \begin{bmatrix} 0 & -1 & -1 \\ -\frac{1}{2}\sqrt{2} & -\frac{1}{2}\sqrt{2} & -1 \\ -\frac{1}{2}\sqrt{2} & \frac{1}{2}\sqrt{2} & -1 \\ 0 & 0 & -1 \\ 0 & 0 & -1 \\ 0 & 0 & -1 \\ 0 & 0 & -1 \\ 0 & 0 & -1 \end{bmatrix} \cdot \begin{bmatrix} 1 \\ a_{yx} \\ a_{yz} \end{bmatrix} = g \begin{bmatrix} 0 & 0 & 0 & 1 \\ \frac{1}{2}\sqrt{2} & 0 & \frac{1}{2}g & 1 \\ -\frac{1}{2}\sqrt{2} & 0 & -\frac{1}{2}g & 1 \\ 0 & 0 & 0 & 1 \\ -1 & 0 & 0 & 1 \\ 0 & 0 & 0 & 1 \\ 0 & -1 & 0 & 1 \\ 0 & 0 & 0 & 1 \end{bmatrix} \cdot \begin{bmatrix} a_m \\ a_n \\ a_y \end{bmatrix}$$

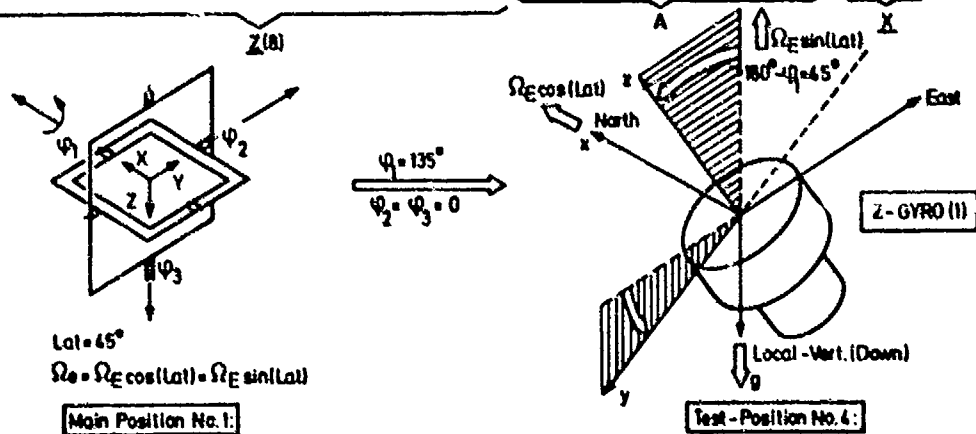


Fig. 11: REGRESSION-MODEL FOR MULTI-POSITION-TEST

8-Position-Test

$$\text{Var}(\hat{\underline{x}}) = \sigma^2 \cdot \begin{bmatrix} 0,36/g & 0 & 0 & -0,06/g \\ 0 & 0,5/g^2 & 0 & 0 \\ 0 & 0 & 2/g^4 & 0 \\ -0,06/g & 0 & 0 & 0,14 \end{bmatrix} \Rightarrow \begin{aligned} \sigma(\hat{m}) &= 0,006 \text{ } ^\circ/\text{h}/g \\ \sigma(\hat{q}) &= 0,007 \text{ } ^\circ/\text{h}/g \\ \sigma(\hat{n}) &= 0,014 \text{ } ^\circ/\text{h}/g^2 \\ \sigma(\hat{b}_y) &= 0,004 \text{ } ^\circ/\text{h}/g \end{aligned}$$

24-Position-Test

$$\text{Var}(\hat{\underline{x}}) = \sigma^2 \cdot \begin{bmatrix} 0,125/g & 0 & 0 & 0 \\ 0 & 0,125/g & 0 & 0 \\ 0 & 0 & 0,7/g^4 & 0 \\ 0 & 0 & 0 & 0,04 \end{bmatrix} \Rightarrow \begin{aligned} \sigma(\hat{m}) &= 0,004 \text{ } ^\circ/\text{h}/g \\ \sigma(\hat{q}) &= 0,004 \text{ } ^\circ/\text{h}/g \\ \sigma(\hat{n}) &= 0,008 \text{ } ^\circ/\text{h}/g^2 \\ \sigma(\hat{b}_y) &= 0,002 \text{ } ^\circ/\text{h}/g \end{aligned}$$

Fig. 12: COVARIANCE-ANALYSIS RESULTS FOR ONE GYRO-AXIS

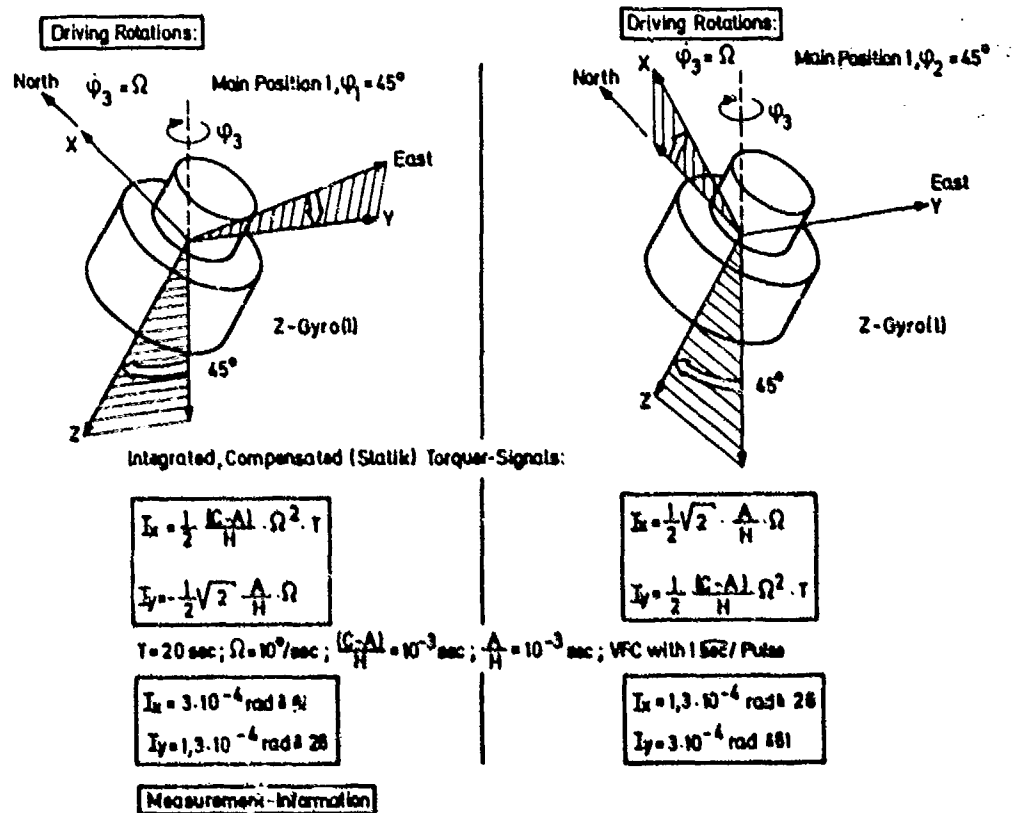


Fig. 13: VERIFICATION OF ANISOINERTIA-AND ANGULAR-ACCELERATION-TEST

4.3 Parameters for the compensation of dynamic errors

4.3.1 General Remarks

On the basis of the compensation for the dynamic errors shown in Figure 6, the following dynamic effects have to be taken into consideration:

- angular acceleration term ($A/H \cdot \omega$)
- anisoinertia term ($(C-A)H \cdot \omega_1 \cdot \omega_2$)
- motor coupling ($C/H \cdot \dot{\alpha}_t \cdot \omega$)

For simultaneous harmonic motions about the spin axis and about one of the input axes there further occurs the so-called pick-off-rectification effect which is taken into account for the compensation according to Figure 6 by measuring the pick-off angles. Due to the large bandwidth of the gyro caging loops for aircraft applications (large caging gain) the pick-off angles are small in this case. For this reason a compensation is often not required. As can be seen from Figure 6 no particular parameter is involved in the compensation of pick-off angle effects.

The parameters of the three above mentioned components are determined by the design of the gyro. They can be measured with a slide-gauge, so to speak and are not subject to considerable changes from gyro to gyro. For this reason it is therefore not appropriate to speak of sensor error parameters here. The gyro manufacturer can indicate these parameters accurately. A dynamic test is merely performed for verifying the manufacturing data. The motor coupling term should not be further considered here as its verification requires special measurements in the frequency domain to discern it from the frequency-independent anisoinertia-term. This goes beyond the scope of this paper. For the two other components various procedures are contemplated in the following where the application of which is based on the available test equipment.

4.3.2 Anisoinertia-term

Again only gyro 1 (z-gyro) is considered in the following.

The general measurement equations show that this term can be excited by simultaneous angular rates ω_z and ω_x respectively ω_z and ω_y .

For verifying $(C-A)H$ the sensor block is oriented as shown in Figure 13 and rotated about the vertical axis of the test table (ψ_3) at constant angular rate Ω during the time T . The thus generated angular rates ω_z and ω_y respectively ω_z and ω_x excite contributions in the torquer signals M_x/H and M_y/H generated by $(C-A)H$.

If these torquer signals are compensated for the known static error portions and integrated the signals I_x and I_y shown in Figure 13 will result.

Let us assume that these integrated values are available as pulse sequences at the output of voltage/frequency converters with a pulse weight of 1 arcsec.

For $T = 20$ sec, $\Omega = 10^\circ/\text{sec}$ the number of generated pulses for typical values $(C-A)H$ is readily measurable so that $(C-A)H$ can be verified as shown in Figure 13.

If ± 1 pulse is assumed as uncertainty, the accuracy for the determination of $(C-A)/H$ is in the order of 2%.

The parameter A/H determining the angular acceleration term is also excited during this test. The reason is the angular acceleration phase necessary to obtain the constant table rate. Its measuring accuracy is approximately 4% for the assumed test conditions. Another test method is described in paragraph 4.3.3.

By impressing sinusoidal or uniform angular rates Figure 14 shows two further procedures for the verification of $(C-A)H$.

In this respect it is always assumed that the measured torquer signals are compensated for the other error-model portions which are assumed to be known.

For sinusoidal excitation about the Y and Z-axis (spin-axis of the z-gyro (1)) of the sensor block the torquer signal M_x/H contains besides the nominal term the portions proportional to $(C-A)H$ shown in Fig. 14.

The latter can be considered as error $\Delta\omega_y$ in the measurement of ω_y .

The portions are independent of the frequency of the excitation signals as long as it is smaller than the bandwidth of the caging loops. For typical value of $(C-A)H = 10^{-3}$ sec the rectified portion causes a drift of $\Delta\omega_y = 0.02^\circ/\text{h}$ per $10^\circ/\text{sec}$ amplitude of the angular rate input.

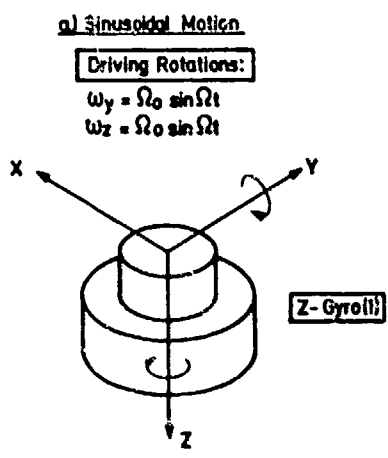
The motor coupling is also excited by ω_z if the frequency of the test signals is not smaller than 1 - 2 Hz.

Figure 14b shows an alternative possibility for the verification of $(C-A)H$. The sensor block is tilted on the test table about the X-axis through 45° so that for ψ_3 -rotations about the vertical axis of the test table angular rates ω_y and ω_z of the sensor block will occur.

For constant positive and negative rates $\dot{\psi}_3 = \pm \Omega$ the x-torquer signal is recorded. The sum of both torquer signals contains as useful information the portion (C-A)H. This leads with the numerical values shown in Figure 14 to an amount of 6°/h for the sum of the torquer signals. This value can be readily measured with a suitable test equipment.

4.3.3 Angular-acceleration term

As shown in paragraph 4.3.2, during the tests indicated in Figure 13 information is also obtained about the parameter A/H which determines the angular-acceleration-term. In order to excite this term in the x-torquer signal of the z-gyro an angular acceleration $\dot{\omega}_x$ is necessary. In this basis Figure 15 shows two further test-possibilities. In Figure 15a this term is excited by a sinusoidal rate about the x-axis.



Measurement:

$$\frac{1}{(1-DSFy)} \cdot \frac{M_x}{H} = \omega_y \cdot \dots \cdot \frac{(C-A)}{H} \cdot \omega_z \cdot \omega_y$$

- $\cdot \Omega_0 \sin(\Omega t)$ ← Nominal Term
- $\cdot \frac{(C-A)}{H} \cdot \frac{\Omega_0^2}{2} \cos(2\Omega t)$ ← Harmonic Pseudo Drift
- $\cdot \frac{(C-A)}{H} \cdot \frac{\Omega_0^2}{2}$ ← Rectified Drift

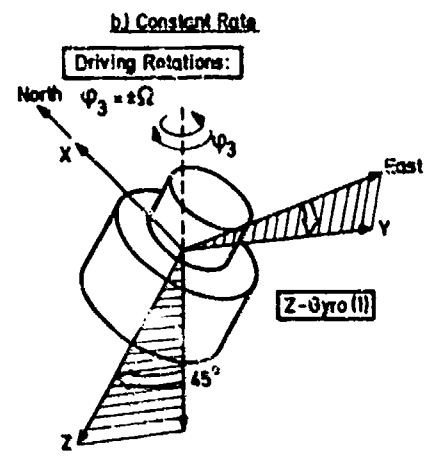
Reaction:

$$\Delta \bar{\omega}_y = \frac{(C-A)}{H} \cdot \frac{\Omega_0^2}{2}$$

$\frac{C-A}{H} = 10^{-3} \text{ sec}; \Omega_0 = 1^\circ/\text{sec}$

↓

$$\Delta \bar{\omega}_y = 0,02^\circ/\text{h}$$



Measurement:

$$\frac{1}{(1-DSFy)} \left[\frac{M_x}{H} /_+ + \frac{M_x}{H} /_- \right] = -\sqrt{2} \cdot \Omega s$$

- ← Earth Rate (Neglect)
- $\cdot \frac{(C-A)}{H} \cdot \Omega^2$ ← Useful Inform.
- $\cdot \frac{(C-A)}{H} \cdot \Omega^2$ ← To Be Neglected

Reaction:

$$\text{Torquing-Rate-Sum} = \frac{(C-A)}{H} \cdot \Omega^2$$

$\frac{C-A}{H} = 10^{-3} \text{ sec}; \Omega = 10^\circ/\text{sec}$

↓

$$\text{Torquing-Rate-Sum} = 6^\circ/\text{h}$$

Fig.14: VERIFICATION OF ANISOMERTIA-TERM

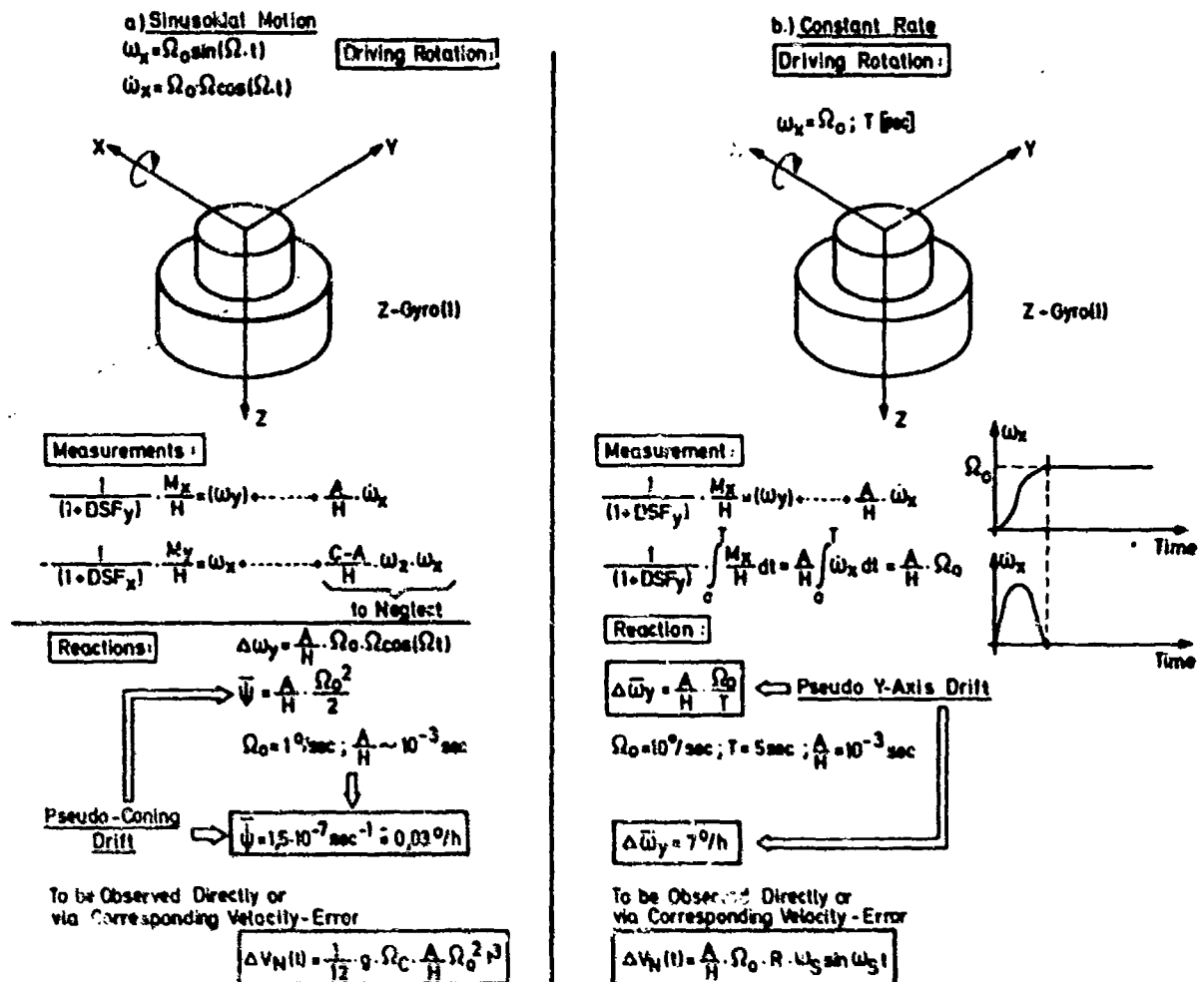


Fig. 15: VERIFICATION OF ANGULAR-ACCELERATION-TERM

The compensated torquing signal M_x/H contains a part $\Delta \omega_y$ according to $A/H \cdot \Omega_0 \cdot \Omega \cdot \cos(\Omega \cdot t)$. Together with the nominal sinusoidal rate ω_x measured by the torquing-signal M_y/H this gives rise to a pseudo-coning motion. This in turn causes a rectified drift about the third axis (heading-drift $\bar{\psi}$) which might be observed directly or from resultant velocity errors in the full inertial navigation system.

An alternative more direct method is shown in Figure 15b. A step-rate-input about the x-axis produces an observable averaged y-axis rate output $\Delta \bar{\omega}_y$, which is $7^\circ/\text{h}$ for a step-rate-input of $10^\circ/\text{sec}$, averaged over a time interval of 5 sec. Again this apparent y-axis drift could be observed directly or deduced from resulting velocity errors. Here the velocity error is caused by the averaged error rate $\Delta \bar{\omega}_y$, entering the schuler-loop as an impulse-perturbation.

5. Determination of the accelerometer parameters

The parameters of the accelerometers can also be determined by a multi-position test as described in paragraph 4.2.2 for the gyro.

For this purpose a linearization of the measurement equation (see Figure 7) is however required. The linearization provides the following error-model for the x-accelerometer:

$$\frac{U_x}{SF_x} - a_x = DK_x \cdot a_x + E_{xz} \cdot a_z + E_{xy} \cdot a_y + KQ_x \cdot a_x^2 + B_x \quad (5.1)$$

Figure 16 shows the linear regression model for a 6-position test. For this test those 6 positions of the 24 general positions are selected in which each surface of the sensor block is pointing once on downward direction. These positions are specially marked in Figure 16. Looking at the measurement matrix shown, it contains at least five linearly independent row-vectors so that the parameter vector is observable.

It results from the variances computed according to (4.18) and shown in Figure 17 for the elements of the parameter vector that the measurement noise σ^2 is already reduced performing the 6-position-test. The variances are computed supposing a measurement-noise of $\sigma^2 = (10^{-4}g)^2$.

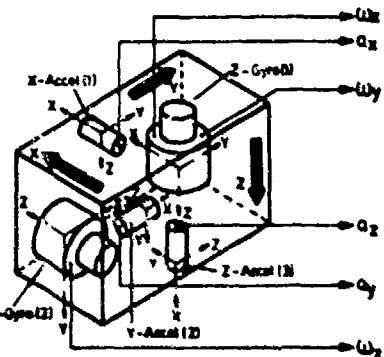
As in the 24-position test more redundant information is available, the parameters can of course be determined more accurately, namely by the factor $\sqrt{24/6} = 2$.

The variances of the 24-position test apply similiary to all three accelerometers.

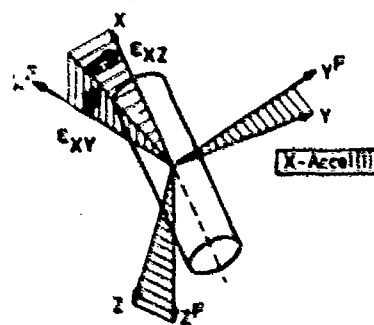
A relatively high correlation appears between bias and KQ_x (the g^2 -model-term) with the correlation coefficient of

$$\rho(B_x, KQ_x) = -0,69$$

Main Posit. Nr.	Position of the Test-table	Roll-Attitude		
		ϕ Roll	ψ Pitch	χ Yaw
1		0°	0°	0°
		45°	0°	0°
		90°	0°	0°
		135°	0°	0°
		180°	0°	0°
		225°	0°	0°
2		0°	90°	-90°
		0°	-45°	-90°
		0°	0°	-90°
		0°	45°	-90°
		0°	135°	-90°
		0°	180°	-90°
3		0°	0°	90°
		90°	45°	90°
		90°	90°	90°
		90°	135°	90°
		90°	180°	90°
		90°	225°	90°



Sensor Block



Linear X-Acceleration Model

$$\frac{U_x}{\sigma_{F_x}} = a_x \cdot [a_x \ a_y \ a_z \ a_x^2 \ 1] \cdot \begin{bmatrix} DK_x \\ ExZ \\ ExY \\ KQ_x \\ B_x \end{bmatrix}$$

Regression-Model For 6-Position-Test

$$\begin{bmatrix} \frac{U_x}{\sigma_{F_x}}(1) \\ \vdots \\ \frac{U_x}{\sigma_{F_x}}(6) \end{bmatrix} = \begin{bmatrix} 0 & 0 & 0 & 0 & 1 \\ 0 & 0 & 0 & 0 & 1 \\ 0 & 0 & 0 & 0 & 1 \\ 0 & 0 & 0 & 0 & 1 \\ 0 & 0 & 0 & 0 & 1 \\ 0 & 0 & 0 & 0 & 1 \end{bmatrix} \cdot \begin{bmatrix} DK_x \\ ExZ \\ ExY \\ KQ_x \\ B_x \end{bmatrix} + \begin{bmatrix} v(1) \\ \vdots \\ v(6) \end{bmatrix}$$

Measured Accel-Sign.
Determined From Test-Table Posit.
Unknown Param. Vect.
Maximum Noise

Z
A
X
V

Fig. 16: ACCELEROMETER REGRESSION-MODEL

B-Position-Test		
$\text{Var}(\hat{\underline{z}}) = \sigma^2 \cdot$	$\begin{bmatrix} 0,5/g^2 & 0 & 0 & 0 & 0 \\ 0 & 0,5/g^2 & 0 & 0 & 0 \\ 0 & 0 & 0,5/g^2 & 0 & 0 \\ 0 & 0 & 0 & 0,75/g^4 & -0,25/g^2 \\ 0 & 0 & 0 & -0,25/g^2 & 0,25 \end{bmatrix}$	\Rightarrow
		$\sigma(\text{DK}_x) = 0,71 \cdot 10^{-4}$ $\sigma(\text{EK}_{xz}) = 0,71 \cdot 10^{-4}$ $\sigma(\text{EK}_{xy}) = 0,71 \cdot 10^{-4}$ $\sigma(\text{KQ}_x) = 0,87 \cdot 10^{-4}/g$ $\sigma(\text{B}_x) = 0,50 \cdot 10^{-4}/g$
24-Position-Test		
$\text{Var}(\hat{\underline{z}}) = \sigma^2 \cdot$	$\begin{bmatrix} 0,125/g^2 & 0 & 0 & 0 & 0 \\ 0 & 0,125/g^2 & 0 & 0 & 0 \\ 0 & 0 & 0,125/g^2 & 0 & 0 \\ 0 & 0 & 0 & 0,3/g^4 & -0,1/g^2 \\ 0 & 0 & 0 & -0,1/g^2 & 0,075 \end{bmatrix}$	\Rightarrow
		$\sigma(\text{DK}_x) = 0,35 \cdot 10^{-4}$ $\sigma(\text{EK}_{xz}) = 0,35 \cdot 10^{-4}$ $\sigma(\text{EK}_{xy}) = 0,35 \cdot 10^{-4}$ $\sigma(\text{KQ}_x) = 0,54 \cdot 10^{-4}/g$ $\sigma(\text{B}_x) = 0,27 \cdot 10^{-4}/g$
	$\sigma^2 = (10^{-4}g)^2$	

Fig. 17: COVARIANCE FOR THE X-ACCELEROMETER

Again this correlation is spurious. It is based on the same reasons as those described for the gyro under 4.2.2.

Some further remarks should be made here concerning the linearization of the error-model. The measurement equation of the X-accelerometer (1) (Figure 7) for instance, can be expressed in a somewhat different way as shown in Figure 15.

In the linearization the second nonlinear part proportional to the scale factor error is neglected. It can be considered as additional measurement noise for the linear regression. As such it deteriorates of course the accuracy of the optimal parameter-vector estimate.

Figure 16 shows how the nonlinear portion can be taken into account for the determination of the parameter vector \underline{x} by way of iteration.

Starting from the linear model an estimated value \underline{x} is first determined through linear regression. This value can now be used for estimating the nonlinear portion of the error-model. The measurement vector \underline{z} is now corrected by this portion, and a new, corrected estimated value \underline{x}_c is determined for the parameter vector through linear regression, applying the corrected measurement-vector.

This operation is repeated by iteration until the desired accuracy is achieved which is preset by the intrinsic measurement noise. Tests performed in [3] have shown that 2-3 iterations are sufficient in most cases.

This procedure can of course be similarly used for taking into account nonlinear portions in the gyro model.

X-Accelerometer Equation

$$\frac{U_x}{SF_x} - a_x = [a_x \ a_y \ -a_z \ a_x^2 \ 1] \cdot \begin{bmatrix} DK_x \\ \epsilon_{xz} \\ \epsilon_{xy} \\ KQ_x \\ B_x \end{bmatrix} \quad \text{Linear Model}$$

$$+ DK_x \cdot [a_y \ -a_z \ a_x^2 \ 1] \cdot \begin{bmatrix} \epsilon_{xz} \\ \epsilon_{xy} \\ KQ_x \\ B_x \end{bmatrix} \quad \text{Nonlinear Part}$$

$$\underline{Z} = A \cdot \underline{X} + DK_x \cdot N \cdot \underline{X}_1 + Y$$

Z: As in Fig. 16
M: As in Fig. 16
X: As in Fig. 16
Y: As in Fig. 16

$$\underline{X}_1 = [\epsilon_{xz} \ \epsilon_{xy} \ KQ_x \ B_x]; N = \begin{bmatrix} a_y(1) & -a_z(1) & a_x^2(1) & 1 \\ \vdots & \vdots & \vdots & \vdots \\ a_y(n) & -a_z(n) & a_x^2(n) & 1 \end{bmatrix}$$

Convergent Iteration

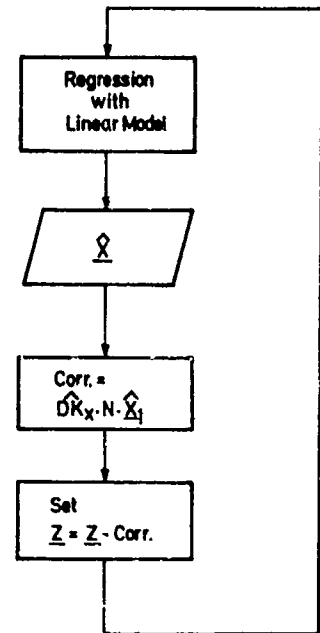


Fig. 18: ACCOUNTING FOR NONLINEAR PART IN ACCELEROMETER-MODEL

6. Variation of the number of model-parameters

The typical accelerometer model for the multi-position test will be used here to shortly indicate a linear regression procedure for a variable number of model parameters. In practical operation one is of course interested in keeping the sensor models as simple as possible. If the regression is however performed with a too simple model, larger estimated errors will result for the parameters (cf. also chapter 5, nonlinear portion).

The linear model, for instance, can be extended and recast as shown in equation (6.1).

$$\underbrace{\begin{bmatrix} \frac{U_x}{SF_x} (1) \\ \frac{U_x}{SF_x} (2) \\ \vdots \\ \frac{U_x}{SF_x} (n) \end{bmatrix}}_{\underline{Z}} = \underbrace{\begin{bmatrix} a_x(1) \\ a_x(2) \\ \vdots \\ a_x(n) \end{bmatrix}}_{A_m} + \underbrace{\begin{bmatrix} a_x(1) & a_y(1) & -a_z(1) & 1 & a_x(1)^2 & a_x(1)^3 & a_x(1)a_z(1) \\ a_x(2) & a_y(2) & -a_z(2) & 1 & a_x(2)^2 & a_x(2)^3 & a_x(2)a_z(2) \\ \vdots & \vdots & \vdots & \vdots & \vdots & \vdots & \vdots \\ a_x(n) & a_y(n) & -a_z(n) & 1 & a_x(n)^2 & a_x(n)^3 & a_x(n)a_z(n) \end{bmatrix}}_{A_{n-m}} \cdot \underbrace{\begin{bmatrix} DK_x \\ \epsilon_{xz} \\ \epsilon_{xy} \\ B_x \\ KQ_x \\ KC_x \\ KR_x \end{bmatrix}}_{\begin{bmatrix} \underline{\Delta}_m \\ \underline{\Delta}_{n-m} \end{bmatrix}} \quad (6.1)$$

$$\underline{Z} = (A_m | A_{n-m}) \cdot \begin{bmatrix} \underline{\Delta}_m \\ \underline{\Delta}_{n-m} \end{bmatrix} + Y$$

The following quantities can be computed with this problem formulation:

- Estimated value $\hat{x}_{m,m}$; assuming that only the first m-parameters of the parameter-vector \underline{x} are taken into account in the model.

$$\hat{x}_{m,m} = [A_m^T \cdot A_m]^{-1} \cdot A_m^T \cdot z \quad (6.2)$$

- Estimated value $\hat{x}_{m,n}$; for the first m-parameters assuming that all n-parameters of the parameter vector \underline{x} are taken into account in the model.

$$\hat{x}_{m,n} = \hat{x}_{m,m} - [A_m^T A_m]^{-1} A_m^T \cdot A_{n-m} \cdot [A_{n-m}^T \cdot A_{n-m} - A_{n-m}^T \cdot A_m [A_m^T A_m]^{-1} \cdot A_m^T \cdot A_{n-m}]^{-1} A_{n-m}^T [z - A_m \hat{x}_{m,m}] \quad (6.3)$$

- Estimated value $\hat{x}_{n-m,n}$ for the second (n-m) parameters of the parameter vector \underline{x} ; assuming that all n-parameters are taken into account in the model of equation (6.1).

$$\hat{x}_{n-m,n} = [A_{n-m}^T \cdot A_{n-m} - A_{n-m}^T \cdot A_m [A_m^T A_m]^{-1} \cdot A_m^T \cdot A_{n-m}]^{-1} \cdot A_{n-m}^T \cdot [z - A_m \hat{x}_{m,m}] \quad (6.4)$$

It is thus possible for given measurements and accuracy requirements to find the minimal order sensor model.

7. Application of test-methods to calibrate the Modular-Strapdown-System (MSS)

7.1 Introductory remarks

So far test-procedures have been described and treated in general. The following paragraphs are dealing with the application of these procedures for a particular system. First of all this system is briefly described.

With respect to potential applications in guidance and control of aircrafts, an experimental strapdown navigation system has been developed and built within the scope of the German Future Aircraft Technology Research Program (ZTL).

The following requirements have been established

- evaluation of the attitude angles and angular velocities in digital form
- autonomous alignment
- flexibility with respect to matching different accuracy categories by modular structure
- medium accuracy navigation performance of the experimental system
- possibility to update the system by external nav aids.

For calibration purposes the MSS has been submitted to various position- and ratetests at IABC test facilities in Munich. It is the objective of the following paragraphs to demonstrate the applicability and feasibility of the proposed test-procedures to evaluate the basic system parameters of a strapdown system.

7.2 Description of the MSS

7.2.1 Inertial Measurement Unit (IMU)

The Figure 19 shows the inertial measurement unit (IMU), consisting of two parts: the electronic box, containing the caging loops, power amplifier V/F-converters etc., and the inertial sensor unit with two dynamically tuned two degrees of freedom Teledyne gyro SDG5 and three Systron Donner accelerometers SD 4813A-1PX. Figure 20 gives a closer view of the sensor unit.

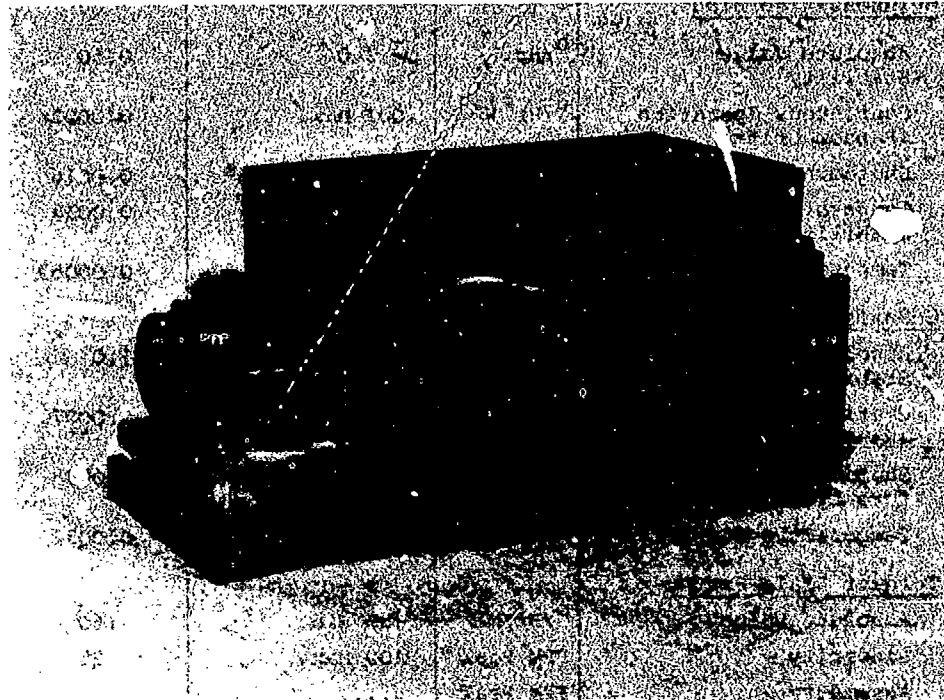


Fig.19: INERTIAL MEASUREMENT UNIT OF THE STRAPDOWN SYSTEM

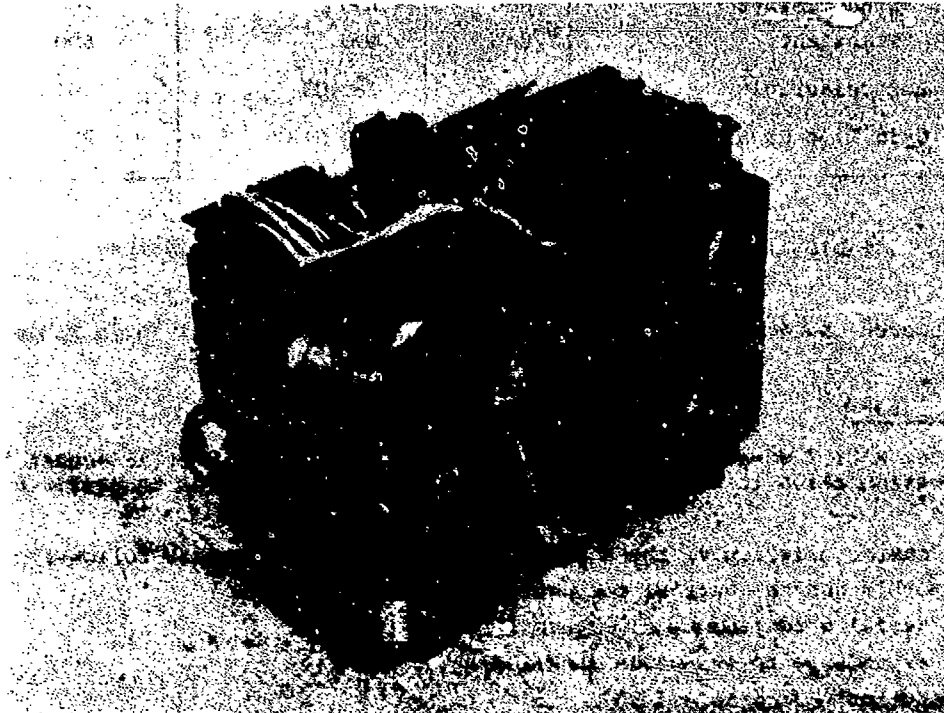


Fig.20: SENSOR UNIT

Parameter	Units	Specification Value	Typical Value (Mean)
<u>G-Insensitive Bias</u>			
Absolute Value Stability	$^{\circ}/\text{Hr}$	$0^{\pm} 2.0$	0.50
Continuous Operation (Random Drift)	$^{\circ}/\text{Hr } 1\sigma$.001 Max.	0.0005
Shutdown Repeatability	$^{\circ}/\text{Hr } 1\sigma$	101 Max.	0.0016
Temperature Cycle Stability	$^{\circ}/\text{Hr } 1\sigma$	0.0033
Temperature Sensitivity	$^{\circ}/\text{Hr}/^{\circ}\text{F}$	$0^{\pm} .002$	0.00059
<u>G-Sensitive Bias</u>			
Absolute Value Stability	$^{\circ}/\text{Hr}/\text{G}$	$0^{\pm} 1.0$	1.0
Continuous Operation (Random Drift)	$^{\circ}/\text{Hr}/\text{G } 1\sigma$.002 Max.	0.0007
Shutdown and Temperature Cycle Repeatability	$^{\circ}/\text{Hr}/\text{G } 1\sigma$	0.008
Temperature Sensitivity	$^{\circ}/\text{Hr}/\text{G}/^{\circ}\text{F}$	$0^{\pm} .02$	0.0032
<u>Torquer Scale Factor</u>			
Absolute Value	$^{\circ}/\text{Hr}/\text{MA}$	150 Min.	160
Linearity	PPM Peak	100 Max.	25
Asymmetry	PPM Peak	3
Temperature Sensitivity	PPM/ $^{\circ}\text{F}$	$.230^{\pm} 20$.229
<u>Axis Alignment</u>			
Absolute Value	Sec	60 Max.	30
Stability	Sec	10
<u>Angular Rate Capability</u>			
Steady State	$^{\circ}/\text{Sec}$	100	100
Transient	$^{\circ}/\text{Sec}$	400	500
Anisoeasticity	$^{\circ}/\text{Hr}/\text{g}^2$	$0^{\pm} .03$.01
Gyro Time Constant	Seconds	100 Min.	200

Table 1: Teledyne SDG-5 Gyro Performance Characteristics

The performance characteristics of the Teledyne SDG5 gyros are given in Table 1.

7.2.2 Computer

The computer MIDI 2 does performance all computations of the inertial sensor data. Within the test configuration it serves as preprocessor and by its DMA as transmitter of the IMU test data.

The basic characteristics of the MIDI 2 computer are summarized as follows:

- programmable general purpose computer
- 16 bit serial words; addresses , operation code parallel
- memory expandable to 4 k words (RAM/ROM)
- 8 μ /operation
- modular structure of the functional units
- programmable time basic generator
- DMA channel
- TTL technology
- MIL specified

7.2.3 Error Model of the MSS

The error model for a single gyro resp. accelerometer has been discussed in the previous chapters. From these equations the whole error model of the MSS has been deduced and is presented in Figure 21, as far as the static error parameters are concerned.

Gyro 1

$$-\frac{M_x}{H} = [1 + DSF_x(T)] [\omega_x + \alpha_{xz} \cdot \omega_y - \alpha_{xy} \cdot \omega_z - l_m(T) \cdot a_x - l_q \cdot a_y + l_n \cdot a_x \cdot a_z + b_x(T)]$$

$$\frac{M_x}{H} = [1 + DSF_y(T)] [\omega_y + \alpha_{yx} \cdot \omega_z - \alpha_{yz} \cdot \omega_x - l_m(T) \cdot a_y + l_q \cdot a_x + l_n \cdot a_y \cdot a_z + b_y(T)]$$

Gyro 2

$$\frac{M_z}{H} = [1 + DSF_z(T)] [\omega_z + \alpha_{zy} \cdot \omega_x - \alpha_{zx} \cdot \omega_y - l_m(T) \cdot a_z + l_q \cdot a_y + l_n \cdot a_z \cdot a_x + b_z(T)]$$

Accel. 1

$$\frac{U_x}{SF_x} = [1 + DK_x(T)] [a_x + \epsilon_{xz} \cdot a_y - \epsilon_{xy} \cdot a_z + KQ_x \cdot a_x^2 + B_x(T)]$$

Accel. 2

$$\frac{U_y}{SF_y} = [1 + DK_y(T)] [a_y + \epsilon_{yx} \cdot a_z - \epsilon_{yz} \cdot a_x + KQ_y \cdot a_y^2 + B_y(T)]$$

Accel. 3

$$\frac{U_z}{SF_z} = [1 + DK_z(T)] [a_z + \epsilon_{zy} \cdot a_x - \epsilon_{zx} \cdot a_y + KQ_z \cdot a_z^2 + B_z(T)]$$

Fig. 21: SENSOR ERROR MODEL OF THE MODULAR STRAPDOWN SYSTEM MSS

7.2.4 Accuracy Requirements upon the Tests

Prior to the tests it is necessary to specify how accurate the error parameters have to be determined to meet the demands put on the system performances. A common figure of merit for inertial navigation systems is the navigation accuracy expressed in nautical miles per hour.

From system analysis it is well known how single error sources propagate through the system. For the medium accuracy of the MSS it was stated that the uncompensated part of each significant error source should not exceed the limit of 1nm/h. From this statement some dozens requirements upon the accuracy of determining the error parameters by static tests have been deduced.

The most important results are summarized in Table 2 and 3. The values shown refer to an aircraft with an assumed velocity of 400 kn.

ERROR	NOTATION	ACCURACY	UNITS
BIAS	B_X, B_Y	$3 \cdot 10^{-4}$	G
SCALEFACTOR	DSF	$3 \cdot 10^{-4}$	G/G^2
	KQ	$3 \cdot 10^{-4}$	
MISALIGNMENT			
LEVEL	α_{XY}	$1 \cdot 10^{-4}$	RAD
	α_{YX}		
AZIMUTH	α_{XZ}	$2,5 \cdot 10^{-3}$	RAD
	α_{YZ}		

Table 2: Accuracy Requirements Upon Accelerometer Parameters

ERROR	NOTATION	ACCURACY	UNITS	NOTE
<u>BIAS</u>	B_X, B_Y	0,016	$^{\circ}/H$	NAV MODE
	B_X, B_Y	0,025	$^{\circ}/H$	ALIGN MODE
	B_Z	0,28	$^{\circ}/H$	NAV MODE
<u>SCALEFACTOR</u>	DSFK	$3,9 \cdot 10^{-4}$	-	CIRCULAR
<u>MISALIGNMENT</u>				FLIGHT
LEVEL	α_{XY}	$4,6 \cdot 10^{-5}$	RAD	CIRCULAR
	α_{YX}			FLIGHT
AZIMUTH	α_{XZ}	10^{-3}	RAD	NOT CRITICAL
	α_{YZ}			
Z-AXIS	α_{ZK} α_{ZY}			
<u>MASS UNBALANCE</u>				
GYRO 1	M^1	0,7	$^{\circ}/H/G$	ACCEL.FLIGHT
GYRO 1	M^1	0,1	$^{\circ}/H/G$	ALIGN MODE
GYRO 2	M^2	0,2	$^{\circ}/H/G$	STATION.FLIGHT
<u>QUADRATURE</u>				
GYRO 1	Q^1	0,7	$^{\circ}/H/G$	ACCEL.FLIGHT
GYRO 2	Q^2	1	$^{\circ}/H/G$	NOT CRITICAL

Table 3: Accuracy Requirements upon Gyro Parameters

7.3 Test Configuration

The philosophy of calibrating a strapdown system by tests consists basically in submitting the system to accurately known accelerations and angular velocities, observing the system output quantities, comparing them with the well defined input quantities and explaining the differences by the influence of various system error sources.

In Fig.22 a schematic view of the test configuration is shown how it has been built up at IABG in Munich. The IMU of the Strapdown System is fixed to the inner gimbal of the three axis test table. The test table is driven by the Interdata 8/32 Computer and is capable to orientate the IMU deliberately with respect to earth gravitational and rotational vector. Furtheron it is possible to rotate the IMU with very accurate constant angular velocity.

From the IMU leads a data link to the MSS navigation computer MIDI. By DMA the preprocessed data are transmitte to the Interdata 8/32 Computer and are recorded then together with the relevant data from the 3 axis test table on magnetic tapes.

The main processing of the test data runs off line on a IBM 370 Computer at Bodenseewerk in Überlingen.

In the sequel the essential features of the tests are described in more detail.

7.3.1 Three Axis Test Table

The three axis test table type 53 W from Contraves-Goerz Corporation is described in /3/ .

In Table 4 the performance characteristics which are of importance for the MSS test are listed.

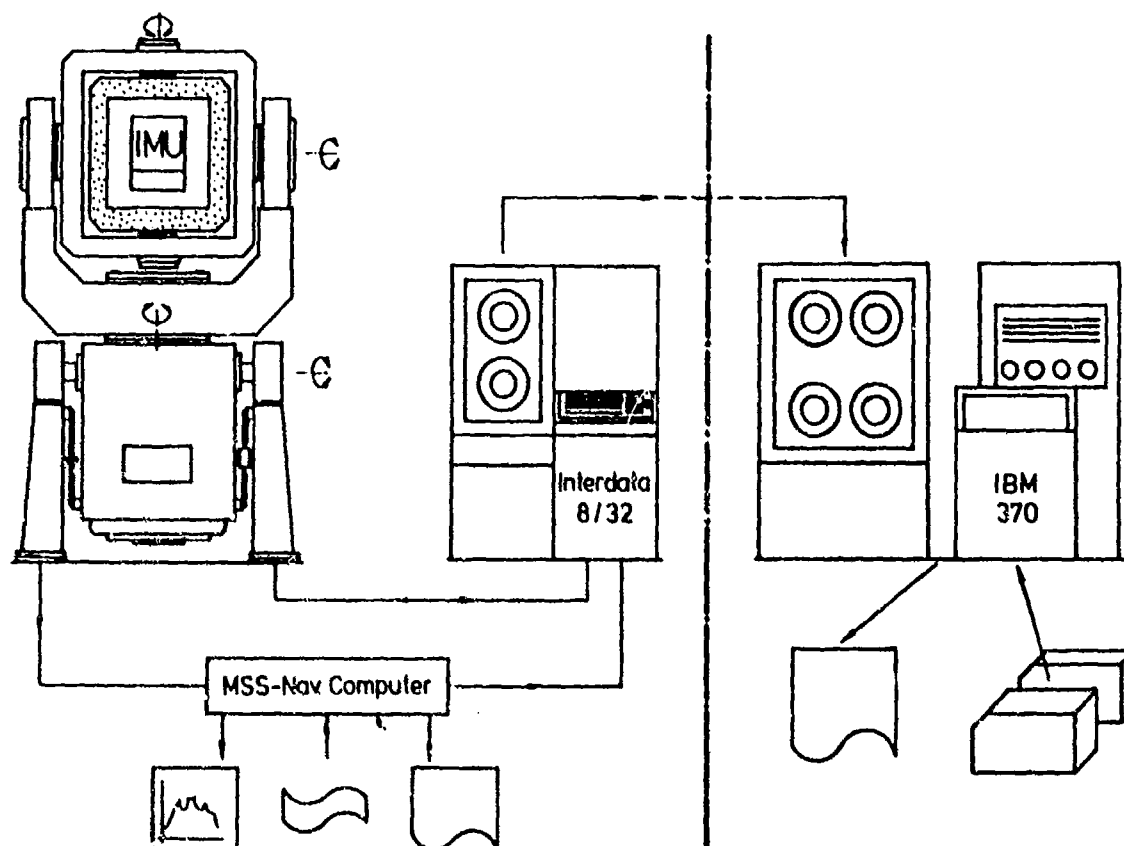


Fig. 22: TESTCONFIGURATION

<u>Angular Rates</u>	
Roll	400°/s
Pitch and Yaw	200°/s
<u>Angular Accelerations</u>	
Roll	500°/s ²
Pitch	300°/s ²
Yaw	200°/s ²
<u>Angle Accuracy</u>	
Solution	0,0001°
Absolute positioning	0,003°
Orthogonality	0,001°

Table 4: Performance characteristics of the 53 W
Contraves-Goerz Three Axis Test Table.

Data Transmission and Recording

The gyroscopes and the accelerometers torquer currents are measured by the voltage dropping at scale resistors. The voltages in turn are converted in the IMU by Voltages-to-Frequency-Converter into puls trains. In the navigation computer the pulses are accumulated and read out at constant time intervals. While navigating, the computer updates every 20 msec the quaternions, and every 100 msec an updating of the navigation occurs. In the test configuration, shown in Fig.23, the accumulated increments are transmitted every 200 ms via DMA to the Interdata computer. The navigation computer drives also an eight channel analogue recorder, which serves as a quick look instrument as it allows to observe continuously sensor signals and various navigation quantities.

Besides the pure sensor signals all relevant data are transmitted and recorded together with the reference data from the test table on magnetic tapes. In Table 5 the content of a data telegram is listed.

As a plausibility check the Interdata computer looks at the navigation position coordinates and interrupts the trial if the drift exceeds a given value.

The test records are finally sent to the Bodenseewerk at Überlingen where the processing of the test data with the IBM 370 computer starts.

<u>SENSOR SIGNALS</u>	
3	ANGULAR INCREMENTS
3	VELOCITY INCREMENTS
2	GYRO TEMPERATURES
4	GYRO PICK OFFS
<u>NAVIGATION COMPUTER DATA</u>	
4	QUATERNION ELEMENTS
3	ATTITUDE ANGLES
3	VELOCITIES
2	POSITIONCOORDINATES
1	ALTITUDE
<u>FLIGHT SIMULATOR DATA</u>	
3	ATTITUDE ANGLES
1	ANGULAR RATE

Table 5: Content of a data telegram

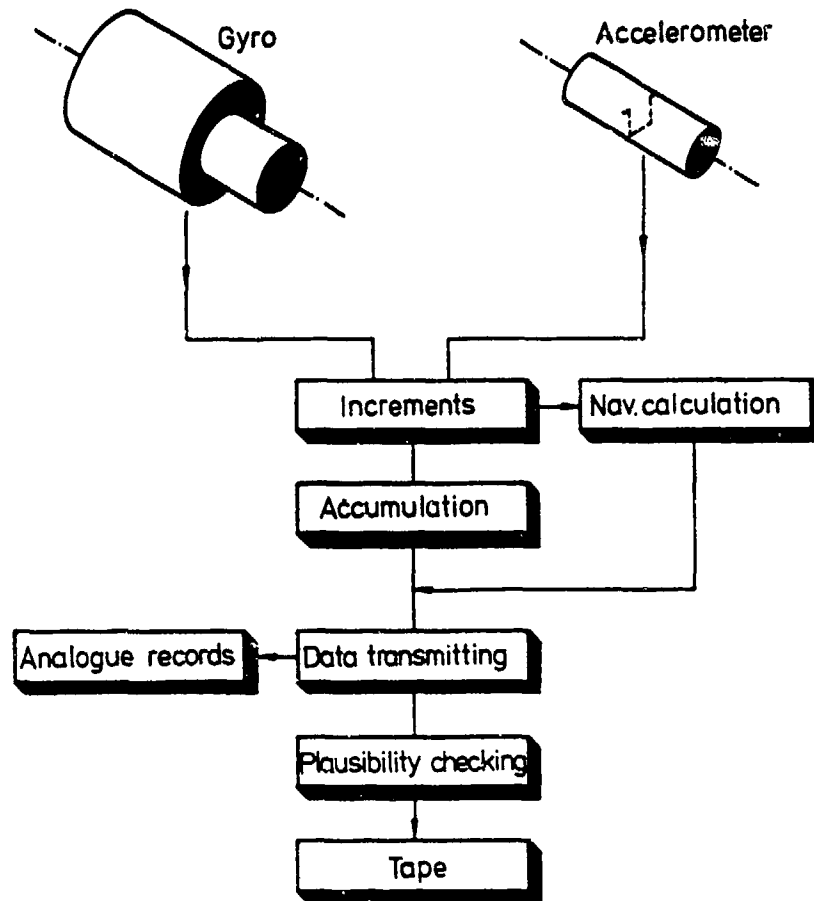


Fig.23: READ OUT AND RECORD OF TEST DATA

7.4 Test Procedures

7.4.1 24-Position-Static-Test

The 24-position-test is used for determining the parameters of the acceleration dependent error terms of a gyro (cf. 4.2.2)

- mass unbalance
- quadrature term
- anisoelectricity
- bias

The same procedure is used to calibrate the accelerometer parameters (cf. 5.)

- bias
- scale factor
- misalignment of the sensitive axes
- acceleration square term

The 24-position-test is characterized by positioning the IMU in 24 different orientation relative to the gravitation vector. The test starts with the first main position shown in Fig. 10.

For 10 minutes the sensor signals are read out, transmitted to the Interdata computer which in its turn completes the MSS data by the sampling the attitude angles of the three axis test table and adding them to the MSS data. All data were temporary recorded on a disc.

After ten minutes the orientation of the MSS is automatically changed by 45 degree until all eight positions belonging to a main position are completed. The trial is finished by writing the disc data on a magnetic tape.

7.4.2 Rate Test

The rate test is used to determine the parameters of the angular velocity error terms of the gyro

- scale factor
- misalignment of the sensitive axis.

The rate test is characterized by rotating the IMU about its three axis with accurately known angular velocities.

Similarly to the 24-position-test, the main orientations are defined in Figure 10. In each main orientation the IMU is rotated clockwise and counterclockwise with constant angular velocities 0, 0.1, 0.3, 1, 3, 10 Deg/h about the vertical axis of the three axis test table.

The measurement time is 36 sec in all cases. Start and stop of the rotation is however outside the measuring intervals in order to avoid dynamic effects.

Data read out and recording is identical to the 24 position test.

7.5 Determination of the Error Parameters

7.5.1 Processing of the Test Data

The continuous recording of the whole set of test data as shown in Table 5 with a sampling period of 200 msec generates a great amount of data, only a minor part of which is needed for the calibration process. The major part is not yet used, but is reserved for a deeper analysis of the overall system performance of the MSS later on.

A data reduction process is carried out with the aim to get the measurement vectors for the following linear regression processes. A survey of handling the test data is presented in Fig. 24. The main steps of data processing are

- retrieving the information from the tapes
- change into physical units
- plausibility checking of the data
- data reduction by accumulating the sensors increments
- determining the basic statistics of the data
- generating the measurement vectors
- selection of one of the preprogrammed error models
- performance of the linear regression
- determining the confidence intervals
- printing of the results

In the sequel these steps are described in more detail.

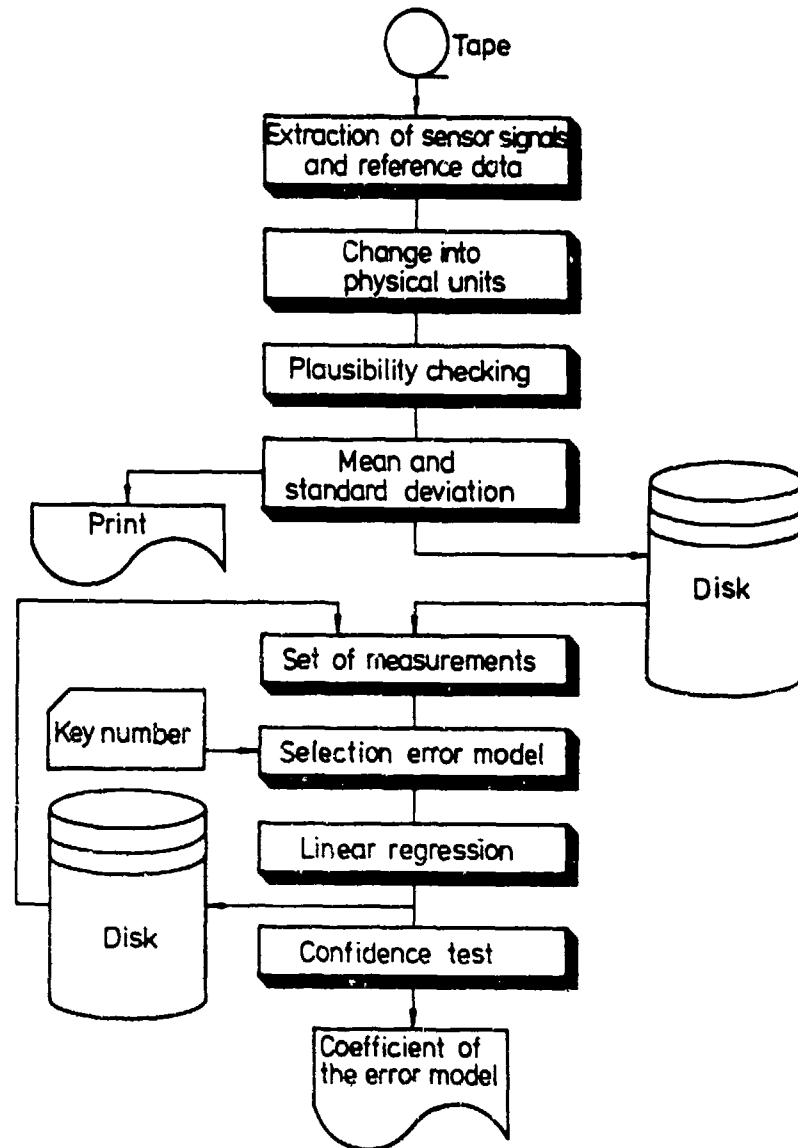


Fig. 24: PROCESSING OF THE TEST DATA

7.5.2 Data Reduction

A data file begins with a header which contains the marginal information about the test such as date, trial no., initial conditions, applied angular velocity etc. This information is printed as a header.

The data telegrams are then read out, piece by piece. Each time the sensor increments and the attitude of the test table are extracted, non relevant informations are omitted. The sensor outputs from each telegram are compared with corresponding values derived theoretically from the attitude resp. angular velocity of the three axis test table. When a pre-selected tolerance (e.g. 10 per cent) is surmounted, the content of the data telegram is supposed to be not plausible and is therefore omitted. This plausibility checking is principally thought as an aid for preserving the results from errors in the data transmission.

Within one trial all sensor increments are accumulated, the mean value, the mean square value, and the standard deviation of the mean value are derived.

The mean values of each trial of ten minutes are arranged in an array which serves as a measurement vector for the following linear regression process. In this way the data of the 24-position-test are reduced to 6 vectors (three gyros and three accelerometer axis) with 24 elements, the data of the rate test are reduced to 3 vectors with 27 elements. For further processing these vectors are stored on a disc memory.

7.5.3 Evaluation of the Error Parameters

7.5.3.1 Linear Regression

For estimation of the error parameters the linear regression method (least square adjustment) is applied, as described in paragraph 4.2.2.

For application of linear regression to the rate- and 24-positions-test, the error model from Figure 21 has to be adapted to equation (4.13).

This is done by

- linearizing the error model equation and neglecting higher order terms (cf. chap. 7.5.3.2)
- introducing the values of the gravity acceleration a_f and angular velocity ω_1 from test conditions into the equation
- integrating the error model equations over the measurement time.

As an example, the resulting set of measurement equations for the gyro x-axis is shown in (7.1)

X Axis Gyro Error Model:

$$-\frac{M_y}{H} = [kDSF_x(T)] [\omega_x + a_{xz} \omega_y - a_{xy} \omega_z - j_m(T) \cdot a_x - l_q \cdot a_y + l_n \cdot a_x \cdot a_z + b_x(T)] \quad (7.1)$$

X Axis Gyro Measurement Model for Linear Regression: $\underline{z} = A\underline{x} + \underline{y}$

(7.2)

$$\begin{bmatrix} Z_1 \\ \cdot \\ \cdot \\ \cdot \\ \cdot \\ \cdot \\ Z_n \end{bmatrix} = \begin{bmatrix} l_{x1} & l_{y1} & -l_{z1} & -j_{x1} & j_{y1} & j_{xiz1} & T_1 \\ \cdot & \cdot & \cdot & \cdot & \cdot & \cdot & \cdot \\ \cdot & \cdot & \cdot & \cdot & \cdot & \cdot & \cdot \\ \cdot & \cdot & \cdot & \cdot & \cdot & \cdot & \cdot \\ \cdot & \cdot & \cdot & \cdot & \cdot & \cdot & \cdot \\ \cdot & \cdot & \cdot & \cdot & \cdot & \cdot & \cdot \\ l_{xn} & l_{yn} & -l_{zn} & -j_{xn} & j_{yn} & j_{xizn} & T_n \end{bmatrix} \cdot \begin{bmatrix} DSF_x \\ a_{xz} \\ a_{yz} \\ l_m \\ l_q \\ l_n \\ b_x \end{bmatrix} \quad (7.3)$$

scale factor
misalignment
misalignment
mass unbalance
quadrature term
anisoeasticity
bias

Abbreviations:

$$l_{xi} = \int_0^{T_i} \omega_x dt, \quad l_{yi} = \int_0^{T_i} \omega_y dt, \quad l_{zi} = \int_0^{T_i} \omega_z dt \quad (7.4)$$

$$Z_i = \int_0^{T_i} (-M_y/H - \omega_x) dt \quad (7.5)$$

$$j_{xi} = \int_0^{T_i} a_x dt, \quad j_{yi} = \int_0^{T_i} a_y dt, \quad j_{xiz} = \int_0^{T_i} a_y a_z dt \quad (7.6)$$

Singularities

Care must be taken on singularities of the inverting process of the $(A^T A)$ matrix.

Singularity occurs when a column of the A matrix is zero or numerically near zero. Then the corresponding error parameter is not observable, the linear regression fails. In this case the nonobservable error parameters have to be omitted and the regression has to be done with the reduced error model (cf. chapter 7.5.3.3).

7.5.3.2 Iterative Linear Regression

The application of the linear regression in a straightforward way, will not yield the result wanted, as the accuracy of the parameters determined will be very different.

To obtain optimal results, the covariance matrix $(A^T A)^{-1}$ has been analysed in detail in paragraph 4.2.2. The result for the gyro x-axis is presented schematically in Fig. 25. In the rate test as well as in the 24-position test only certain parameters can be determined with sufficient accuracy. The other parameters are either not observable or only observable in a linear combination with some others, or they are observable with only insufficient accuracy. Similar results apply for the accelerometer x-axis shown in Fig.26.

An optimal use of all information is attained when the effects of those parameters which are not only scarcely observable are corrected by preprocessing the measurement vector \underline{z} . The vector of the known parameters then is reduced by these parameters.

This procedure can be done iteratively. The principle is shown in Fig. 27. The single steps are as follows:

1. Determining of DSP, α_j , α_{ix} by the rate test data
2. Correcting the 24-position-test data by DSP, α_j , α_{ix} effects from step 1.
3. Determining of m, q, n, b with preprocessed data from step 2.
4. Correcting of the rate test data by m, q, n, b effects from step 3.
5. Repeating the procedure at step 1 with data from step 4

Test	Mean Position	Parameter of the Gyro Error Model						
------	---------------	-----------------------------------	--	--	--	--	--	--

Rate Test		DSP _x	α_{xx}	α_{xy}	m^1	q^1	n^1	b_u
	1							
	2							
	3							
	1-2-3							

24 Position Test		DSP _x	α_{xx}	α_{xy}	m^1	q^1	n^1	L_y
	1							
	2							
	3							
	1-2-3							


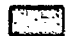


-  Determinable with sufficient accuracy
-  Determinable with insufficient accuracy
-  Not observable
-  Observable only as linear combination

Fig.25: OBSERVABILITY OF THE GYRO x-AXIS PARAMETERS

Test	Mean Position	Parameter of the Accel. Error Model				
------	---------------	-------------------------------------	--	--	--	--

24 Position Test		ΔK_x	ϵ_{xx}	ϵ_{xy}	ΔQ_x	B_x
	1					
	2					
	3					
	1-2-3					



-  Determinable with sufficient accuracy
-  Not observable

Fig.26: OBSERVABILITY OF THE ACCELEROMETER x-AXIS PARAMETERS

Preprocessing of the Test Data

The knowledge of known effects or parameters allows the correction of the raw gyro test data, denoted for this purpose as vector \underline{W}' , in the following manner (see Fig.28):

In first step the raw data \underline{W}' are corrected by multiplying them with the best known scale factor SCP.
 In the second step the effect of the other known error parameters, arranged in the partial correction vector \underline{x}_C^*

$$\underline{x}_C^* = [\alpha_{1j}(n-1), \alpha_{1k}(n-1), m(n-1), q(n-1), n(n-1), b(n-1)]^T \quad (7.7)$$

are calculated by the expression $\hat{A}^* \underline{x}_C^*$ and subtracted from scaled data $\underline{W}' \cdot \text{SCP}$. The star in \underline{x}_C^* and \hat{A}^* denotes the omitting of the elements corresponding to the scale factor error DSP as this parameter has to be treated separately.

The resulting vector

$$\underline{z}(n) = \underline{W}' \cdot \text{SCP}(n-1) - \hat{A}^* \underline{x}_C^*(n-1) \quad (7.8)$$

is now the basic measurement vector for subsequent linear regression. The result of the regression has then to be interpreted as iterative improvement of the scale factor SCP (n-1) and the correction-vector $\underline{x}_C^*(n-1)$.

Temperature Compensation

The preprocessing procedure serves also to correct the test data for temperature effects.

As can be seen from the gyro manufacturer's data sheet, scale factor, mass unbalance and bias show a linear temperature dependance. By known temperature coefficients these effects can be accounted for. For this purpose the gyro temperature is continuously measured and recorded with each data telegram and accounted for in the preprocessing procedure.

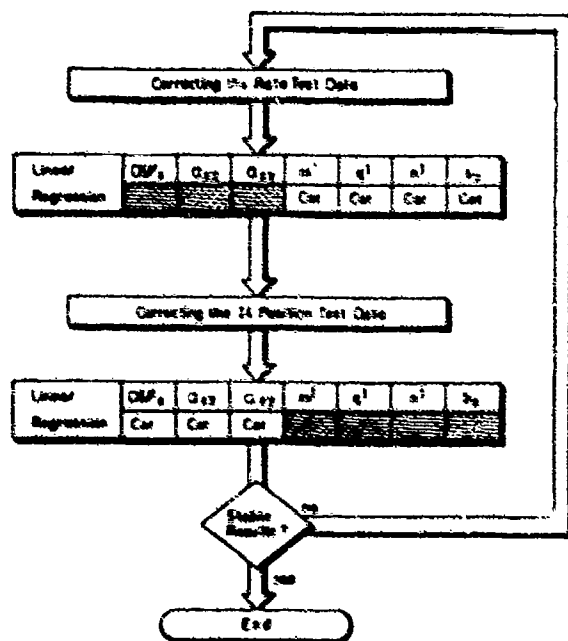


Fig.27: OPTIMAL USE OF ALL TEST DATA BY ITERATIVE LINEAR REGRESSION

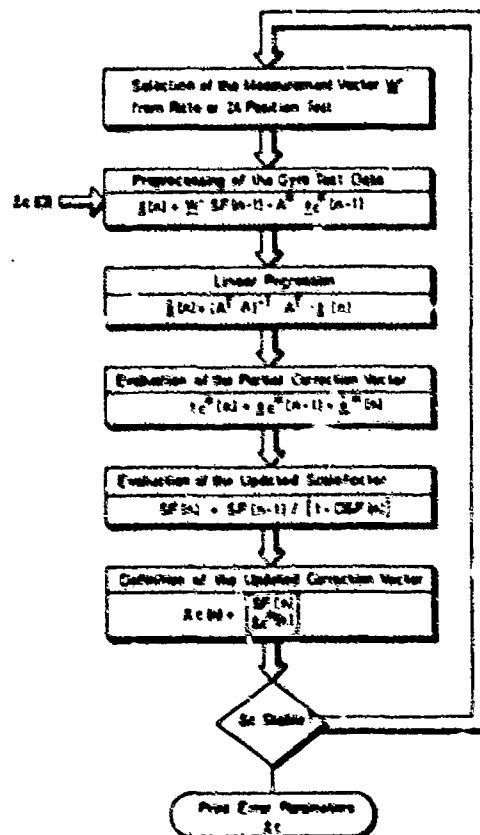


Fig.28: PREPROCESSING OF THE TEST DATA

Solution for Nonlinearities

The linear measurement model (7.2) was deduced from the error model (7.1) by neglecting the nonlinear higher order error terms such as

$$DSF_x \cdot (-ma_y + qa_x - na_x a_z + b_x)$$

From the values in Table 1 an estimation shows that under certain conditions this expression may correspond to a drift in the order of $0.1^\circ/h$, so that the neglect assumption will not hold and a pure linear regression will give false results.

The iterative application of the linear regression discussed above yield a solution of this problem, as in a second iteration run for which the linearity assumption is surely valid, the false parameters are corrected automatically.

Scale Factor for the Real Time Error Compensation

In the linearized error model (7.2) the scale factor error DSF can only be determined as coefficient to the input angular velocity of the three axis table. For the real time error compensation procedure in the navigation computer, the scale factor has however to be applied to the angular velocity measured by the strapdown gyros. This problem is also solved by the iterative linear regression. As is shown in Fig.28, by the preprocessing procedure the scale factor is indeed applied to the gyro output and not to the input angular velocity of the three test table.

Variation of the Error Models

The linear regression software system contains the option to use several different error models. By selection of a key number the complete error model from Fig.21 can be substituted by an reduced or by an extended error model (cf. also paragraph 6).

The use of error models in which single error parameters are omitted is necessary when test data are processed for which one or several parameters are not observable. For these cases the calibration software allows to compensate fully the effects of the canceled error parameter in the frame of the preprocessing procedure.

But also for judging the importance of the single error parameters it is very useful to be able to omit or to add single error terms in the error model.

Confidence Test

A very helpful means for judging whether an error parameter is significantly different from zero or not is a statistical confidence test.

A test of the hypothesis that the estimated value of the error parameter in the regression error model is significantly different from zero can be checked by comparing the value of the parameter x_i to its standard deviation σ_{x_i} , derived from (4.20).

Under the assumption that the measurement noise is normally distributed the random variable

$$t_i = x_i / \sigma_{x_i} \quad (5-15)$$

obeys a Student t-distribution.

Therefore $100 \cdot (1-q)\%$ confidence limits for x_i can be defined by

$$x_i \pm t_i(n-m, 1-q/2) \cdot \sigma_{x_i} \quad (7.9)$$

$n-m$ = degree of freedom

n = number of measurements

m = number of parameter determined

$(1-q/2)$ = percentage point of the t-distribution.

For the 24 position test and for the rate test the value t_i is found to be approximately 2 for 95% confidence limits and 23 degrees of freedom.

The parameter values from the linear regression are now said to be significant different from zero, if

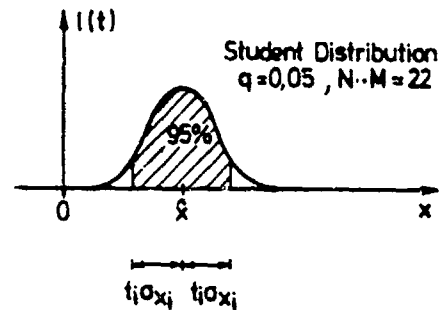
$$\frac{x_i}{2 \cdot \sigma_{x_i}} > 1 \quad (7.10)$$

Not significant values defined by

$$\frac{x_1}{2 \cdot \sigma_{x1}} \leq 1 \quad (7.11)$$

do not play any important role provided, that the confidence limits are smaller than stated in the accuracy requirements. This situation is illustrated in Figure 29.

Parameter is significantly different from 0:



Parameter is not significantly different from 0:

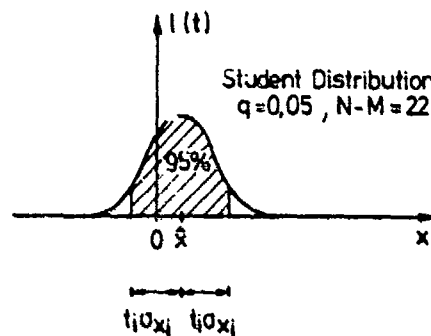


Fig.29:
CONFIDENCE TEST

Software Test

In order to test the complete software that was written in FORTRAN IV and further to test whether the subroutines for the matrix inversion are sufficient accurate a set of sensor error parameters were arbitrary defined. With the help of the error model, fictitious sensor signals were generated and fed to the computer program.

The values of the sensor parameters which were evaluated by the calibration software were in accordance with the original values in the order of $5 \cdot 10^{-7}$.

References

- /1/ D.K.Joos
Comparison of typical gyro errors for strapdown applications DGON-Symposium Gyro-Technology, Sept. 1977, Stuttgart, Germany
- /2/ P.J.Donoghue, L.B.Cotter
Test and evaluation of a dry tuned strapdown-gyroscope in a system environment
- /3/ H.Bertler
Test-facilities and procedures for strapdown-systems, DGON-Symp.Gyro-Technology, Sept. 1978, Bochum, Germany
- /4/ P.Eykhoff
System Identification, J.Wiley and Sons, London, 1974

15/ Kendall M., Stuart A.

The advanced theory of statistics
Charles Griffin and Company Ltd. London 1963

List of Symbols:

$\alpha_{ij}, \epsilon_{ij}$	misalignment of ith-sensor axis about jth-axis
m	mass-unbalance coefficient
q	quadrature coefficient
n	anisoelectricity coefficient
$\frac{C-A}{H}$	anisoinertia coefficient
C	rotor polar moment of inertia
A	rotor transverse moment of inertia
H	angular momentum
a_i	acceleration along ith sensorblock-axis
ω_i	angular-rate about ith sensorblock-axis
b_i	gyro bias about i-th sensorblock-axis
DSF_i	scalefactor error of ith sensorblock-axis
DK_i	i-accelerometer scalefactor-error
KQ_i	quadratic error-coefficient of i-accelerometer
KC_i	cubic error-coefficient of i-accelerometer
KR_i	cross-coupling coefficient of i-accelerometer
B_i	bias of i-accelerometer
α_t	motor phase angle
M_i	torque about ith gyro axis
U_i	output-voltage of i-accelerometer
T	temperature
t_i	i-distributed testvariable

REPORT DOCUMENTATION PAGE

1. Recipient's Reference	2. Originator's Reference AGARD-AG-254	3. Further Reference ISBN 92-835-1383-5	4. Security Classification of Document UNCLASSIFIED								
5. Originator Advisory Group for Aerospace Research and Development North Atlantic Treaty Organization 7 rue Ancelle, 92200 Neuilly sur Seine, France											
6. Title ADVANCES IN INERTIAL NAVIGATION SYSTEMS AND COMPONENTS											
7. Presented at											
8. Author(s)/Editor(s) Edited by Dr Helmut Sorg			9. Date April 1981								
10. Author's/Editor's Address Universitaet Stuttgart Institut A fuer Mechanik Pfaffenwaldring 9, D-7000 Stuttgart, FRG			11. Pages 142								
12. Distribution Statement This document is distributed in accordance with AGARD policies and regulations, which are outlined on the Outside Back Covers of all AGARD publications.											
13. Keywords/Descriptors <table border="0" style="width: 100%;"> <tr> <td style="width: 50%;">Inertial navigation</td> <td style="width: 50%;">Laser gyroscopes</td> </tr> <tr> <td>Components</td> <td>Strapdown systems</td> </tr> <tr> <td>Gyroscopes</td> <td>Cost engineering</td> </tr> <tr> <td>Dry bearings</td> <td>Reliability</td> </tr> </table>				Inertial navigation	Laser gyroscopes	Components	Strapdown systems	Gyroscopes	Cost engineering	Dry bearings	Reliability
Inertial navigation	Laser gyroscopes										
Components	Strapdown systems										
Gyroscopes	Cost engineering										
Dry bearings	Reliability										
14. Abstract <p>This AGARDograph, prepared at the request of the Guidance and Control Panel of AGARD, covers the state-of-the-art characterized by three major developments in the last decade: the dry tuned gyro, the laser gyro and the strapdown technology, taking into consideration cost reduction and higher reliability.</p>											

<p>AGARDograph No.254 Advisory Group for Aerospace Research and Development, NATO ADVANCES IN INERTIAL NAVIGATION SYSTEMS AND COMPONENTS Edited by Dr Helmut Sorg Published April 1981 142 pages</p> <p>This AGARDograph, prepared at the request of the Guidance and Control Panel of AGARD, covers the state-of-the-art characterized by three major developments in the last decade: the dry tuned gyro, the laser gyro and the strapdown technology, taking into consideration cost reduction and higher reliability.</p> <p>ISBN 92-835-1383-5</p>	<p>AGARD-AG-254</p> <p>Inertial navigation Components Gyroscopes Dry bearings Laser gyroscopes Strapdown systems Cost engineering Reliability</p>	<p>AGARDograph No.254 Advisory Group for Aerospace Research and Development, NATO ADVANCES IN INERTIAL NAVIGATION SYSTEMS AND COMPONENTS Edited by Dr Helmut Sorg Published April 1981 142 pages</p> <p>This AGARDograph, prepared at the request of the Guidance and Control Panel of AGARD, covers the state-of-the-art characterized by three major developments in the last decade: the dry tuned gyro, the laser gyro and the strapdown technology, taking into consideration cost reduction and higher reliability.</p> <p>ISBN 92-835-1383-5</p>	<p>AGARD-AG-254</p> <p>Inertial navigation Components Gyroscopes Dry bearings Laser gyroscopes Strapdown systems Cost engineering Reliability</p>
<p>AGARDograph No.254 Advisory Group for Aerospace Research and Development, NATO ADVANCES IN INERTIAL NAVIGATION SYSTEMS AND COMPONENTS Edited by Dr Helmut Sorg Published April 1981 142 pages</p> <p>This AGARDograph, prepared at the request of the Guidance and Control Panel of AGARD, covers the state-of-the-art characterized by three major developments in the last decade: the dry tuned gyro, the laser gyro and the strapdown technology, taking into consideration cost reduction and higher reliability.</p> <p>ISBN 92-835-1383-5</p>	<p>AGARD-AG-254</p> <p>Inertial navigation Components Gyroscopes Dry bearings Laser gyroscopes Strapdown systems Cost engineering Reliability</p>	<p>AGARDograph No.254 Advisory Group for Aerospace Research and Development, NATO ADVANCES IN INERTIAL NAVIGATION SYSTEMS AND COMPONENTS Edited by Dr Helmut Sorg Published April 1981 142 pages</p> <p>This AGARDograph, prepared at the request of the Guidance and Control Panel of AGARD, covers the state-of-the-art characterized by three major developments in the last decade: the dry tuned gyro, the laser gyro and the strapdown technology, taking into consideration cost reduction and higher reliability.</p> <p>ISBN 92-835-1383-5</p>	<p>AGARD-AG-254</p> <p>Inertial navigation Components Gyroscopes Dry bearings Laser gyroscopes Strapdown systems Cost engineering Reliability</p>

4
AGARD

NATO  OTAN

7 RUE ANCELLE · 92200 NEUILLY-SUR-SEINE
FRANCE

Telephone 745.08.10 · Telex 610176

**DISTRIBUTION OF UNCLASSIFIED
AGARD PUBLICATIONS**

AGARD does NOT hold stocks of AGARD publications at the above address for general distribution. Initial distribution of AGARD publications is made to AGARD Member Nations through the following National Distribution Centres. Further copies are sometimes available from these Centres, but if not may be purchased in Microfiche or Photocopy form from the Purchase Agencies listed below.

NATIONAL DISTRIBUTION CENTRES

BELGIUM

Coordonnateur AGARD - VSL
Etat-Major de la Force Aérienne
Quartier Reine Elisabeth
Rue d'Evere, 1140 Bruxelles

CANADA

Defence Science Information Services
Department of National Defence
Ottawa, Ontario K1A 0K2

DENMARK

Danish Defence Research Board
Østerbrogades Kaserne
Copenhagen Ø

FRANCE

O.N.E.R.A. (Direction)
29 Avenue de la Division Leclerc
92320 Châtillon sous Bagneux

GERMANY

Fachinformationszentrum Energie,
Physik, Mathematik GmbH
Kernforschungszentrum
D-7514 Eggenstein-Leopoldshafen 2

GREECE

Hellenic Air Force General Staff
Research and Development Directorate
Holargos, Athens

ICELAND

Director of Aviation
c/o Flugrad
Reykjavik

UNITED STATES

National Aeronautics and Space Administration (NASA)
Langley Field, Virginia 23365
Attn: Report Distribution and Storage Unit

THE UNITED STATES NATIONAL DISTRIBUTION CENTRE (NASA) DOES NOT HOLD STOCKS OF AGARD PUBLICATIONS, AND APPLICATIONS FOR COPIES SHOULD BE MADE DIRECT TO THE NATIONAL TECHNICAL INFORMATION SERVICE (NTIS) AT THE ADDRESS BELOW.

PURCHASE AGENCIES

Microfiche or Photocopy

National Technical
Information Service (NTIS)
5285 Port Royal Road
Springfield
Virginia 22161, USA

Microfiche

Space Documentation Service
European Space Agency
10, rue Mario Nikis
75015 Paris, France

Microfiche

Technology Reports
Centre (TRI)
Station Square House
St. Mary Cray
Orpington, Kent BR5 3RP
England

Requests for microfiche or photocopies of AGARD documents should include the AGARD serial number, title, author or editor, and publication date. Requests to NTIS should include the NASA accession report number. Full bibliographical references and abstracts of AGARD publications are given in the following journals:

Scientific and Technical Aerospace Reports (STAR)

published by NASA Scientific and Technical
Information Facility
Post Office Box 8757
Baltimore/Washington International Airport
Maryland 21240, USA

Government Reports Announcements (GRA)

published by the National Technical
Information Service, Springfield
Virginia 22161, USA